SOME ELECTRIC AND MAGNETIC PROPERTIES OF Cr IMPURITIES DISSOLVED IN EXCHANGE ENHANCED HOSTS

By

R. M. ROSHKO

A thesis submitted to the Faculty of Graduate Studies of the University of Manitoba in partial fulfilment of the requirements for the degree of Doctor of Philosophy.

Department of Physics
University of Manitoba
February , 1979.

SOME ELECTRIC AND MAGNETIC PROPERTIES
OF Cr IMPURITIES DISSOLVED IN EXCHANGE ENHANCED HOSTS

BY

ROY MICHAEL ROSHKO

A dissertation submitted to the Faculty of Graduate Studies of the University of Manitoba in partial fulfillment of the requirements of the degree of

DOCTOR OF PHILOSOPHY

Abstract

The electrical resistivity and A.C. magnetic susceptibility of several PdCr alloys containing between .05 and 18 at. % Cr and several PtCr alloys containing between .05 and 21 at. % Cr have been measured over the temperature range 1.4 to 300K. The incremental resistivities of the most dilute PdCr and PtCr alloys examined ($.05 \leq c \leq 0.3$ at. % Cr) are shown to contain a temperature-dependent contribution which can be fitted with a high degree of accuracy to an expression of the form $\Delta\rho(T) = Ac + Bc\,\ell n(T^2 + \theta^2)^{\frac{1}{2}}$ (although deviations from Matthiessen's rule restrict the temperature range over which the fits can be carried out to $T \geq 68$K for PdCr and $T \geq 45$K for PtCr). These fits yield a single-impurity characteristic temperature θ_s for Cr impurities of ~43K in Pd and ~73K in Pt. Similar fits at higher concentrations ($5 \leq c \leq 12$ at. % Cr for PtCr and $4 \leq c \leq 10$ at. % Cr for PdCr) show that, while the above expression for $\Delta\rho(T)$ provides a good description of the incremental resistivity data at "high" temperatures, systematic deviations between the measured and "predicted" $\Delta\rho(T)$ occur at "low" temperatures and these are attributed to interactions between Cr impurities. For the PtCr alloys containing between 5 and 12 at. % Cr and for the Pd - 4, 5, and 6 at. % Cr alloys these deviations are such that the measured values for both $\Delta\rho(T < \theta)$ and $d[\Delta\rho(T << \theta)]/dT$ are larger than the "predicted" values. For the Pd - 8 and 10 at. % Cr alloys, $\Delta\rho(T)$ exhibits a broad maximum at low temperatures which is characteristic of an

extended magnetic freezing of the impurity moments (although the delay in the appearance of the maximum until the Cr concentration has reached 8 at. % suggests that the conventional long range RKKY coupling is relatively ineffective in these systems, with any extended freezing arising primarily from direct d-d overlap between nearest-neighbour Cr impurities). Moreover, the data on more concentrated <u>Pd</u>Cr alloys containing between 11 and 18 at. % Cr show that the behaviour of <u>Pd</u>Cr resembles that of canonical spin glasses : at low temperatures $\Delta\rho(T) \propto AT^{3/2}$ with $A \propto -\log c$ over the concentration range investigated, while at higher temperatures $\Delta\rho(T)$ passes through an inflection point (at T_{INFL}) and then a maximum (at T_{MAX}) above which it decreases with increasing temperature. There are, however, several quantitative differences between <u>Pd</u>Cr and canonical spin glasses : both T_{MAX} and $\Delta\rho(T_{MAX}) - \Delta\rho(0)$ are typically an order of magnitude smaller than in canonical spin glasses of comparable concentration, while the slope of $\Delta\rho(T)$ above T_{MAX} is about an order of magnitude larger than in canonical spin glasses. These differences probably arise from the fact that canonical spin glasses are "good" moment systems (T_K or $\theta_s << T_{INFL}$) whereas <u>Pd</u>Cr is not ($\theta_s \sim T_{INFL}$). No maximum is observed in the incremental resistivities of any of the <u>Pt</u>Cr alloys examined here. However, both the electrical resistivity and A.C. susceptibility data suggest the occurrence of anomalous behaviour above about 17 at. % Cr, which appears to coincide with the onset of an atomic order-disorder transformation in <u>Pt</u>Cr : the resistivity $\rho(T)$ possesses an inflection point, a "knee" and a high-temperature slope, $\left.\frac{d\rho}{dT}\right|_{T > T_{KNEE}}$, which increases abruptly on going from the disordered to

the ordered phase, while the A.C. susceptibility exhibits a maximum as a function of temperature. From this and existing static magnetization and specific heat data, it is inferred that magnetic freezing of the spin glass type occurs, brought about primarily by direct d-d overlap between nearest-neighbour Cr impurities, which also serves to stabilize the moment on the Cr site. Finally, the effect of interactions between Cr impurities on the electrical resistivity is summarized by plotting the difference $\Delta\rho(1.5K) - \Delta\rho(4.2K)$ as a function of the nominal Cr concentration for both the PdCr and PtCr systems. From these plots it can be seen that the difference $\Delta\rho(1.5K) - \Delta\rho(4.2K)$ initially increases with increasing Cr concentration, passes through a maximum (at ~5 at. % for PdCr and ~11 at. % for PtCr) and then decreases with a further increase in Cr content. This type of behaviour is interpreted in terms of a competition between (a) moment stabilization at a single impurity site, and (b) correlations between moments at different impurity sites, and the peak indicates a critical concentration which separates the two regimes.

ACKNOWLEDGEMENTS

I would like to thank Professor Gwyn Williams who supervised this research project and whose many helpful comments and suggestions contributed immeasurably to the success of this work. I would also like to thank Dr. Iman Maartense for his invaluable advice relating to the measurement and interpretation of the A.C. susceptibility data, and Professor Paul Gaunt for many illuminating discussions concerning the magnetic properties of spin glasses and related systems.

TABLE OF CONTENTS

Chapter 3 Results and Discussion 127.

CHAPTER 1

THEORETICAL CONCEPTS

1.1 Introduction

When atoms with partially filled inner shells (transition metals or rare earths) are dissolved in small amounts as substitutional impurities in nonmetallic hosts, they often assume a definite ionic valence state and exhibit the corresponding Hund's rule magnetic moment (although crystal field effects may have to be taken into account). In the case of metallic hosts, however, the presence of the broad conduction band tends to delocalize the magnetic electrons (i.e., the d electrons in transition metals or the f electrons in rare earths) and hence to destroy the atomic moment. Even if transition metal or rare earth impurities show signs of possessing a well-defined magnetic moment at high temperatures, they often appear to lose it when the temperature is lowered.

Of the theories which set out to solve the problem of local moment *formation* in metals from first principles, the most important are the Friedel model [1, 2], the Anderson model [3] and the Hirst model [4]. (The Hirst model is perhaps more aptly described as a moment *survival* rather than a moment formation model.) In essence, these theories attempt to answer the following question : Given a single transition metal or rare earth impurity embedded in an otherwise nonmagnetic metal, what are the conditions under which the impurity will be "magnetic" ? Much of the difficulty in solving this problem lies in the apparently dual character of the d-shell or f-shell electrons : on the one hand (as in free atoms), these electrons are responsible for the observed magnetic moments which seem to be well localized on the impurity sites, while, on the other hand, they also participate to some degree in the conduction process. The Friedel and Anderson models rely on the application of the Hartree-Fock one-electron (or single-particle) approximation, treating the Coulomb and other intra-ionic interactions, which are responsible for Hund's rules in atomic d- and f-shells, as weak perturbations, and describing the electronic states of the impurity's magnetic shell (the d-shell in transition elements or the f-shell in rare earths) in terms of virtual bound states (a virtual bound state is a state strongly admixed with the free electron states of the conduction band and having a finite energy width). Recently the question has been raised as to whether these traditional models are really appropriate to describe existing systems, since they tend to strongly overemphasize the itinerant aspects of the problem. The Hirst model (or the configuration-based approach), on the other hand, leaves the original ionic-type many-electron states of the impurity untouched, and predicts much more specifically than does the Friedel-Anderson model the conditions under which the moment does not survive. According to this model, the ionic many-electron states can normally only be perturbed and only rarely be wiped out by interactions with the conduction electrons.

As far as interpreting the experimental data obtained from measurements of the electric and magnetic properties of dilute "magnetic" alloys, two theories are currently available which have met with some success : the s-d model [5] and the localized spin fluctuation (LSF) model [6, 7]. In the s-d model, the impurity is assigned a well-defined spin $\vec{S}$ which interacts with the conduction electrons through a spin-dependent potential (the so-called s-d exchange potential) of the form $H_{sd} = - J \vec{S} \cdot \vec{s}$, where J is the exchange coupling constant and $\vec{s}$ is the conduction electron spin. This model provides an explanation for the phenomenon of the resistivity minimum (known as the "Kondo effect"), as well as a useful description of the spin polarization around the impurity and indirect interactions between spins (the so-called RKKY interaction). Since it starts from the assumption of a static spin (and hence magnetic moment), the s-d exchange model omits any consideration of the dynamics of the local moment or, in other words, the time scale over which a moment exists. This is precisely the aspect of the local moment problem with which the localized spin fluctuation (LSF) model is concerned. According to this model, the question of the existence of a magnetic moment is a matter of <u>time</u> ; i.e., the fundamental question is whether or not the fluctuations in the spin density at the impurity site can be sufficiently slow that, on the time scale of a given experimental probe, there <u>appears</u> to be a magnetic moment. However, whether approached from the point of view of the s-d exchange model, or from the postulate that virtual bound states of the Friedel-Anderson type, while satisfying some criterion for being nonmagnetic, are capable of undergoing local spin fluctuations (in the spirit of the LSF model), it is always possible to specify approximately some single-impurity characteristic temperature T_s (either the Kondo temperature T_K or the LSF temperature T_{sf}) above which local moment behaviour is detected in various properties, and below which the impurities appear to lose their magnetic moments.

The s-d model and the LSF model describe the behaviour of an isolated impurity dissolved in a metallic host. However, as the impurity concentration is increased above the dilute (or single-impurity) limit, interactions between different impurity spins become important, even at very low concentrations, with the dominant interaction mechanism being the long-range, oscillatory RKKY interaction [8, 9, 10] -- indirect exchange mediated by the conduction electrons. For "good" moment systems (where the temperature characteristic of the interactions is greater than any possible single-impurity characteristic temperature T_s for all concentrations of solute above a small fraction of 1 at.%), these interactions lead, at low temperatures, to a cooperative freezing of the impurity moments in random orientations and such a disordered ground state is currently described as a spin glass. For systems where the impurity moments are not well defined (i.e., LSF systems), the role of interactions appears to be initially to stabilize (or slow down) the spin fluctuations, with spin glass behaviour being observed once interactions have driven T_s below the spin glass ordering temperature.

1.2 Friedel Model

The Friedel model [1, 2] considers the case of a single first row transition metal atom dissolved substitutionally in a simple or noble metal host. For simplicity, the transition impurity is assumed to possess a single, orbitally nondegenerate atomic d state $|d\rangle$ with an unperturbed energy E_0 which lies within the conduction band of the host, as shown in FIG.1.2-1.

In order to describe the modifications to the atomic d state as a result of embedding it in the conduction band, Friedel introduced an s-d covalent admixture interaction, V, between the localized d state and the conduction electron states $|k\rangle$. The effect of this mixing interaction is to induce transitions between the localized d state and the conduction band states. Friedel showed that, as a result of these mixing transitions, the localized state is shifted in energy from its unperturbed value E_0 and acquires a finite energy width 2Δ as shown in FIG.1.2-2, forming what is known as a virtual bound state (VBS). In terms of the covalent admixture matrix element, $\langle d|V|k\rangle$, the energy shift Γ and the width 2Δ of the virtual level are given by [2]

$$\Gamma = \text{p.p.} \int \frac{|\langle d|V|k\rangle|^2}{\varepsilon - \varepsilon_k}\, d^3k \qquad (1.2\text{-}1)$$

and

$$2\Delta = 2\pi\, \overline{|\langle d|V|k\rangle|^2}\, N(\varepsilon) \quad . \qquad (1.2\text{-}2)$$

$N(\varepsilon)$ is the density of states with energy ε in the conduction band of

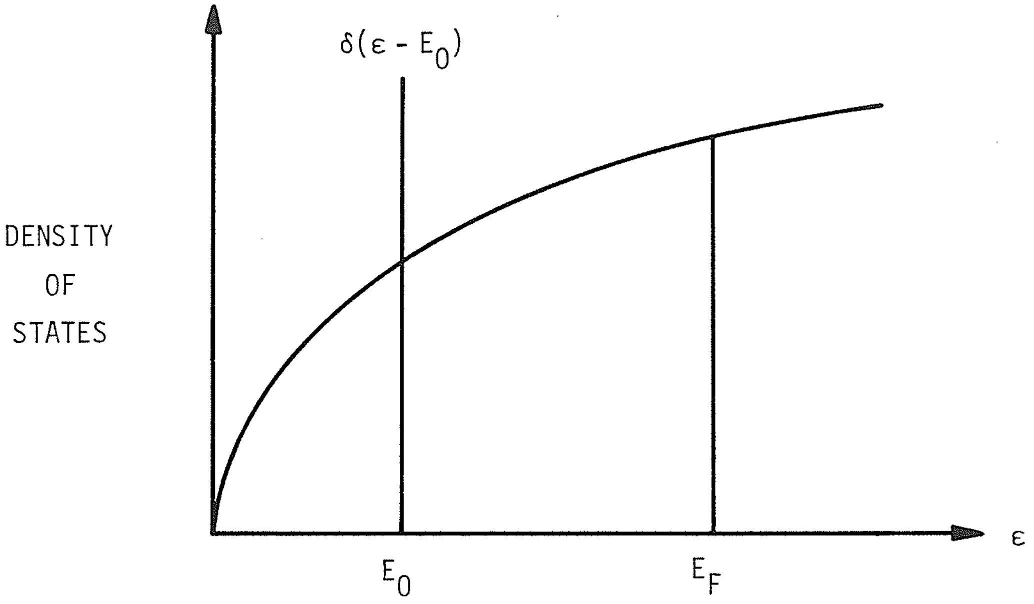

FIG.1.2-1. An atomic d state, with unperturbed energy E_0, embedded in a free-electron conduction band.

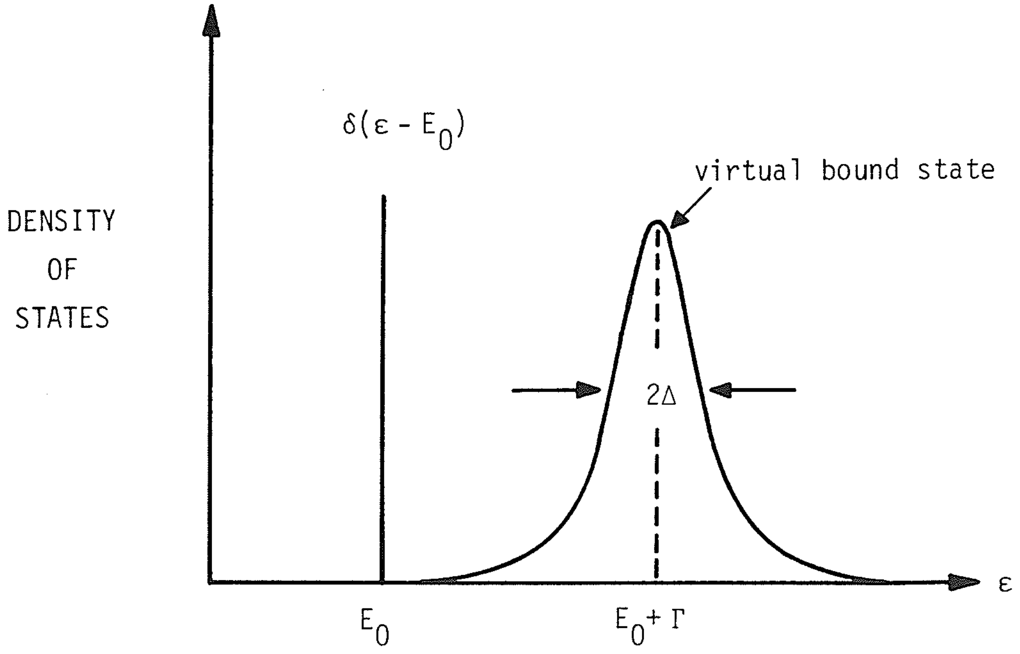

FIG.1.2-2. The s-d mixing interaction shifts and broadens the atomic d state, forming a virtual bound state with a finite energy width 2Δ.

the host and $\overline{|\langle d|V|k\rangle|^2}$ denotes the average value of the admixture matrix element between the localized state and those conduction electron states which lie on a surface of constant energy ε in k-space. Thus the sharp δ-function d level at E_0 is replaced by a virtual d level, with width 2Δ, centered around $E_d = E_0 + \Gamma$.

If Δ is assumed to be constant, then the density of states of the virtual level per spin direction, $\rho_{d\sigma}(\varepsilon)$, has the following Lorentzian form [2] :

$$\rho_{d\sigma}(\varepsilon) = \frac{1}{\pi}\,\frac{\Delta}{(\varepsilon - E_d)^2 + \Delta^2} \quad . \tag{1.2-3}$$

Thus the number of electrons up to energy ε in the virtual level with spin σ is given by

$$n(\varepsilon) = \int_{-\infty}^{\varepsilon} \rho_{d\sigma}(\varepsilon)\, d\varepsilon = \frac{1}{\pi}\arctan\left(\frac{\Delta}{E_d - \varepsilon}\right) \quad . \tag{1.2-4}$$

From Eq.(1.2-4), it follows that an orbitally nondegenerate virtual d state can accomodate a maximum of <u>one</u> electron per spin orientation. [If the virtual state is orbitally degenerate, then an extra factor of $(2\ell+1)$ must be included in Eqs.(1.2-3) and (1.2-4) :

$$\rho_{d\sigma}(\varepsilon) = \frac{2\ell+1}{\pi}\,\frac{\Delta}{(\varepsilon - E_d)^2 + \Delta^2} \quad , \tag{1.2-5}$$

and $$n(\varepsilon) = \frac{2\ell + 1}{\pi} \arctan\left(\frac{\Delta}{E_d - \varepsilon}\right) \quad , \tag{1.2-6}$$

with $\ell = 2$. Thus an orbitally degenerate virtual d state can accomodate a maximum of $(2\ell+1)$ electrons per spin orientation.]

The concept of a virtual bound state can also be approached from the point of view of scattering theory. The transition impurity first gives up all its s and d valence electrons to the conduction band of the host. The excess charge +Ze of the impurity over the host creates a spherically symmetric potential, V(r), which scatters the conduction electrons. A partial wave analysis [11, 12, 13] of the scattering shows that the presence of the impurity gives rise to an extra density of states in the conduction band which is given by [14]

$$\Delta N(\varepsilon) = \frac{2}{\pi} \sum_{\ell} (2\ell + 1) \frac{d\delta_{\ell}(\varepsilon)}{d\varepsilon} \quad , \tag{1.2-7}$$

where $\delta_{\ell}(\varepsilon)$ is the ℓth partial wave phase shift and the factor $2(2\ell+1)$ accounts for spin and orbital degeneracy. Eq.(1.2-7) leads directly to the Friedel sum rule [1, 2], which relates the excess impurity charge Z to the phase shifts at the Fermi energy :

$$Z = \frac{2}{\pi} \sum_{\ell} (2\ell + 1)\ \delta_{\ell}(E_F) \quad . \tag{1.2-8}$$

Since the potential V(r) is almost but not quite strong enough to accept a true bound d state, a scattering resonance will occur in the $\ell = 2$ partial waves at an energy E_r in the conduction band. Near such a resonance, the δ_2 phase shift increases rapidly from nearly 0 to nearly π over a narrow energy range, according to the expression [2]

$$\delta_2(\varepsilon) = \arctan\left(\frac{\Delta}{E_r - \varepsilon}\right) \quad , \tag{1.2-9}$$

as shown in FIG.1.2-3, where 2Δ is the width of the resonance. From Eqs.(1.2-7) and (1.2-9), the corresponding $\ell = 2$ density of states per spin direction is given by

$$\rho_{d\sigma}(\varepsilon) = \frac{2\ell+1}{\pi}\frac{d\delta_2(\varepsilon)}{d\varepsilon} = \frac{2\ell+1}{\pi}\frac{\Delta}{(\varepsilon - E_r)^2 + \Delta^2} \quad . \tag{1.2-10}$$

This expression is identical to Eq.(1.2-5) if the resonance energy E_r is identified with the virtual state energy $E_d = E_0 + \Gamma$. If Δ is small (i.e., if the resonance is sharp), the total electronic charge attracted by the potential is strongly concentrated in the vicinity of the impurity, giving rise to a virtual bound state with a narrow spread in energy around E_r. The electronic structure of the alloy is thus equivalent to that obtained previously by mixing a localized d state with the conduction band.

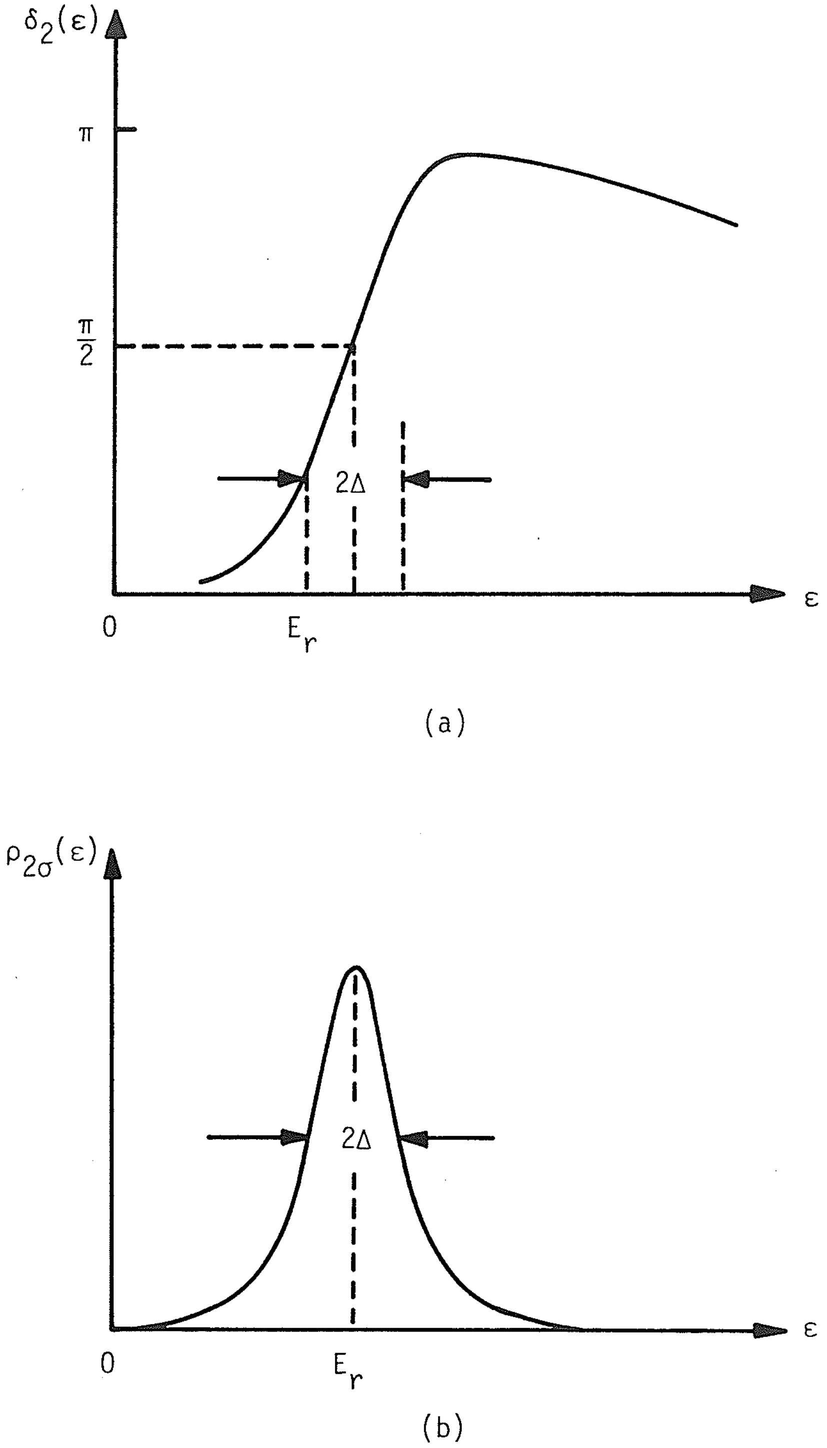

FIG.1.2-3. (a) The behaviour of the $\ell = 2$ partial wave phase shift near a scattering resonance.

(b) The corresponding $\ell = 2$ density of states due to the scattering resonance.

If the intra-atomic interactions between the localized d electrons are neglected, the virtual bound states for both spin orientations will have the same energy. However, since the electrons in a virtual level are almost as well localized as in an atom, exchange and correlation effects, which are responsible for Hund's rules in atomic d shells, must also be important in virtual d levels, particularly for a narrow level. When these effects prevail, the virtual bound state splits into two substates, with opposite spin directions and different energies, as shown in FIG.1.2-4. As a result, the spin up and spin down virtual states accomodate unequal numbers of electrons up to the Fermi level and a magnetic moment results, localized on the impurity site. Using a simple variational argument [2], Friedel derived a condition for the lifting of spin degeneracy, and hence for the formation of a magnetic moment on the impurity site. If U is the effective exchange energy for a pair of localized d electrons of <u>opposite</u> spin then, for an orbitally degenerate, Lorentzian virtual bound state, this condition is given by

$$\frac{(2\ell + 1)\,U}{\pi} \, \frac{\Delta}{(E_d - E_F)^2 + \Delta^2} > 1 \quad , \qquad (1.2\text{-}11)$$

or, from Eq.(1.2-4),

$$\boxed{U\rho_{d\sigma}(E_F) > 1} \quad . \qquad (1.2\text{-}12)$$

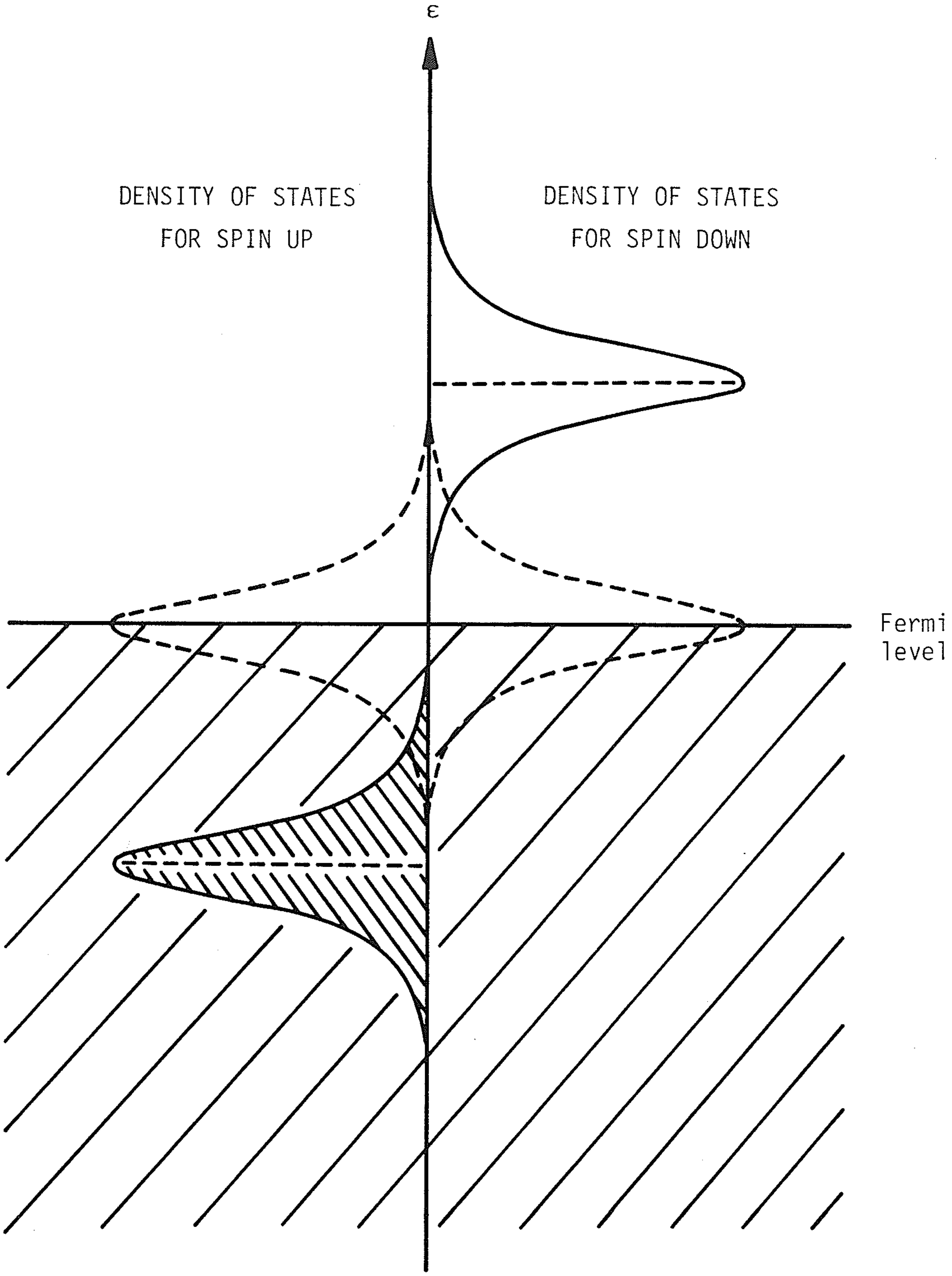

FIG.1.2-4. The lifting of spin degeneracy and the formation of a localized magnetic moment for a Lorentzian virtual bound state. The dotted curves indicate the positions of the spin-up and spin-down virtual levels in the nonmagnetic case.

For a given value of U, this condition is more easily satisfied the closer E_d is to the Fermi level E_F. For $E_d = E_F$, the condition (1.2-11) takes the simple form

$$\frac{U}{\Delta} > \frac{\pi}{(2\ell + 1)} \quad . \qquad (1.2\text{-}13)$$

1.3 Anderson Model

In order to put Friedel's ideas on a more quantitative basis, Anderson proposed the following simple model [3] to describe the electronic structure of a metal containing a single impurity atom with one or more inner-shell orbitals. The essential features of the model are contained in the Anderson Hamiltonian :

$$H = H_{cond} + H_{imp} + H_{kd} \quad . \tag{1.3-1}$$

H_{cond} is the unperturbed conduction electron Hamiltonian of the pure host metal :

$$H_{cond} = \sum_{k,\sigma} \varepsilon_k n_{k\sigma} \tag{1.3-2}$$

$$n_{k\sigma} = c^*_{k\sigma} c_{k\sigma} \quad ,$$

where ε_k is the energy of the free-electron state with wavevector k, $n_{k\sigma}$ is the occupation number operator for the state with wavevector k and spin σ, and $c^*_{k\sigma}$ and $c_{k\sigma}$ are the corresponding creation and annihilation operators.

H_{imp} is the full Hamiltonian of the isolated impurity atom (or ion). In the Anderson model, the impurity is represented by a single nondegenerate d-shell orbital ϕ_d which is described by the following Hamiltonian :

$$H_{imp} = E_0(n_{d+} + n_{d-}) + U\, n_{d+}n_{d-} \quad . \qquad (1.3\text{-}3)$$

E_0 is the unperturbed energy of the d orbital on the impurity atom and n_{d+} and n_{d-} are the numbers of spin up (+) and spin down (-) localized d electrons, respectively. The term $U\, n_{d+}n_{d-}$ in Eq.(1.3-3) represents the intra-atomic Coulomb repulsion between electrons of opposite spin in the localized orbital. This term describes the tendency toward the formation of a magnetic moment on the impurity by reducing the probability of double occupancy of the localized orbital. U is the Coulomb correlation integral which is given by

$$U = \int |\phi_d(\vec{r}_1)|^2 \frac{e^2}{r_{12}} |\phi_d(\vec{r}_2)|^2 \, d\tau_1 \, d\tau_2 \quad . \qquad (1.3\text{-}4)$$

According to Eq.(1.3-3), the state with one electron (of either spin up or down) has the energy E_0, while the state with two electrons (of opposite spin) has the energy $2E_0 + U$. The addition of a second electron thus introduces the Coulomb repulsion between the two opposite-spin electrons in the same orbital and increases the energy of the d state by $E_0 + U$. FIG.1.3-1 shows the unperturbed energies of the spin up and spin down electrons in the localized d orbital superimposed on the conduction electron density of states of the host.

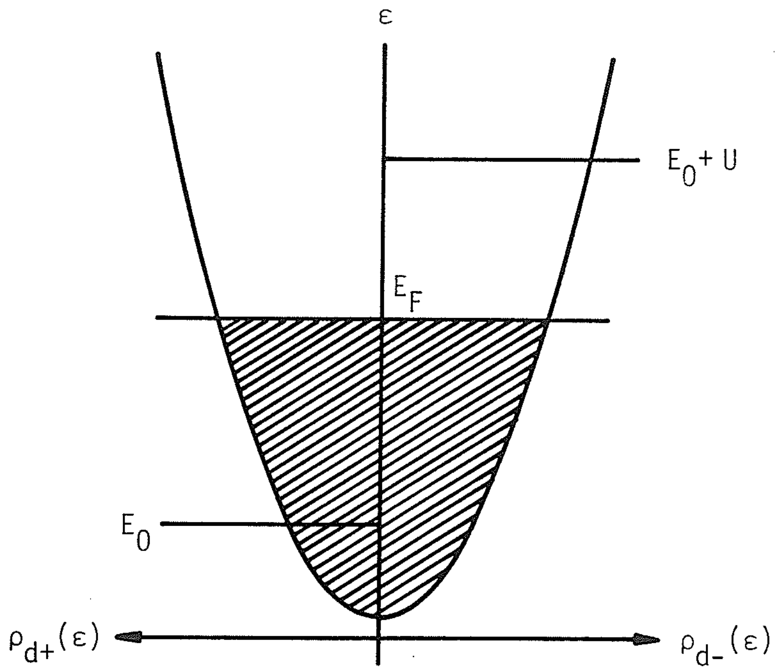

FIG. 1.3-1. Unperturbed energy levels in the absence of s-d admixture.

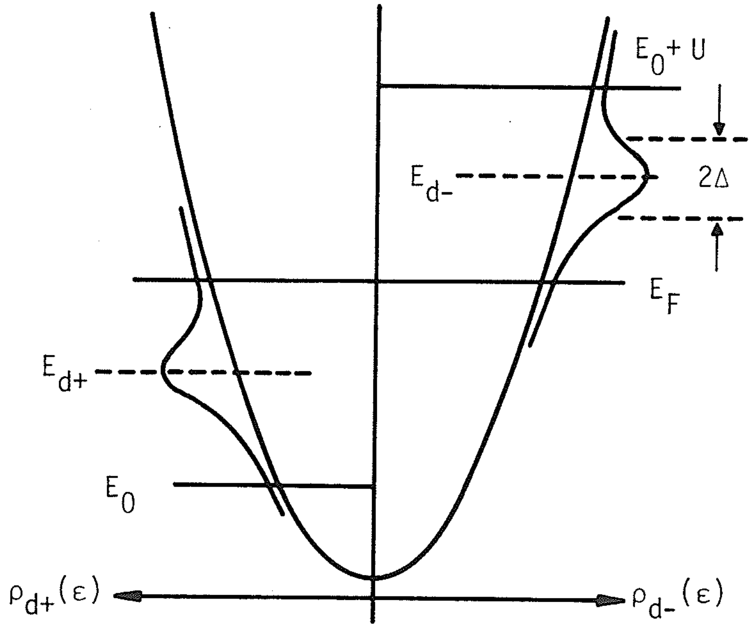

FIG. 1.3-2. Density of state distributions in a magnetic case. The "humps" at $E_{d+} = E_0 + U < n_{d-} >$ and $E_{d-} = E_0 + U < n_{d+} >$ are the virtual d levels, of width 2Δ, for up and down spins, respectively.

The third term, H_{kd}, in the Anderson Hamiltonian is a one-electron term which allows for the mixing of the conduction electron state k with an electron in one of the localized d levels. Normally, H_{kd} is taken to be of the form

$$H_{kd} = \sum_{k,\sigma} V_{kd}(c^*_{k\sigma}c_{d\sigma} + c^*_{d\sigma}c_{k\sigma}) \quad , \tag{1.3-5}$$

where V_{kd} is the covalent admixture matrix element between the d state and the conduction electron states, $c^*_{k\sigma}$ creates a conduction electron of momentum k and spin σ, while $c_{d\sigma}$ destroys a d state electron of spin σ and the other quantities are their conjugates. The s-d mixing interaction thus describes the tendency to delocalize the d electrons and to destroy impurity magnetism.

The complete Hamiltonian for the one-orbital Anderson model is thus

$$H = \sum_{k,\sigma} \varepsilon_k n_{k\sigma} + \sum_{\sigma} E_0 n_{d\sigma} + U n_{d+}n_{d-} + \sum_{k,\sigma} V_{kd}(c^*_{k\sigma}c_{d\sigma} + c^*_{d\sigma}c_{k\sigma}) \quad . \tag{1.3-6}$$

Since the Anderson Hamiltonian describes a system of interacting particles (through the Coulomb term $U n_{d+}n_{d-}$), it must be treated within the one-electron Hartree-Fock approximation. In the HF approach, the interaction term $U n_{d+}n_{d-}$ is replaced by

$$U n_{d+} < n_{d-} > + U < n_{d-} > n_{d+} \quad , \tag{1.3-7}$$

so that the one-electron HF Hamiltonians for up and down spins are given by

$$H_{HF}^{\sigma} = H_{cond} + \sum_{\sigma} \left[E_0 + U < n_{d-\sigma} > \right] n_{d\sigma} + H_{kd} \quad . \tag{1.3-8}$$

When these equations are solved using the Green's function techniques described by Anderson [3], it is shown that, as a result of the s-d mixing interaction, the sharp spin up and spin down impurity energy levels of FIG.1.3-1, with unperturbed energies E_0 and $E_0 + U$ respectively, are shifted and broadened into virtual bound states. The energies of the virtual states are given by

$$E_{d\sigma} = E_0 + U < n_{d-\sigma} > \quad , \tag{1.3-9}$$

while the "width parameter" Δ of the virtual states is given by

$$\Delta = \pi \, \overline{|V_{kd}|^2} \, N(\varepsilon) \quad , \tag{1.3-10}$$

where $N(\varepsilon)$ is the density of states with energy ε in the conduction band of the host. Moreover, if Δ is assumed to be a constant, independent of $E_{d\sigma}$, then the density of states of the virtual d level with spin σ has the following Lorentzian form :

$$\rho_{d\sigma}(\varepsilon) = \frac{1}{\pi} \frac{\Delta}{(\varepsilon - E_{d\sigma})^2 + \Delta^2} \quad . \tag{1.3-11}$$

FIG.1.3-2 shows the two virtual states (in a typical magnetic case) in terms of their distributions $\rho_{d\sigma}(\varepsilon)$ from Eq.(1.3-11), centered around their self-consistent energies $E_{d\sigma}$ from Eq.(1.3-9).

The occupation numbers, $<n_{d\sigma}>$, of the virtual levels at $T = 0$ are given by integrating Eq.(1.3-11) for the density of states up to the Fermi energy E_F :

$$<n_{d\sigma}> = \int_{-\infty}^{E_F} \rho_{d\sigma}(\varepsilon)\, d\varepsilon = \frac{1}{\pi} \cot^{-1}\left(\frac{E_{d\sigma} - E_F}{\Delta}\right) \quad . \qquad (1.3\text{-}12)$$

When this expression is combined with Eq.(1.3-9) for the virtual state energies $E_{d\sigma}$, two coupled self-consistent equations are obtained :

$$\begin{aligned} <n_{d+}> &= \frac{1}{\pi} \cot^{-1}\left(\frac{E_0 - E_F + U<n_{d-}>}{\Delta}\right) \\ <n_{d-}> &= \frac{1}{\pi} \cot^{-1}\left(\frac{E_0 - E_F + U<n_{d+}>}{\Delta}\right) \quad . \end{aligned} \qquad (1.3\text{-}13)$$

Depending on the relative values of the different parameters $E_0 - E_F$, U and Δ, this system of equations may have a single solution with $<n_{d+}> = <n_{d-}>$, in which case the impurity is nonmagnetic, or, in addition, two symmetrical solutions with $<n_{d+}> \neq <n_{d-}>$, in which case the impurity is magnetic. Eq.(1.3-13) can be solved graphically by plotting $<n_{d+}>$ against $<n_{d-}>$ using the first equation and vice versa for the second equation ; the crossing points of these curves yield the solutions. The "magnetic" behaviour of the impurity can be conveniently summarized in the "phase" diagram in FIG.1.3-3. For given values of the Coulomb integral U and the d-state energy relative to the Fermi energy, $E_0 - E_F$, there is a critical value of the level width Δ_c. For larger values of Δ the impurity is nonmagnetic while for $\Delta < \Delta_c$ the impurity is magnetic. The equation for the boundary line separating the magnetic and nonmagnetic regions in FIG.1.3-3 is given by the instability condition :

$$\frac{d < n_{d+} >}{d < n_{d-} >} = -1 \quad ,$$

or

$$\frac{U \Delta}{\pi \left[(E_{d\sigma} - E_F)^2 + \Delta^2 \right]} = 1 \quad ,$$

or

$$\boxed{U \rho_{d\sigma}(E_F) = 1} \quad . \qquad (1.3\text{-}14)$$

Clearly the most favourable case for magnetism occurs when the virtual level falls self-consistently at the Fermi energy in which case the instability condition is given by

$$\frac{U}{\Delta} = \pi \quad . \qquad (1.3\text{-}15)$$

The solution of the Anderson model discussed above requires the

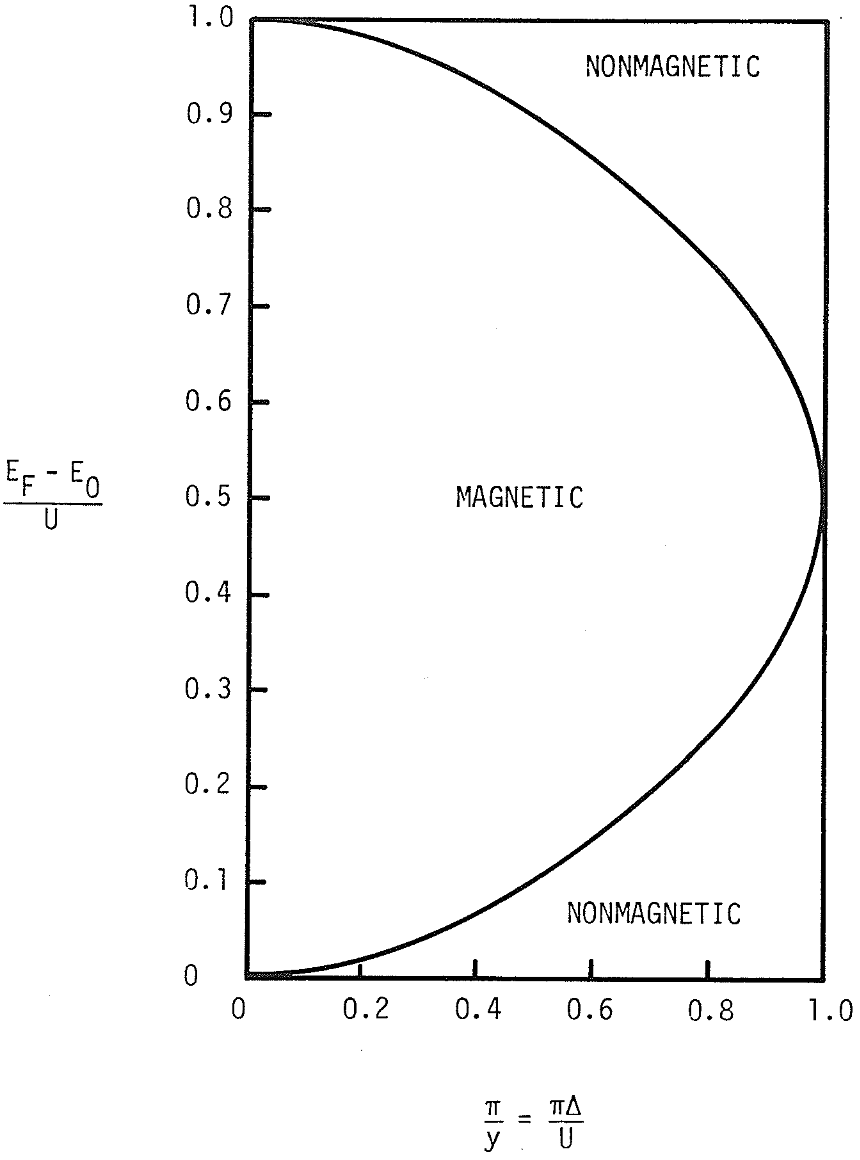

FIG. 1.3-3. Regions of magnetic and nonmagnetic behaviour in the Anderson model.

application of the Hartree-Fock approximation. Such a decoupled-fermion approximation is equivalent to saying that a given electron remains in the localized state for a sufficiently short time that it does not obtain detailed information on the occupation of other spin states or orbitals. Since the addition of an electron raises the energy by an amount of the order of the Coulomb energy U, the uncertainty principle requires a one-electron lifetime <u>less</u> than $\hbar/U$ in order that the Hartree-Fock approximation be valid. Such a lifetime is indeed provided by the mixing interaction which broadens the localized d state into a virtual state with an associated one-electron lifetime of the order of $\hbar/\Delta$. Thus the region of validity of the HF decoupled-fermion approach is limited to a range of parameters such that

$$\frac{\hbar}{\Delta} < \frac{\hbar}{U} \quad ,$$

or

$$\frac{U}{\Delta} < 1 \quad . \tag{1.3-16}$$

For smaller values of the level width, electron-electron correlations play an important role and must be taken into account. Thus the HF approximation is <u>not</u> adequate to describe the physical system when $U/\Delta >> 1$. Notice that it is in this limit (i.e., small Δ/U) that the spin up and spin down electrons become strongly correlated via the Coulomb interaction to avoid simultaneous occupancy of the localized level, thereby forming a magnetic moment.

1.4 The Configuration-Based Approach To Magnetic Impurities In Metals : The Hirst Model

The Friedel and Anderson models tend to overemphasize the itinerant aspects of local moment formation, treating the Coulomb interaction and other intra-ionic correlations between local electrons as weak perturbations. In the configuration-based approach to 3d and 4f impurities in metals, the unperturbed impurity states are taken to be the conventional ionic many-electron states corresponding to well-defined configurations $3d^n$ or $4f^n$, with intraconfigurational splitting into L-S multiplets, crystalline electric field levels, spin-orbit levels and so on. According to this model, these ionic many-electron states can normally only be perturbed and can only rarely be wiped out by interactions with the conduction electrons. The integral occupation of the impurity's 3d or 4f shell is thus a central feature of the model and is assumed to be a consequence of intra-ionic Hund's rule correlations.

In the Hirst model [4], a potentially magnetic impurity in a metal is described by a generalized Anderson Hamiltonian of the form

$$H = H_{ion} + H_{cond} + H_{mix} \quad . \tag{1.4-1}$$

H_{ion} describes the localized intra-atomic interactions at the impurity site and is given by

$$H_{ion} = - V n + \frac{U n(n-1)}{2} + H_{intra} \quad , \qquad (1.4\text{-}2)$$

where n is an operator for the total number of 3d (or 4f) electrons. V is the nuclear potential energy at the impurity site and contributes a term proportional to n. U is the 3d-3d (or 4f-4f) Coulomb interaction and yields an energy proportional to the number of pairs of 3d (or 4f) electrons. H_{intra} symbolizes the intraconfigurational splitting energies which are responsible for the formation of L-S multiplets, crystal field levels, spin-orbit levels and so on.

H_{cond} represents the energy of the non-interacting conduction electrons of the host and is given by

$$H_{cond} = \sum_{k,\sigma} \varepsilon_k a^*_{k\sigma} a_{k\sigma} \quad , \qquad (1.4\text{-}3)$$

where ε_k is the energy of a conduction electron with wavevector k and spin σ, and $a^*_{k\sigma}$ and $a_{k\sigma}$ are the corresponding creation and annihilation operators.

H_{mix} is a one-electron mixing interaction between the localized impurity states and the conduction electron states and may be written as

$$H_{mix} = V_{mix} \sum_k \sum_\ell \sum_\sigma (a^*_{k\ell\sigma} c_{\ell\sigma} + c^*_{\ell\sigma} a_{k\ell\sigma}) \quad , \qquad (1.4\text{-}4)$$

where $c^*_{\ell\sigma}$ and $c_{\ell\sigma}$ are the creation and annihilation operators for the 3d (or 4f) electrons and ℓ is the orbital angular momentum. A partial-wave description is used for the conduction electrons and the mixing interaction conserves orbital angular momentum.

The term H_{ion} describes a tendency toward the formation of ionic many-electron states belonging to definite configurations $3d^n$ and $4f^n$. The mixing interaction H_{mix}, on the other hand, tends to break up the configurations and mix the 3d (or 4f) electrons into the conduction band. The basic physics of the impurity problem is contained in a competition between these two tendencies. A natural measure of the mixing strength is given by the quantity

$$\Delta = \pi \, |V_{mix}|^2 \, N(E_F) \quad , \tag{1.4-5}$$

where $N(E_F)$ is the density of conduction-electron states at the Fermi level, while the Coulomb energy U provides a measure of the strength of H_{ion}. For potentially magnetic impurities, U is much larger than Δ and the physically appropriate approach is to deal with H_{ion} first, before considering mixing effects.

The configuration-based ionic energy-level scheme, in the absence of mixing interactions, is shown in FIG.1.4-1. If the intraconfigurational splittings are neglected, the energies E(n) of the various configurations, n, fall on a parabola which is defined by the

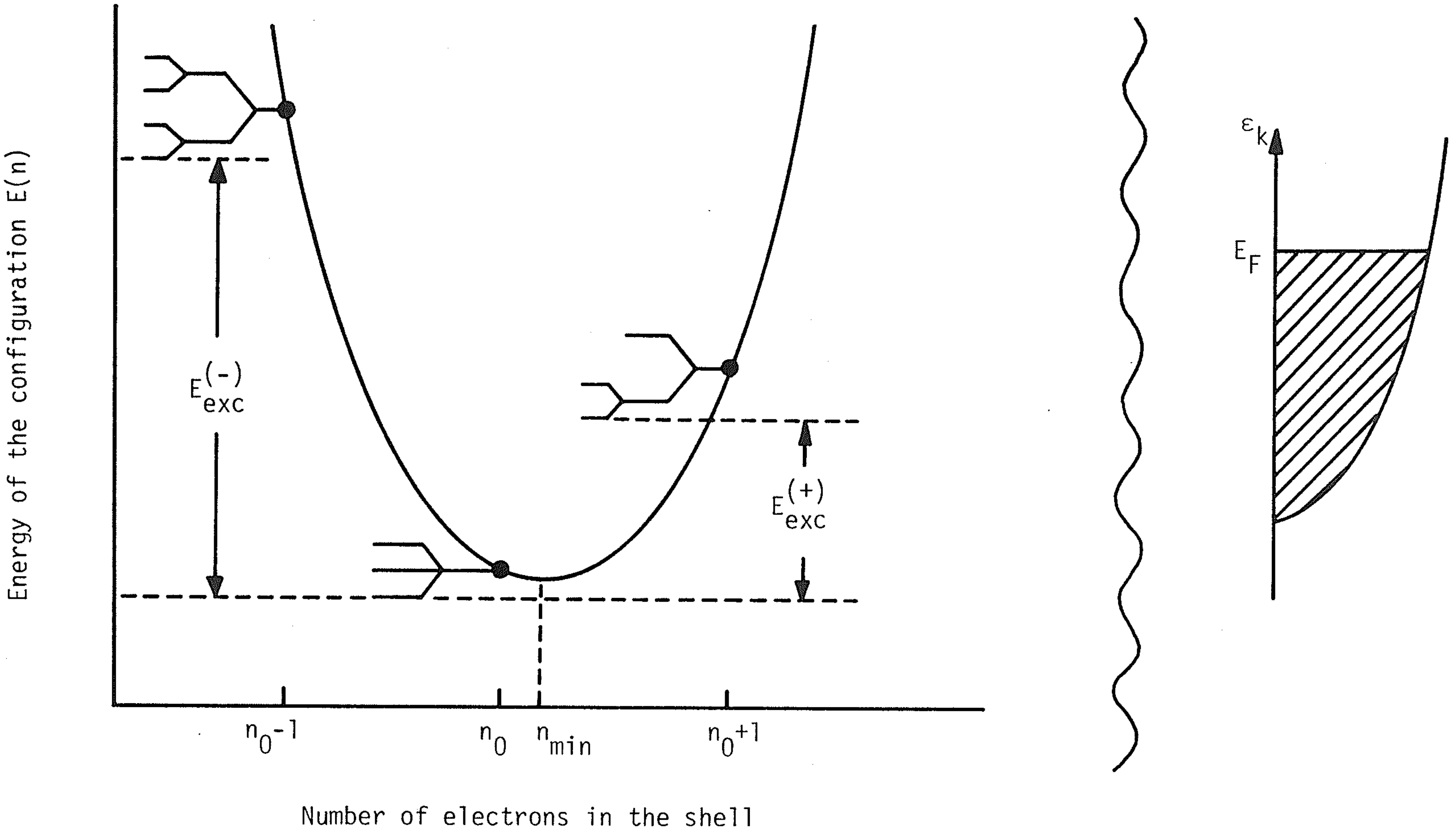

FIG.1.4-1. Configuration-based energy levels of an ion with stable configuration n_0 in the absence of mixing interactions. Intraconfigurational splittings are indicated schematically. $E_{exc}^{(+)}$ and $E_{exc}^{(-)}$ are the interconfiguration excitation energies when $E_F = 0$ (i.e., when the Fermi energy is chosen as the zero of one-electron energies).

first two terms in Eq.(1.4-2) :

$$E(n) = \frac{1}{2}n(n-1)\,U - Vn + \text{const} \qquad (1.4\text{-}6)$$

$$= \frac{1}{2}(n - n_{min})^2\,U + \text{const} \quad , \qquad (1.4\text{-}7)$$

where $n_{min} = \frac{V}{U} + \frac{1}{2}$. FIG.1.4-1 shows the stable configuration n_0 and, in addition, the neighbouring configurations n_0+1 and n_0-1, with intraconfigurational splitting indicated schematically. The conduction-electron states, which are occupied up to the Fermi energy, are shown on the right. Since each ionic energy level represents the total energy of a many-electron state, a direct comparison with the conduction-electron levels is physically meaningless. Only differences between the energies of the impurity levels, not the absolute energies, can have physical significance. The vertical wavy line in FIG.1.4-1 is intended to emphasize this point.

If the impurity is initially in the lowest level of the stable configuration n_0 in FIG.1.4-1, the minimum interconfiguration excitation energy needed to reach the configuration n_0-1 is obtained when the 3d (or 4f) electron removed from the impurity is put into the conduction band at the Fermi energy. If intraconfigurational splittings are neglected, then the required energy is

$$E^{(-)}_{exc} = [\,E(n_0-1) + E_F\,] - E(n_0) = E_F + V - U(n_0-1) \quad , \qquad (1.4\text{-}8)$$

where $E(n_0)$ and $E(n_0-1)$ are given by Eq.(1.4-6). Similarly, the minimum energy needed to add a 3d (or 4f) electron is

$$E^{(+)}_{exc} = E(n_0+1) - [E(n_0) + E_F] = -V + Un_0 - E_F \quad . \qquad (1.4\text{-}9)$$

In the zero-mixing limit, the condition for the configuration n_0 to be stable is that both of these energies be positive :

$$E^{(+)}_{exc} \ \underline{\text{and}} \ E^{(-)}_{exc} > 0 \quad . \qquad (1.4\text{-}10)$$

From FIG.1.4-1, it is apparent that the configuration n_0 with the lowest energy depends on n_{min} and hence on V/U. Thus if the binding potential V is decreased, eventually n_0-1 becomes the stable configuration. The point where the two configurations are equally stable is referred to as CONFIGURATION CROSSOVER and is illustrated in FIG.1.4-2 (curve b). The value of n_{min} at the crossover between the two configurations n_0 and n_0-1 is given by

$$n_{min}(\text{at configuration crossover}) = n_0 - \frac{1}{2} \quad , \qquad (1.4\text{-}11)$$

so that crossover occurs when $\frac{V}{U} = n_0 - 1$.

The conduction electrons interact with the localized electrons through the mixing term H_{mix} in Eq.(1.4-4). The effect of the mixing

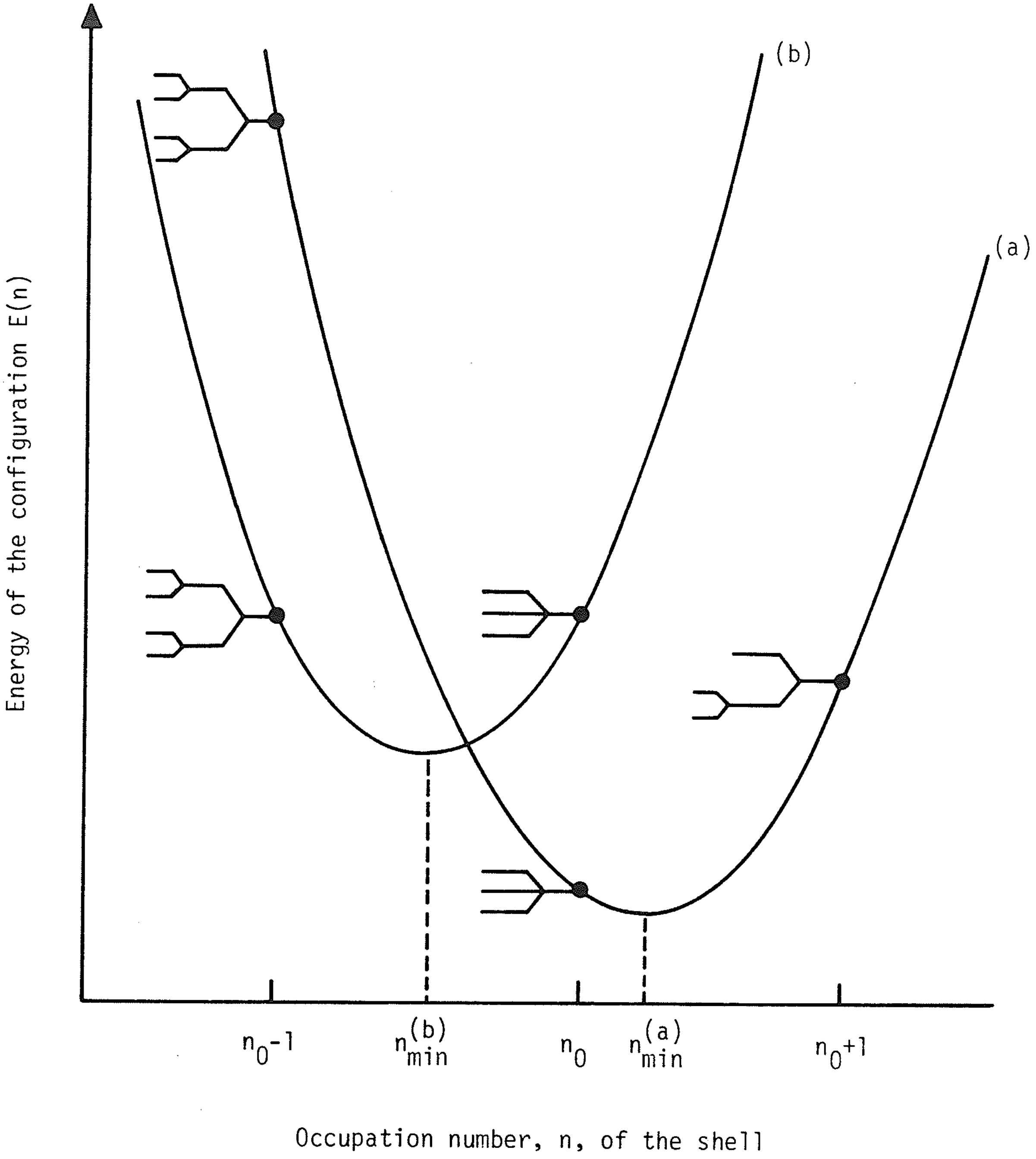

FIG.1.4-2. (a) Ionic energy levels for an impurity with stable configuration n_0.

(b) Configuration-based energy levels of an ion at the crossover between the configurations n_0 and n_0-1.

interaction is to transfer electrons from the impurity's 3d (or 4f) shell to the conduction band and back and this results in an ionic energy level width $\Delta = \pi \, |V_{mix}|^2 \, N(E_F)$ provided that intra-ionic energy conservation requirements do not interfere with the mixing process. If the impurity in FIG.1.4-1 is initially in the stable configuration n_0, mixing transitions can only occur if the ion is excited from the ground state $E(n_0)$ to the next higher state, either $E(n_0+1)$ or $E(n_0-1)$, and this happens only if the mixing strength Δ is larger than the excitation energy, $E_{exc}^{(+)}$ or $E_{exc}^{(-)}$. If $\Delta < E_{exc}^{(+)}$ and $E_{exc}^{(-)}$, the mixing interaction is inoperative, the impurity remains in the stable configuration n_0, and the intraconfigurational level structure remains well-defined. By contrast, if the impurity is initially in the unstable configuration $n_0 - 1$ in FIG.1.4-1, it will spontaneously absorb a conduction electron via the mixing interaction in order to return to the stable configuration n_0, and the excited state acquires an energy width Δ. The lifetime broadening Δ therefore applies only to those impurity levels which are energetically unstable relative to levels belonging to other configurations. This includes all energy levels belonging to excited configurations but may also apply to the higher intraconfigurational energy levels of the ground configuration.

Thus, the condition for a particular configuration n_0 to be stable in the presence of a finite mixing strength Δ, is that the interconfiguration excitation energies, $E_{exc}^{(+)}$ and $E_{exc}^{(-)}$, be not merely positive but larger than the mixing strength Δ :

$$E_{exc}^{(+)} \ \underline{\text{and}} \ E_{exc}^{(-)} > \Delta \quad . \qquad (1.4\text{-}12)$$

This ensures that spontaneous mixing transitions are suppressed by energy-conservation requirements. When a more detailed calculation is performed, the condition for configurational stability in the presence of finite mixing becomes :

$$E_{exc} > \Delta \text{ , with } E_{exc} = \left\{ \left[E_{exc}^{(+)}\right]^{-1} + \left[E_{exc}^{(-)}\right]^{-1} \right\}^{-1} \quad . \qquad (1.4\text{-}13)$$

The behaviour of a 3d or 4f impurity in a metal can be conveniently described by a configurational "phase" diagram, shown in FIG.1.4-3, obtained by plotting Eq.(1.4-13) in the plane of the binding potential V and the mixing strength Δ. The solid curve represents a plot of $\Delta = E_{exc}$ so that the equation of the curve is given by

$$\Delta = E_{exc} = \frac{E_{exc}^{(+)} E_{exc}^{(-)}}{E_{exc}^{(+)} + E_{exc}^{(-)}} = \frac{(2n-1)\,U\,V - n(n-1)\,U^2 - V^2}{U} \quad , \qquad (1.4\text{-}14)$$

or

$$\frac{\Delta}{U} = (2n-1)\,\frac{V}{U} - n(n-1) - \frac{V^2}{U^2} \quad , \qquad (1.4\text{-}15)$$

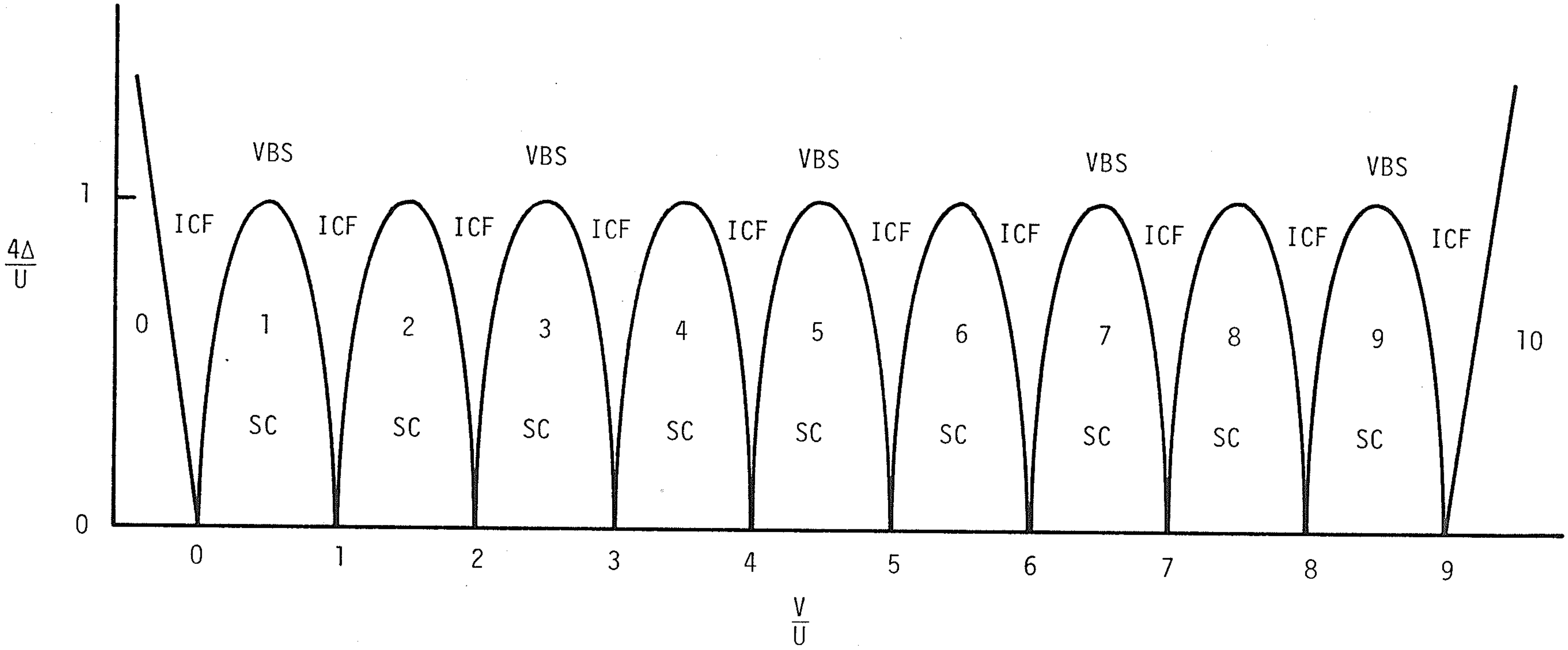

FIG.1.4-3. Configurational "phase" diagram for an impurity ion in the plane of the binding potential V and the mixing strength Δ. The integers denote the regions of stability of the various configurations. ICF and VBS denote regions of interconfiguration fluctuations and virtual bound state spin fluctuations, respectively. The nominal "phase" boundaries symbolize continuous change-over between the different limiting types of behaviour.

where Eqs.(1.4-8) and (1.4-9) (with $E_F = 0$) have been used for $E_{exc}^{(+)}$ and $E_{exc}^{(-)}$. Above the curve, $\Delta > E_{exc}$, while below the curve, $\Delta < E_{exc}$.

For $\Delta = 0$, corresponding to the isolated impurity, each configuration n is stable over a range of V given by $n - 1 \leq \frac{V}{U} \leq n$, with configuration crossover occurring at $V = 0, U, 2U, \ldots$. For finite Δ, the configuration stability condition ($E_{exc} > \Delta$) is most easily satisfied for a value of V lying at the middle of the stability range of the isolated impurity, i.e., when $\frac{V}{U} = n - \frac{1}{2}$ for the configuration n, in which case Eq.(1.4-13) becomes $\Delta < \frac{U}{4}$. For a value of V corresponding to configuration crossover of the isolated ion, the maximum allowed Δ approaches zero.

The interior parts of the stable-configuration "phase" in FIG.1.4-3, where $\Delta \ll E_{exc}$, correspond to extreme configurational stability. In these regions, the behaviour of the impurity approaches that of an isolated ion. Consequently the stabilization of a single configuration is the condition for local-moment behaviour of an impurity.

Outside the regions of configurational stability, it is possible to distinguish two other types of behaviour. In the upper part of the "phase" diagram, where $\Delta > \frac{U}{4}$, the mixing is so strong as to effectively break down the configurational energy-level scheme. In this region, nonmagnetic virtual bound state theory, in the sense of the Anderson model, is applicable, where the Coulomb and other intra-ionic interactions are treated as weak perturbations.

The portions of the "phase" diagram lying between the stable-configuration "phases" correspond to the INTERCONFIGURATION FLUCTUATION (ICF) regime. Since these regions are close to the crossover between two configurations, say n and $n-1$, there will be spontaneous fluctuations between the two, driven by the mixing interaction. However, since the mixing strength Δ is not large compared to U, the various ionic configurations remain well-defined, as does the intraconfigurational level structure on a scale coarser than Δ. For an impurity in the ICF region, the physically appropriate approach is to project away all impurity states belonging to configurations other than n and $n-1$.

Where do real impurities lie in the configurational "phase" diagram in FIG.1.4-3 ? For 4f impurities, where $\Delta/U \sim 10^{-3}$, one is very close to the V axis and FIG.1.4-3 indicates that configuration stability is by far the most probable, but configuration crossover with ICF behaviour is also possible. For 3d impurities, it appears that Δ/U can sometimes be large enough to put the system into the VBS region, where practically nonmagnetic behaviour results. This is probably the case for 3d impurities in such hosts as Al, where the large density of states is expected to yield a large Δ. However, cases such as Mn in noble-metal hosts, where nearly ideal local-moment behaviour is observed, show that Δ/U can be small enough to put a 3d impurity well into the interior of a stable-configuration "phase".

1.5 The s-d Model

The s-d model starts with the assumption that the impurity possesses a well-defined magnetic moment (i.e., the impurity is in the strongly magnetic region of the Anderson model where $U/\Delta \gg 1$ or in the interior of a stable-configuration "phase" in the Hirst model where $E_{exc} \gg \Delta$) and characterizes the impurity by simply assigning it a spin $\vec{S}$, which interacts with the conduction electron spins $\vec{s}$ through an exchange interaction represented by the Hamiltonian

$$H_{sd} = - J \vec{S} \cdot \vec{s} \quad , \qquad (1.5\text{-}1)$$

where J is the exchange coupling constant. (In the Hirst model, Eq.(1.5-1) is appropriate for an S-state impurity only. For a non-S-state impurity, the orbital degrees of freedom of the impurity must be taken into account and the resulting coupling contains not only an exchange term of the form $-J \vec{S} \cdot \vec{s}$, but also large terms which couple the orbital degrees of freedom of the impurity to those of the conduction electrons [15].) In terms of the conduction electron creation and annihilation operators $c^*_{k\sigma}$ and $c_{k\sigma}$, Eq.(1.5-1) may be written as follows

$$H_{sd} = - \frac{J}{2N} \sum_{k,k'} \left[\left(c^*_{k+} c_{k'+} - c^*_{k-} c_{k'-} \right) S_z + c^*_{k+} c_{k'-} S_- + c^*_{k-} c_{k'+} S_+ \right] \qquad (1.5\text{-}2)$$

where N is the total number of lattice points and $S_\pm$ are the raising and lowering operators for the components of $\vec{S}$.

An exchange coupling of the form of Eq.(1.5-1) is contained implicitly in the Anderson model and arises from the covalent admixture interaction H_{kd} between the localized d state and conduction electron states k. Anderson showed that, in addition to shifting and broadening the impurity energy levels, the s-d mixing interaction also shifts the energies of the free-electron states in the conduction band. For the conduction electron state with wavevector k, spin σ and unperturbed energy ε_k, this energy shift is given by [3]

$$\Delta E_{k\sigma} = \frac{|V_{kd}|^2 \, (\varepsilon_k - E_{d\sigma})}{(\varepsilon_k - E_{d\sigma})^2 + \Delta^2} \quad , \qquad (1.5\text{-}3)$$

where $E_{d\sigma}$ and Δ are the energy and width, respectively, of the virtual d level with spin σ. If the impurity is <u>magnetic</u>, then the virtual level for one spin orientation, say spin up, is below the Fermi level and filled, while the spin-down virtual level is above the Fermi level and empty. It follows that the energy shift for spin up ($\sigma = +$) conduction electrons at the Fermi surface ($\varepsilon_k = E_F$) is <u>positive</u> since $E_{d+} < E_F$, while the energy shift for spin down ($\sigma = -$) conduction electrons at the Fermi surface is <u>negative</u> since $E_{d-} > E_F$. Thus the effect of the admixture is to raise the Fermi level for spin up conduction electrons and lower the Fermi level for spin down conduction electrons as shown in FIG.1.5-1. In order to equalize the Fermi levels,

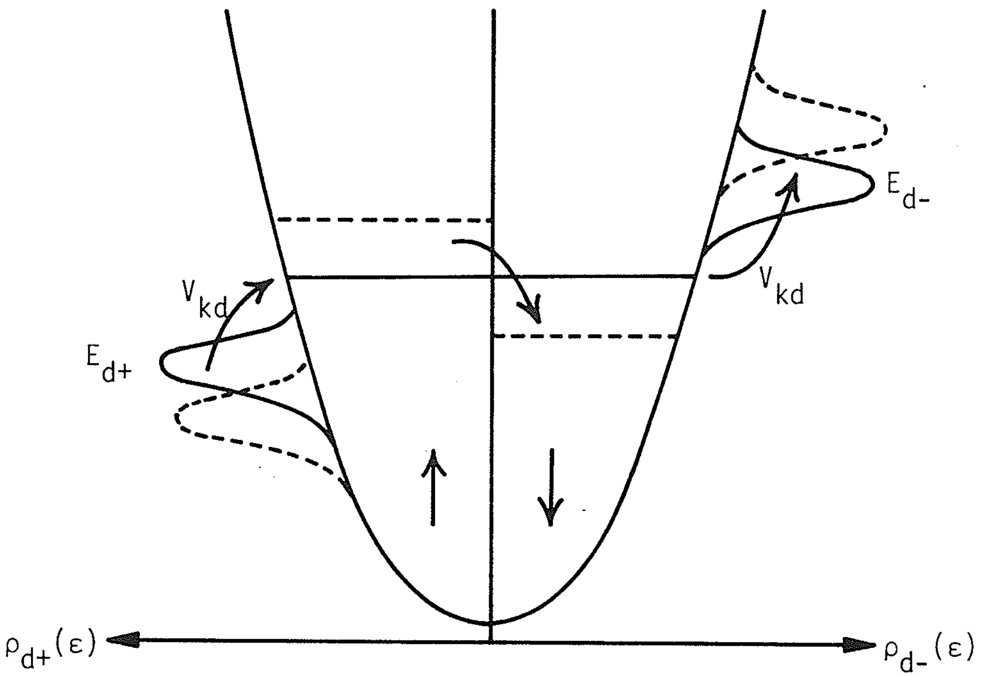

FIG.1.5-1. Shift of the spin-up and spin-down conduction electron Fermi levels due to the mixing interaction between the localized and Fermi surface electrons. The solid lines represent the energy levels before Fermi surface-local electron admixture.

spin-up conduction electrons "flow" into spin-down states, resulting in a conduction electron spin polarization which is <u>antiparallel</u> to the impurity spin. It is as though an <u>antiferromagnetic</u> exchange coupling ($J < 0$) existed between the impurity spin and the conduction electron spins. The above arguments were placed on a sound mathematical basis by Schrieffer and Wolff, who applied a canonical transformation to the Anderson Hamiltonian to eliminate the mixing interaction V_{kd} to first order. Schrieffer and Wolff showed that when $U/\Delta >> 1$, the Anderson Hamiltonian transforms into an effective exchange interaction of the form $-J_{eff}\vec{S}\cdot\vec{s}$ with

$$J_{eff} = |V_{kd}|^2 \left[(E_0 - E_F)^{-1} + (E_F - E_0 - U)^{-1}\right] \qquad (1.5\text{-}4)$$

for conduction electrons at the Fermi surface. The transformation is valid only when the virtual levels are not coincident with the Fermi surface, i.e., when $E_F - E_0 > \Delta$ and $E_0 + U - E_F > \Delta$. Since $E_0 < E_F$ and $E_0 + U > E_F$ for a magnetic impurity in the Anderson model, both terms in Eq.(1.5-4) are negative and $J_{eff} < 0$. Thus the exchange coupling which arises from covalent admixture is <u>antiferromagnetic</u>.

Covalent admixture can also give rise to an effective exchange coupling between the impurity spin and the conduction electron spins in the Hirst model. Within a stable configuration "phase", where $\Delta < E_{exc}$, direct admixture between the ionic energy levels and the conduction electron states is forbidden by energy conservation restrictions. However, there remain higher-order mixing processes in which the impurity reaches another energy level in the stable configuration via virtual transitions to excited (or unstable) configurations. When these are treated by a generalized Schrieffer-Wolff transformation, the result is an effective antiferromagnetic coupling between the 3d impurity and the conduction electrons of the form of Eq.(1.5-1) but with an effective coupling strength given by

$$J_{eff} = - \frac{|V_{mix}|^2}{E_{exc}} < 0 \quad , \tag{1.5-5}$$

where $$E_{exc} = \left\{ \left[E_{exc}^{(+)}\right]^{-1} + \left[E_{exc}^{(-)}\right]^{-1} \right\}^{-1} \quad . \tag{1.5-6}$$

When conventional first order perturbation theory is used to calculate the conduction electron scattering amplitude induced by the s-d exchange interaction in Eq.(1.5-1), it is found that the contribution to the electrical resistivity due to exchange scattering is temperature-independent and is given by [16]

$$\rho_{sd}^{(1)} = \alpha c J^2 S(S+1) \quad , \tag{1.5-7}$$

where c is the impurity concentration and $\alpha = 3\pi m/8e^2 \hbar E_F$ is a constant. However, when the perturbation calculation is extended up to the second

Born approximation [17], the presence of second order spin-flip scattering processes, such as those shown in FIG.1.5-2, leads to an exchange scattering amplitude which is singular at the Fermi surface and hence to a term in the resistivity which varies logarithmically with temperature as follows :

$$\rho_{\text{KONDO}} = \rho_{sd}^{(1)}\left[1 + J\,N(E_F)\,\ell n\left(\frac{k_B T}{D}\right)\right] \quad , \qquad (1.5\text{-}8)$$

where $N(E_F)$ is the density of states in the conduction band at the Fermi energy and D is a constant equal to the conduction electron bandwidth. For temperatures such that $k_B T < D$, $\ell n(k_B T/D)$ is negative and becomes increasingly more negative as the temperature decreases. If J is also negative (corresponding to an antiferromagnetic exchange coupling between the impurity spin and the conduction electron spins such as that induced by covalent admixture), then ρ_{KONDO} increases as the temperature tends to zero. When this is combined with the other contributions to the resistivity due to phonon and ordinary potential scattering, which increase with increasing temperature, the result is a resistivity minimum as shown in FIG.1.5-3 and this is referred to as the KONDO EFFECT.

For $J < 0$, the Kondo resistivity in Eq.(1.5-8) diverges logarithmically as T approaches zero, indicating a breakdown in simple perturbation theory at low temperatures. An estimate of the temperature at which this breakdown occurs can be obtained by setting

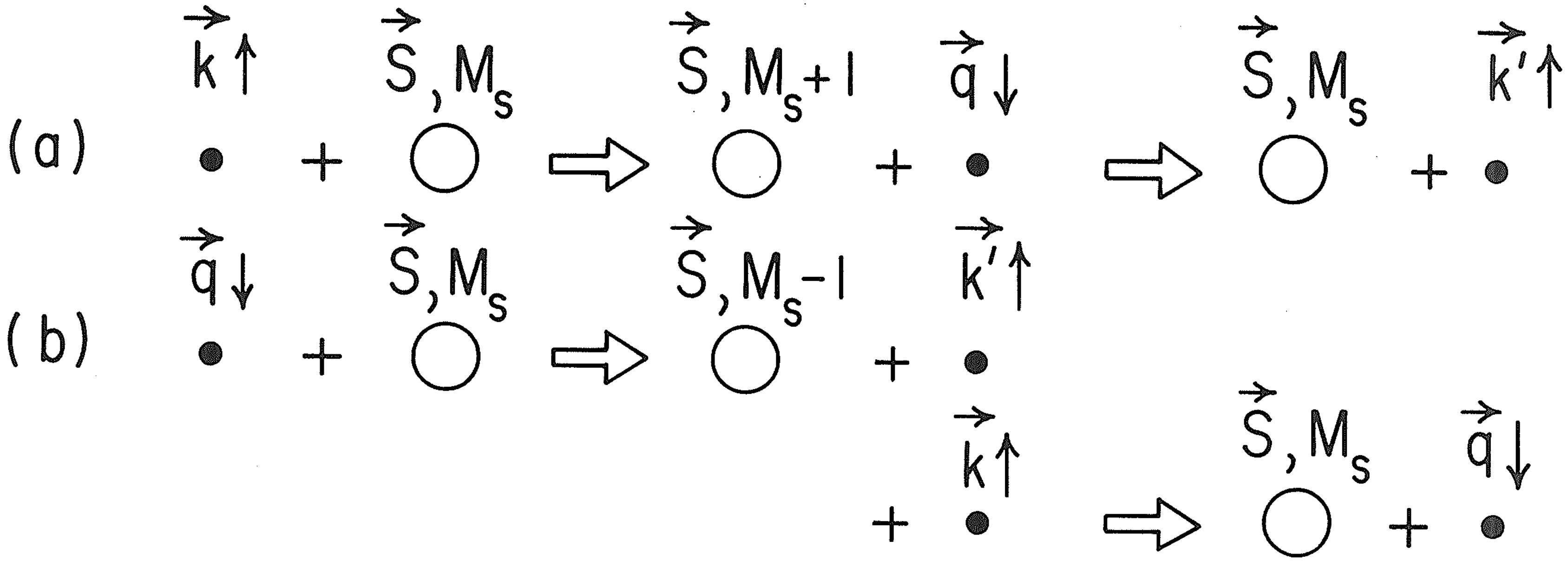

FIG.1.5-2. Some typical spin-flip scattering processes : In (a), a conduction electron in the state $\vec{k}$ with spin up (↑) interacts with the magnetic impurity via the s-d exchange interaction and is scattered to the state $\vec{q}$ of opposite spin (↓), while the z-component of the spin of the impurity, denoted by M_s, flips up to the state M_s+1. Then the conduction electron, now in the state $\vec{q}\downarrow$, interacts with the same local moment again and is scattered into the state $\vec{k}'\uparrow$, while the z-component of the impurity spin returns to its initial value M_s. In (b) the same final state is achieved by reversing the order of the scattering. First, a conduction electron in the state $\vec{q}\downarrow$ is scattered into the state $\vec{k}'\uparrow$ and M_s flips down to M_s-1. Then an electron in $\vec{k}\uparrow$ is scattered into the empty state $\vec{q}\downarrow$ and the z-component of the impurity spin returns to the initial value M_s. The final result is the same : no electron in $\vec{k}\uparrow$, one in $\vec{k}'\uparrow$, and none in $\vec{q}\downarrow$.

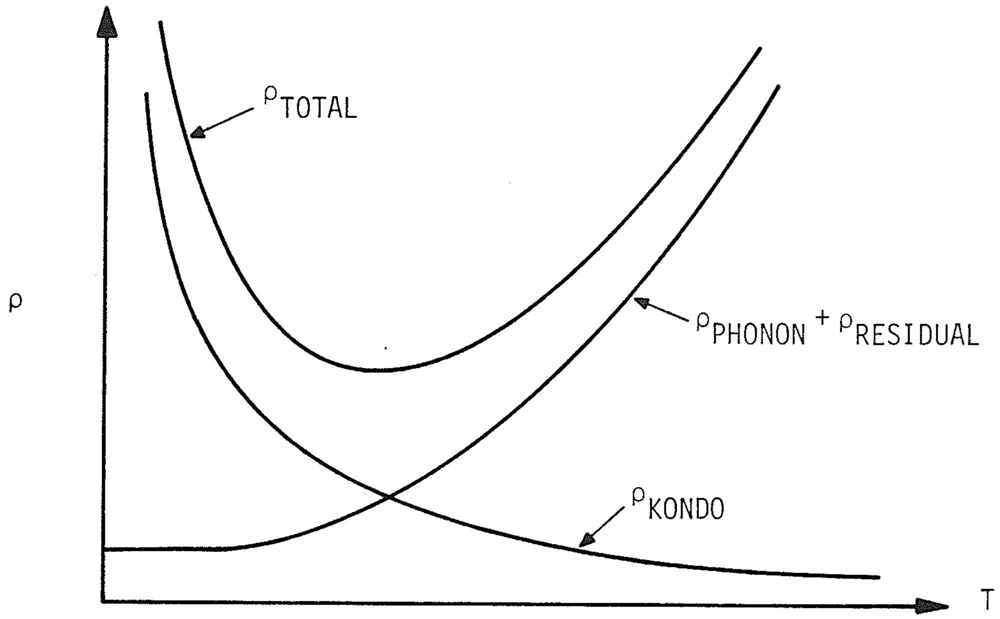

FIG. 1.5-3. The formation of a resistivity minimum (the Kondo effect) for an antiferromagnetic exchange coupling ($J < 0$).

the second term in Eq.(1.5-8) equal to the first term (for lower temperatures the second term becomes larger than the first term and the perturbation series fails to converge). For $J < 0$ this gives

$$1 = -|J|\, N(E_F)\, \ell n\left(\frac{k_B T}{D}\right) \quad , \tag{1.5-9}$$

and this defines the KONDO TEMPERATURE T_K :

$$T_K = \frac{D}{k_B} \exp\left[-\frac{1}{|J|\, N(E_F)}\right] \quad . \tag{1.5-10}$$

It is the characteristic temperature which designates the lower bound of applicability of a perturbation-type calculation.

If the impurity is described by the Hirst model, then the appropriate form for the Kondo temperature, T_K, can be obtained by replacing J by $|V_{mix}|^2/E_{exc}$ and $N(E_F)$ by $\Delta/\pi|V_{mix}|^2$ in Eq.(1.5-10). This gives

$$T_K = \frac{D}{k_B} \exp\left(-\frac{\pi E_{exc}}{\Delta}\right) \quad . \tag{1.5-11}$$

Thus T_K is small in the center of a stable-configuration "phase", where $E_{exc} >> \Delta$, and increases as one moves from the interior toward the boundary of the stable-configuration "phase" where $E_{exc} = \Delta$.

When more sophisticated techniques based on many-body perturbation theory [18], double time Green's functions [19], or dispersion theory [20, 21] were applied to the s-d Hamiltonian in an attempt to remove the Kondo divergence and to gain some insight into the behaviour of the exchange-coupled impurity-conduction electron spin system for $T < T_K$, it was found that below the Kondo temperature the system undergoes a gradual transition to a nonmagnetic ground state, with the effective magnetic moment of the system becoming progressively weaker with decreasing temperature and eventually vanishing at $T = 0$. However the true nature of the ground state was only recently revealed by Wilson [22], who made use of "scaling theory" [23] to achieve the exact zero temperature solution. Wilson's approach was based on the following physical observations :

1. The characteristic temperature T_K determines the energy scale for the Kondo problem.

2. The high energy cut-off (D) cannot be important for the dynamics of the Kondo problem.

The first observation allows a separation of energy and temperature regimes. At low temperatures (more precisely, for $T << T_K$), the local moment and conduction electrons (the "Kondo system") are locked into the ground state. Thermal fluctuations are insufficient to excite the system. The Kondo energy, $k_B T_K$, is thus a measure of the "binding energy" for the system. For $T >> T_K$, the system unlocks, and the simple high-temperature perturbation theory leading to Eq.(1.5-8) suffices.

The second observation allows one to obtain the character of the condensed state. If T_K is in fact a fixed measure of the energy scale, it should be possible to change the bandwidth D and not affect the character of the low energy ($\ll k_B T_K$) excitations of the system. Since, at low temperatures, the only important electronic states cover the region of width $D' \simeq k_B T \ll D$, this means that, with some reservations, it is possible to eliminate the rest of the states provided that the interaction is renormalized : $J \rightarrow J'$. The question then is what will happen to J' when $D' \rightarrow 0$.

The Kondo temperature T_K is given by the following expression (for J of arbitrary sign) :

$$1 = J\,N(E_F)\,\ell n\left(\frac{k_B T_K}{D}\right) \quad . \qquad (1.5\text{-}12)$$

If $D \rightarrow D + \delta D$, then T_K will remain the same only if $J \rightarrow J + \delta J$ where from Eq.(1.5-12),

$$\frac{\delta D}{D} = \left[\frac{1}{J^2\,N(E_F)}\right]\delta J \quad . \qquad (1.5\text{-}13)$$

Thus if $\delta D < 0$, which is equivalent to narrowing the bandwidth and lowering the temperature, then $\delta J < 0$. But for antiferromagnetic exchange, J is <u>negative</u>, so that as $D \rightarrow 0$, $J \rightarrow -\infty$. This is the ground state of the Kondo problem for antiferromagnetic exchange. For ferromagnetic exchange ($J > 0$), δJ remains < 0 as D diminishes, and therefore $J \to 0$ is the ground state.

Thus for antiferromagnetic exchange, the ground state of the system ($J \to -\infty$) must be a nonmagnetic singlet with completely correlated localized moment and conduction electron spins. Because the energy scale has been preserved throughout this process, at $T \ll T_K$ this state can never be broken by energy conserving transitions (i.e., the spin-flip scattering rate must vanish). For the ferromagnetic case ($J \to 0$), the local spin and conduction electrons are not locked together at all. There are spatial correlations but no pairing, and the local moment of the "complex" is fully developed.

The low temperature antiferromagnetic Kondo problem thus reduces to an estimate of the response of the electron gas to the bound singlet. Recently, Nozieres [24] suggested a simple physical model with which it appears that finite temperature properties can be calculated rather directly. Nozieres pointed out that, while the nonmagnetic singlet ground state (at $J \to -\infty$) cannot be broken with finite energy excitations, virtual excitations into 0 or 2 electron states (i.e., triplet states) become possible at finite temperatures where J is also finite. Under such circumstances, one has an essentially nonmagnetic impurity, but with fluctuations at the impurity site giving rise to a temporary magnetic moment. Using Fermi liquid theory [25], Nozieres found the following form for the resistivity for $T \ll T_K$:

$$\rho(T \ll T_K) = \rho(0)\left[1 - \frac{\pi^2}{3}\left(\frac{T}{T_K}\right)^2\right] \quad , \qquad (1.5\text{-}14)$$

where $\rho(0)$ is the zero temperature resistivity (i.e., the unitarity limit).

1.6 The Localized Spin Fluctuation Model

The concept of localized spin fluctuations (LSF) was first proposed by Lederer and Mills [6] in order to describe the time-dependent fluctuations in the magnetization at the site of a nearly magnetic transition metal impurity dissolved in a paramagnetic host. The electrical resistivity due to the scattering of conduction electrons from the LSF can exhibit two types of behaviour depending on the affinity between the impurity and host : if the impurity and host have similar electronic structure (e.g. a Ni impurity in a Pd host) the resistivity is an increasing function of temperature, whereas if the impurity and host have a different electronic structure (e.g. a transition impurity in a noble metal host) the resistivity decreases with increasing temperature.

For isoelectronic alloys, such as RhFe, IrFe, PtFe, and PdNi, where the host and impurity have similar electronic structure, potential scattering effects and the associated Friedel bound state can be neglected. A simple physical picture of localized spin fluctuations in these alloys was provided by Lederer and Mills [6]. When a spatially uniform, static magnetic field is applied to a pure paramagnetic metal, a spin polarization is induced in the conduction electron gas. If the effect of interactions between the electrons is ignored, then the response of the conduction electron spins to the applied magnetic field is given by the Pauli paramagnetic susceptibility [26]

$$\chi_P = \mu_B^2 N(E_F) \quad , \qquad (1.6\text{-}1)$$

where $N(E_F)$ is the density of states in the conduction band at the Fermi level. When the Coulomb interactions between the conduction electrons are taken into account, then a simple Hartree-Fock (HF) theory [27] shows that the spin susceptibility of the metal is larger than the Pauli free-electron susceptibility by the factor $[1 - U N(E_F)]^{-1}$:

$$\chi_s = \frac{\chi_P}{[1 - U N(E_F)]} \quad , \qquad (1.6\text{-}2)$$

where U is the intra-atomic Coulomb interaction between two electrons in the same unit cell and $[1 - U N(E_F)]^{-1}$ is called the "exchange enhancement" factor. In transition metals the presence of a narrow d band, which crosses the Fermi surface and has a high density of states at the Fermi energy E_F, can lead to a significant exchange enhancement of the spin susceptibility. If $U N(E_F) > 1$, the susceptibility diverges and the system is unstable with respect to the ferromagnetic state. For Pd, $U N(E_F) \simeq 0.9$ [28] and the repulsive intra-atomic Coulomb interactions are so strong that the d band is near the threshold of magnetic instability.

Now suppose that a single transition metal impurity is added to the host matrix described above. It is convenient to assume that the electrons move in a band of the tight binding form ; the d bands of transition metals have the character of tight binding bands, so that this discussion is particularly appropriate to transition metal hosts. In this case, the intra-atomic Coulomb interaction U_I between two electrons in the impurity cell will differ from the value U_0 appropriate to the host. If $U_I > U_0$, then a uniform magnetic field will induce a spin polarization in the impurity cell which is larger than that induced in the host matrix, because the exchange enhancement effect is larger for electrons in the impurity cell. In fact, if the host is paramagnetic and if U_I exceeds a certain critical value $U_I^{(c)}$, then Hartree-Fock (HF) theory predicts that the paramagnetic state becomes locally unstable [3], and a magnetic moment forms on the impurity site.

The discussion up to this point has been confined to the enhancement of the spin moment near the impurity cell induced by a static external field. However, this enhanced static response implies that the intrinsic fluctuations in spin density in the conduction electron gas of a paramagnetic host will have an amplitude in the vicinity of the impurity cell which is large compared to their amplitude in the host matrix far from the impurity. These locally enhanced spin density fluctuations are termed localized spin fluctuations (LSF) and lead to a striking temperature-dependent contribution from electron-electron scattering to the electrical resistivity of the alloy.

If the exchange enhancement in the host matrix is appreciable and if $U_I < U_0$, then the Coulomb interactions lead to a local suppression of the response of the host matrix to an applied magnetic field, and the enhanced spin fluctuations characteristic of the host will be suppressed near the impurity.

The exchange-enhanced fluctuations in magnetization (or spin density) at the site of a nonmagnetic transition metal impurity have a finite lifetime τ_{sf} called the spin fluctuation lifetime. The electric and magnetic properties of an impurity undergoing spin fluctuations are a consequence of the finite lifetime of the LSF. At low temperatures, when the conduction electron thermal lifetime $\tau_{therm} = \hbar/k_B T$ is longer than the spin fluctuation lifetime τ_{sf}, the conduction electrons "see" the fluctuations in magnetization at the impurity site and the impurity will appear to be nonmagnetic. However, when the thermal energy $k_B T$ is larger than $\hbar\tau_{sf}^{-1}$ so that the conduction electron thermal lifetime is shorter than the spin fluctuation lifetime, the conduction electron, as a probe, does not have time to see that the magnetization on the impurity site is fluctuating before losing memory of its own spin through thermal fluctuations. In this region, the spin fluctuation is indistinguishable from a genuine spin and the resistivity displays the logarithmic temperature dependence characteristic of the scattering of conduction electrons by a well-defined local moment. The transition from nonmagnetic to magnetic behaviour is smooth and occurs near the spin fluctuation temperature T_{sf} which is the temperature at which the conduction electron thermal lifetime is equal to the spin fluctuation lifetime :

$$T_{sf} = \frac{\hbar}{k_B \tau_{sf}} \quad . \qquad (1.6\text{-}3)$$

The spin fluctuation temperature T_{sf} is thus the analog of the Kondo temperature T_K in the s-d model.

Lederer and Mills [6] showed that at sufficiently low temperatures ($T \ll T_{sf}$), the scattering of conduction electrons from enhanced spin density fluctuations (LSF) at the site of a nearly magnetic transition metal impurity leads to a large concentration-dependent contribution to the electrical resistivity which increases as T^2 with increasing temperature. Kaiser and Doniach [7] extended the calculation of Lederer and Mills to higher temperatures and obtained a universal curve for the spin fluctuation resistivity in which the temperature dependence changes gradually from T^2 to T at temperatures of the order of 0.25 of the characteristic temperature T_{sf} ($k_B T_{sf}$ is the energy of the peak in the localized spin fluctuation excitation spectrum). At higher temperatures the model predicts a significant decrease with temperature in the local exchange enhancement leading to a reduction of the scattering below the linear law. Recently, Rivier and Zlatic [29] developed a formalism which is capable of yielding an expression for the spin fluctuation resistivity which is valid at all temperatures. The expression obtained by Rivier and Zlatic is

$$\rho_{\ell sf}(T) = A\left[1 - \left\{1 + \pi\left(\frac{T}{T_{sf}}\right) + \psi\left(\frac{1}{2} + \frac{1}{2\pi}\frac{T_{sf}}{T}\right) - \psi\left(1 + \frac{1}{2\pi}\frac{T_{sf}}{T}\right)\right\}^{-1}\right] \qquad (1.6\text{-}4)$$

where ψ is the digamma function. The resistivity in Eq.(1.6-4) is a universal function of T/T_{sf} and is plotted in FIG.1.6-1 as a function of the reduced temperature $x^{-1} = 2\pi\, T/T_{sf}$. The knee occurring around $x^{-1} = 2\pi$ (i.e., at the spin fluctuation temperature $T = T_{sf}$) separates the nonmagnetic and magnetic regimes. The resistivity exhibits four distinct temperature dependences :

(i) At very low temperatures, the resistivity increases as $\rho_{\ell sf} = \frac{1}{2}\pi^2 (T/T_{sf})^2$.

(ii) At temperatures of the order of 0.9 $(T_{sf}/2\pi)$ the resistivity becomes linear : $\rho_{\ell sf} = \gamma(T - \theta)$ where $\gamma = 1.12/T_{sf}$ and $\theta = 0.67\, T_{sf}$.

(iii) Above the spin fluctuation temperature T_{sf} the resistivity is logarithmic, $\rho_{\ell sf} = C + B\, \ell n(T/T_{sf})$ where $B = 0.24$ and $C = 0.68$, which is characteristic of the scattering of conduction electrons by a target having an internal structure (here : up and down).

(iv) Finally, as $T \to \infty$ the resistivity approaches the unitarity limit as $\rho_{\ell sf} = 1 - (T_{sf}/T)$.

When a transition metal impurity is placed in a simple or noble

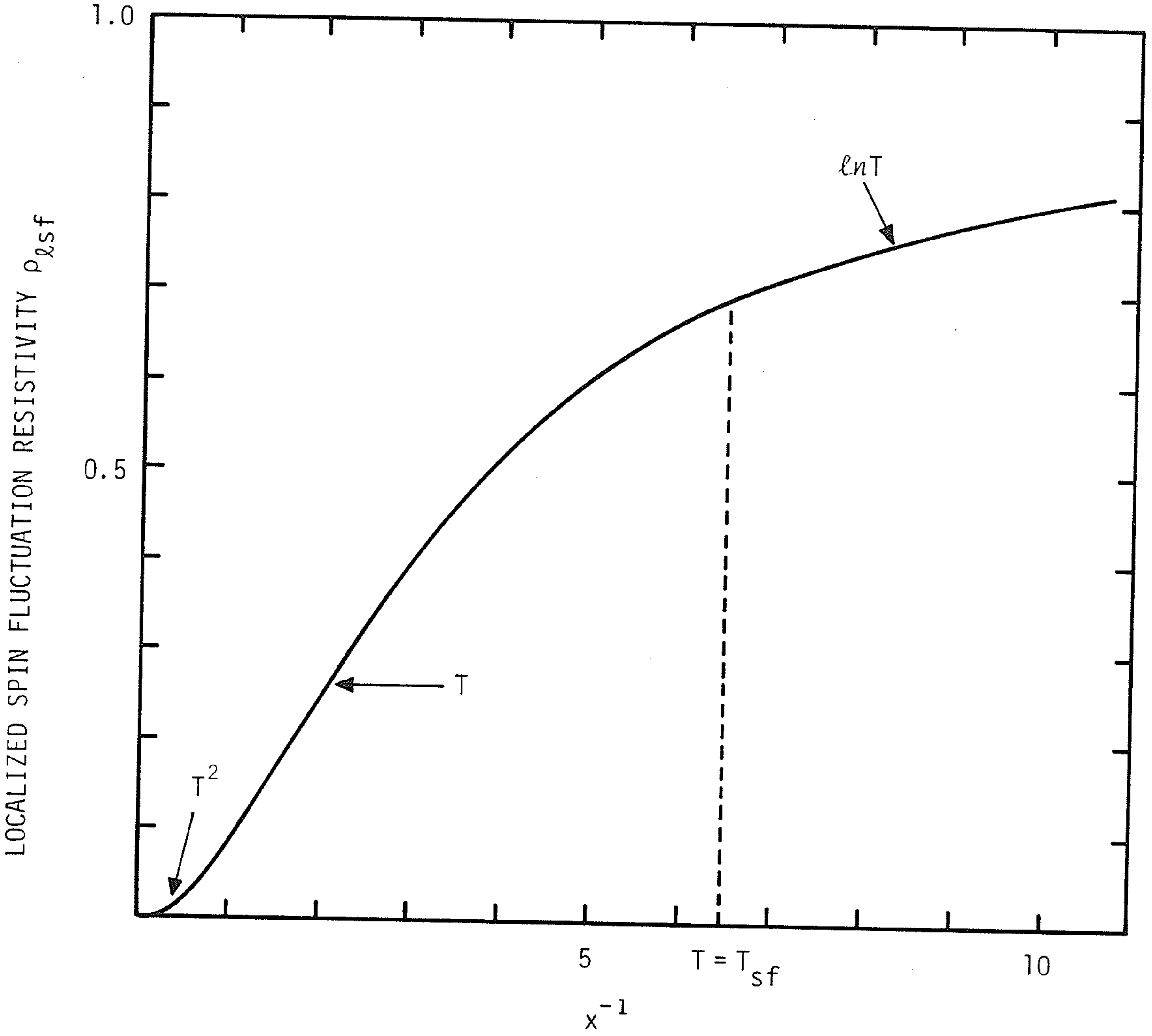

FIG.1.6-1. A plot of Eq.(1.6-4) for the LSF resistivity in isoelectronic alloys as a function of the reduced temperature $x^{-1} = 2\pi T/T_{sf}$. The vertical dotted line indicates the spin fluctuation temperature and the beginning of the logarithmic region.

metal host the effect of potential scattering can no longer be neglected. Under these circumstances, the electrostatic potential at the impurity site is strong enough to produce a virtual bound d state (or scattering resonance) in the conduction band of the host and the Friedel-Anderson model provides an appropriate description of the system. A simple physical picture of localized spin fluctuations in the Friedel-Anderson model was first provided by Rivier and Zuckermann [30, 31] and Caplin and Rizzuto [32]. Consider a Friedel-Anderson nonmagnetic virtual bound state (i.e., $U \rho_{d\sigma}(E_F) < 1$) . In its ground state it contains an equal number of localized spin-up and spin-down electrons, but excitations with an unequal number become of lower and lower energy as $U \rho_{d\sigma}(E_F)$ approaches unity (the Friedel-Anderson condition for the impurity to become magnetic). If the excitation has an energy ε above that of the ground state, then it follows from the uncertainty principle that the lifetime, $\tau_{sf} \sim \hbar/\varepsilon$, of the excitation (and its associated magnetic moment) becomes longer and longer as one approaches the Hartree-Fock condition for the appearance of a static local moment. In fact, a more rigorous treatment [30] shows that, for a single nondegenerate virtual d state of energy E_d and width Δ, the lifetime τ_{sf} of these "magnetic" excitations (i.e., the spin fluctuation lifetime) is given by

$$\tau_{sf} = \frac{\pi \rho_d(E_F)}{1 - U \rho_d(E_F)} \quad . \qquad (1.6\text{-}5)$$

Thus when $U\rho_d(E_F) = 1$, the lifetime τ_{sf} becomes infinite and a static local moment appears. FIG.1.6-2 shows a plot of the spin fluctuation lifetime τ_{sf} [Eq.(1.6-5)] for the case of a virtual level at the Fermi energy ($E_d = E_F$) where $\rho_d(E_F) = 1/\pi\Delta$. Localized spin fluctuations in the Anderson model are thus a consequence of the dynamics of a nonmagnetic virtual bound state which is fluctuating between its nonmagnetic ground state and a magnetic excited state at a rate τ_{sf}^{-1}.

As in isoelectronic alloys, the electric and magnetic properties of an impurity undergoing spin fluctuations in the sense of the Anderson model are determined by the time scale of the LSF. When the LSF are fast compared with thermal fluctuations (i.e., when $\tau_{sf} < \hbar/k_BT$), the impurity appears to be nonmagnetic and contributes an enhanced temperature-independent Pauli susceptibility. However when the spin fluctuation lifetime is longer than the thermal lifetime (i.e., when $\tau_{sf} > \hbar/k_BT$), the temporary magnetic moment may have sufficient time to equilibrate in an applied magnetic field or to flip the spin of a conduction electron and so will contribute a Curie susceptibility and a logarithmic resistivity. An impurity in the "slow LSF" regime therefore appears to be magnetic.

Rivier and Zlatic [33] calculated the resistivity due to the scattering of conduction electrons by a virtual bound state undergoing spin fluctuations and obtained the following expression for the LSF resistivity :

$$\rho_{\ell sf}(T) = \left[1 - 2\,\ell n 2 - \left(\frac{2\alpha T_{sf}}{T}\right)^{-1} + 2\,\psi\left(\frac{2\alpha T_{sf}}{T}\right) - 2\,\psi\left(\frac{\alpha T_{sf}}{T}\right)\right]^{-1} \qquad (1.6\text{-}6)$$

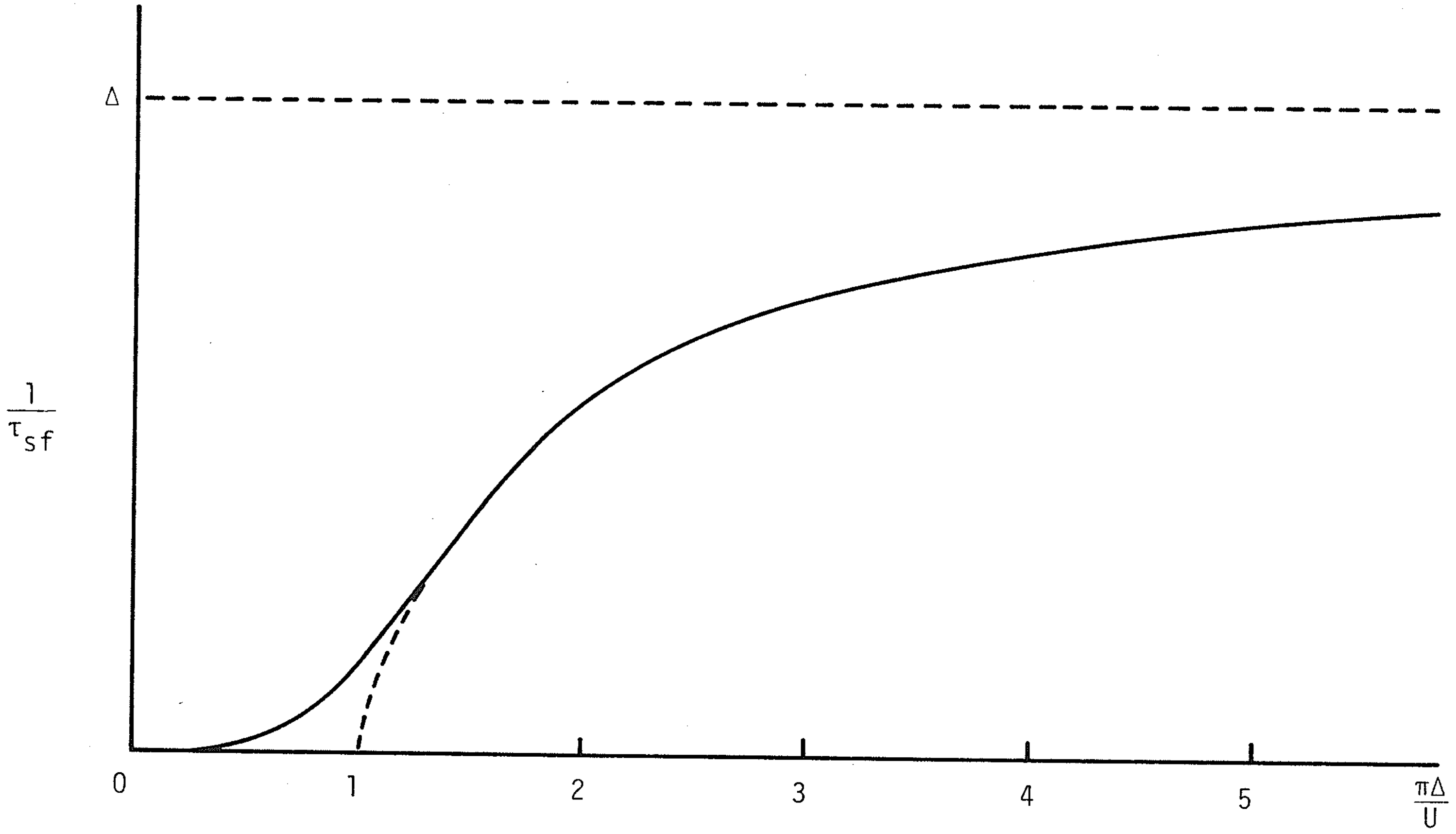

FIG.1.6-2. A plot of the spin fluctuation lifetime τ_{sf} as a function of $\pi\Delta/U$ for the case of a virtual level at the Fermi energy ($E_d = E_F$). The dashed curve is the result of Eq.(1.6-5), which predicts an infinite lifetime when $U/\pi\Delta > 1$ (the magnetic HF limit). The solid curve for $\pi\Delta/U < 1$ is a schematic representation of the "true" behaviour of τ_{sf} in this region.

where ψ is the digamma function and $\alpha^{-1} = 2\pi U\rho_d(E_F)$. This expression is plotted in FIG.1.6-3 as a function of the reduced temperature $x^{-1} = 2\pi U\rho_d(E_F)\, T/T_{sf}$. The resistivity decreases with increasing temperature. Four different temperature dependences can be distinguished :

(i) At very low temperatures ($T \ll T_{sf}$), the resistivity varies as $\rho_{\ell sf} = 1 - \alpha(T/T_{sf})^2$, with $\alpha = (\pi\, U\, \rho_d(E_F)/\surd 2)^2$.

(ii) As the temperature increases, the resistivity becomes linear : $\rho_{\ell sf} = \alpha[\, 1 - \beta(T/T_{sf})\,]$ where $\alpha = 1.0742$ and $\beta = \pi\, U\, \rho_d(E_F)/2.831$.

(iii)Above the LSF temperature T_{sf} , the resistivity exhibits the logarithmic dependence characteristic of magnetic impurities: $\rho_{\ell sf} = A - B\, \ell n T$.

(iv) Finally, for $T \to \infty$, the resistivity tends to zero as T_{sf}/T.

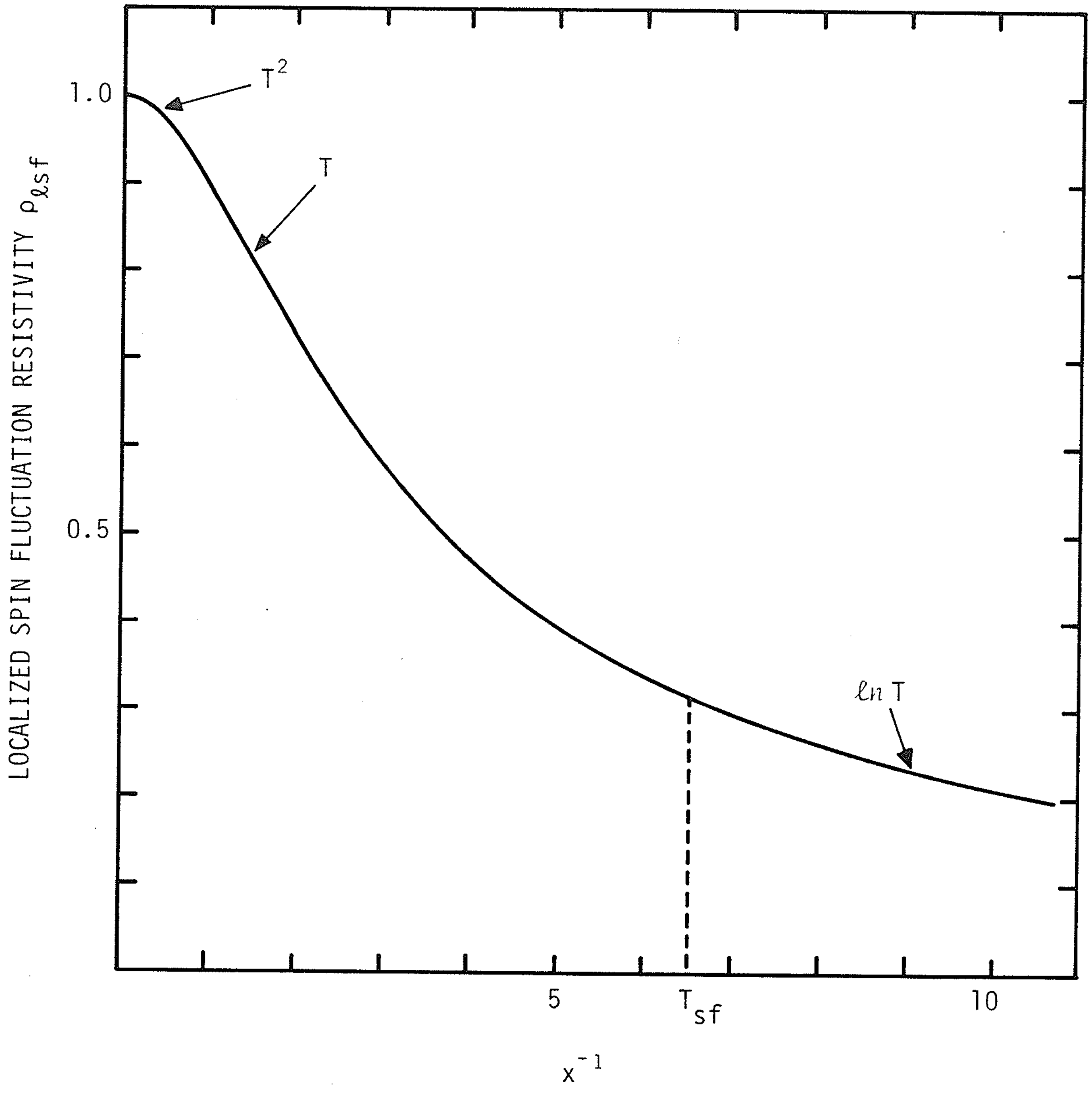

FIG.1.6-3. A plot of Eq.(1.6-6) for the LSF resistivity in non-isoelectronic alloys as a function of the reduced temperature $x^{-1} = 2\pi U \rho_d(E_F) T/T_{sf}$. The vertical dotted line marks the spin fluctuation temperature T_{sf}, above which the resistivity is logarithmic.

1.7 Interactions Between Impurities Via Conduction Electron Spin Polarization

The s-d exchange interaction, $-J\vec{S}\cdot\vec{s}$, between a magnetic impurity and the conduction electrons induces a spin polarization in the conduction electron gas and this, in turn, leads to an indirect coupling between the magnetic moments on different impurity atoms. This indirect interaction between magnetic impurities via conduction electron spin polarization is referred to as the Ruderman-Kittel-Kasuya-Yosida (RKKY) interaction [8, 9, 10].

An expression for the spin polarization induced in the conduction electron gas by a magnetic impurity can be obtained by assuming a δ-function exchange interaction between the impurity spin $\vec{S}$ and the conduction electron spins $\vec{s}_i$ of the form

$$-J\sum_i \vec{S}\cdot\vec{s}_i\ \delta(\vec{r}_i) \quad , \tag{1.7-1}$$

where the impurity spin is assumed to be located at $\vec{r}=0$ and J is the exchange coupling constant (J can be either positive or negative). Each conduction electron thus experiences an effective magnetic field due to the impurity spin which is given by

$$\vec{H}_{eff}(\vec{r}) = +\frac{J}{g\mu_B}\vec{S}\ \delta(\vec{r}) \quad . \tag{1.7-2}$$

The response of the conduction electron gas to this effective field can be obtained by making use of the following expression [34] for the spin polarization $\vec{s}(\vec{r})$ due to an arbitrary static magnetic field $\vec{H}(\vec{r})$:

$$\vec{s}(\vec{r}) = \frac{1}{g\mu_B} \sum_{\vec{q}} \vec{H}(\vec{q})\ \chi(\vec{q})\ \exp(i\vec{q}\cdot\vec{r}) \quad . \tag{1.7-3}$$

In this expression, $\chi(\vec{q})$ is the wavevector-dependent susceptibility of the conduction electron gas, while $\vec{H}(\vec{q})$ is the Fourier transform of $\vec{H}(\vec{r})$. Since the Fourier transform of $\vec{H}_{eff}$ is

$$\vec{H}_{eff}(\vec{q}) = + \frac{J}{g\mu_B} \vec{S} \quad , \tag{1.7-4}$$

it follows from Eq.(1.7-3) that the spin polarization induced by $\vec{H}_{eff}$ is given by

$$\vec{s}(\vec{r}) = \frac{J}{g^2\mu_B^2} \left[\sum_{\vec{q}} \chi(\vec{q})\ \exp(i\vec{q}\cdot\vec{r}) \right] \cdot \vec{S} \quad . \tag{1.7-5}$$

Thus $\vec{s}(\vec{r})$ is proportional to the Fourier transform of $\chi(\vec{q})$.

For a free, non-interacting electron gas, the susceptibility $\chi(\vec{q})$ is given by [35]

$$\chi_0(\vec{q}) = 2\mu_B^2\, N(E_F)\, U(q/2k_F) \quad , \tag{1.7-6}$$

where $N(E_F)$ is the conduction electron density of states at the Fermi energy, and $U(x)$ is the Lindhard function :

$$U(x) = \frac{1}{2}\left[1 + \frac{1-x^2}{2x}\,\ln\left|\frac{1+x}{1-x}\right|\right] \quad . \tag{1.7-7}$$

When the free-electron value for $\chi(\vec{q})$ is substituted into Eq.(1.7-5) and the sum over $\vec{q}$ evaluated by converting it into an integral [36], the result for the free-electron spin polarization is

$$\vec{s}_{RKKY}(\vec{r}) = -\,A\,J\left[\frac{\cos 2k_F r}{(2k_F r)^3} - \frac{\sin 2k_F r}{(2k_F r)^4}\right]\cdot \vec{S} \tag{1.7-8}$$

where A is a constant depending on the Fermi energy E_F, the Fermi wavevector k_F and the number of lattice points per unit volume in the crystal. Eq.(1.7-8) is known as the RKKY spin polarization and is plotted in FIG.1.7-1 (curve 1) as a function of the distance r from the impurity. From FIG.1.7-1 and Eq.(1.7-8), it can be seen that the RKKY spin polarization has the following characteristic features : (a) Most of the spin polarization is confined to a small region in the vicinity of the impurity atom. Moreover, the sign of the spin polarization in this region depends upon the sign of the exchange coupling constant J. Thus, for $J > 0$, the spin polarization is parallel to the impurity spin (resulting in a so-called "giant moment" when exchange enhancement effects are taken into account), while for $J < 0$, the spin polarization is antiparallel to the impurity spin. (b) For large values of r, the

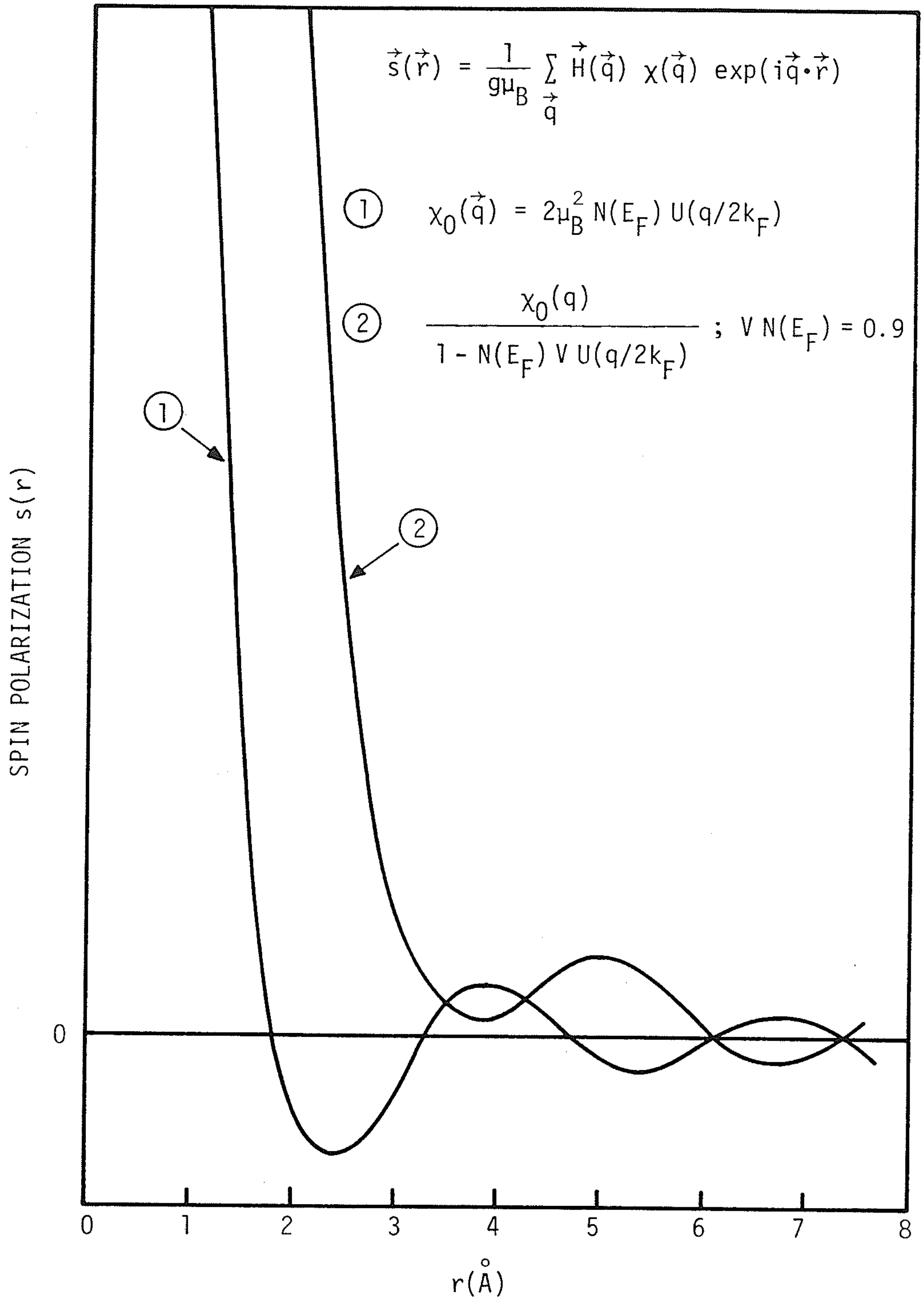

FIG.1.7-1. The spin polarization around a δ-function magnetic field probe for ① a noninteracting electron gas, and ② an interacting electron gas with $V N(E_F) = 0.9$.

spin polarization oscillates with a period $(2k_F)^{-1}$ and the amplitude of the oscillations decreases rapidly as $1/r^3$.

The free-electron RKKY spin polarization in Eq.(1.7-8) is appropriate for simple metal hosts where the conduction electrons are essentially noninteracting. However, in transition metal hosts like Pd and Pt, where the d electrons which contribute to the conduction process are confined to a narrow band, the effect of Coulomb interactions between the conduction electrons must be taken into account and the free electron susceptibility $\chi_0(q)$ must be replaced by the susceptibility of an interacting electron gas. If the Coulomb interactions are assumed to be δ-functions of strength V localized on the lattice sites, then the susceptibility of an interacting electron gas is given by [35] :

$$\chi(q) = 2\mu_B^2 \frac{N(E_F)\, U(q/2k_F)}{1 - N(E_F)\, V\, U(q/2k_F)} = \frac{\chi_0(q)}{1 - N(E_F)\, V\, U(q/2k_F)} \quad , \quad (1.7\text{-}9)$$

where U(x) is the Lindhard function defined in Eq.(1.7-7). As a result of the exchange enhancement factor $\eta = [\, 1 - N(E_F)\, V\, U(q/2k_F)]^{-1}$, the susceptibility of the host in the presence of electron-electron interactions is <u>enhanced</u> over its free electron value $\chi_0(q)$ for all q. However the enhancement is much greater for small q as shown in FIG.1.7-2.

From Eq.(1.7-5), it follows that the spin polarization induced

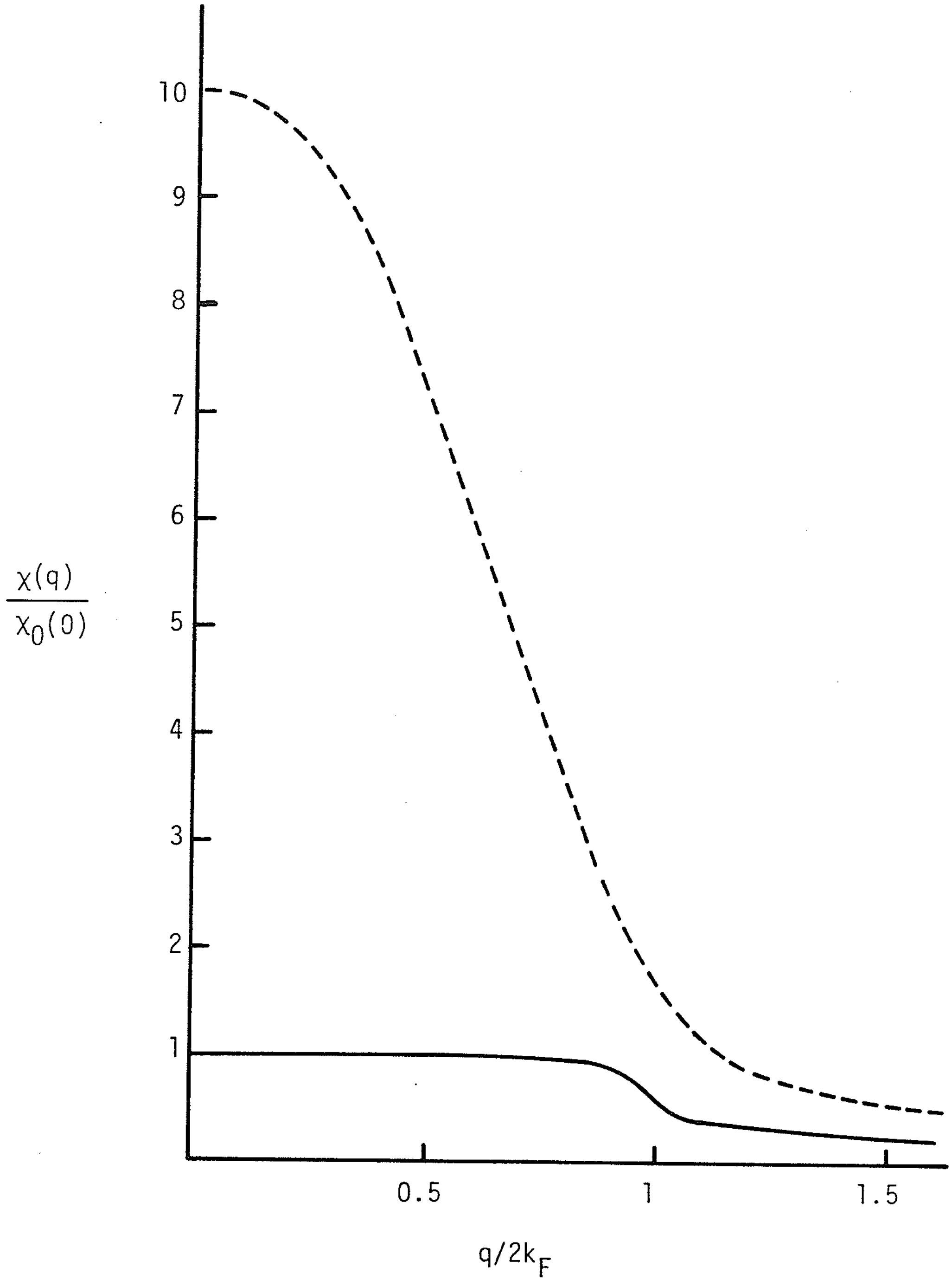

FIG.1.7-2. The normalized q-dependent susceptibility of an electron gas. The solid curve represents the free-electron susceptibility $\chi_0(q)$; the dashed curve represents the interacting-electron-gas susceptibility for the case $V\,N(E_F) = 0.9$. Note that the enhancement is q-dependent, being largest at low q.

in an interacting electron gas by a magnetic impurity is given simply by the Fourier transform of the exchange enhanced susceptibility $\chi(q)$ in Eq.(1.7-9). Since the effect of exchange enhancement is to "build up" the low q region so that $\chi(q)$ looks more and more peaked at low q as $N(E_F)V$ increases, the result is a longer and longer range for $\vec{s}(r)$ in r-space as the condition for ferromagnetic instability in the host $[N(E_F)\,V = 1]$ is approached. The exchange enhancement thus pushes out the first zero of the RKKY oscillations and increases their amplitude as shown in FIG.1.7-1 (curve 2). However, at sufficiently large distances from the impurity the spin polarization is again oscillatory. If the finite range of the Coulomb interaction is also taken into account, then the V appearing in Eq.(1.7-9) becomes effectively q-dependent. This causes an even more rapid rise in $\chi(q)$ with decreasing q and accordingly contributes to make the range of the spin polarization even longer.

The conduction electron spin polarization provides a mechanism for the indirect coupling of the magnetic moments on two magnetic impurities. Consider a magnetic impurity with spin $\vec{S}_i$ occupying the lattice site $\vec{R}_i$ in a metal. As a result of the s-d exchange interaction, the conduction electrons develop an oscillatory spin polarization $\vec{s}(\vec{r}-\vec{R}_i)$, given by Eq.(1.7-8), in the vicinity of the impurity. If there is another magnetic impurity with spin $\vec{S}_j$ at $\vec{R}_j$, it interacts with this induced spin polarization via the s-d exchange interaction, $-J\vec{S}_j\cdot\vec{s}(\vec{r}-\vec{R}_i)\,\delta(\vec{r}-\vec{R}_j)$, leading to an indirect coupling between the localized spins of the form

$$\mathcal{H}_{RKKY} = J(R_{ij})\,\vec{S}_i \cdot \vec{S}_j \quad , \qquad (1.7\text{-}10)$$

with an indirect exchange coupling constant $J(R_{ij})$ given by

$$J(R_{ij}) = A\,J^2 \left[\frac{\cos 2k_F R_{ij}}{(2k_F R_{ij})^3} - \frac{\sin 2k_F R_{ij}}{(2k_F R_{ij})^4} \right] \quad , \qquad (1.7\text{-}11)$$

where $R_{ij} = |\vec{R}_i - \vec{R}_j|$. This exchange-type interaction is known as the <u>RKKY interaction</u>. From Eq.(1.7-11), it can be seen that the strength of the interaction falls off as $1/R_{ij}^3$ for large values of R_{ij} and that the sign of the coupling constant J <u>oscillates</u> with a period $(2k_F)^{-1}$.

1.8 Interactions Between Impurities Via Covalent Admixture

Interactions between impurities can also arise from s-d and d-d covalent admixture. These interactions can be studied by generalizing the Anderson model to treat the problem of two similar impurity atoms, each possessing a single nondegenerate d orbital, dissolved in a metal. The generalized Anderson Hamiltonian has the following form :

$$\begin{aligned} H = & \sum_{k,\sigma} \varepsilon_k n_{k\sigma} + \sum_{\sigma} E_0(n_{1\sigma} + n_{2\sigma}) + U(n_{1+}n_{1-} + n_{2+}n_{2-}) \\ & + \sum_{i=1,2} \sum_{k,\sigma} V_{ik}(c^*_{k\sigma}c_{i\sigma} + c^*_{i\sigma}c_{k\sigma}) + \sum_{\sigma} V_{12}(c^*_{1\sigma}c_{2\sigma} + c^*_{2\sigma}c_{1\sigma}) \ . \qquad (1.8\text{-}1) \end{aligned}$$

The first term represents the energy of the free electrons in the conduction band ; ε_k and $n_{k\sigma}$ are the energy and occupation number operator for the conduction electron state with wavevector k and spin σ. The second and third terms constitute the Hamiltonian for the <u>unperturbed</u> atomic d orbitals on the two impurities ; E_0 is the unperturbed energy of the atomic d states (labelled 1 and 2) in the absence of mixing interactions, U is the Coulomb repulsion between opposite spin electrons in the same d orbital, and $n_{i\sigma}$ is the occupation number operator for the ith d orbital with spin σ. The fourth term describes the mixing between each localized d state and the free electron states in the conduction band ; V_{ik} is the covalent admixture matrix element between the conduction electron state k and the ith d orbital, and $c^*_{k\sigma}$ $(c_{k\sigma})$ and $c^*_{i\sigma}$ $(c_{i\sigma})$ are the creation (annihilation) operators for the conduction electron state $k\sigma$ and the atomic d orbital $i\sigma$, respectively. The last term represents the direct covalent admixture between the two d orbitals, and V_{12} is the transfer integral (or admixture matrix element) between the two d states.

From Eq.(1.8-1), it follows that interactions between impurities arising from covalent admixture can have one of two forms : (a) an indirect coupling, mediated by the conduction electrons, arising from the s-d mixing between each d orbital and the free electron states of the conduction band (the fourth term in Eq.(1.8-1)), or (b) a direct coupling, between nearest-neighbour impurities, due to the direct overlap of the two d orbitals (the fifth term in Eq.(1.8-1)).

(a) Indirect coupling via s-d admixture

When the impurities are far enough apart so that the two d orbitals are non-overlapping, the last term in Eq.(1.8-1) can be neglected. Under these conditions, the impurities interact indirectly via the s-d mixing term (the fourth term) in Eq.(1.8-1). This indirect interaction is referred to as double-resonance coupling and can be visualized simply as follows.

Consider two impurities, each with a single nondegenerate d orbital and separated by a distance R. For isolated, noninteracting impurities the effect of the s-d mixing term in Eq.(1.8-1) is to broaden each atomic d state into a virtual d state, with an energy $E_{d\sigma}$ and a density of states $\rho_{d\sigma}(\varepsilon)$ which are given by

$$E_{d\sigma} = E_0 + U < n_{-\sigma} > + \Gamma \quad , \tag{1.8-2}$$

and $$\rho_{d\sigma}(\varepsilon) = \frac{1}{\pi} \frac{\Delta}{(\varepsilon - E_{d\sigma})^2 + \Delta^2} \quad . \tag{1.8-3}$$

Γ and Δ are the energy shift and width of the virtual d state, respectively, and are related to the admixture matrix element $V_{ik} = < k|V|d_i >$ between the atomic d state $|d_i >$ and the conduction electron states $|k >$ by

$$\Gamma_i - i\Delta_i = \sum_k \frac{|< k|V|d_i >|^2}{\varepsilon + is - \varepsilon_k} \quad . \tag{1.8-4}$$

If a conduction electron with wavevector $\vec{k}$ and spin σ, described by the plane wave $|k > = \exp(i\vec{k}\cdot\vec{r})$, is scattered by the electrostatic potential due to the first impurity, then, for large values of r, the wavefunction of the scattered electron is given by [37]

$$\psi_k^\sigma \simeq \exp(i\vec{k}\cdot\vec{r}) + \frac{\exp(ikr)}{kr} \exp(i\delta_1^\sigma) \sin \delta_1^\sigma \quad , \tag{1.8-5}$$

where δ_1^σ is the $\ell = 2$ partial wave phase shift due to the first impurity (all the other phase shifts for which $\ell \neq 2$ have been neglected). This electron is then scattered by the electrostatic potential due to the second impurity and the problem can be treated exactly as in the original single-impurity Anderson model. In particular, in the vicinity of the second impurity, the conduction electron states are mixed with the localized d state $|d_2\rangle$. However, since the conduction electrons are no longer described by simple plane waves, the admixture matrix element $\langle k|V|d_2\rangle$ must be replaced by [38]

$$\langle \psi_k^\sigma|V|d_2^\sigma\rangle = \langle k|V|d_2\rangle \left[\exp(i\vec{k}\cdot\vec{R}) + \frac{\exp(ikR)}{kR} \exp(i\delta_1^\sigma) \sin\delta_1^\sigma \right] \qquad (1.8\text{-}6)$$

where $\langle k|V|d_2\rangle$ is the admixture matrix element between a plane wave state $|k\rangle$ and the localized d state $|d_2\rangle$. When Eq.(1.8-6) for $\langle \psi_k^\sigma|V|d_2^\sigma\rangle$ is substituted into Eq.(1.8-4) in place of $\langle k|V|d_2\rangle$, the following expression is obtained for the effective energy shift Γ_2' and width Δ_2' for the virtual d state on the second impurity :

$$\Gamma_2' - i\Delta_2' = \Gamma_2 - i\Delta_2 - \Delta_2 \sin\delta_1^\sigma \, \frac{\exp[\,i\,(2kR + \delta_1^\sigma)]}{(kR)^2} \quad , \qquad (1.8\text{-}7)$$

where Γ_2 and Δ_2 are the energy shift and width for the <u>isolated</u> second impurity. Thus the presence of the first impurity (via the phase shift δ_1^σ) modifies the effective energy shift Γ_2' and width Δ_2' of the virtual d state on the second impurity. This, in turn, leads to a change in the number of localized d electrons on the second impurity and consequently an indirect coupling between the two impurities.

The problem of double-resonance coupling between impurities has been treated formally, with the use of Green's functions, by Blandin [39] and Caroli [40]. For two nondegenerate virtual d states separated by a distance R, the following expression is obtained for the interaction energy due to double-resonance coupling, for large values of R :

$$E_{int}(R) \simeq \frac{E_F}{\pi} \sum_{\sigma} \sin \delta_1^{\sigma} \; \sin \delta_2^{\sigma} \; \frac{\cos(2k_F R + \delta_1^{\sigma} + \delta_2^{\sigma})}{(k_F R)^3} \quad , \qquad (1.8\text{-}8)$$

where δ_1^{σ} and δ_2^{σ} are the phase shifts produced by an isolated impurity and k_F is the Fermi wavevector.

(b) Direct coupling via d-d covalent admixture

When the impurities are nearest-neighbours, the interactions will be dominated by direct d-d covalent admixture between the two localized d orbitals (the last term in Eq.(1.8-1)) and $|V_{12}| >> |V_{1k}|$ and $|V_{2k}|$. The effect of d-d covalent admixture between two impurity atoms on the populations, $n_{1\sigma}$ and $n_{2\sigma}$, of the virtual d states and on the magnitude of the localized moments has been studied in detail, in the Hartree-

Fock approximation, by Moriya [41] and Alexander and Anderson [42], using the Green's function formalism described by Anderson in the solution of the single-impurity problem [3]. In particular, when both impurities are magnetic, and if $V_{12}/U << 1$, then a calculation of the interaction energy due to d-d covalent admixture shows that the localized moments can be aligned either parallel or antiparallel to each other and the sign of the magnetic coupling is determined by the following simple rules :

(a) Atoms with nearly half-filled d shells (like Cr or Mn) have a tendency to couple antiferromagnetically.

(b) As the number of d electrons increases (Fe and Co), there is an increasing tendency towards ferromagnetic coupling.

The theory is also applicable to the case where one of the impurity atoms is initially nonmagnetic. Under these conditions, the covalent admixture between the two impurity atoms induces a spin polarization in the originally nonmagnetic atom and, for small values of V_{12}/U, the following qualitative conclusions are obtained as to the sign of the induced moment :

(a) Atoms with nearly half-filled d shells have a tendency to be polarized antiparallel to the neighbouring atomic moment, while atoms with nearly filled d shells have a preference for parallel spin polarization.

(b) As for the magnetic atom, one with a nearly half-filled d shell has a tendency to polarize neighbouring atoms antiparallel, while one with a nearly filled d shell has a tendency to induce a parallel spin polarization in a neighbouring nonmagnetic atom.

1.9 Spin Glasses : The Cluster Relaxation Model

A spin glass is a nonmagnetic metal containing a small concentration of magnetic impurities located at random and exhibits no long range magnetic order at any temperature, in spite of having its impurity spins frozen in random orientations at low temperatures. The impurity spins interact via the RKKY coupling mechanism, i.e., a long ranged, oscillatory, indirect exchange interaction mediated by the conduction electrons. The absence of long range magnetic order is a consequence of the randomness in the positions of the spins together with the oscillatory nature of their interaction.

In order to exhibit spin glass behaviour in its simplest form, an alloy system must satisfy two important requirements : (a) the impurities should have a high solubility in the host (at least up to 10 at. %), and (b) the Kondo temperature of the system should be low ($T_K < 1K$), so that one has "good" magnetic moments and no complications are encountered with the weakening of the local moments at low temperatures. Of the systems consisting of 3d transition metals dissolved as impurities in the noble metal hosts copper, silver, and gold, there seem to be five highly favourable combinations which satisfy the above two requirements. These are $\underline{Au}Fe$, $\underline{Au}Cr$, $\underline{Au}Mn$, $\underline{Ag}Mn$, and $\underline{Cu}Mn$, and the spin glass regime occurs roughly between 0.5 and 10 at. % impurity.

Systematic studies of the electric and magnetic properties of these five archetypal noble metal host - 3d transition impurity spin glasses show that the following features are characteristic of all five systems : (a) The magnetic susceptibility measured in a small alternating field exhibits a sharp peak (or cusp) at the "freezing" temperature T_0 [43], as shown in FIG.1.9-1. However, the application of a static external field of a few hundred Oersteds wipes out the cusp, replacing it by a broad maximum. (b) The static susceptibility (i.e., the magnetization in a constant field) may have a different behaviour depending on the experimental conditions. The magnetization, measured after cooling to $T < T_0$ in zero field, is reversible (i.e., no after effect and no remanent magnetization) as long as the measuring field H is smaller than a critical value H_c, and the corresponding reversible susceptibility, defined by the slope $\left.\frac{M(H)}{H}\right|_{H \to 0}$ of the magnetization measured in a field H smaller than H_c, has a thermal behaviour [44, 45] which is identical to that of the susceptibility measured in an alternating field (i.e., sharp cusp). When the measuring field H is higher than H_c, and for $T < T_0$, the magnetization loses its reversibility [46, 47, 48] and an isothermal remanent magnetization (I.R.M.) is observed when the field is suppressed. The corresponding susceptibility, obtained by taking M(H)/H on a first magnetization curve with $H > H_c$, exhibits a broad maximum as a function of temperature. Cooling the sample to $T < T_0$ in an external field H_e results in a thermoremanent magnetization (T.R.M.) and a displaced hysteresis loop [49]. Both the I.R.M. and the T.R.M.

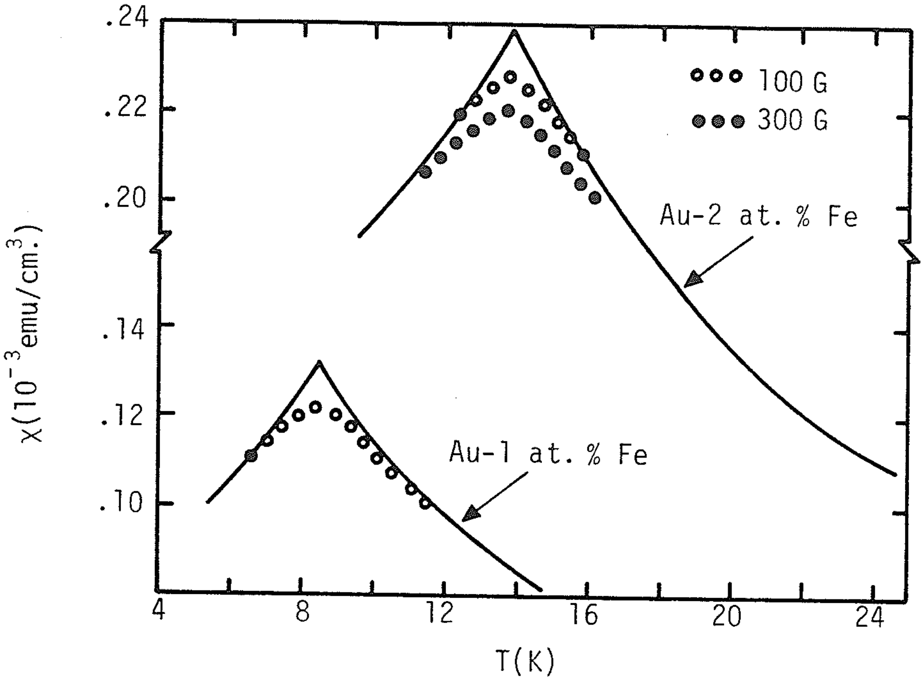

FIG.1.9-1. The behaviour of the low-field A.C. susceptibility of a typical spin glass with increasing external field. The solid lines represent the zero-field limit [43].

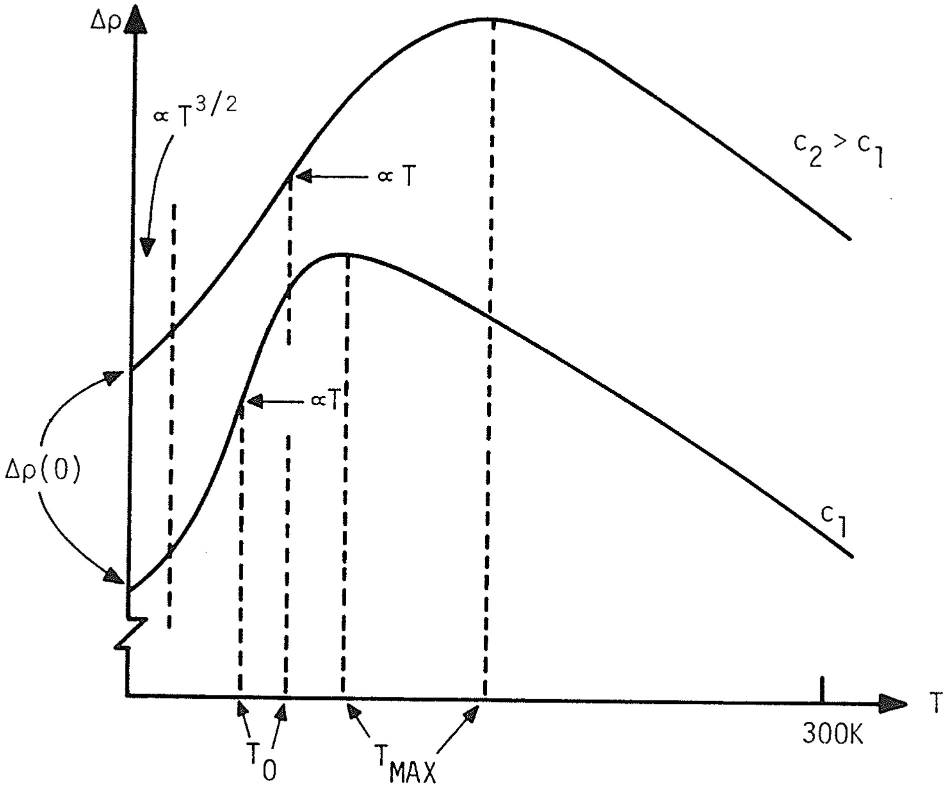

FIG.1.9-2. The behaviour of the "magnetic" component of the electrical resistivity of a typical spin glass.

decay with characteristic relaxation times $\tau_i(c,H,T)$. (c) The behaviour of the "magnetic" component of the electrical resistivity [50] is illustrated schematically in FIG.1.9-2. The resistivity has a large residual contribution, $\Delta\rho(0)$, due to the "disorder" scattering from the randomly frozen spin glass matrix. As the temperature is increased, the resistivity initially increases as $A(c)T^{3/2}$, with $A(c)$ decreasing weakly with increasing concentration, i.e., $A(c) \propto -\ell n c$ or $c^{-1/5}$. At higher temperatures, the temperature dependence changes from $T^{3/2}$ to T, and the resistivity passes through an inflection point and then a maximum at temperature T_m, above which it falls off with increasing temperature. In <u>Au</u>Fe, there appears to be a good correlation between the temperature of the maximum in $d(\Delta\rho)/dT$ (i.e., the temperature of the inflection point in $\Delta\rho(T)$) and the temperature of the cusp in the A.C. susceptibility [51]. However, this relationship breaks down for <u>Au</u>Mn and <u>Au</u>Cr. Rivier and Adkins [52] have suggested that the initial $T^{3/2}$ temperature dependence is a consequence of conduction electron scattering from the elementary excitations of a spin glass. Since a spin glass is characterized by a lack of well-defined long range order, any spin flip excitation on an impurity site is unable to propagate like a magnon, but dies away with some diffusion constant Λ. Starting from such an assumption, Rivier and Adkins have shown that the resistivity increases initially as $(T/\Lambda)^{3/2}$. The negative slope of $\Delta\rho(T)$ above the maximum is probably due to single-impurity Kondo scattering since, at these temperatures, the impurity spins are essentially noninteracting.

The magnetic properties of spin glasses can be interpreted in terms of a simple, physical model [53] which requires two basic assumptions : the presence of large, independent, strongly internally coupled magnetic clusters and an anisotropy barrier to the coherent rotation of the cluster moments. It is assumed, as usual, that the impurity spins interact via the long range oscillatory RKKY exchange interaction which has the form

$$\mathcal{H} = - \sum_{<ij>} J(R_{ij}) \vec{S}_i \cdot \vec{S}_j \qquad (1.9\text{-}1)$$

where $$J(R) = \frac{A \cos(2k_F R)}{(2k_F R)^3} \quad , \quad k_F R >> 1. \qquad (1.9\text{-}2)$$

At any given temperature T, a magnetic cluster is defined as a group of spins which are linked by exchange bonds (i.e., by RKKY exchange interactions) with magnitudes greater than the thermal energy kT. Thus all the spins in a cluster are completely aligned by their internal fields and each cluster is free to rotate as a rigid body in response to an applied magnetic field. An equivalent geometrical picture of magnetic clusters can be obtained by replacing supra-thermal exchange bonds by bonds whose spatial length is less than a "thermal cutoff length" R_c, such that the internal field from a spin at this distance is down to thermal values :

$$S|J(R_c)| \sim \frac{AS}{(2k_F R_c)^3} = kT \quad . \qquad (1.9\text{-}3)$$

The clusters are thus temperature dependent : as T is reduced, the maximum allowed bond length R_c increases and the clusters grow in size.

By analogy with the properties of normal superparamagnetic particles discussed by Néel [54], a blocking temperature T_B is associated with each of these clusters, above which the cluster behaves superparamagnetically and below which the cluster magnetization is frozen. In the superparamagnetic state, each cluster has only two stable orientations determined by the minima in the anisotropy energy density and separated by an energy barrier E_A. Transitions between these two states require thermal activation over the energy barrier E_A and occur at the rate

$$1/\tau = C\exp(-E_A/kT) \quad , \text{ for } E_A >> kT, \qquad (1.9\text{-}4)$$

with $C \simeq 10^8 - 10^{10}$ sec.$^{-1}$ [55]. When the relaxation time τ of the cluster becomes longer than the measuring time τ_m the cluster moment appears to be frozen and the corresponding blocking temperature T_B is given by

$$E_A(T_B) = kT_B\, \ell n(C\tau_m) \quad . \qquad (1.9\text{-}5)$$

Thus, in a typical static magnetization experiment where the measurement is performed over a finite time interval τ_m, all those clusters with relaxation times $\tau < \tau_m$ respond with the full D.C. susceptibility, whereas those with $\tau > \tau_m$ are blocked and contribute nothing. An equivalent approach, appropriate for A.C. measurements at frequency ω, is to give all clusters for which $\omega\tau < 1$ the full D.C. susceptibility and to ignore the rest. If a significant fraction of the spin system evolves into magnetic clusters with about the same amount of anisotropy energy E_A, and hence approximately the same relaxation times τ, their simultaneous freezing will cause a sizeable perturbation to the susceptibility which measures their dynamical response, resulting in a peak in the low-field A.C. susceptibility. Because of the exponential variation of the relaxation time τ with the inverse temperature $1/T$ and the anisotropy energy E_A, which is itself strongly temperature dependent, this freezing occurs over a narrow temperature interval such that on a linear scale it appears to be sharp. The rounding off of the cusp, which is produced by the application of an additional moderate steady field, is consistent with the above relaxation picture, since the presence of a static magnetic field introduces asymmetry in the relaxation times of superparamagnetic particles causing a broadening of the distribution of blocking temperatures, even among a collection of identical superparamagnetic particles [56].

The relaxation model also predicts a time-dependent remanent magnetization : when the exciting field H is removed, the clusters begin to relax over their anisotropy energy barriers and the magnetization decays logarithmically with time [45] :

$$M(t) = M(0) - S\,\ell n t. \tag{1.9-6}$$

References

1. J. Friedel, Can. J. Phys. 34, 1190 (1956) ; Nuovo Cimento Suppl. 7, 287 (1958) ; A. Blandin and J. Friedel, J. Phys. radium 20, 160 (1959).
2. E. Daniel and J. Friedel, in Proceedings of the IXth International Conference on Low Temperature Physics, edited by J. G. Daunt, D. O. Edwards, F. J. Milford, and M. Yaqub (Plenum Press, New York, 1965), page 933.
3. P. W. Anderson, Phys. Rev. 124, 41 (1961).
4. L. L. Hirst, Phys. Kondens. Mat. 11, 255 (1970) ; in Magnetism and Magnetic Materials - 1974, edited by C. D. Graham, Jr., G. H. Lander, and J. J. Rhyne, AIP Conference Proceedings No. 24 (American Institute of Physics, New York, 1975), P. 11.
5. C. Zener, Phys. Rev. 81, 440 (1951).
6. P. Lederer and D. L. Mills, Phys. Rev. 165, 837 (1968).
7. A. B. Kaiser and S. Doniach, Intern. J. Magnetism 1, 11 (1970).
8. M. A. Ruderman and C. Kittel, Phys. Rev. 96, 99 (1954).
9. T. Kasuya, Progr. Theoret. Phys. (Kyoto) 16, 45 (1956).
10. K. Yosida, Phys. Rev. 106, 893 (1957).
11. J. Friedel, Adv. Phys. (Phil. Mag. Suppl.) 3, 446 (1954).
12. W. Kohn and S. H. Vosko, Phys. Rev. 119, 912 (1960).
13. N. F. Mott and H. S. W. Massey, "The Theory of Atomic Collisions" (Oxford, Clarendon Press, 3rd edition, 1965), pp. 19 - 52.
14. J. M. Ziman, "Principles of the Theory of Solids" (Cambridge, University Press, 2nd edition, 1972), pp. 157 - 9.
15. L. L. Hirst, Z. Physik 244, 230 (1971).

16. K. Yosida, Phys. Rev. 107, 396 (1957).

17. J. Kondo, Progr. Theoret. Phys. (Kyoto) 32, 37 (1964).

18. A. A. Abrikosov, Physics 2, 5 (1965).

19. Y. Nagaoka, Progr. Theoret. Phys. (Kyoto) 37, 13 (1967) ; Phys. Rev. 138, A1112 (1965).

20. H. Suhl and D. Wong, Physics 3, 17 (1967).

21. H. Suhl, Phys. Rev. 138, A515 (1965) ; Physics 2, 39 (1965) ; Phys. Rev. 141, 483 (1966).

22. K. G. Wilson, in Collective Properties of Physical Systems, Nobel Symposium 24 (Academic Press, New York, 1974), p. 68.

23. These ideas were initially developed for phase transitions -- K. G. Wilson and M. E. Fisher, Phys. Rev. Lett. 28, 240 (1972) -- and applied most lucidly to the Kondo problem by M. Fowler, Phy. Rev. B6, 3422 (1972).

24. P. Nozieres, J. Low Temp. Phys. 17, 31 (1974).

25. P. Nozieres, "Theory of Interacting Fermi Systems" (W. A. Benjamin, New York, 1964).

26. C. Kittel, "Introduction to Solid State Physics" (Wiley, New York, 4th edition, 1971), p. 518.

27. E. C. Stoner, Proc. Roy. Soc. (London) A165, 372 (1938).

28. S. Doniach and S. Engelsberg, Phys. Rev. Lett. 17, 750 (1966).

29. N. Rivier and V. Zlatic, J. Phys. F : Metal Phys. 2, L99 (1972).

30. N. Rivier and M. J. Zuckermann, Phys. Rev. Lett. 21, 904 (1968).

31. N. Rivier, M. Sunjic, and M. J. Zuckermann, Phys. Lett. 28A, 492 (1969).

32. A. D. Caplin and C. Rizzuto, Phys. Rev. Lett. 21, 746 (1968).

33. N. Rivier and V. Zlatic, J. Phys. F : Metal Phys. 2, L87 (1972).

34. R. M. White, "Quantum Theory of Magnetism" (McGraw-Hill, New York, 1970), p. 82.

35. P. A. Wolff, Phys. Rev. 120, 814 (1960).

36. Ref. 34, page 199.

37. G. Baym, "Lectures on Quantum Mechanics" (W. A. Benjamin, Inc., Reading, Massachusetts, 1974), page 199.

38. Eq.(1.8-6) follows directly if the mixing interaction, V, is assumed to be a δ-function.

39. A. Blandin, in Proceedings of the International School of Physics "Enrico Fermi", Course XXXVII, 1966 (Academic Press, New York, 1967), page 393.

40. B. Caroli, J. Phys. Chem. Solids 28, 1427 (1968).

41. T. Moriya, as in Ref. 39, page 206.

42. S. Alexander and P. W. Anderson, Phys. Rev. 133, A1594 (1964).

43. V. Cannella and J. A. Mydosh, Phys. Rev. B6, 4420 (1972) ; in Magnetism and Magnetic Materials - 1972, edited by C. D. Graham , Jr. and J. J. Rhyne, AIP Conference Proceedings No. 10 (American Institute of Physics, New York, 1973), p. 785 ; in Proceedings of the International Conference on Magnetism (Publ. House Nauka, Moscow, 1974) 2, 74.

44. J. L. Tholence and R. Tournier, J. Phys. (Paris) 35 C4, 229 (1974).

45. C. N. Guy, J. Phys. F : Metal Phys. 7, 1505 (1977).

46. J. S. Kouvel, J. Phys. Chem. Solids 21, 57 (1961) ; J. Phys. Chem. Solids 24, 795 (1963).

47. O. S. Lutes and J. L. Schmidt, Phys. Rev. 134, A646 (1964) ; Phys. Rev. 125, 433 (1962).

48. J. Owen, M. E. Brown, V. Arp and A. K. Kip, J. Phys. Chem. Solids 2, 85 (1957).

49. R. J. Borg and T. A. Kitchens, J. Phys. Chem. Solids 34, 1323 (1973).

50. P. J. Ford and J. A. Mydosh, J. Phys. (Paris) 35 C4, 241 (1974).

51. J. A. Mydosh, P. J. Ford, M. P. Kawatra and T. E. Whall, Phys. Rev. B10, 2845 (1974).

52. N. Rivier and K. Adkins, J. Phys. F : Metal Phys. 5, 1745 (1975).

53. D. A. Smith, J. Phys. F : Metal Phys. 4, L266 (1974) ; J. Phys. F : Metal Phys. 5, 2148 (1975).

54. L. Neel, C. R. Acad. Sci. Paris 228, 664 (1949) ; Ann. Geophys. 5, 99 (1949).

55. F. D. Stacey and S. K. Banerjee, "The Physical Principles of Rock Magnetism" (Amsterdam : Elsevier, 1974).

CHAPTER 2

EXPERIMENTAL METHODS

2.1 Measurement of Electrical Resistivity

This section begins with a brief, general description of the method and equipment used to obtain temperature-dependent resistivities for the various alloys.

The alloys were prepared by melting together appropriate amounts of the pure elements in an argon arc furnace and then formed into long, thin strips approximately 10 cm. long, 0.2 cm. wide and, typically, .01 cm. in thickness. Small cross-sectional area-to-length ratios (form factors) were used in order to obtain reasonably high resistance values (between $\sim 10^{-3}$ and 10^{-1} ohms). Sets of up to six alloys, of differing percentage composition, were mounted in a 6-sample holder, and the resistances of the samples were measured using a standard four-probe technique [1].

Since resistivity as a function of temperature was being measured, a means of varying and controlling the temperature was necessary. Below 4.2K temperatures were obtained by pumping on a liquid helium bath, and stabilized with a manostat in the pumping line. Oil and mercury manometers were used to determine the precise temperatures. Above 4.2K, a heater in a feedback circuit was used to obtain and regulate the temperatures, and precise measurements were made with a nonlinear gas thermometer.

A more detailed discussion of the equipment now follows.

2.1.1 The Vacuum System

FIG.2.1-1 shows a flow diagram of the vacuum system. The main pump, for refrigerating the helium bath and hence the samples, was an Edwards High Vacuum Ltd. Speedivac ES 330 with a pumping capacity of about 330 liters per minute. A Speedivac vapour diffusion pump, backed by a Speedivac ES 100 mechanical pump, was used to control the pressure in the inner and outer vacuum cans, and to evacuate the reference side of the manometers. The pressure monitoring system was composed of a Pirani gauge for use in the range 760 mm. to 10^{-3} mm. Hg, and a Penning gauge for pressures down to 10^{-7} mm. Hg.

The inner vacuum can (IVC) was machined from $2\frac{1}{2}$" diameter solid brass stock and was attached to the gas thermometer bulb using 12 symmetrically located # 2-32 bolts and an indium O-ring seal. Details of this construction are shown in FIG.2.1-2. The IVC was suspended from the top plate of the outer vacuum can (OVC) by two low thermal conductivity stainless steel tubes. The outer vacuum can was attached to the OVC top plate with Wood's metal. The entire vacuum can assembly was suspended from the cryostat top plate by three stainless steel tubes, each about $2\frac{1}{2}$ feet long. One of these tubes served as a guide for inserting the He^4 transfer tube when filling the He dewar, one was a vacuum line to the OVC, and the third was a vacuum line to the IVC as well as a channel for the hook-up wires to the samples.

The hook-up wires consisted of twenty-two # 38 enamelled copper

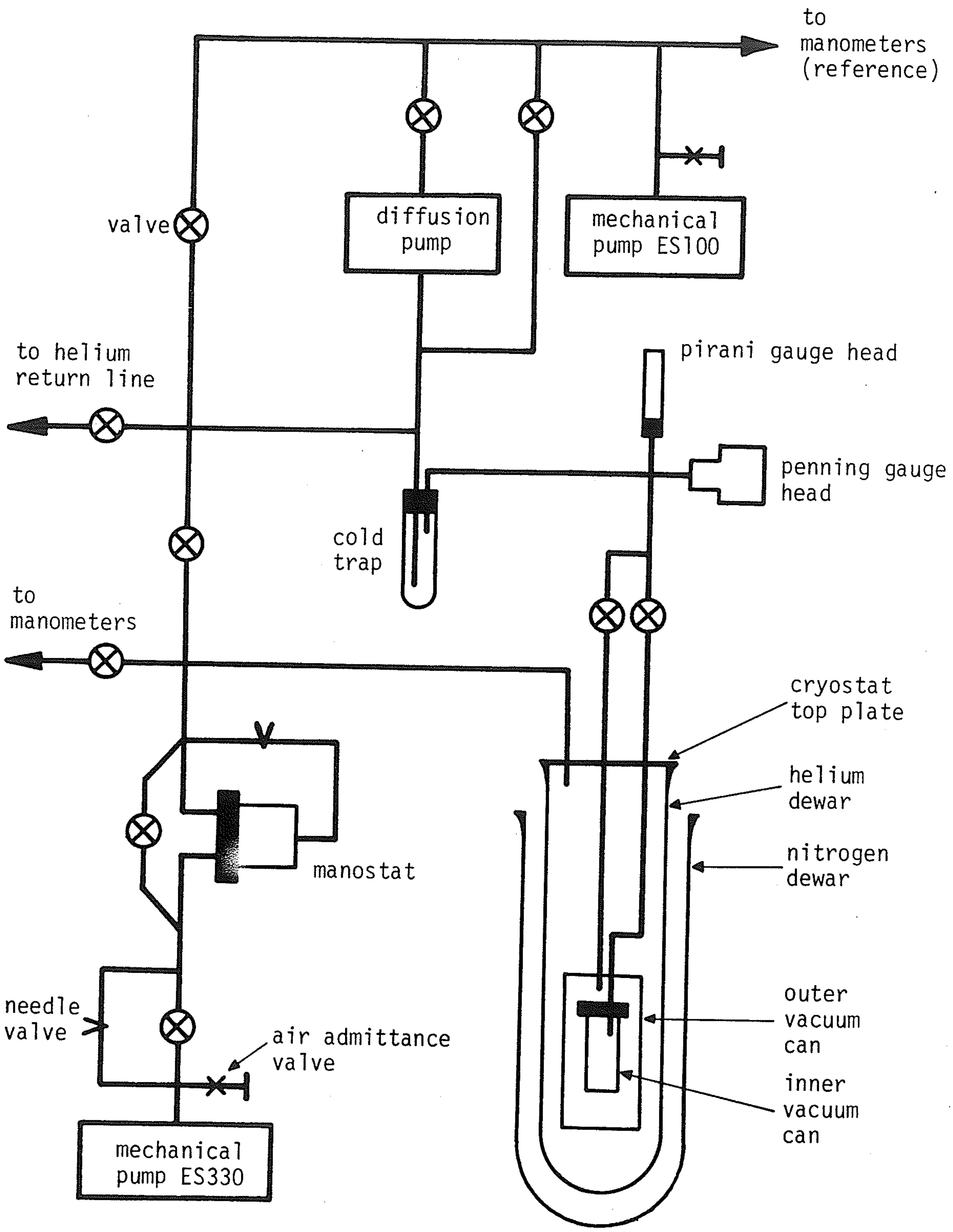

FIG.2.1-1 Block Diagram of the Vacuum System.

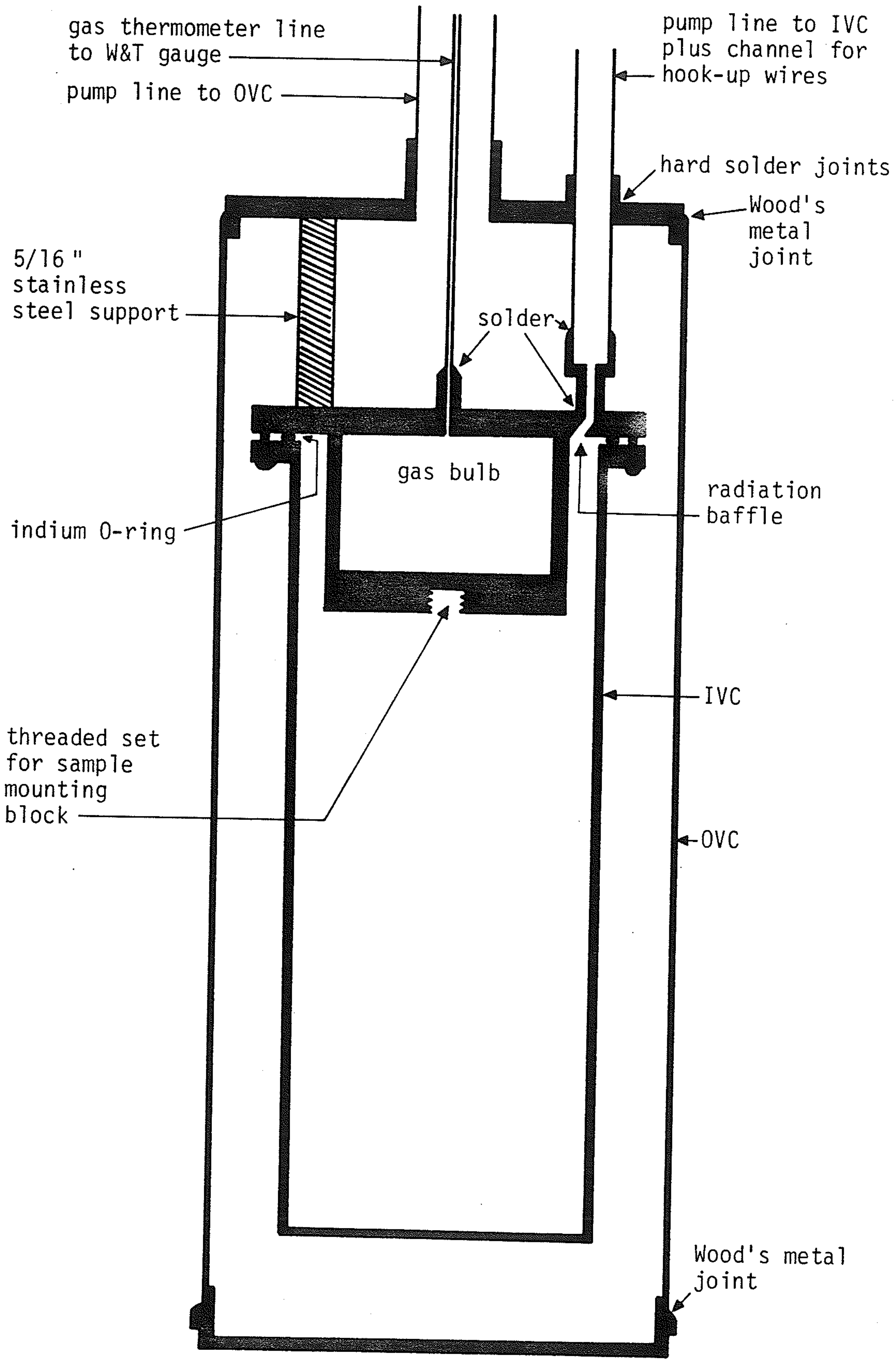

FIG.2.1-2 Details of the OVC, IVC, and Gas Bulb.

wires bound in a Systoflex insulating sheath. These were connected to various points on the mounting block (12 to voltage contacts, 2 current supply wires, 3 to the temperature sensing carbon resistor, 2 for the heater coil, and 3 spare). The wires were passed through one of the stainless steel columns to the cryostat top plate, where they were fed through a brass "lead-through" capable of accepting up to 22 wires. Silicone seal was used to seal the wires to the lead-through, and Stycast epoxy cement provided a vacuum tight connection between the lead-through and a machined brass mount. Details of the top plate assembly are shown in FIG.2.1-3.

2.1.2 The Sample Block

The sample mounting block was machined from oxygen-free high thermal conductivity (OFHC) pure copper stock in approximately the dimensions shown in FIG.2.1-4. The upper end of the block terminates in about a $\frac{1}{4}''$ length of $\frac{1}{4}''$ N.C. threads for fitting to the bottom of the gas thermometer bulb. Slots were machined in the block for the knife-edge sample supports and heaters, and a hole was drilled through the center of the block in order to accomodate the temperature sensing carbon resistor.

The block was designed to accept up to six samples, each of these to be mounted on a pair of knife-edge supports located near opposite ends of the block, about 8 cm. apart. These supports were

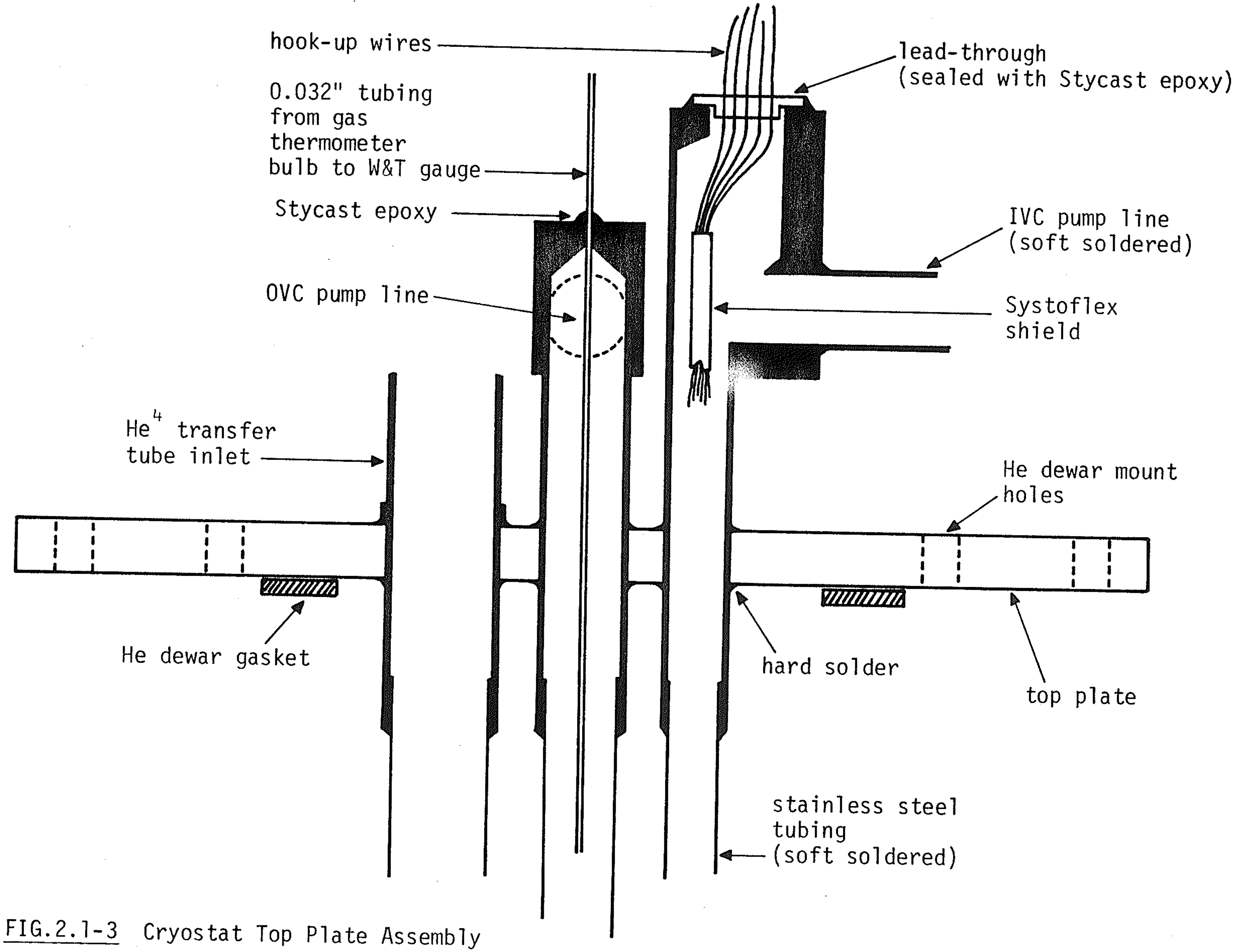

FIG.2.1-3 Cryostat Top Plate Assembly

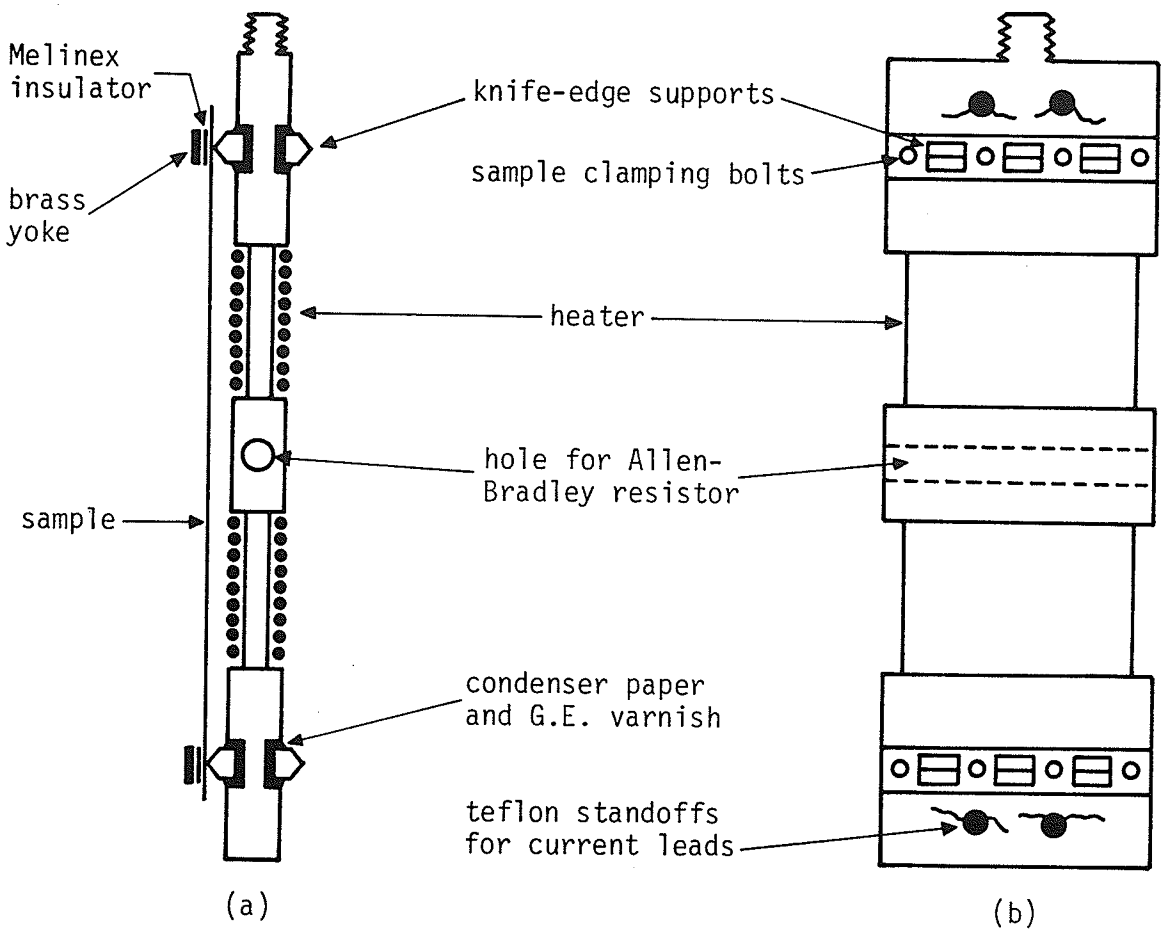

FIG.2.1-4 (a) Edge-view of Mounting Block.
(b) Face-view of Mounting Block.

electrically insulated from the block with strips of newsprint paper, and fastened in place with generous amounts of General Electric (G.E.) No. 7031 varnish. The varnish provided reasonably good thermal contact between the knife-edge supports and the sample block.

Four #2-32 bolts, a Mylar insulating strip, and a thin brass yoke held the ends of the samples in good electrical and thermal contact with the knife-edge supports. Wires soldered to the base of each knife-edge support provided the voltage tap-off connections. The samples were connected in series by soldering copper shunts between consecutive ends, and the end-points of the series were connected to the current supply leads.

Two heater coils were wound around the copper sample block, one for active use, the second as a standby. Each heater was formed from 20 feet of 0.036" diameter enamelled Cupron wire having a room temperature resistance of about 500 ohms. Since Cupron has a very low temperature coefficient of resistance this value changes very little, even at low temperatures.

For temperature sensing, an Allen-Bradley carbon resistor (100 Ω nominal value) was fitted into the hole in the center of the sample block, and fastened in place with G.E. varnish to ensure good thermal contact. The temperature dependence of the resistance is roughly logarithmic, increasing with decreasing temperature as shown in FIG.2.1-5, and this calibration curve was used to select approximate temperature points. The actual temperatures were obtained more

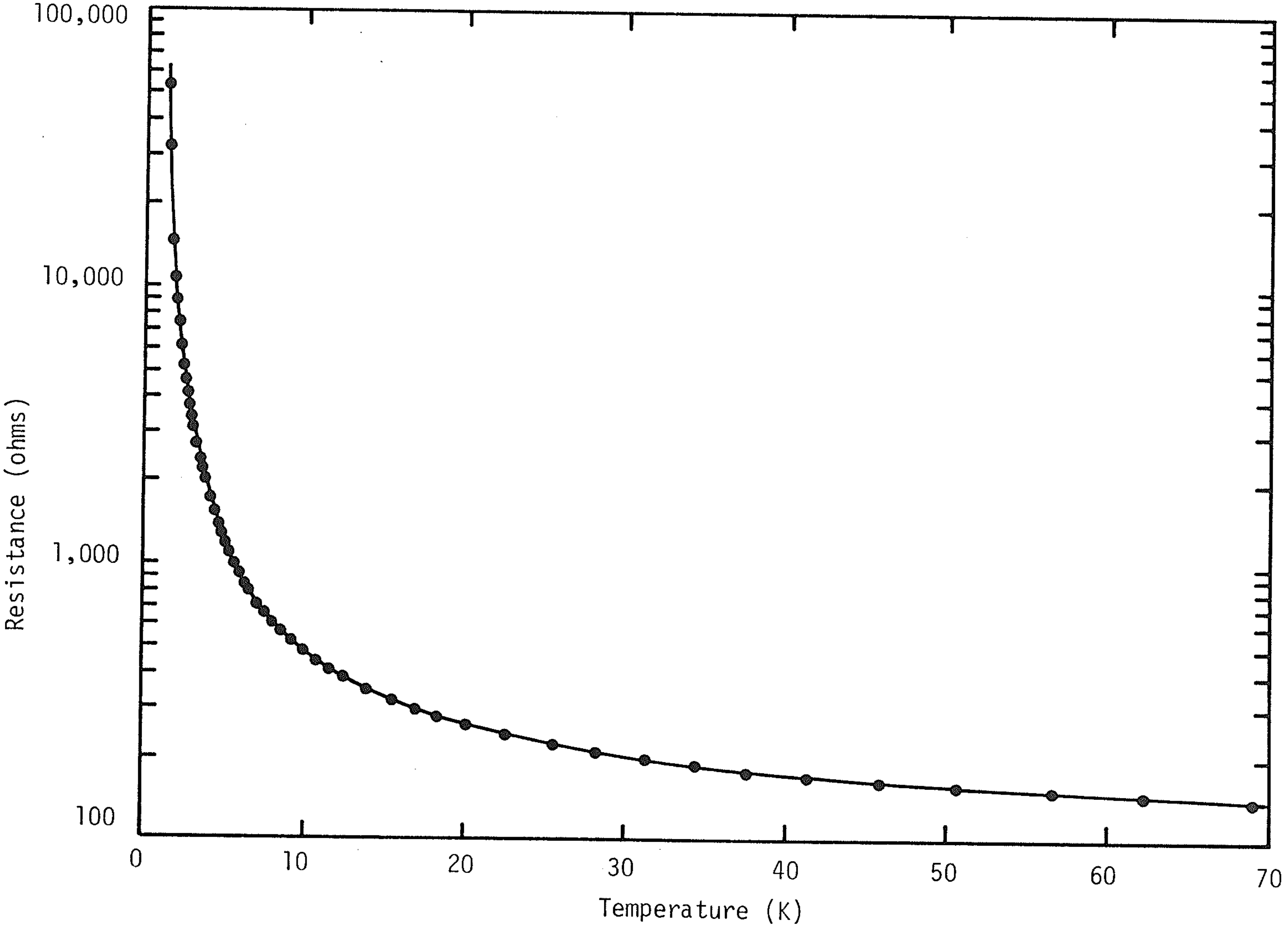

FIG.2.1-5 Resistance Versus Temperature Characteristics of the Allen-Bradley Resistor.

precisely by other means.

2.1.3 Electronics

FIG.2.1-6 outlines in block diagram form the electronic system used to determine the resistance of the samples at a particular temperature. A Guildline constant current source (model 9770 B), stable to 1 part in 10^6 , was used to supply a highly stable current to the series connected samples. A Guildline low-thermal selector switch (model 9145 A10) applied the voltage drop from across a particular sample to a Tinsley Diesselhorst thermoelectric-free potentiometer (type 3589 R). The potentiometer, in combination with a Tinsley photocell galvanometer amplifier (type M.S.2 45 E), was used to measure both the sample voltage and current. (The potentiometer-galvanometer combination was capable of measuring potential differences as small as 10^{-8} volts.) The current through the samples was determined by measuring the voltage that it produced across an 0.1 Ω Guildline standard resistor (model 9200) connected in series with the specimens. A Tinsley thermoelectric-free reversing switch (type 4092) allowed voltage measurements to be taken in both the "forward" and "reverse" directions, thus eliminating thermal emf's in the potentiometer circuit (i.e., external to the cryostat).

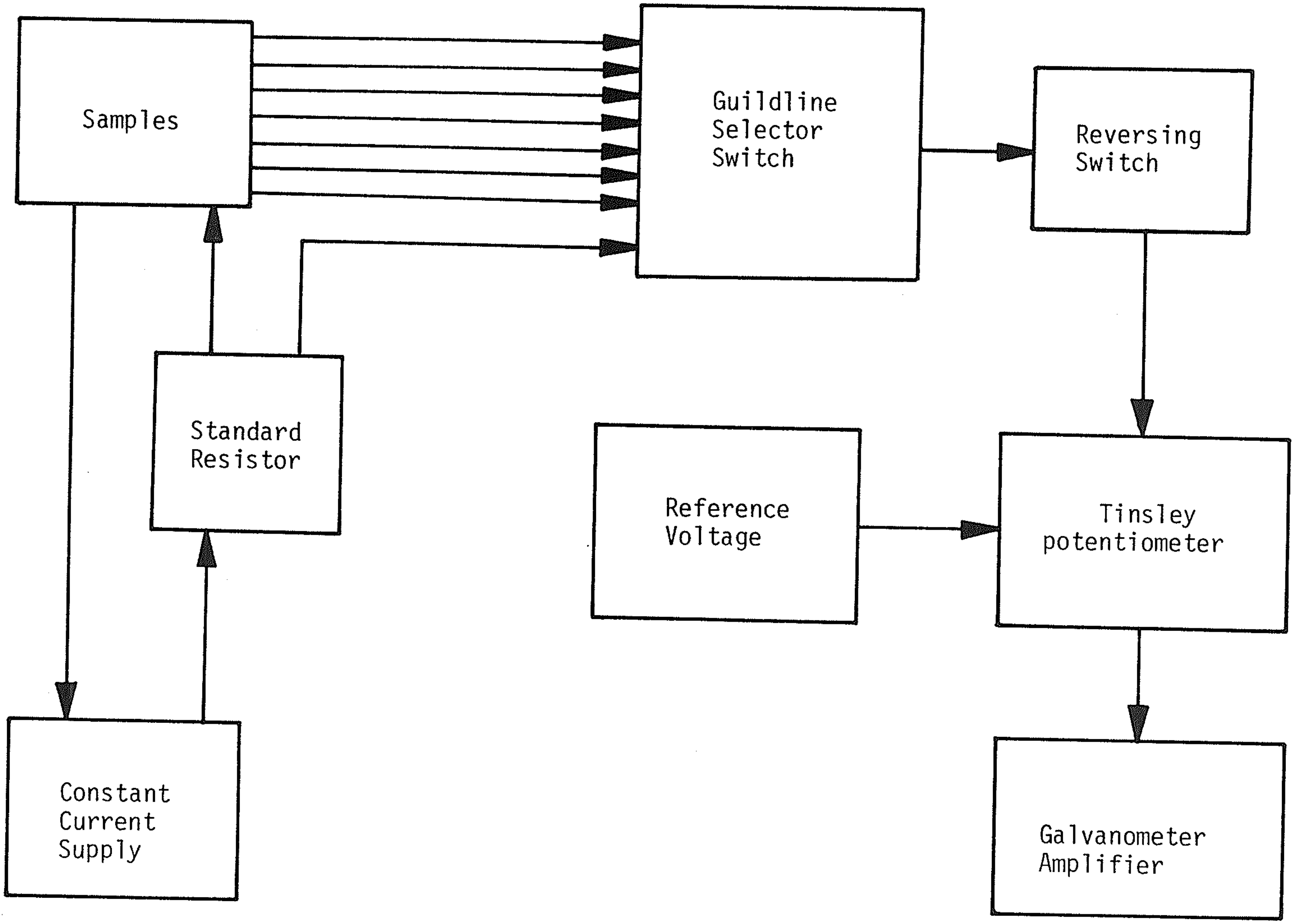

FIG.2.1-6 Block Diagram of the Electronics.

2.1.4 A.C. Bridge Circuit

The temperature of the samples was controlled using an A.C. phase-sensitive Wheatstone Bridge (see FIG.2.1-7). The Allen-Bradley resistor, in thermal contact with the mounting block, formed one branch of the sensitive bridge circuit. A resistance box (R_B) in another arm of the bridge, together with the temperature-vs-resistance curve in FIG.2.1-5, was used to "dial" an approximate temperature. The output of the bridge was fed into a phase-sensitive detector which supplied a D.C. feedback current to the heater to achieve temperature regulation to within 0.5%.

The feedback current from the bridge was sufficient to obtain regulated temperatures up to about 25K. Above this point, a Heathkit IP-27 power supply was connected in series with the output of the detector, thus permitting temperatures up to room temperature to be achieved.

2.1.5 The Manostat

FIG.2.1-8 illustrates the construction of the manostat, which was a flexible-membrane aneroid type [2]. It was used to achieve high temperature stability below 4.2K by controlling the vapour pressure above the liquid helium bath. Pressure control was achieved via the motion of a thin (~0.01") latex rubber membrane which responds to the

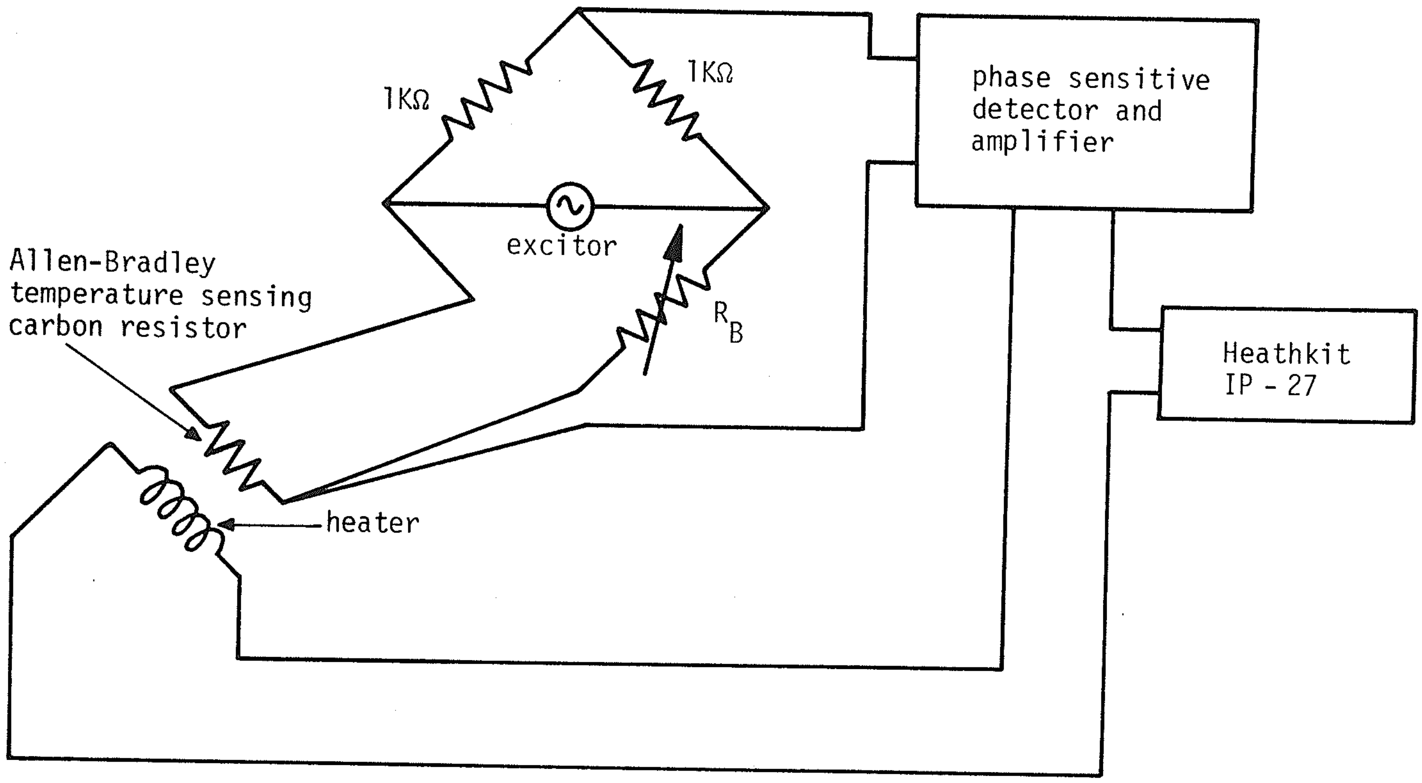

FIG.2.1-7 A.C. Bridge Circuit.

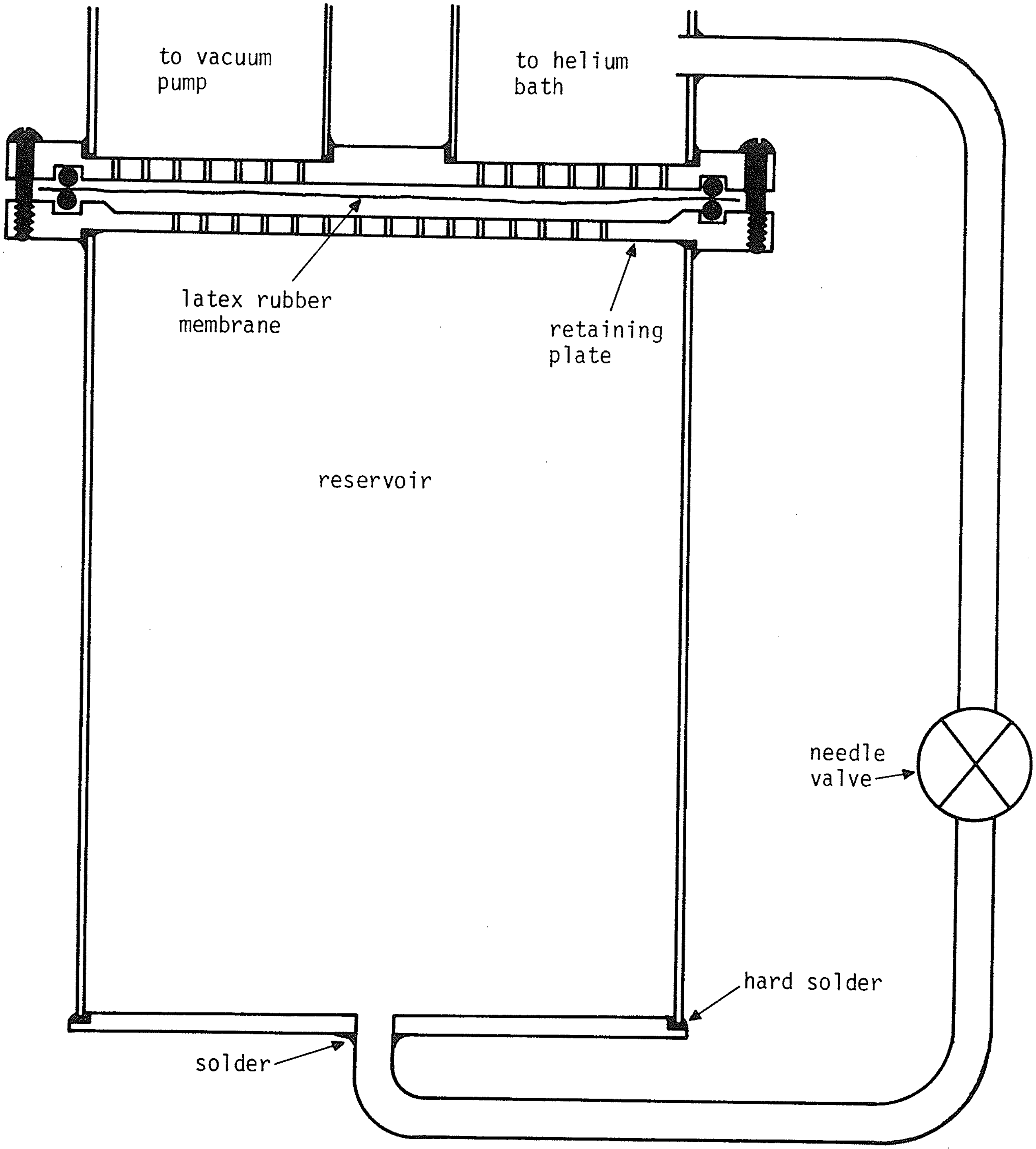

FIG.2.1-8 Manostat Construction (drawn to scale).

differential between the bath pressure and the reference pressure in the reservoir. If the reference pressure exceeds that of the bath, the inlet is sealed and remains so until the differential is reversed, at which time the membrane is forced back, opening the inlet and allowing enough vapour to escape to restore the bath pressure to the reference level.

The reservoir was constructed from a machined brass cylinder which was hard-soldered to a solid disc at one end and to a perforated retaining plate at the other. This plate had 177, $\frac{1}{16}''$ holes drilled through it to permit fast response to small pressure differentials and to protect against membrane rupture in case of large or sudden pressure changes. The inlet and outlet ports were similarly perforated to protect the membrane.

2.1.6 The Manometer System

The temperature of the samples below 4.2K was monitored with a system of manometers connected to the helium bath as shown in FIG.2.1-9. The system was composed of two manometers, one with mercury for use over the pressure range ~3 cm. to 85 cm. Hg and one with oil for use below this range, and measured temperatures to better than 5 millidegrees. Apiezon B low vapour pressure oil was used and a comparison of oil and mercury pressures in the range 1 cm. to 3 cm. Hg showed that the oil had a density of 0.06350 times that of mercury.

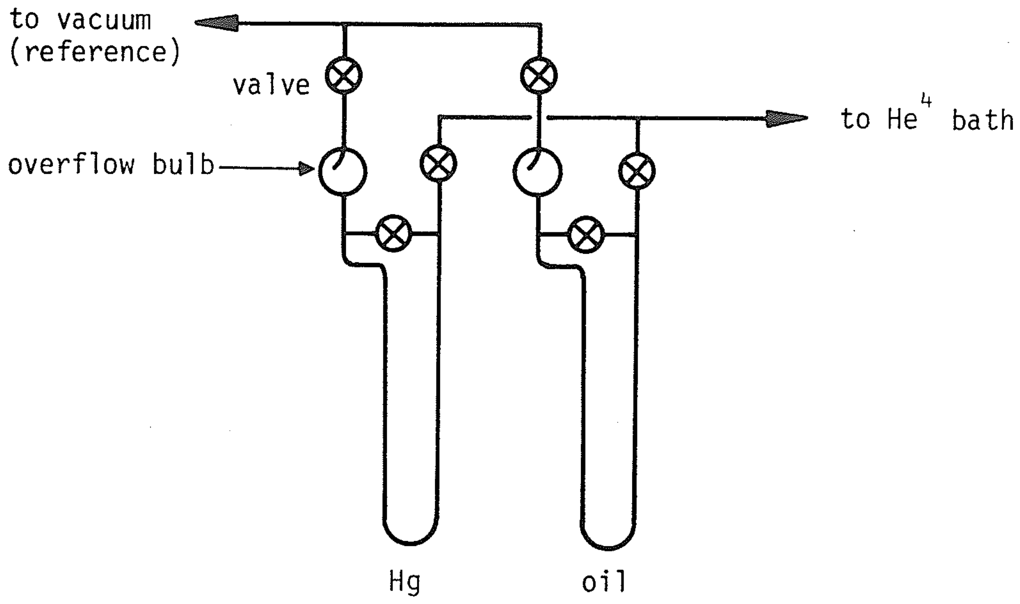

FIG.2.1-9 Manometer Arrangement.

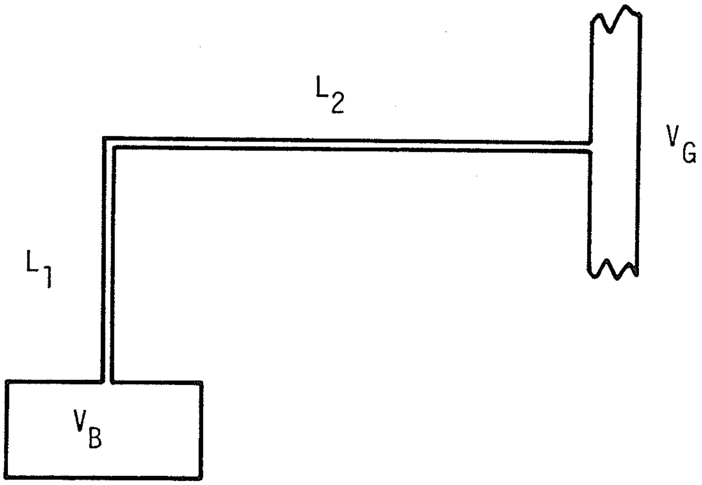

FIG.2.1-10 Schematic of Gas Thermometer.

The measured pressures were converted into temperatures using helium vapour pressure tables (Ref. 2, page 367).

2.1.7 The Gas Thermometer

Temperatures above 4.2K were measured with a non-linear gas thermometer. This device is composed of a machined brass gas bulb, in thermal contact with the sample mounting block, connected to a series 1500 Wallace and Tiernan (W & T) pressure gauge via 0.032 " O.D. stainless steel tubing. The tubing, of wall thickness 0.004 ", runs unbroken from the gas bulb to the W & T gauge. However, for the sake of discussion, it is convenient to divide the tubing into two portions as shown in FIG.2.1-10. L_1 (= 28.7 ") is the length of the tubing inside the cryostat, while L_2 (= 109 ") is the portion outside the cryostat which remains essentially at room temperature.

The nonlinearity of the gas thermometer was due mainly to the dead space volume consisting of the length L_2 of stainless steel tubing, gauge fittings, and the pressure-dependent internal volume of the gauge. Other contributions to nonlinearity were the thermal gradient along L_1 between the samples and room temperature, thermal contraction of the gas bulb, and the non-ideality of the He^4 gas due mainly to Van der Waals-type interatomic interactions.

The room temperature gas bulb volume, calculated from measurements of its dimensions, is 1.497 in^3. Its volume at 77K, computed using a table of thermal contractions (Ref. 2, page 377), is 1.481 in^3 and at helium temperature (4.2K) is 1.480 in^3, illustrating that the thermal variance of the volume is essentially "frozen out" below 77K. The calculated volume of the cryostat tube L_1 is $V_{L1} = 0.0130$ in^3 at room temperature, dropping by only 1 % at 77K.

The internal dead space of the W & T gauge was assumed to vary linearly with pressure, thus giving for the total dead space volume of the gas thermometer,

$$V(P) = V_0 + \alpha P \quad , \tag{2.1-1}$$

where V_0 is the pressure-independent portion of the volume, which includes V_{L2}, and α is the gauge constant (actually $V_0 = V_0(T)$, but room temperature variations were small and changes in V_0 entirely negligible). The constants V_0 and α were computed by solving the ideal gas law

$$\sum_i \frac{P_i V_i}{T_i} = \text{constant} \quad , \tag{2.1-2}$$

or $$\frac{P V_B}{T} + \frac{P V_{L1}}{T} + \frac{P V_{L2}}{T_R} + \frac{P(V_0 + \alpha P)}{T_R} = \text{constant} \quad , \tag{2.1-3}$$

at the two fixed temperatures T_R (room temperature) and T_N (77K) for several sets of values of P_R (the pressure at room temperature) and P_N

(the pressure at 77K). Averaged values from the above analysis gave $V_0 = 1.18$ in^3 and $\alpha = 0.00115$ in^3 per inch H_2O pressure.

The pressures measured on the W & T gauge were converted into the corresponding temperatures as follows. First the non-ideality of the He^4 gas was taken into account by replacing the ideal gas law, $PV = RT$, by a virial expansion of the form [3] :

$$\begin{aligned} PV &= A + BP \\ &= \frac{A_0 T}{273.15} + BP \\ &= \frac{A_0 T}{273.15}\left(1 + \frac{273.15\,B}{A_0}\,\frac{P}{T}\right) \quad , \qquad (2.1\text{-}4) \end{aligned}$$

where $A_0 = 0.999488$ for helium gas, and the virial coefficient B is a function of temperature. Thus the equation of state becomes :

$$\frac{PV}{T\left(1 + \frac{273.15\,B}{A_0}\,\frac{P}{T}\right)} = \frac{A_0}{273.15} = \text{constant} \quad , \qquad (2.1\text{-}5)$$

and Eq.(2.1-2) is replaced by

$$\sum_i \frac{P_i V_i}{T_i\left(1 + \frac{273.15\,B_i}{A_0}\,\frac{P_i}{T_i}\right)} = \text{constant} \quad . \qquad (2.1\text{-}6)$$

Letting P be the measured pressure when the sample temperature is T, and assuming a linear temperature gradient from T to T_R along the cryostat tubing L_1, then Eq.(2.1-6) becomes

$$\frac{P V_{L1}}{T_R - T} \ln\left(\frac{T_R + C}{T + C}\right) + \frac{P V_B[1 + \beta(T - T_0)]}{T\left(1 + \frac{273.15 B}{A_0} \frac{P}{T}\right)} + \frac{P(V_0 + \alpha P)}{T_R\left(1 + \frac{273.15 B_R}{A_0} \frac{P}{T_R}\right)} = k\ , \qquad (2.1\text{-}7)$$

where $C = \frac{273.15 \bar{B} P}{A_0}$, $\bar{B}$ is the average value of the virial coefficient B along L_1 between T and T_R, and β is the thermal expansion coefficient of the gas thermometer bulb. The constant k was determined by evaluating Eq.(2.1-7) at the filling temperature T_0 (either 4.2K or 273.15K) and the filling pressure P_0.

The temperature T was computed using successive approximations. As a first approximation, Eq.(2.1-7) was replaced by

$$\frac{P V_{L1}}{T_R} + \frac{P V_B}{T_1} + \frac{P(V_0 + \alpha P)}{T_R\left(1 + \frac{273.15 B_R}{A_0} \frac{P}{T_R}\right)} = k \qquad ,$$

giving, as a first estimate for the temperature,

$$\frac{1}{T_1} = \frac{1}{V_B}\left[\frac{k}{P} - \frac{V_{L1}}{T_R} - \frac{V_0 + \alpha P}{T_R\left(1 + \frac{273.15 B_R}{A_0} \frac{P}{T_R}\right)}\right] . \qquad (2.1\text{-}8)$$

Next, correction was made for the neglect of the "*ℓn*" factor in Eq.(2.1-7) using this first estimate for T :

$$\frac{P\,V_{L1}}{T_R - T_1}\,\ell n\left(\frac{T_R + C}{T_1 + C}\right) + \frac{P\,V_B}{T_2} + \frac{P(V_0 + \alpha P)}{T_R\left(1 + \frac{273.15\,B_R}{A_0}\,\frac{P}{T_R}\right)} = k \quad ,$$

and an improved temperature value was obtained :

$$\frac{1}{T_2} = \frac{1}{V_B}\left[\frac{k}{P} - \frac{V_{L1}}{T_R - T_1}\,\ell n\left(\frac{T_R + C}{T_1 + C}\right) - \frac{V_0 + \alpha P}{T_R\left(1 + \frac{273.15\,B_R}{A_0}\,\frac{P}{T_R}\right)}\right] , \qquad (2.1\text{-}9)$$

where $\bar{B} = \bar{B}\left(\frac{T_1 + T_R}{2}\right)$. Finally, the thermal contraction of the gas bulb and the neglect of the virial coefficient B were accounted for using this second estimate for T :

$$\frac{P\,V_{L1}}{T_R - T_2}\,\ell n\left(\frac{T_R + C}{T_2 + C}\right) + \frac{P\,V_B[1 + \beta(T_2 - T_0)]}{T_3\left(1 + \frac{273.15\,B}{A_0}\,\frac{P}{T_2}\right)} + \frac{P(V_0 + \alpha P)}{T_R\left(1 + \frac{273.15\,B_R}{A_0}\,\frac{P}{T_R}\right)} = k \quad ,$$

where $\bar{B} = \bar{B}\left(\frac{T_2 + T_R}{2}\right)$ and $B = B(T_2)$, giving the final value for the temperature :

$$\frac{1}{T_3} = \frac{\left(1 + \frac{273.15\,B}{A_0}\,\frac{P}{T_2}\right)}{V_B[1 + \beta(T_2 - T_0)]}\left[\frac{k}{P} - \frac{V_{L1}}{T_R - T_2}\,\ell n\left(\frac{T_R + C}{T_2 + C}\right) - \frac{V_0 + \alpha P}{T_R\left(1 + \frac{273.15\,B_R}{A_0}\,\frac{P}{T_R}\right)}\right] .$$

(2.1-10)

FIG.2.1-11 illustrates the deviation from linearity of the gas thermometer for the case $T_0 = 4.2K$ and $P_0 = 4.2$.

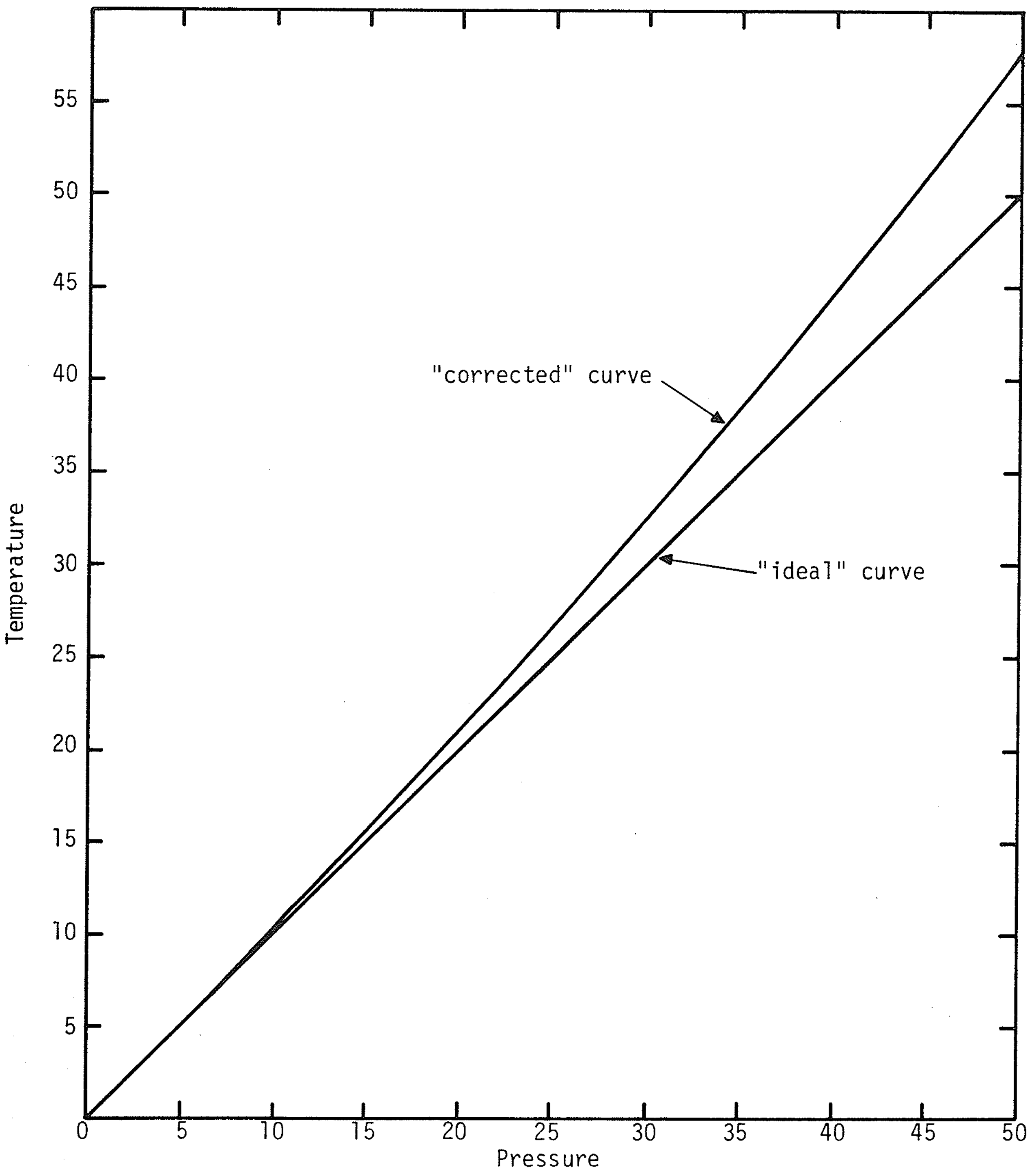

FIG.2.1-11 Illustration of the Non-linearity of the Gas Thermometer for the Case $T_0 = 4.2K$, $P_0 = 4.2$.

2.2 Measurement of A.C. Susceptibility

The A.C. susceptibility of the samples was measured using a phase-locked magnetometer designed by I. Maartense [4]. A block diagram of the electronics is shown in FIG.2.2-1. The system consists of two sensing coils, L_1 and L_2, each of which forms part of a resonant LC circuit. (The resonant circuits are labelled 1 and 2 in FIG.2.2-1). Resonator 1 is allowed to oscillate at its natural frequency, $\omega_1 = \frac{1}{\sqrt{L_1 C}}$, and forms part of an oscillator which is used to drive resonator 2. The signals from the oscillator and from the output of resonator 2 are compared in a phase detector which is sensitive to signal phase, but not amplitude. The phase detector converts the phase difference between the two signals into an equivalent D.C. voltage which is used to control the resonant frequency (ω_2) of resonator 2 by means of a voltage-dependent reactance element. If the LC products of the two resonators are identical (i.e., if $\omega_1 = \omega_2$), then the output signals from the oscillator and resonator 2 will be in phase and the output from the phase detector is zero. If a sample with a permeability is now inserted into the coil of resonator 2, thus changing the effective LC product (and hence the resonant frequency) of the resonator, the two signals will be out of phase and the magnetic susceptibility of the sample is proportional to the corresponding correction voltage required on the control reactance in order to make the effective LC product (and thus the resonant frequency) of resonator 2 equal to that

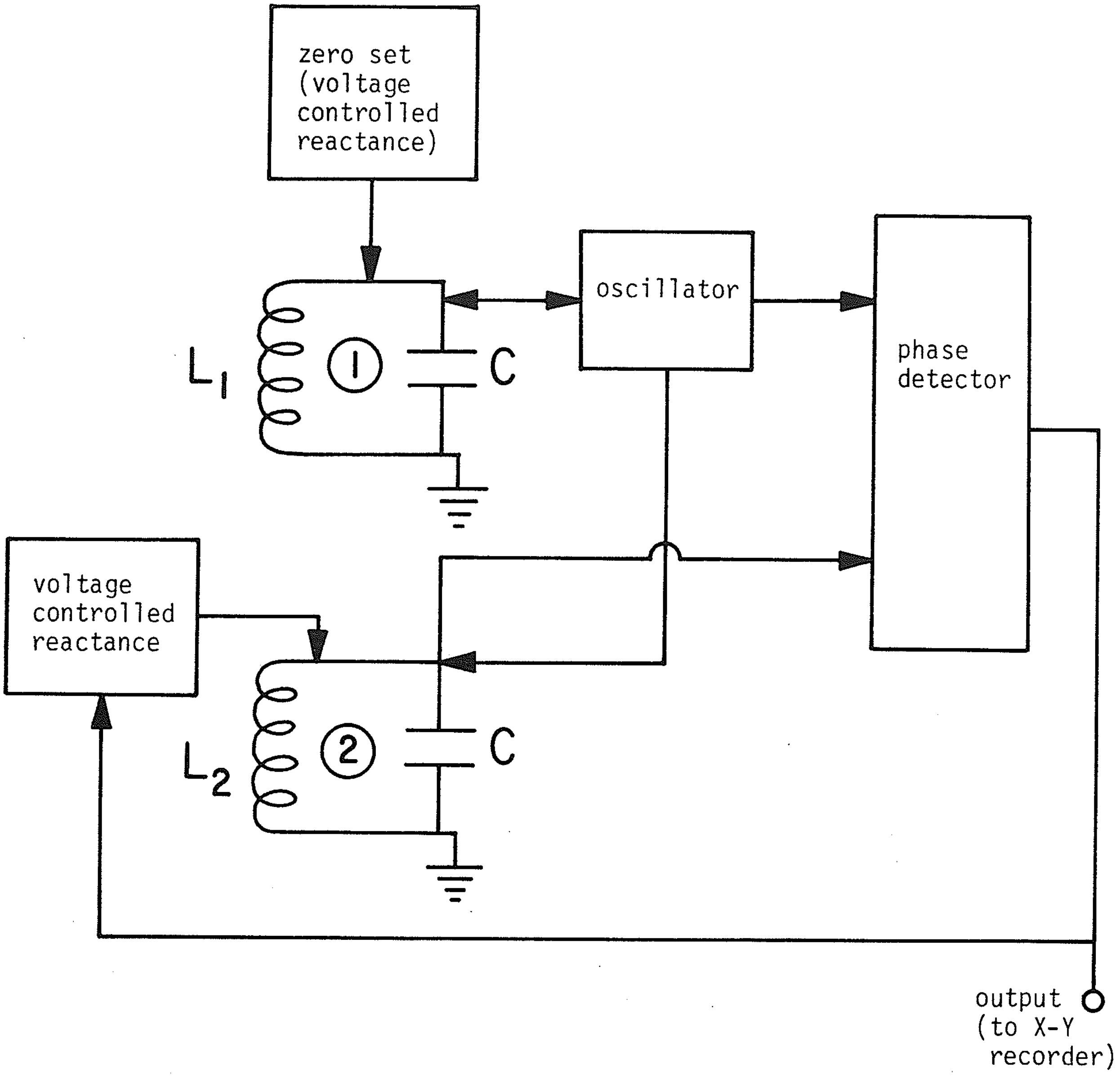

FIG.2.2-1 Block Diagram of Electronics for Measuring A.C. Susceptibility.

of resonator 1. The output of the magnetometer was fed into an X-Y recorder which was used to plot the susceptibility of the sample as a function of thermocouple voltage. The "zero set" in FIG.2.2-1 consists of another voltage-variable reactance which can be used to adjust the resonant frequency of resonator 1 (and hence the frequency of the oscillator). This may be necessary if the natural frequencies of the two LC circuits (without a sample in L_2) are initially so mismatched that the phase detector is incapable of supplying the correction voltage required to make ω_2 equal to ω_1.

FIG.2.2-2 shows the arrangement of the sensing coils, the external field coil and the sample probe in the cryostat. The sensing coils each consisted of 4000 turns of 35 gauge enamelled copper wire wound on a nylon coil former (of approximately the dimensions shown in FIG.2.2-2) and had measured inductances of 205 mh and 202 mh. The external field coil in FIG.2.2-2 was used to apply static magnetic fields to the sample and consisted of 3500 turns of 22 gauge enamelled copper wire wound on a brass former. The magnetic field along the axis of the field coil was calculated to be 250 Oe. per ampere of current in the windings. Both the sensing coils and the field coil were immersed in a liquid nitrogen bath in order to (a) eliminate any instability of the sensing coils due to temperature drift and (b) provide a heat sink for the joule heating from the field coil.

The sample was suspended inside a bundle of fine copper wires which was anchored to the bottom of a machined copper block with soft

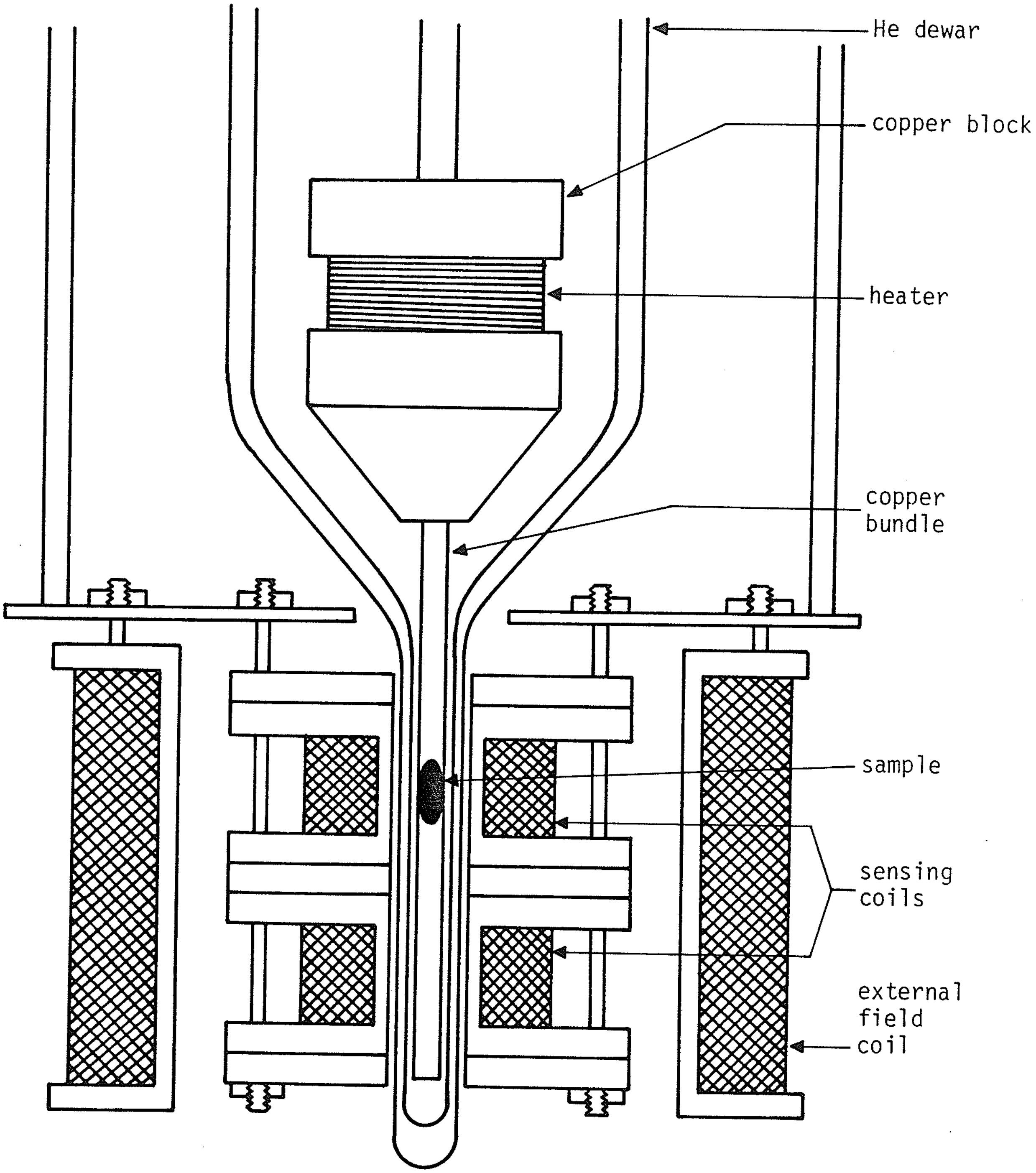

FIG.2.2-2 Arrangement of the Sensing Coils, External Field Coil, and the Sample Probe in the A.C. Susceptibility Cryostat.

solder to ensure good thermal contact. A heater coil of nichrome wire (13.2 Ω/ft and .010" in diameter), wound around the copper block was used to vary the temperature of the sample. The resistance of the heater coil was 50 Ω at room temperature. The temperature of the sample was measured with a Au-.03 at.% Fe-vs-chromel P thermocouple which was embedded in the copper bundle close to the sample. The background signal (primarily due to the copper bundle) was monitored by extracting the sample from the sensing coil at regular intervals.

2.3 Sample Preparation and X-ray Diffraction Measurements

The PdCr and PtCr alloys used in the present investigation were prepared from 99.999 % pure Pd wire, 99.9995 % pure Pt wire, and 99.999 % pure Cr beads, all supplied by Johnson Matthey and Co.(London). The alloys were prepared in the form of 5 gm. buttons by melting together appropriate amounts of the pure metals on the water-cooled copper hearth of an argon arc furnace using a tungsten electrode. Each alloy was inverted and remelted several times to ensure homogeneity. Melting losses were negligibly small. The buttons were cold-rolled into sheets with thicknesses varying from 0.005 cm. (for the very dilute alloys) to 0.025 cm. (for the more concentrated alloys), and resistivity samples in the form of long, thin strips approximately 0.2 cm. wide and 10 cm. long were cut from these sheets. (For the A.C. susceptibility measurements, these strips were folded into a multiple-hairpin shape with contacting surfaces electrically insulated from each other). The specimens were etched to remove surface contamination, washed and then annealed for 24 hours at 650 °C in a vacuum of 10^{-6} Torr (with the exception of a set of five PtCr alloys which required a special heat treatment).

The form factors (cross-sectional area to length ratios) of the samples were determined to within ± 0.5 % using a method described by Loram, Whall and Ford [5]. The knife-edge sample supports (voltage contacts) leave impressions on the samples and the distance (ℓ)

between these marks was measured accurately with a travelling microscope. The density (D) of the samples was computed using the following expression :

$$D = \frac{4}{N a^3} (A_1 x_1 + A_2 x_2) \quad , \qquad (2.3\text{-}1)$$

where N is Avogadro's number, A_1 and A_2 are the atomic weights of the elements used, x_1 and x_2 are the corresponding fractional atomic compositions, and "a" is the concentration-dependent lattice constant of the alloy. The factor 4 indicates that there are four atoms per unit cell in an FCC lattice. Values for the lattice parameters were obtained from lattice spacing data tabulated in W.B.Pearson's "Handbook of Lattice Spacings and Structures of Metals and Alloys" [6].

From the density and an accurate measurement of the mass (M), the volume of the sample ($V = M/D$) was determined. The travelling microscope was used to find the total length (L) of the specimen which, together with the volume, yielded the average cross-sectional area ($A = V/L$). The ratio of the cross-sectional area to the inter-knife-edge distance (ℓ) yielded the required form factor for the specimen ($F = A/\ell$). This method allows the form factor of each specimen to be determined to within ± 0.5 %, even if there is significant irregularity in the cross-sectional area of the specimen. The resistivities (ρ) of the samples were then obtained using the following expression :

$$\rho = R\left(\frac{A}{\ell}\right) \quad , \qquad (2.3\text{-}2)$$

where R is the measured resistance of the sample.

FIG.2.3-1 shows a phase diagram [7] for PtCr, from which it can be seen that the PtCr system undergoes an atomic order-disorder phase transition at around 18 or 19 at. % Cr. In Sec. 3.5, the effect of atomic order on the electrical resistivity and A.C. susceptibility of five PtCr alloys containing 17, 18, 19, 20, and 21 at. % Cr is examined. For each concentration, two resistivity samples were prepared, as described above, and these were subjected to different heat treatments : one of the samples was annealed, in the usual way, at 650 °C for 24 hours in a vacuum of 10^{-6} Torr and then slowly cooled, while the other sample was sealed in a vycor tube under a fraction of an atmosphere (~120 mm. Hg) of Argon gas, annealed at 1170 °C for a period of ~30 minutes, and then quenched rapidly in water. According to the phase diagram in FIG.2.3-1, the "annealing" and "quenching" procedures produce samples which are atomically ordered and disordered, respectively.

The thermal treatments were checked with X-ray diffraction measurements. The measurements were performed on a rotating crystal camera using Cu radiation and a Ni filter. (This camera is useful for polycrystalline samples, and yields diffraction patterns similar to those of powders.) Each sample was mounted on the goniometer head so that one of its long edges was coincident with the rotation axis of the camera and was thus in the path of the incident X-ray beam. The motion of the specimen consisted of an oscillation about this axis

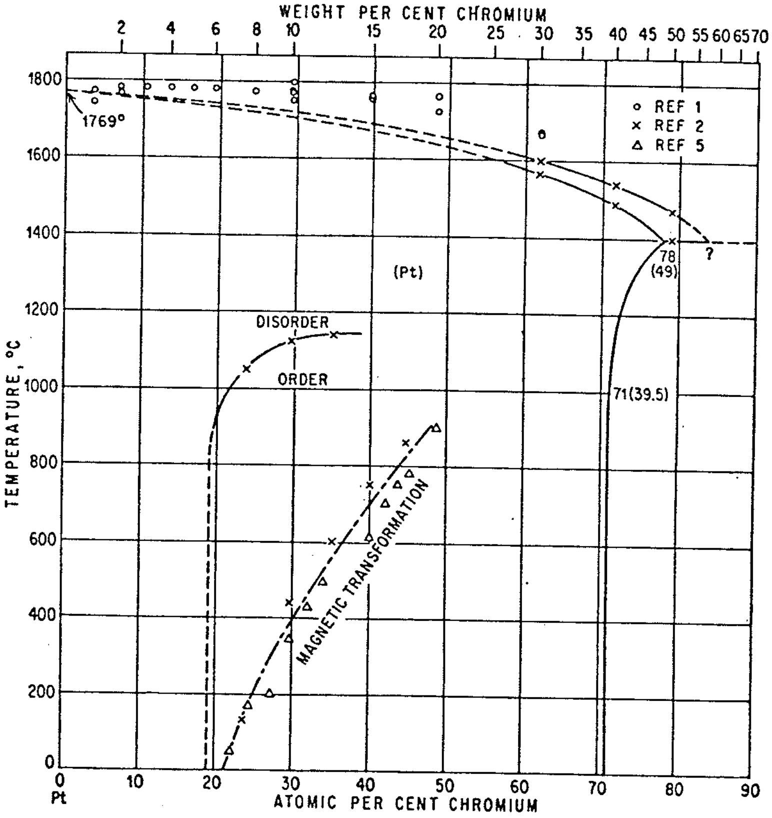

FIG.2.3-1. Phase diagram for the PtCr system showing the presence of an atomic order-disorder transformation at around 18.5 at.% Cr [7].

with an amplitude of 16°. Exposure times were about 8 hours.

FIGS.2.3-2 and 2.3-3 show the results of such X-ray measurements for both the annealed and quenched Pt-21 at. % Cr samples. The quenched sample shows the diffraction pattern characteristic of an FCC lattice, with *no* evidence of superlattice lines, indicating an *atomically disordered* structure. (This result was also obtained for the quenched 17, 18, 19, and 20 at. % Cr samples.) However, superlattice lines are clearly visible in the diffraction pattern of the annealed sample, suggesting an *atomically ordered* arrangement of Cr impurities. These superlattice lines are also present in the diffraction patterns of the annealed Pt-19 and 20 at. % Cr samples and their intensity becomes progressively weaker with decreasing Cr concentration. No superlattice lines were observed in the diffraction patterns of the annealed Pt-17 and 18 at. % Cr samples ; however, the electrical resistivity and A.C. susceptibility data presented in Sec. 3.5 suggests that the annealed 18 at. % Cr sample also possesses some degree of atomic order, although it may be of a short-range nature.

FIG.2.3-2. The diffraction pattern of the DISORDERED (or quenched) Pt-21 at.% Cr sample.

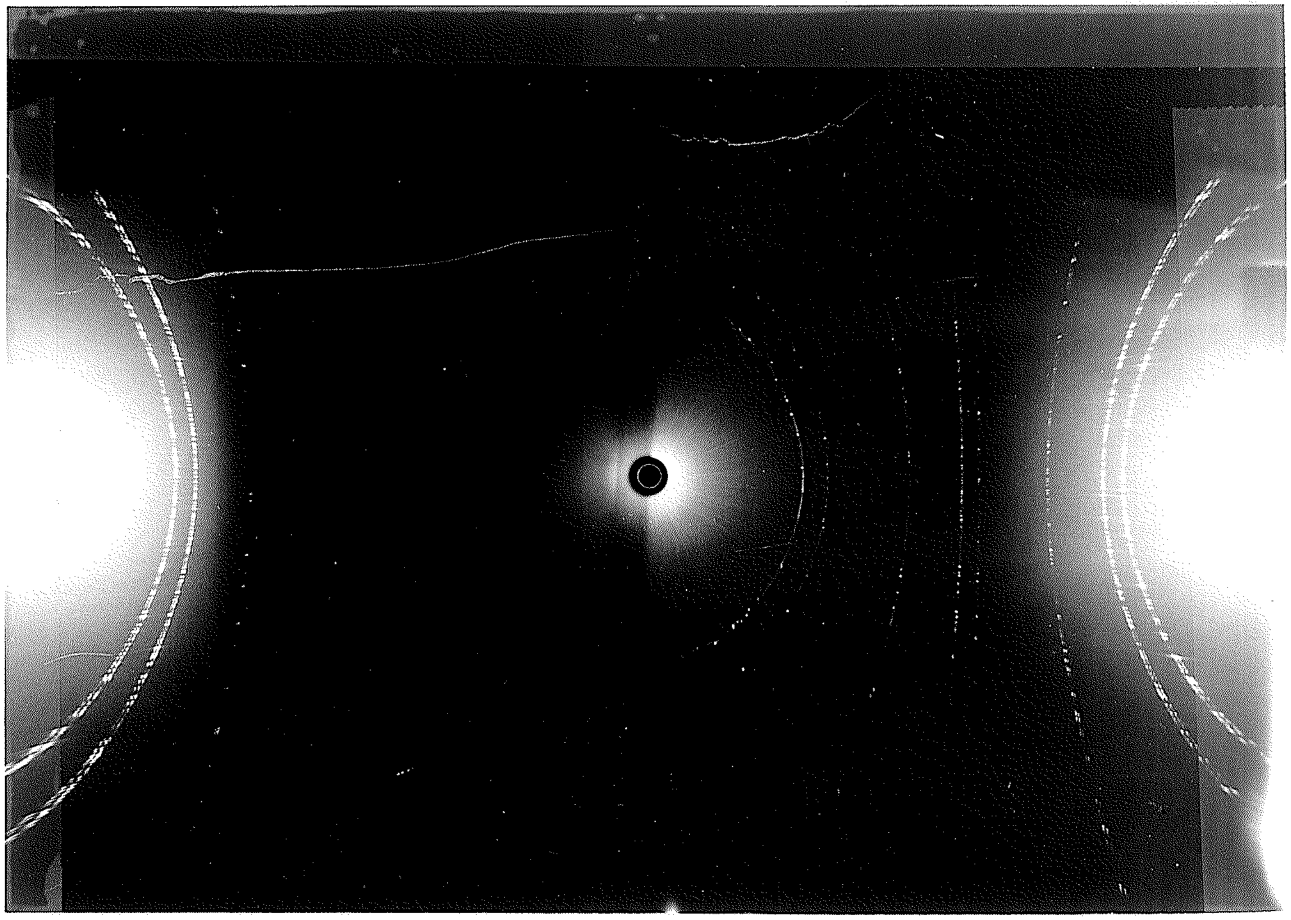

FIG. 2.3 – 2

FIG.2.3-3. The diffraction pattern of the ORDERED (or annealed) Pt-21 at.% Cr sample.

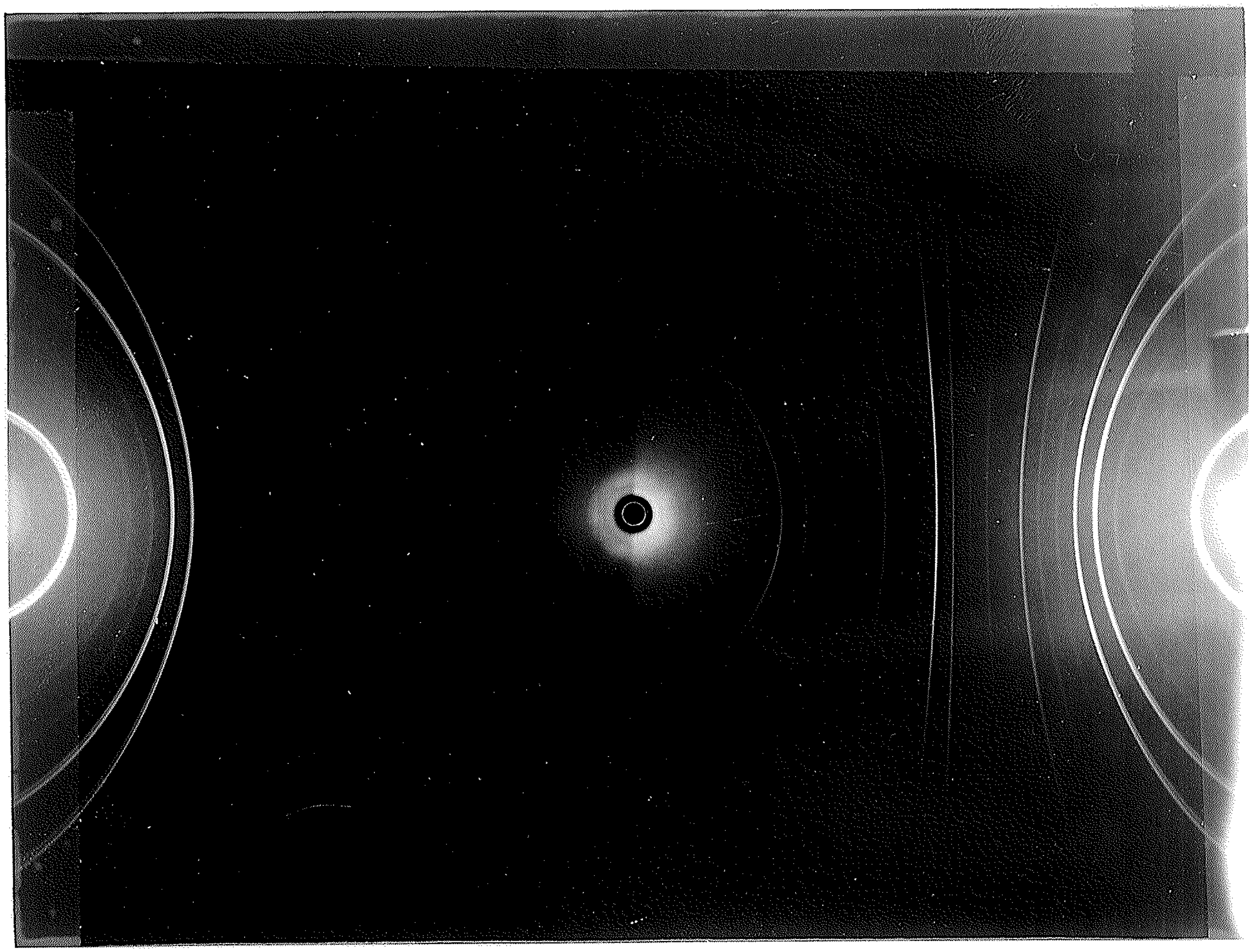

FIG. 2.3-3

References

1. A. D. C. Grassie, G. A. Swallow, Gwyn Williams, and J. W. Loram, Phys. Rev. B3, 4154 (1971).
2. G. K. White, "Experimental Techniques in Low Temperature Physics" (Oxford Press, 2nd edition, 1968), page 244.
3. W. H. Keesom, "Helium" (Elsevier, Amsterdam, 1942), pp. 30-1.
4. I. Maartense, Rev. Sci. Inst. 41, 657 (1970).
5. J. W. Loram, T. E. Whall, and P. J. Ford, Phys. Rev. B2, 857 (1970).
6. W. B. Pearson, "A Handbook of Lattice Spacings and Structures of Metals and Alloys" (Pergamon Press, New York, 1958), pp. 556 and 557.
7. M. Hansen, "Constitution of Binary Alloys" (McGraw-Hill, New York, 1958), page 553.

CHAPTER 3

RESULTS and DISCUSSION

3.1 Introduction

The electric and magnetic properties of dilute alloys consisting of first row transition elements (Ti, V, Cr, Mn, Fe, Co, and Ni) dissolved as substitutional impurities in the noble metal hosts (Cu, Ag, and Au) exhibit a wide variety of anomalous behaviour. In the dilute (or isolated impurity) limit, a substantial portion of the experimental data can be explained in terms of the effect of an exchange interaction, $H_{sd} = -J\vec{S}\cdot\vec{s}$, between the conduction electron spins, $\vec{s}$, and a well-defined localized impurity spin, $\vec{S}$, where J is the exchange coupling constant. When the conduction electron scattering amplitude induced by such an interaction is calculated beyond the first Born approximation [1], using conventional perturbation theory, the following expression for the incremental (or impurity) resistivity, $\Delta\rho(T)$, is obtained :

$$\Delta\rho(T) \propto J^3 \ell n T \quad , \text{ for } T > T_K \quad , \tag{3.1-1}$$

where T_K is the Kondo temperature, i.e., the temperature below which simple perturbation theory is no longer valid. For $J < 0$, this expression reproduces the observed logarithmic increase of $\Delta\rho(T)$ with decreasing temperature. The Kondo temperature T_K is given by

$$k_B T_K = D \exp\left[- \frac{1}{|J|\, N(E_F)} \right] \quad , \tag{3.1-2}$$

where D and $N(E_F)$ are, respectively, the conduction electron bandwidth and the density of states at the Fermi level E_F. Below T_K, the impurity undergoes a gradual transition to a nonmagnetic ground state, with the incremental resistivity at very low temperatures ($T \ll T_K$) having the form

$$\Delta\rho(T \ll T_K) = \Delta\rho(0)\,[\,1 - (T/T_K)^2\,] \quad . \tag{3.1-3}$$

Estimates of the Kondo temperature, T_K, for the 3d-shell transition series as impurities in noble metal hosts reveals a systematic variation of T_K with the position of the impurity in the periodic table [2], as shown in FIG.3.1-1. Above the solid curve, which represents a prediction based on a simple s-d model [2], the impurities are magnetic, while below it they are nonmagnetic.

The interaction H_{sd} also induces a long-range oscillating spin density polarization in the conduction electron gas -- the RKKY spin polarization [3] -- which provides an indirect coupling mechanism between impurities as their concentration (c) is increased above the isolated impurity regime. At high temperatures, when the thermal energy, k_BT, is larger than the interaction energy, the randomly distributed impurity spins behave paramagnetically and contribute a "magnetic" component to the electrical resistivity which increases as $\ell n\, T$ with decreasing temperature. However, as the thermal energy approaches the average RKKY coupling energy, the presence of the

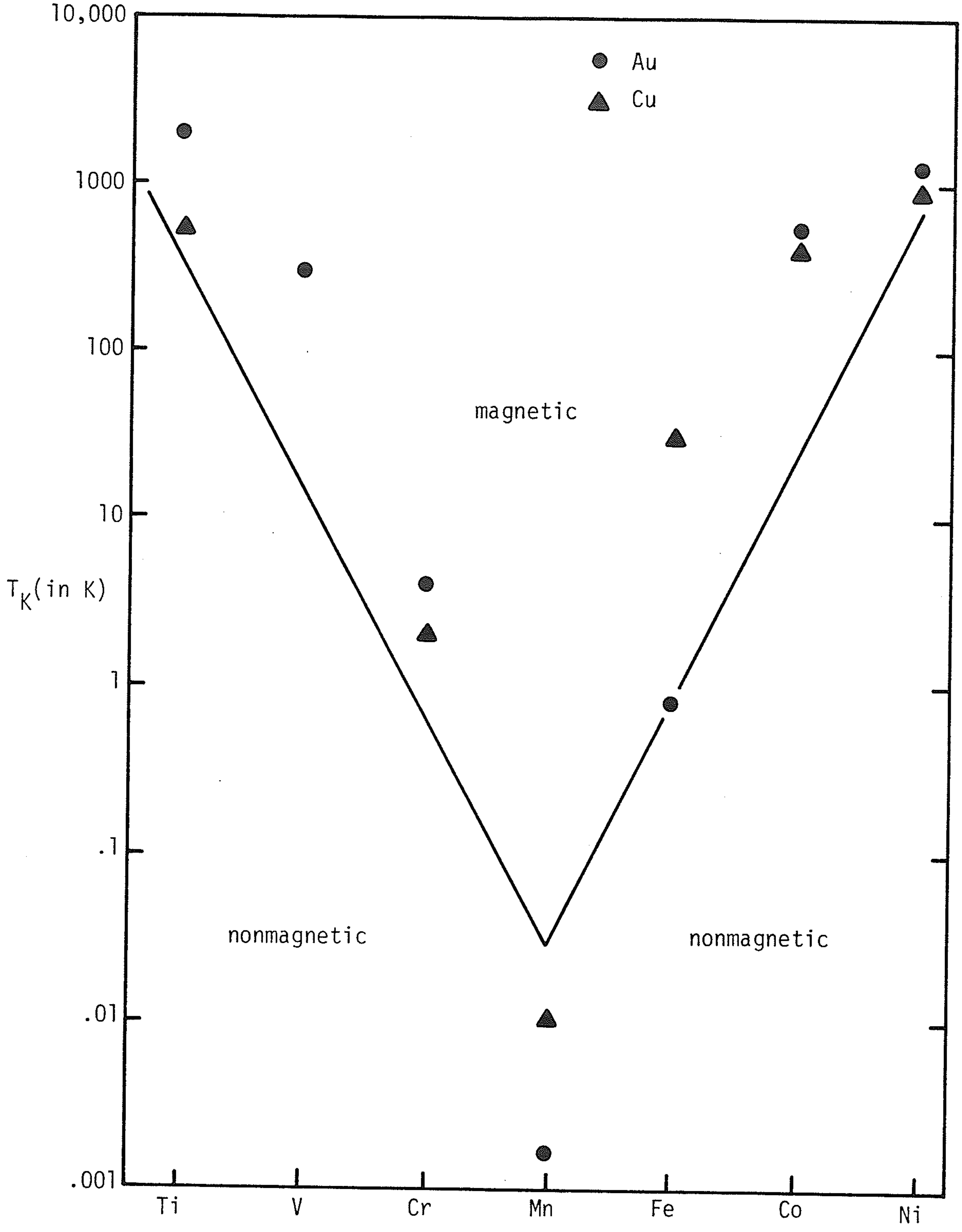

FIG.3.1-1. The variation of the Kondo temperature T_K for the 3d transition metals as impurities in gold and copper hosts.

interactions leads to a reduction in the number of inelastic spin-flip scattering events, and hence a suppression of the logarithmic increase in $\Delta\rho(T)$ with decreasing temperature, eventually resulting in a resistivity maximum at a temperature T_{MAX}, as shown in FIG.3.1-2. Reducing the temperature even further results in a collective freezing of the impurity spins, accompanied by a sharp peak in the A.C. susceptibility at a temperature T_0, as shown in FIG.3.1-2. The nature of the ground state into which these magnetic impurities order as the temperature is reduced in this intermediate concentration regime, is still the subject of considerable speculation. However, the oscillatory sign of the RKKY coupling suggests that the spins become locked into random orientations below the freezing temperature T_0, and the term "spin glass" [4] is currently used to describe such a ground state.

The behaviour of these same first row transition impurities in hosts such as Pd and Pt shows no such uniformity. In these hosts, in the isolated impurity limit, the incremental resistivity is Kondo-like ($\Delta\rho(T)$ increasing with decreasing temperature) only for impurities from the first part of the first transition series (Ti, V, and Cr), with those impurities from the latter part of the series (Mn, Fe, Co, and Ni) inducing a temperature dependence in $\Delta\rho(T)$ of the opposite sign. Loram, White, and Grassie [5] have suggested that a unified description of, at least, the electrical properties of such Pd- and Pt- based alloys can be achieved via the localized spin fluctuation (LSF) model, with the incremental resistivity, $\Delta\rho(T)$, represented by an expression

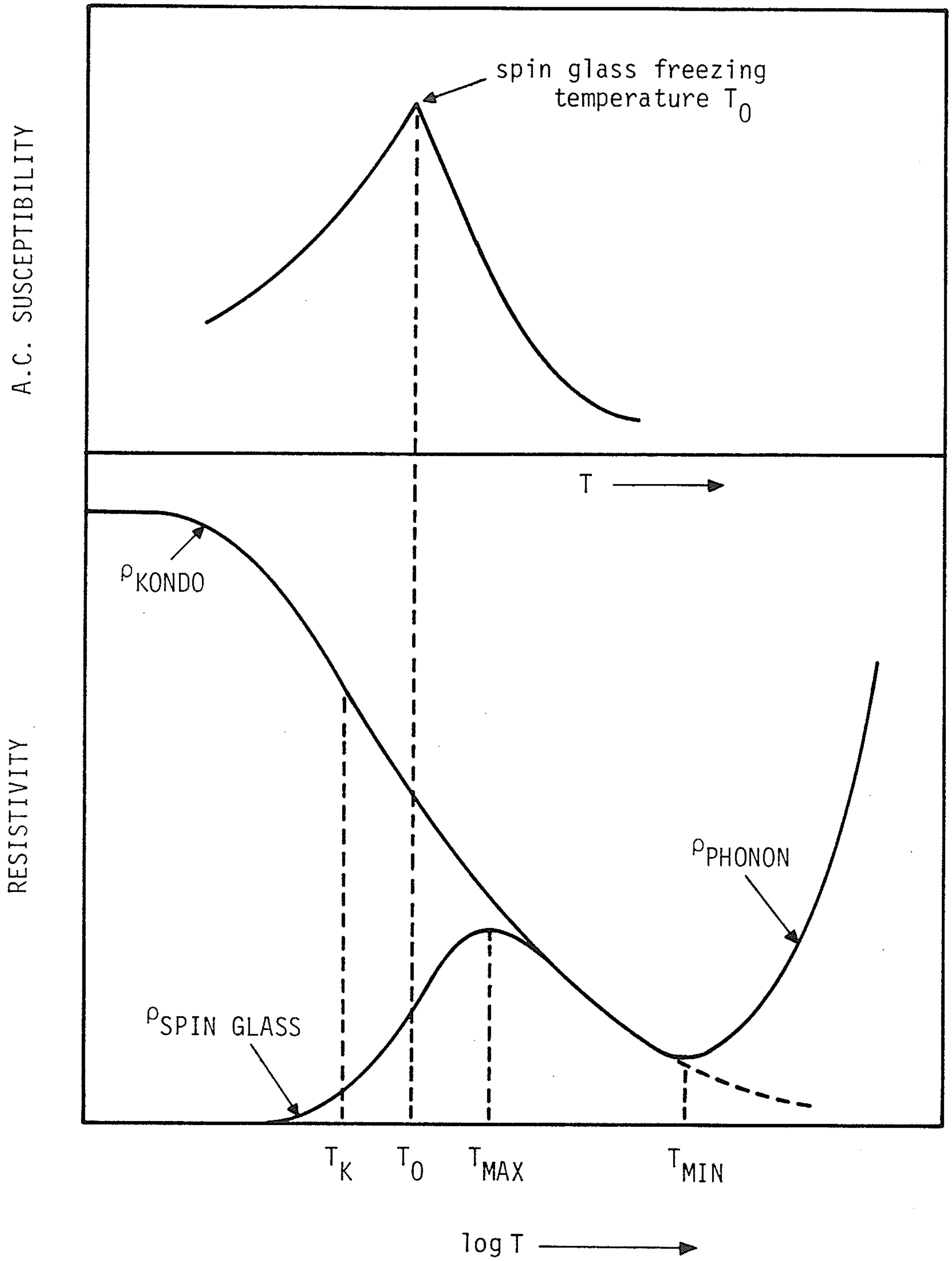

FIG.3.1-2. The behaviour of the A.C. magnetic susceptibility and the electrical resistivity of a typical noble metal host - 3d transition impurity spin glass.

of the form

$$\Delta\rho(T) = Ac + Bc\,\ell n(T^2 + \theta^2)^{\frac{1}{2}} \quad , \qquad (3.1\text{-}4)$$

where θ is to be identified with the LSF temperature (i.e., $\theta = \hbar/k_B\tau_{sf}$). This function was chosen because it closely resembles the universal curves predicted by Kaiser and Doniach [6] and Rivier and Zlatic [7], varying as $\ell n\, T$ at high temperatures ($T \gg \theta$) and as T^2 at low temperatures ($T \ll \theta$) :

$$\Delta\rho(T \ll \theta) = Ac + Bc\,\ell n\theta + \frac{1}{2}Bc\,(T/\theta)^2 \quad . \qquad (3.1\text{-}5)$$

Moreover, when the LSF model is phenomenologically modified to include potential scattering of arbitrary strength [5], it is found that the sign of the coefficient B (and hence of the temperature coefficient $d[\Delta\rho(T)]/dT$) is related to the effective valence difference ΔZ between the host and impurity, and to the impurity spin S, via

$$B \propto \sin^2\left(\frac{\pi S}{2\ell + 1}\right)\cos\left(\frac{\pi\,\Delta Z}{2\ell + 1}\right) \quad , \qquad (3.1\text{-}6)$$

where $2\ell + 1$ accounts for the orbital degeneracy of the impurity state under consideration. B is thus <u>positive</u> for Mn, Fe, Co, and Ni impurities in Pd and Pt ($\ell = 2$, $\Delta Z < 5/2$) and <u>negative</u> for Ti, V, and Cr in Pd and Pt ($\ell = 2$, $\Delta Z > 5/2$).

It is interesting to note that an expression of the form of Eq.(3.1-4) has also been predicted from Kondo theory when interactions between impurities and impurity-spin-lattice-relaxation processes are included [8]. In this case the coefficient B is given by

$$B = \frac{3z}{E_F}\left[\frac{3\pi m^*}{2\hbar e^2 E_F}\left(\frac{V}{N}\right)\right] J^3 S(S+1) \quad , \qquad (3.1\text{-}7)$$

where z is the number of s conduction electrons (with effective mass m^*) per atom, E_F is the Fermi energy, and (N/V) is the number of atoms per unit volume. Thus a change in the sign of the temperature coefficient, $d[\Delta\rho(T)]/dT$, requires a change in the sign of the exchange coupling constant J.

As the transition impurity concentration is increased above the single-impurity limit, interaction effects occur, but once again the situation in Pd- and Pt- based alloys is more complicated than in noble metal hosts. For a system of fluctuating impurity spins, the effect of interactions at low temperatures ($T < \theta$) will be twofold :

(a) When $k_BT \sim$ interaction energy, the interactions tend to slow down or stabilize the spin fluctuations at individual impurity sites, resulting in an increase in the spin fluctuation lifetime, τ_{sf}, and a decrease in the spin fluctuation temperature, T_{sf} or θ $(= \hbar/k_B\tau_{sf})$. According to Eq.(3.1-5), this leads to an increase in the magnitude of the low temperature T^2 coefficient, $Bc/2\theta^2$, over its isolated impurity value, so that the values for both $c^{-1}\Delta\rho(T<\theta)$ and $c^{-1}(d[\Delta\rho(T)]/dT)_{T\to 0}$ in the presence of "stabilizing" interactions are larger than the corresponding "single-impurity" values.

(b) As the concentration increases, the interactions begin to induce correlations between fluctuating spins at different impurity sites, and eventually lead to a cooperative freezing of the impurity moments below a temperature T_0. As in noble-metal-based alloys, this freezing is reflected in a decrease in the low temperature incremental resistivity due to the removal of spin-flip scattering events.

The behaviour of the system for a particular impurity concentration c is determined by the competition between these two interaction effects and can be conveniently summarized by the "phase" diagram in FIG.3.1-3. In this figure, the curve labelled "θ" represents the behaviour of the single-impurity characteristic temperature θ (or T_{sf}), which decreases with increasing concentration due to the stabilization of the spin fluctuations (effect (a) above). The curve labelled "T_0" illustrates the behaviour of the freezing temperature, T_0, for a system of well-defined impurity spins ($\theta\to 0$), and increases with increasing concentration. The concentration at which the two curves cross, i.e., where $\theta = T_0$, is denoted by c^*. In the single-impurity ($c\to 0$) limit, the response of the system is determined solely by the single-impurity characteristic temperature θ, above which the impurity exhibits paramagnetic behaviour, and below

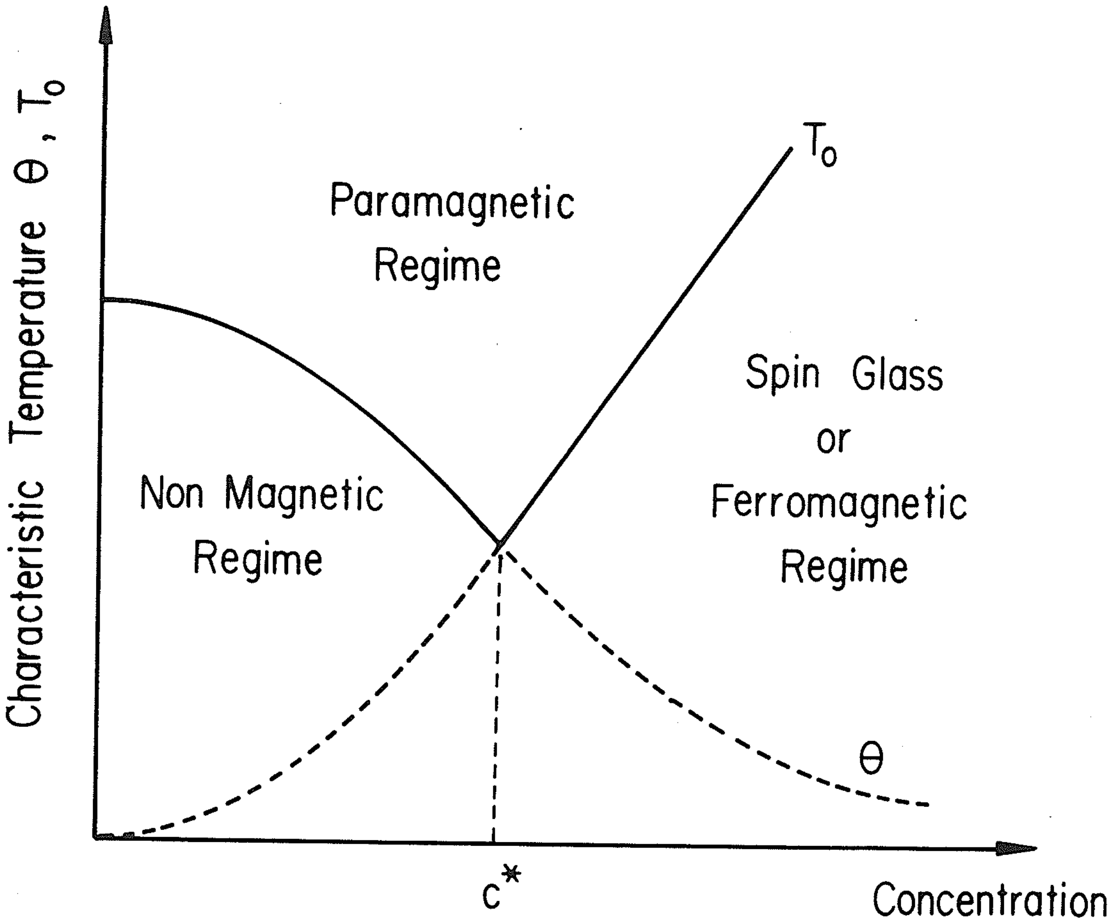

FIG.3.1-3. A "phase" diagram indicating the processes which dominate impurity behaviour in various concentration regimes.

which it becomes progressively less magnetic. For impurity concentrations $c < c^*$, where $\theta > T_0$, the behaviour of the system is dominated by the dynamics of the spin fluctuations, so that the T_0-vs-c curve is shown as a broken line in this region. At higher concentrations, where $c > c^*$ and $T_0 > \theta$, the correlations between impurities, which are responsible for the cooperative freezing of the impurity moments (effect (b) above), are sufficiently strong to overcome the dynamics of the spin fluctuations. For these concentrations, the system behaves paramagnetically at high temperatures ($T \gg T_0$). However, when the temperature is reduced below the T_0-vs-c curve, the system freezes into a spin-glass or ferromagnetic ground state and the corresponding behaviour is dominated by the collective excitations from this ground state. In this region the θ values are of minor importance, so that the θ-vs-c curve is shown as a dashed line.

The consequences of these interaction effects for the electrical resistivity have been outlined previously by Coles et al [9, 10]. Briefly, the behaviour sketched for θ and T_0 as a function of c implies that the difference $|\rho(T_1) - \rho(T_2)|$ with, say, $T_1 = 1.5K$ and $T_2 = 4.2K$, should initially increase as c is increased from the single-impurity limit, peak at concentrations around c^*, where the effects of magnetic ordering begin to play an important role, and then decrease at higher concentrations, where magnetic freezing leads to the removal of spin-flip scattering processes. Such behaviour has already been observed in systems like PdNi and RhFe (see FIG.3.1-4), and the peak in

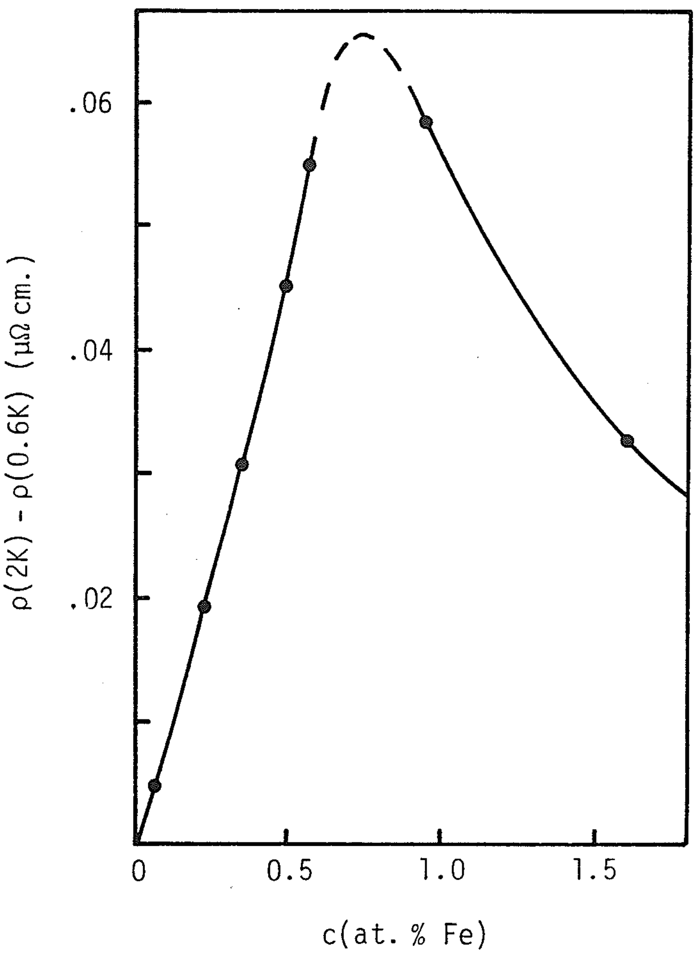

FIG.3.1-4. A plot of ρ(2K) - ρ(0.6K)(in μΩ cm.) for dilute RhFe alloys as a function of the Fe concentration (in at. %). [76]

$|\rho(T_1) - \rho(T_2)|$ indicates a critical concentration for magnetic order.

In the present investigation, the electrical resistivity and A.C. susceptibility of a series of PdCr alloys, containing between .05 and 18 at. % Cr, and PtCr alloys, containing between .05 and 21 at. % Cr, are examined over the temperature range 1.4 to 300K in order to study the way in which interactions between Cr impurities modify the single-impurity behaviour as the Cr concentration is increased from the dilute (or isolated impurity) limit, as well as to determine whether the magnetically ordered ground state resulting from these interactions is similar to that occurring in spin glasses.

3.2 The Behaviour of PtCr and PdCr in the Dilute Limit

In this section, the electrical resistivity of several PdCr and PtCr alloys containing .05, 0.1, 0.2, and 0.3 at. % Cr is examined. For these concentrations, the Cr impurities are expected to be essentially noninteracting, so that the temperature-dependence of the incremental (or impurity) resistivity, $\Delta\rho(T)$, should be characteristic of the scattering processes occurring at a single impurity site.

3.2.1 General Features

In FIGS.3.2-1 and 3.2-2, the measured alloy resistivities, $\rho(T)$, for both the PdCr and PtCr alloys are plotted as a function of temperature from 1.4 to 300K. For all the alloys examined, the resistivity increases monotonically with increasing temperature and exhibits no anomalous features, aside from a slower-than-linear temperature dependence above about 150K. This departure from the linear temperature dependence expected from electron-phonon scattering at high temperatures, indicates the presence of a temperature-dependent contribution to $\rho(T)$ from the Cr impurities. In FIGS.3.2-3 and 3.2-4, the incremental (or impurity) resistivities, $\Delta\rho(T) = \rho_{ALLOY}(T) - \rho_{HOST}(T)$, for all the PdCr and PtCr alloys, are plotted against temperature in order to permit a more detailed examination of the temperature-dependent contribution from electron-impurity scattering. From these

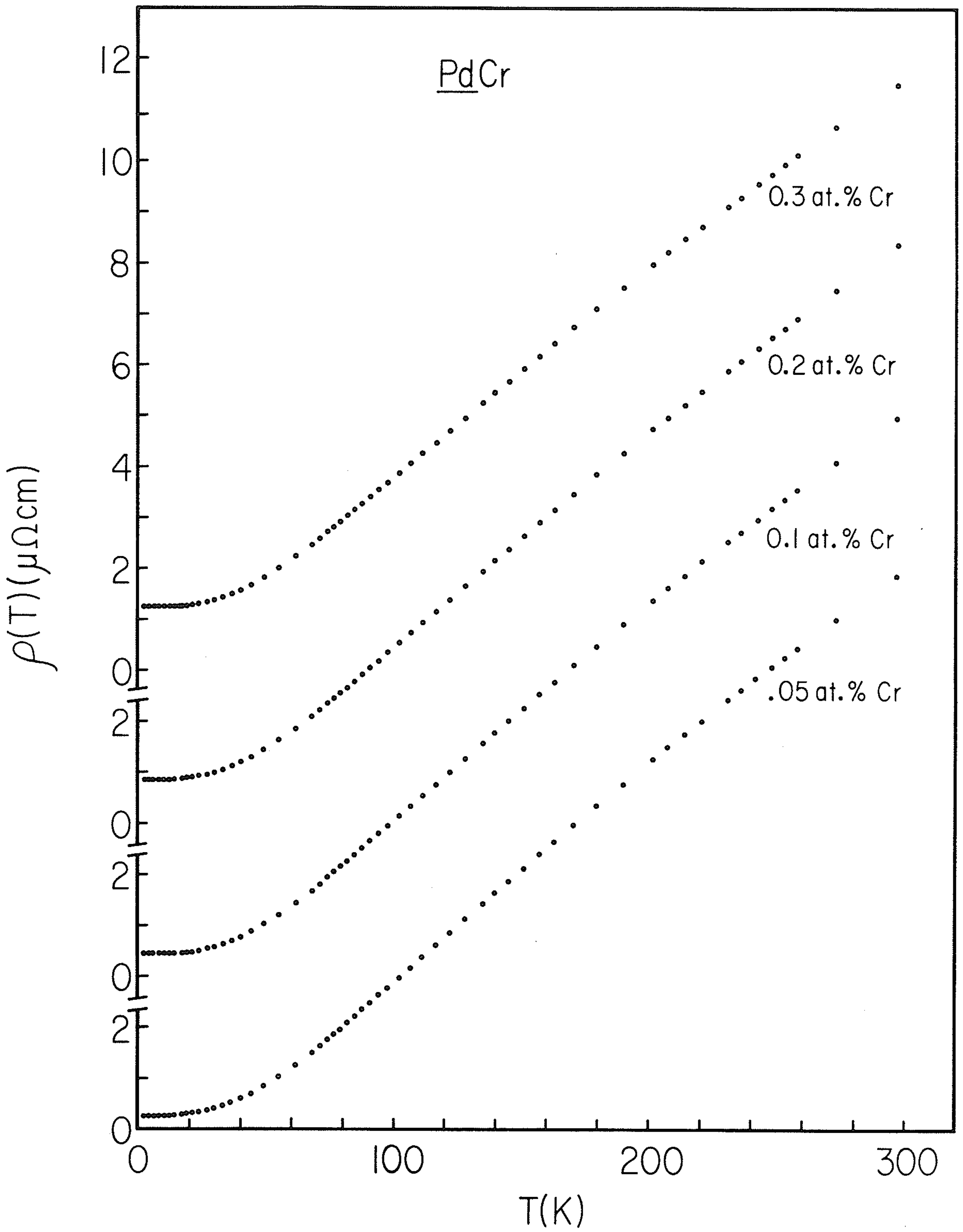

FIG.3.2-1. The measured resistivities ρ(T) (in μΩ cm.) of the Pd-.05, 0.1, 0.2, and 0.3 at.% Cr alloys plotted against temperature T (in K) between 1.4 and 300K.

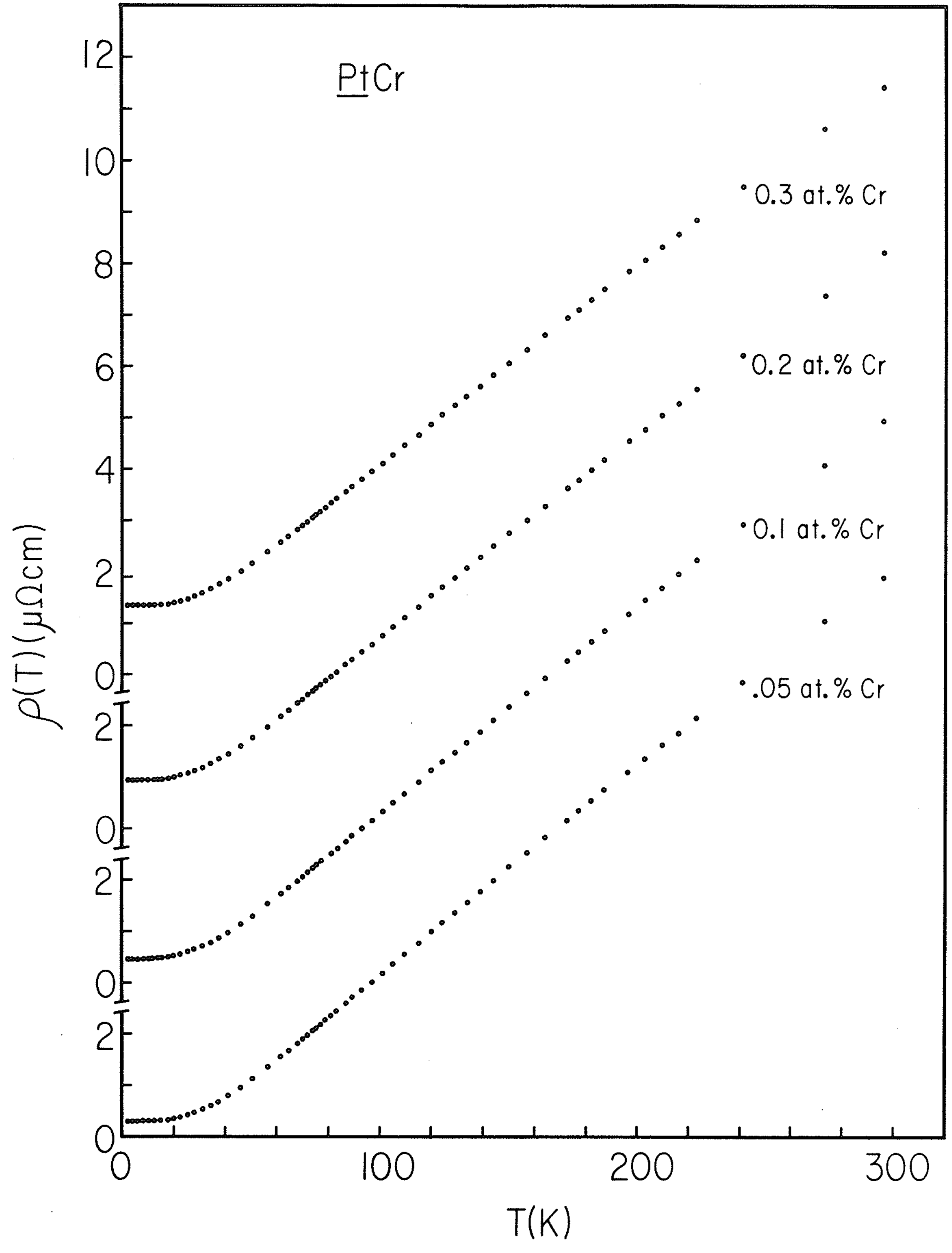

FIG.3.2-2. The measured resistivities ρ(T) (in μΩ cm.) of the Pt-.05, 0.1, 0.2, and 0.3 at. % Cr alloys plotted against temperature T (in K) between 1.4 and 300K.

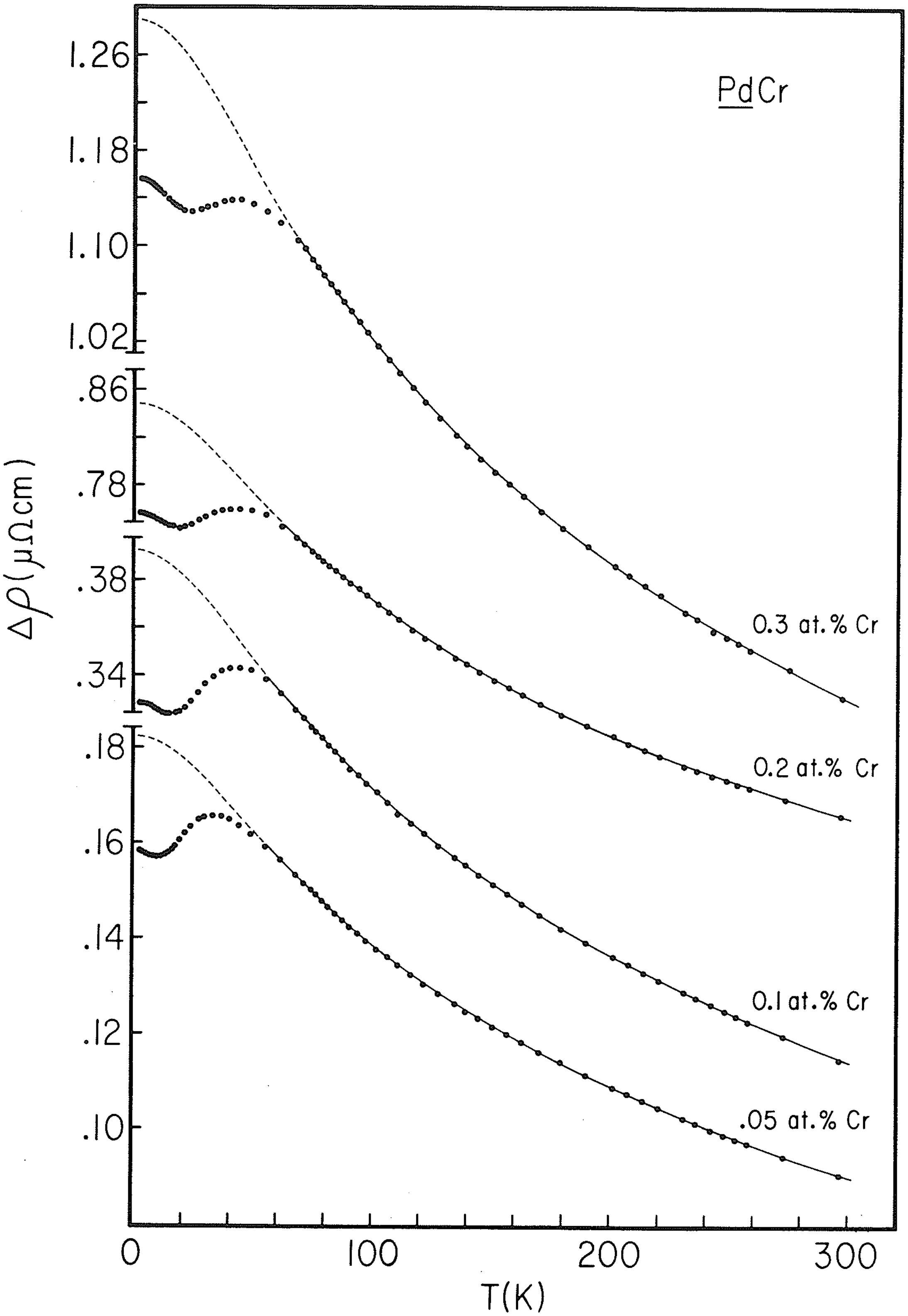

FIG.3.2-3. The incremental resistivities Δρ(T) of the Pd-.05, 0.1, 0.2, and 0.3 at. % Cr alloys plotted against temperature from 1.4 to 300K. The solid curves are fits of the data above 68K to Eq.(3.2-4), while the dashed curves are extensions of these fits to lower temperatures.

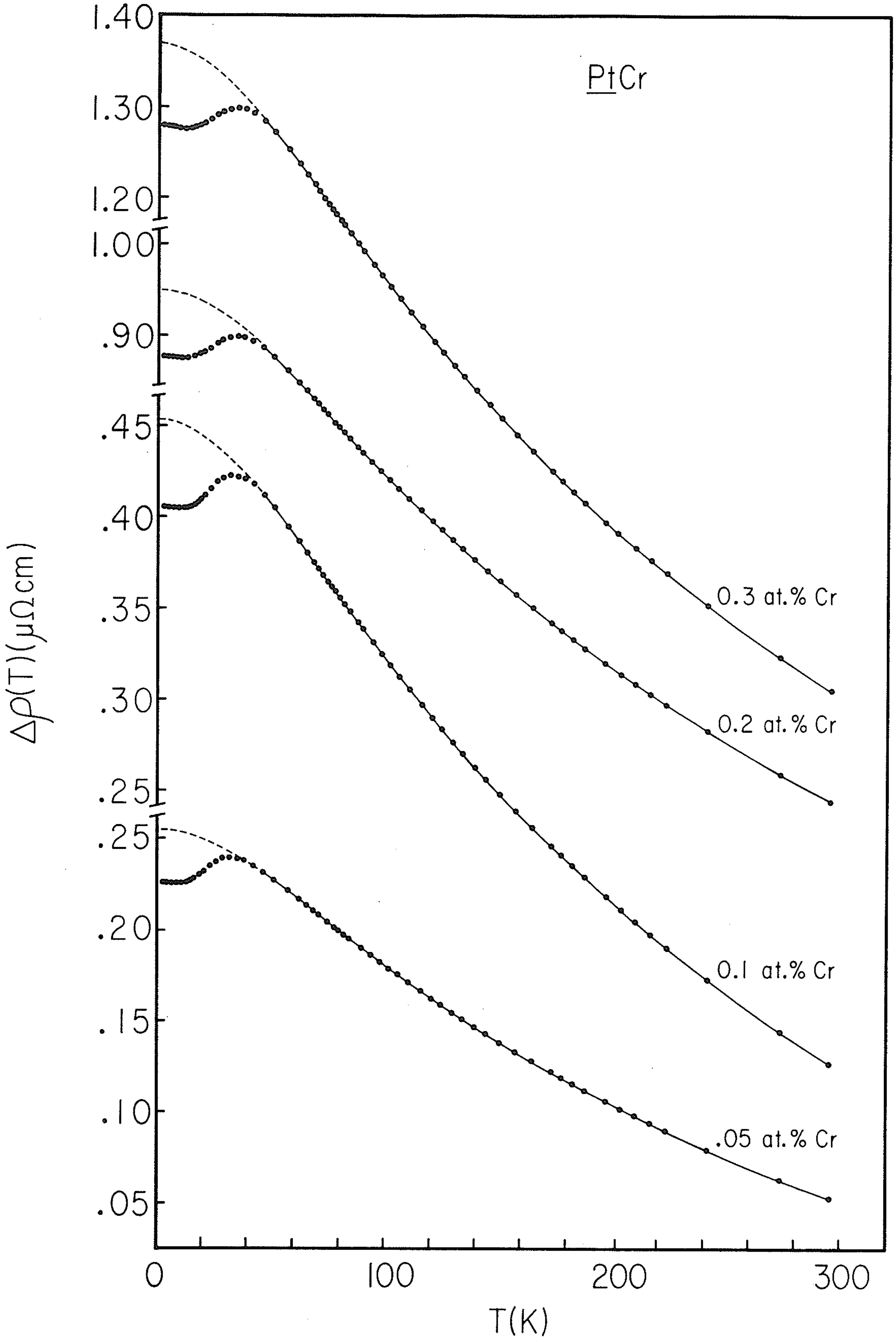

FIG. 3.2-4. The incremental resistivities Δρ(T) of the Pt-.05, 0.1, 0.2, and 0.3 at. % Cr alloys plotted against temperature from 1.4 to 300K. The solid curves are fits of the data above 45K to Eq.(3.2-4), while the dashed curves are extensions of these fits to lower temperatures.

figures, the residual incremental resistivity, $\Delta\rho(T=0)$, can be extracted and these values are plotted in FIG.3.2-5 as a function of the nominal Cr concentration. This figure shows that, for Cr concentrations $c \leq 0.3$ at. %, $\Delta\rho(T=0)$ varies linearly with the nominal Cr concentration in both the PdCr and PtCr systems, with

$$\Delta\rho(T=0) = 3.75 \pm .20 \ \mu\Omega\,\text{cm./at.\% Cr} \quad , \text{ for PdCr,} \qquad (3.2\text{-}1)$$

and $$\Delta\rho(T=0) = 4.26 \pm .15 \ \mu\Omega\,\text{cm./at.\% Cr} \quad , \text{ for PtCr.} \qquad (3.2\text{-}2)$$

These values are in good agreement with those obtained by Star et al [11] for PdCr and PtCr alloys of comparable concentration.

The incremental resistivities in FIGS.3.2-3 and 3.2-4 contain two temperature-dependent contributions. The first contribution decreases monotonically with increasing temperature, resulting in a negative slope, $d[\Delta\rho(T)]/dT < 0$, at low and high temperatures. The second contribution increases with increasing temperature and, in combination with the first, results in a local maximum in $\Delta\rho(T)$ between 30K and 40K. This type of behaviour closely resembles that observed in dilute nonmagnetic alloys [12], where it is attributed to a breakdown in Matthiessen's rule. In its most general form, Matthiessen's rule states that the electrical resistivity of a metal containing impurities is given, at any temperature T, by the expression

$$\rho_{ALLOY}(T) = \rho_{HOST}(T) + \rho_{IMPURITY}(T) \quad , \qquad (3.2\text{-}3)$$

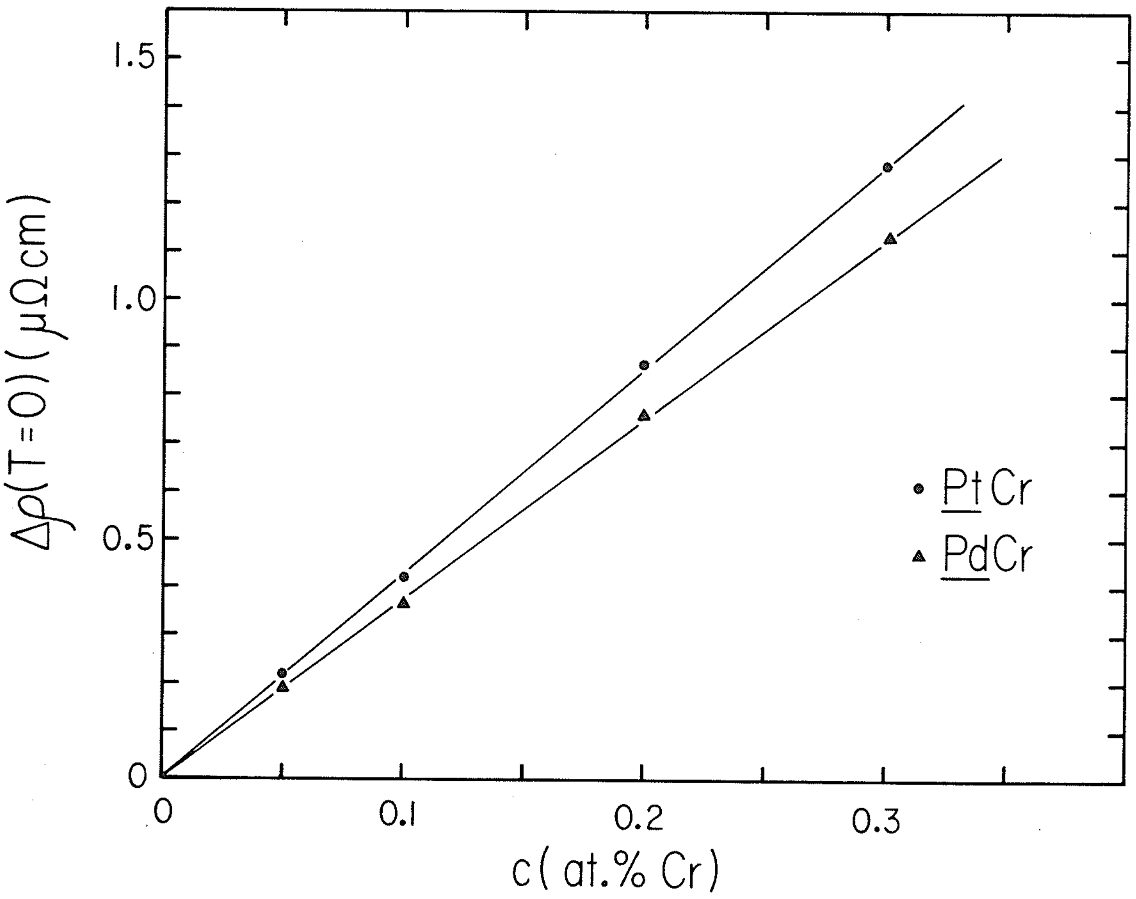

FIG.3.2-5. $\Delta\rho(T = 0)$ (in $\mu\Omega$ cm.) plotted against the nominal Cr concentration c (in at. %) for both the PdCr and PtCr alloys containing between .05 and 0.3 at. % Cr.

where $\rho_{ALLOY}(T)$ is the measured resistivity of the alloy, $\rho_{HOST}(T)$ is the resistivity of the pure host (and is due primarily to electron-phonon scattering), and $\rho_{IMPURITY}(T) = \Delta\rho(T)$ is that due to the impurities (which may or may not be temperature dependent). Basically, Eq.(3.2-3) assumes that the electron-phonon and electron-impurity scattering processes are independent of each other, and that a single (isotropic) relaxation time can characterize each type of scattering. Departures from Matthiessen's rule occur, (a) when the phonon spectrum of the host is modified by the addition of the impurities, (b) when the Fermi surface (or, more generally, the electronic band structure) of the host metal is altered by the presence of the impurities or, (c) when the relaxation times for phonon and impurity scattering have different anisotropies. At the low concentrations examined here, the presence of the impurities is not expected to alter the phonon spectrum or the band structure of the host, so that any deviations from Matthiessen's rule probably arise from the different anisotropies for electron-phonon and electron-impurity scattering. Recent investigations [13, 14] of Matthiessen's rule deviations, defined by $\Delta(T) = \rho_{ALLOY}(T) - \rho_{HOST}(T) - \rho_{IMPURITY}(T)$, in various Pd and Pt based alloys of comparable concentration to those examined here(i.e., $c < 1$ at. %), show that $\Delta(T)$ is negligible at low temperatures and then increases rapidly with increasing temperature, finally levelling off at a temperature-independent plateau, for temperatures $T > 60K$. Clearly, a Matthiessen's rule deviation of this form can account for the local maximum observed in the incremental resistivities in FIGS.3.2-3 and 3.2-4.

3.2.2 High Temperature Fits

Following the discussion in Sec.3.1, an attempt was made to fit the incremental resistivities in FIGS.3.2-3 and 3.2-4 to an expression of the form

$$\Delta\rho(T) = Ac + Bc\,\ell n(T^2 + \theta^2)^{\frac{1}{2}} \quad , \qquad (3.2\text{-}4)$$

using a least-squares fitting procedure. The fitting procedure was based on an evaluation of

$$\frac{1}{N}\left\{\sum_{i=1}^{N}\left[\Delta\rho(T_i)_{MEAS} - \Delta\rho(T_i)_{CALC}\right]^2\right\}^{\frac{1}{2}} \quad , \qquad (3.2\text{-}5)$$

where N is the number of experimental points (labelled i) included in the fit. The best fit was taken as the minimum in Eq.(3.2-5) and denoted rmsd (root-mean-square deviation). For the very dilute alloys examined here, the fit to Eq.(3.2-4) was carried out over a restricted temperature range, $T \geq 68$K for PdCr and $T \geq 45$K for PtCr, where the contribution to $\Delta\rho(T)$ from Matthiessen's rule breakdown was expected to have reached its temperature-independent (high-temperature) plateau.

TABLE 3.2-1. Best-fit parameters for Eq.(3.2-4)

(a) PdCr

ALLOY (at. % Cr)	RANGE OF FIT (K)	RMSD OVER THIS RANGE (10^{-4} μΩ cm./point-at. % Cr)	θ (K)	A (μΩ cm./at. % Cr)	B (μΩ cm./at. % Cr)
.05	68 - 300	6.67	43.5	7.24	- 0.95
0.1	68 - 300	5.35	45.0	8.19	- 1.12
0.2	68 - 300	5.95	43.0	7.61	- 0.89
0.3	68 - 300	6.16	44.0	8.03	- 0.99

(b) PtCr

ALLOY (at. % Cr)	RANGE OF FIT (K)	RMSD OVER THIS RANGE (10^{-3} μΩ cm./point-at. % Cr)	θ (K)	A (μΩ cm./at. % Cr)	B (μΩ cm./at. % Cr)
.05	45 - 300	1.78	73	17.18	- 2.82
0.1	45 - 300	1.43	71.5	14.93	- 2.44
0.2	45 - 300	1.34	74	13.22	- 1.97
0.3	45 - 300	0.90	72.5	11.61	- 1.65

The curves drawn in FIGS.3.2-3 and 3.2-4 are the incremental resistivities computed from Eq.(3.2-4) using the "best-fit" parameters listed in Table 3.2-1. The solid curves in these figures relate to the temperature range actually covered in the fitting scheme (see Table 3.2-1), while the dashed portions of the curves are extensions of the computed fits to lower temperatures, where the situation is complicated by the Matthiessen's rule deviations, previously described. Clearly, an expression of the form of Eq.(3.2-4) provides an excellent description of the experimental data, with the point-by-point deviation of the computed fit from the measured value being, typically, better than 7×10^{-4} $\mu\Omega$ cm./at. % Cr for PdCr and 2×10^{-3} $\mu\Omega$ cm./at. % Cr for PtCr.

An inspection of the "best-fit" parameters in Table 3.2-1 reveals that, over the concentration range investigated here, the best-fit values for the parameters A and B are concentration-independent for PdCr, but decrease (in magnitude) with increasing Cr concentration for PtCr. However, the best-fit values for θ are concentration-independent in both systems, giving a single-impurity ($c \rightarrow 0$) characteristic temperature θ of ~43K for PdCr and ~73K for PtCr.

3.2.3 Low Temperature T^2 Term

At very low temperatures ($T \ll \theta$), Eq.(3.2-4) predicts a T^2 form for the incremental resistivity $\Delta\rho(T)$ (see Eq.(3.1-5)), the coefficient of which is given by

$$T^2\text{-coeff.} = \frac{Bc}{2\theta^2} \quad . \qquad (3.2\text{-}6)$$

In FIGS.3.2-6 and 3.2-7, the measured incremental resistivities, $\Delta\rho(T)$, of all the PdCr and PtCr alloys are plotted against T^2 up to about $T \simeq 6K$. These figures show that, at low temperatures, the incremental resistivities of both the PdCr and PtCr alloys contain a term proportional to T^2. Table 3.2-2 lists the "measured" T^2-coefficients obtained from these plots, as well as the "predicted" T^2-coefficients computed from Eq.(3.2-6), using the "best-fit" values for the parameters B and θ deduced from the "high-temperature" fits (see Table 3.2-1).

An inspection of Table 3.2-2 shows that the measured and predicted T^2-coefficients are in reasonably good agreement for the PtCr alloys, but not for the PdCr alloys. A possible source of this discrepancy lies in the procedure used to extract the measured T^2-coefficients from the experimental data. The resistivity of both pure Pd and pure Pt contains a large, positive T^2 term at low temperatures [15, 16] which arises from conduction electron-paramagnon scattering (i.e., the scattering of s conduction electrons from enhanced spin-density fluctuations in the d band). Thus the resistivities of the PdCr and PtCr alloys examined here contain contributions from two T^2 terms : the first contribution arises from the scattering of conduction

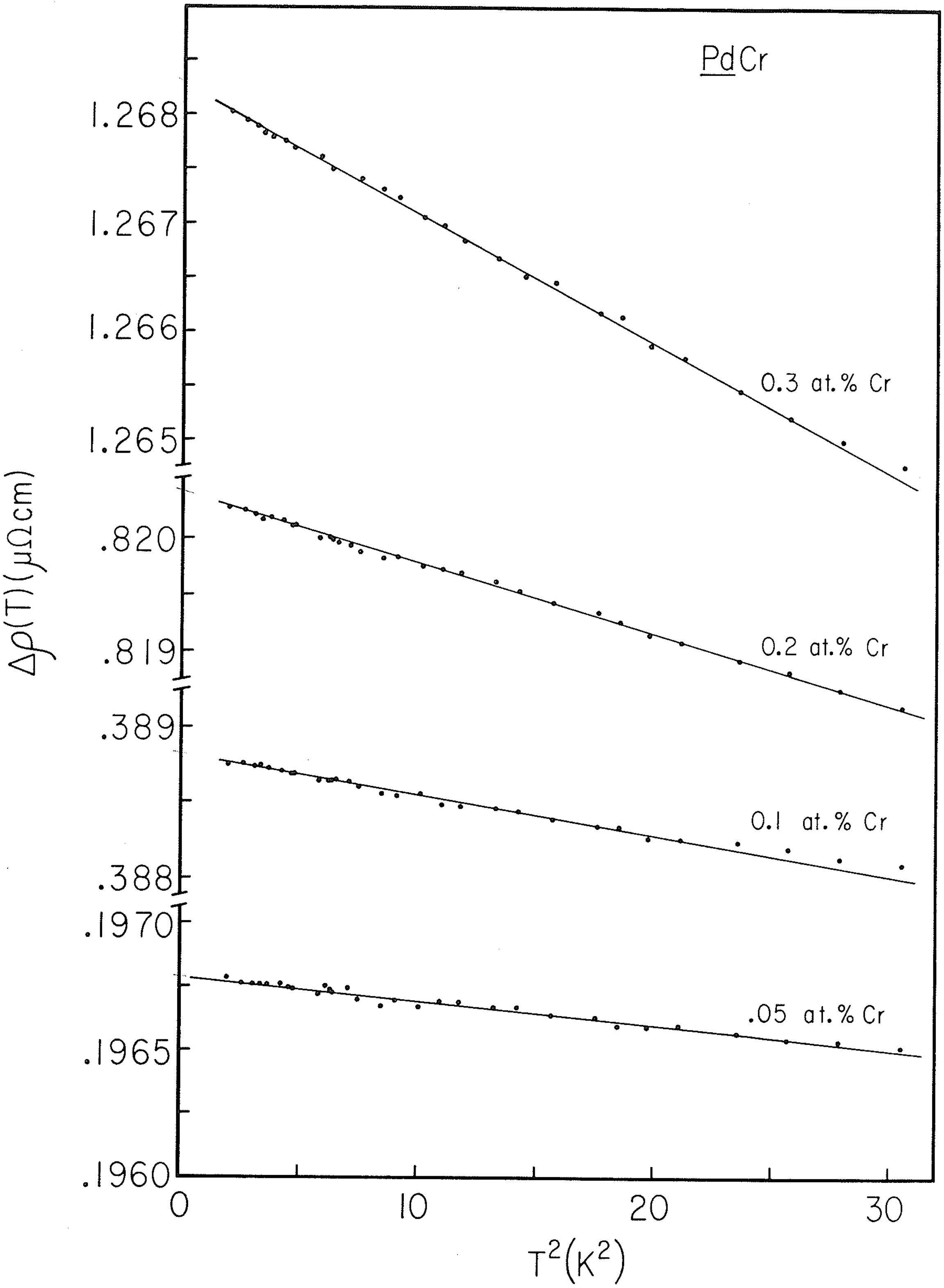

FIG.3.2-6. The incremental resistivities $\Delta\rho(T)$ of the Pd-.05, 0.1, 0.2, and 0.3 at. % Cr alloys plotted against the square of the temperature up to about $T \simeq 6K$.

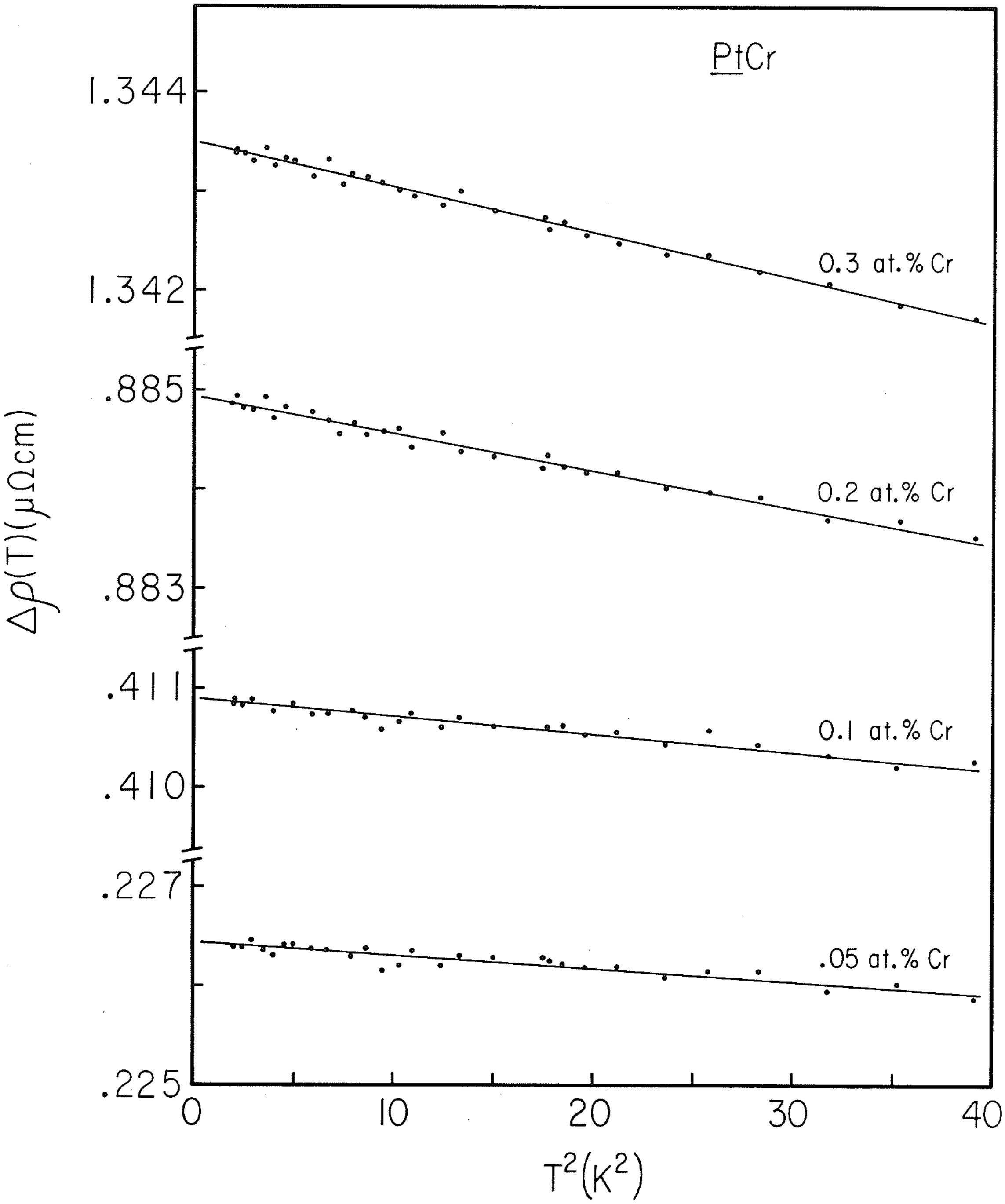

FIG.3.2-7. The incremental resistivities $\Delta\rho(T)$ of the Pt-.05, 0.1, 0.2, and 0.3 at. % Cr alloys plotted against the square of the temperature up to about $T \simeq 6K$.

TABLE 3.2-2. List of T^2 - coefficients

(a) PdCr

ALLOY (at. % Cr)	T^2 - COEFF. FROM $\Delta\rho$-vs-T^2 PLOTS ($\mu\Omega$ cm./K^2)	PREDICTED T^2 - COEFF. = $\frac{Bc}{2\theta^2}$ ($\mu\Omega$ cm./K^2)
.05	-0.93×10^{-5}	-1.26×10^{-5}
0.1	-2.65×10^{-5}	-2.76×10^{-5}
0.2	-6.15×10^{-5}	-4.82×10^{-5}
0.3	-1.20×10^{-4}	-7.65×10^{-5}

(b) PtCr

ALLOY (at. % Cr)	T^2 - COEFF. FROM $\Delta\rho$-vs-T^2 PLOTS ($\mu\Omega$ cm./K^2)	PREDICTED T^2 - COEFF. = $\frac{Bc}{2\theta^2}$ ($\mu\Omega$ cm./K^2)
.05	-1.38×10^{-5}	-1.32×10^{-5}
0.1	-1.75×10^{-5}	-2.38×10^{-5}
0.2	-3.78×10^{-5}	-3.60×10^{-5}
0.3	-4.60×10^{-5}	-4.68×10^{-5}

electrons from LSF and is associated specifically with the presence of the Cr impurities, while the second contribution is the T^2 term of the host, discussed above. The T^2-coefficient due to the impurities (i.e., from contribution one, above) was obtained from the experimental data by subtracting the resistivity of the pure host from the resistivity of the alloy, and then plotting the result (i.e., $\Delta\rho(T)$) as a function of T^2. This procedure is equivalent to subtracting the T^2 term of the pure host from the T^2 term of the alloy. However, this method clearly neglects any changes in the T^2 term of the host due to alloying, and this could account for any discrepancies between the "measured" and "predicted" values for the impurity T^2-coefficient. The data in Table 3.2-2 suggests that the T^2 term of pure Pd is more sensitive to alloying than that of pure Pt.

3.2.4 Discussion

The incremental resistivity, $\Delta\rho(T)$, of several dilute PdCr and PtCr alloys containing between .05 and 0.3 at. % Cr has been shown to contain a temperature-dependent contribution which can be fitted, at "high" temperatures ($T \geq 68K$ for PdCr and $T \geq 45K$ for PtCr), to an expression of the form $\Delta\rho(T) = Ac + Bc\,\ell n(T^2 + \theta^2)^{\frac{1}{2}}$, with the single-impurity characteristic temperature θ for Cr impurities estimated at ~43K in Pd and ~73K in Pt. In addition, the measured incremental resistivities for all the alloys exhibit a limiting, low-temperature

T^2 dependence, which is consistent with the low-temperature expansion of the above expression, i.e., $\Delta\rho(T \ll \theta) \propto (T/\theta)^2$.

With the above estimates for the single-impurity characteristic temperature θ, the corresponding characteristic energies, $k_B\theta$ ($\sim 4 \times 10^{-3}$ eV for <u>Pd</u>Cr and $\sim 6 \times 10^{-3}$ eV for <u>Pt</u>Cr), are orders of magnitude smaller than even the most conservative estimates of the width of a virtual bound state for 3d impurities ($\Delta \geq 0.5$ eV for 3d impurities). Moreover, as shown in FIG.3.2-8, the single-impurity characteristic temperature θ for first row transition impurities in Pd and Pt varies with the position of the impurity in the periodic table [17] in much the same way as the Kondo temperature, T_K, for these same impurities in noble metal hosts (see FIG.3.1-1), being low at the center of the series (Mn) and high near the ends (Ti and Ni).

Both the variation and magnitude for θ suggest that an interpretation of single-impurity behaviour in terms of the configuration-based model of Hirst [18, 19] is more appropriate than one based on the virtual bound state (VBS) description of Friedel and Anderson :

1. In terms of the traditional Friedel-Anderson VBS approach, it is difficult to understand how energy differences, $k_B\theta$, as small as 10^{-5} eV can be resolved at the impurity site, against such a broad single-particle "uncertainty" Δ. This, however, is precisely the strong point of a configuration-based approach, since it rules out, on energy conservation grounds, first order impurity-conduction electron

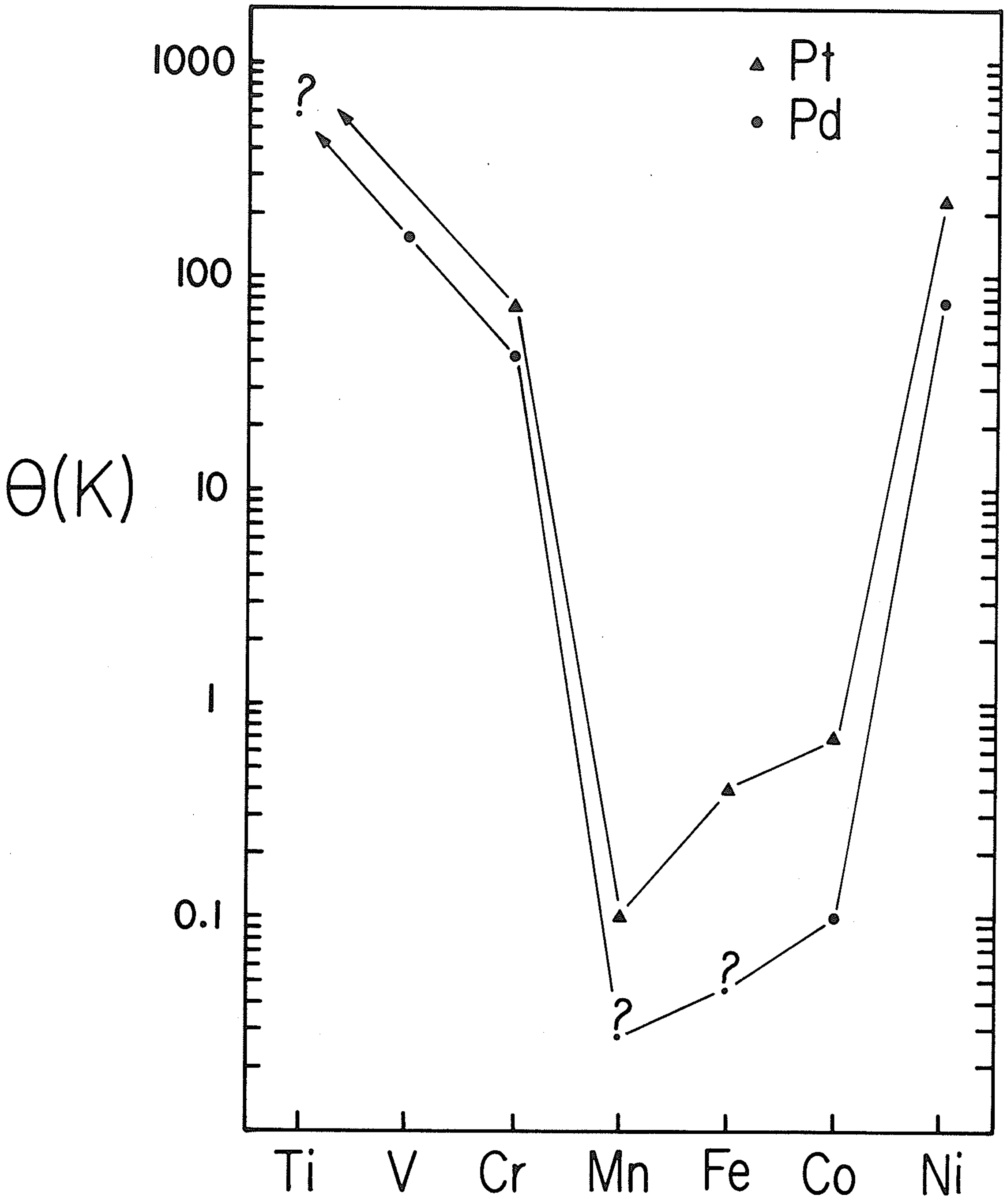

FIG.3.2-8. The estimated single-impurity characteristic temperature θ (in K) for various first transition series impurities in Pd and Pt.

mixing processes (which would presumably mask such structure) in those situations where the interconfigurational energy differences, E_{exc}, are substantially larger than the potential impurity energy level width, Δ.

2. Recalling that the single-impurity characteristic temperature is given by $T_K = T_F \exp(-\pi E_{exc}/\Delta)$ in the Hirst model, then the data in FIG.3.2-8 implies large values for the ratio E_{exc}/Δ near the center of the diagram (Mn, Fe), with the ratio presumably decreasing towards either end (Ti, Ni). A significant reduction in the E_{exc}/Δ ratio can lead to either interconfiguration fluctuation (ICF) behaviour or localized spin fluctuation (LSF) behaviour. However, the high value for θ for Ni and Ti, coupled with the expectation that 3d-4d covalent admixture should be rather large in Pd and Pt hosts, suggests the applicability of an LSF approach for these impurities, with the mixing strength Δ $(= \pi |V_{MIX}|^2 N(E_F))$ being sufficiently strong to cause admixture between several many-electron states at the impurity site. Impurities near the center of the series (Mn, Fe, and Co), on the other hand, with a very low value of θ, are probably best described in terms of a single many-electron configuration, which is stable (at least in first order) against admixture with the conduction electron states.

Cr impurities appear to lie between these two extremes, having a single-impurity characteristic temperature θ estimated at ~43K in Pd and ~73K in Pt. Consequently, it is uncertain whether Cr impurities should be described as (a) having a well-defined spin (i.e., configurationally stable) with a high Kondo temperature T_K, or

(b) configurationally unstable but with a comparatively low LSF temperature, T_{sf}.

3.3 Interaction Effects and the Onset of Magnetic Order

In this section, the electrical resistivity of five PdCr alloys containing 4, 5, 6, 8, and 10 at. % Cr and five PtCr alloys containing 5, 6, 8, 10, and 12 at. % Cr is examined over the temperature range 1.4 to 300K.

3.3.1 General Features of the Resistivity

In FIG.3.3-1, the measured resistivities, $\rho(T)$, of the five PdCr alloys containing between 4 and 10 at. % Cr are plotted as a function of temperature T from 1.4 to 300K. The data for the 4, 5, and 6 at. % Cr alloys possess well-defined resistivity minima [20, 21, 22] occurring at approximately $T_{MIN} \simeq 65$, 70, and 75K, respectively. Furthermore, the data on these three less-concentrated PdCr alloys do not display, in an obvious manner, the effects of impurity-impurity interactions (via a resistivity maximum at low temperatures). This contrasts with the behaviour of the 8 and 10 at. % Cr alloys. The data on the 8 at. % Cr sample possesses a resistivity minimum at a temperature $T_{MIN} \simeq$ 75-80K. Below this minimum, $\rho(T)$ initially increases with decreasing temperature, but then flattens considerably as the temperature is further reduced. The resistivity of the Pd- 10 at. % Cr alloy clearly demonstrates the onset of magnetic ordering via a broad maximum centered around $T_{MAX} \simeq 20K$, below a rather weak local minimum at $T_{MIN} \simeq 55K$.

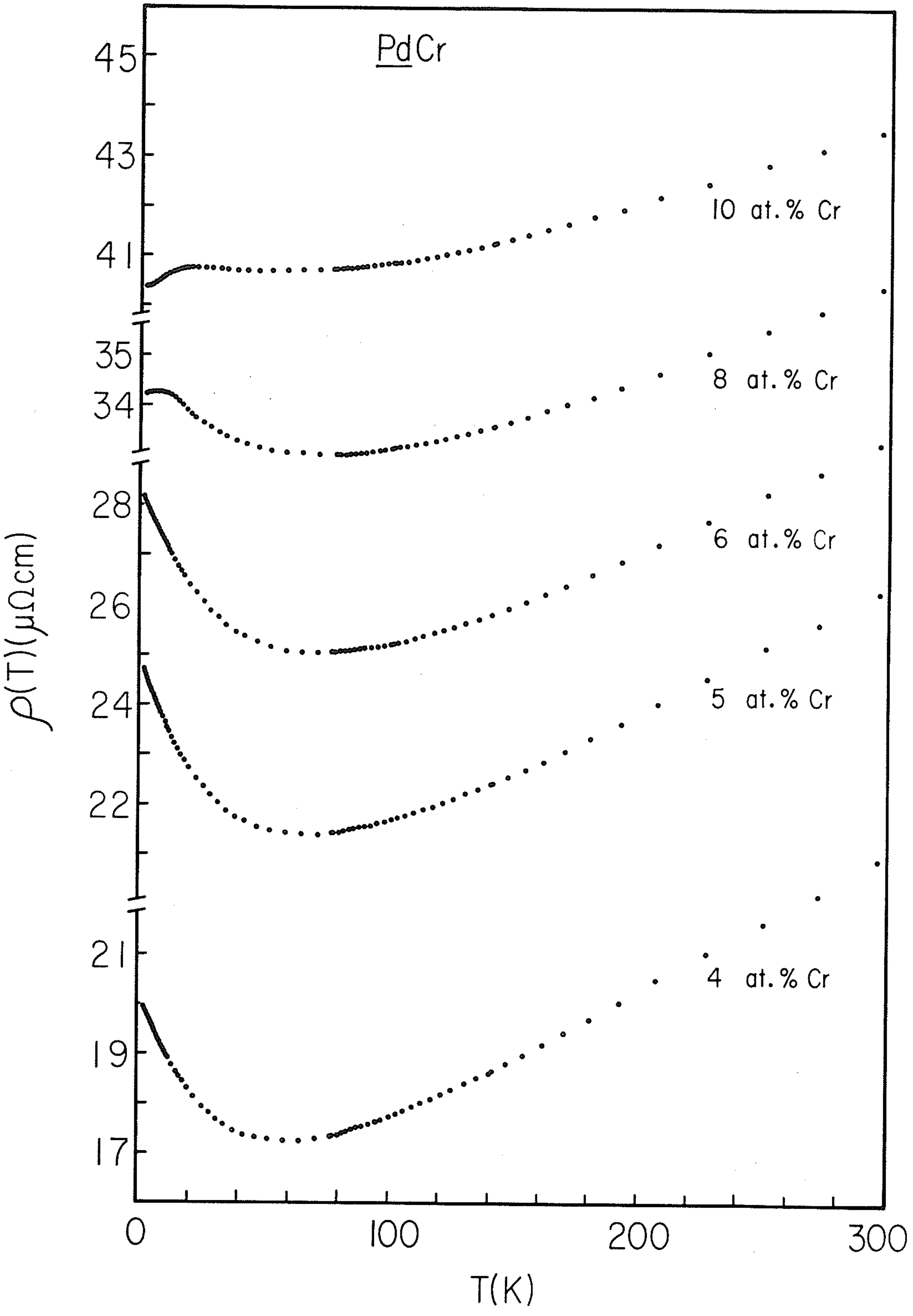

FIG.3.3-1. The measured resistivities ρ(T) of the five PdCr alloys containing between 4 and 10 at.% Cr plotted against temperature between 1.4 and 300K.

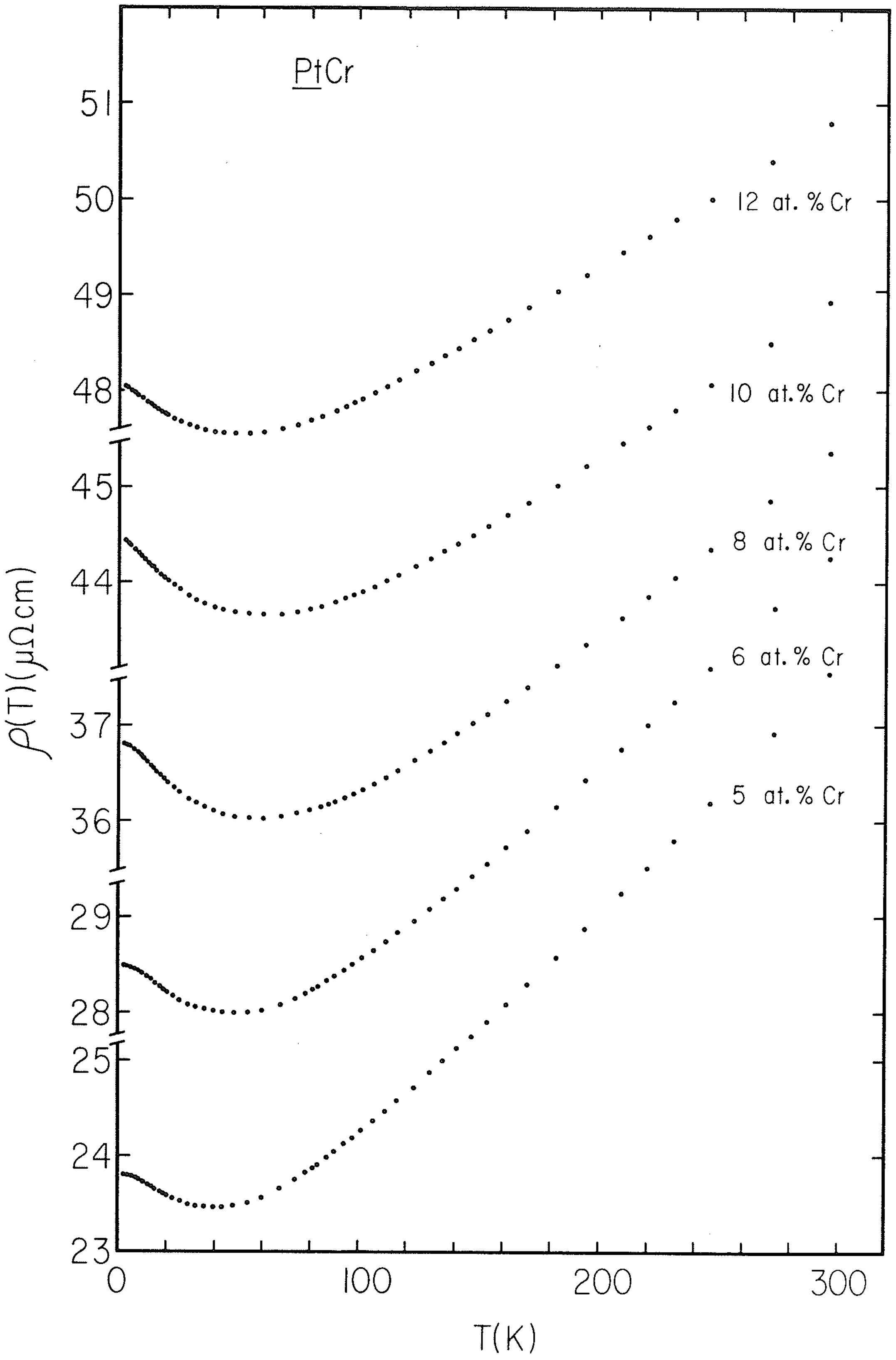

FIG.3.3-2. The measured resistivities ρ(T) of the five PtCr alloys containing between 5 and 12 at. % Cr plotted against temperature between 1.4 and 300K.

TABLE 3.3-1. Estimates for T_{MIN} and T_{MAX}

(a) PdCr

ALLOY (at. % Cr)	T_{MIN} (K)	T_{MAX} (K)
4	65 ± 3	NO MAXIMUM
5	70 ± 3	NO MAXIMUM
6	75 ± 3	NO MAXIMUM
8	75 - 80* ± 3	4 ± 0.75
10	55* ± 3	20 ± 1

* local, not absolute, minima

(b) PtCr

ALLOY (at. % Cr)	T_{MIN} (K)	T_{MAX} (K)
5	40 ± 3	NO
6	50 ± 3	MAXIMUM
8	58 ± 3	IN
10	63 ± 3	THESE
12	49 ± 3	ALLOYS

In FIG.3.3-2, the measured resistivities, $\rho(T)$, of the five PtCr alloys containing between 5 and 12 at. % Cr are plotted as a function of temperature from 1.4 to 300K. All of the PtCr alloys possess a well-defined resistivity minimum, with the temperature, T_{MIN}, at which the minimum occurs initially increasing with increasing Cr concentration, from 40K for Pt-5 at. % Cr to 63K for Pt-10 at. % Cr, and then decreasing to 49K in the Pt-12 at. % Cr alloy, as can be seen from Table 3.3-1. One striking difference between the observed behaviour of the PdCr and PtCr systems concerns the onset of magnetic order. In PdCr, magnetic ordering occurs for a Cr concentration $c \simeq 8$ at. %, whereas, in PtCr, such effects are clearly absent above 1.4K, even in the 12 at. % Cr alloy. This point will be discussed in more detail later.

3.3.2 Incremental Resistivity --- High Temperatures

In FIGS.3.3-3, 3.3-4, and 3.3-5, the incremental resistivities, $\Delta\rho(T) = \rho_{ALLOY}(T) - \rho_{Pt}(T)$, of the five PtCr alloys are plotted against temperature from 1.4 to 300K. Since an expression of the form

$$\Delta\rho(T) = Ac + Bc\,\ell n(T^2 + \theta^2)^{\frac{1}{2}} \qquad (3.3\text{-}1)$$

was shown, in Section 3.2, to accurately reproduce the observed incremental resistivities of the very dilute PtCr alloys containing between .05 and 0.3 at. % Cr, a similar fit was attempted on the more

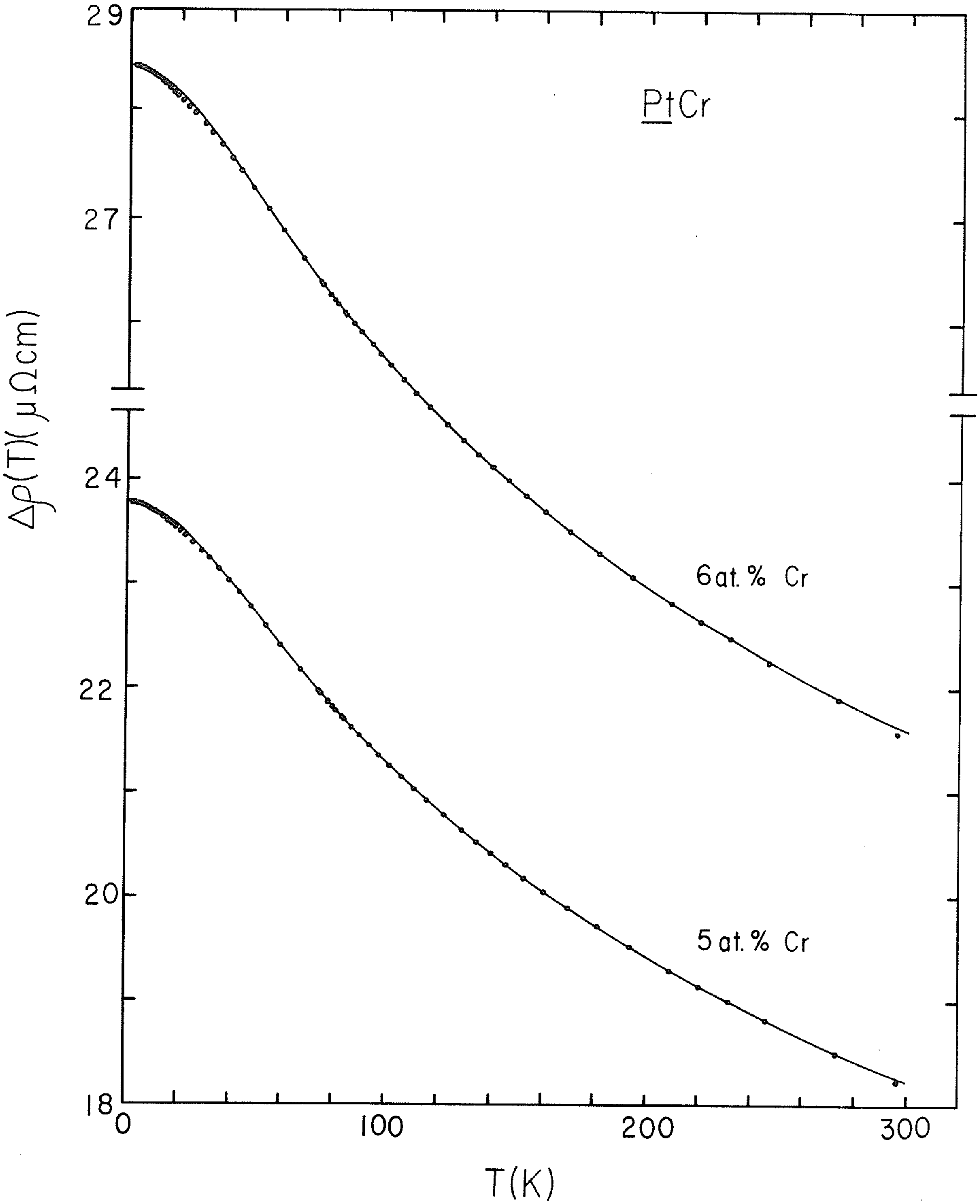

FIG.3.3-3. The incremental resistivities Δρ(T) of the Pt-5 and 6 at.% Cr alloys plotted against temperature from 1.4 to 300K. The solid curves are fits of the data to Eq.(3.3-1) over the entire temperature range.

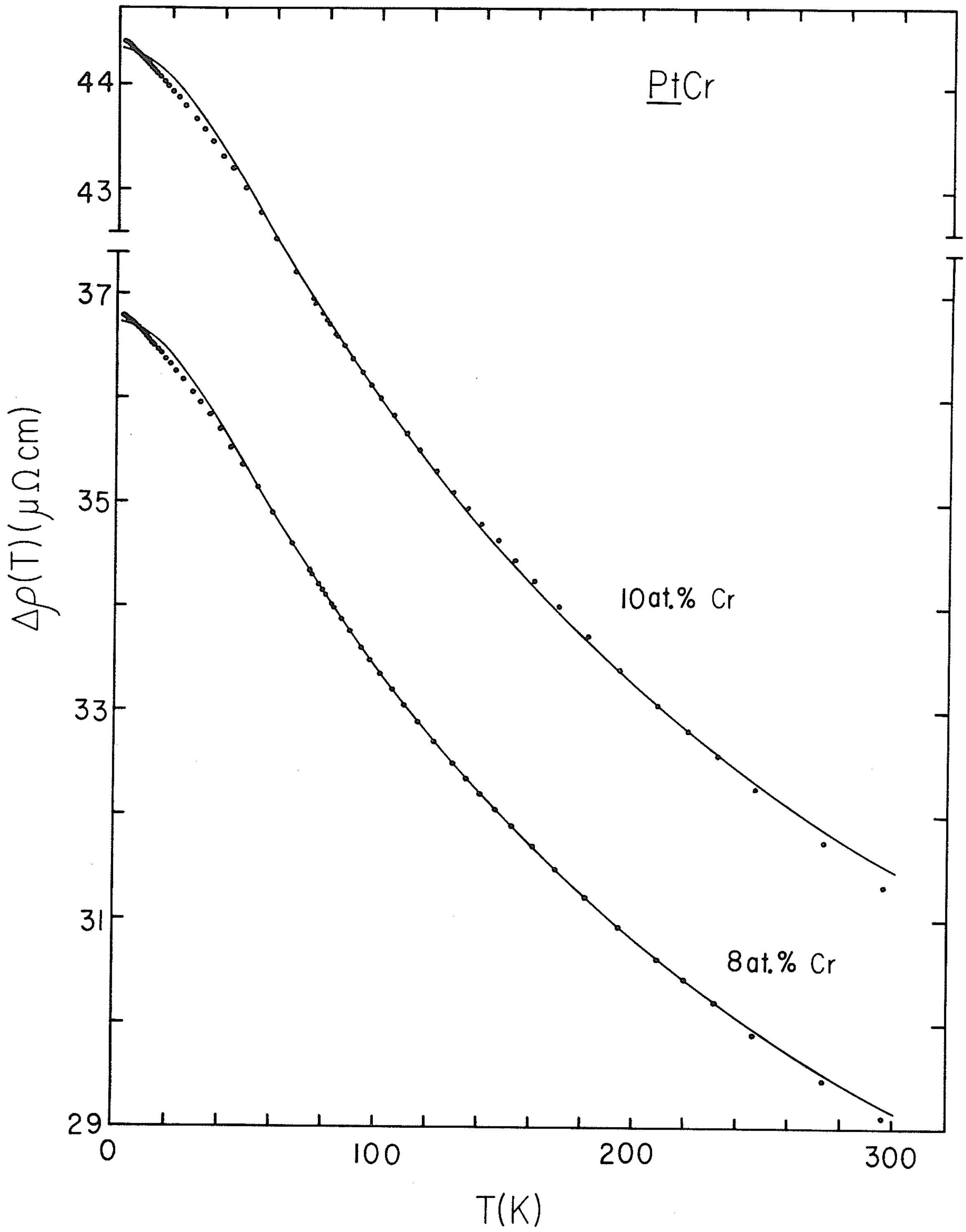

FIG.3.3-4. The incremental resistivities Δρ(T) of the Pt-8 and 10 at. % Cr alloys plotted against temperature from 1.4 to 300K. The solid curves are fits of the data to Eq.(3.3-1) over the entire temperature range.

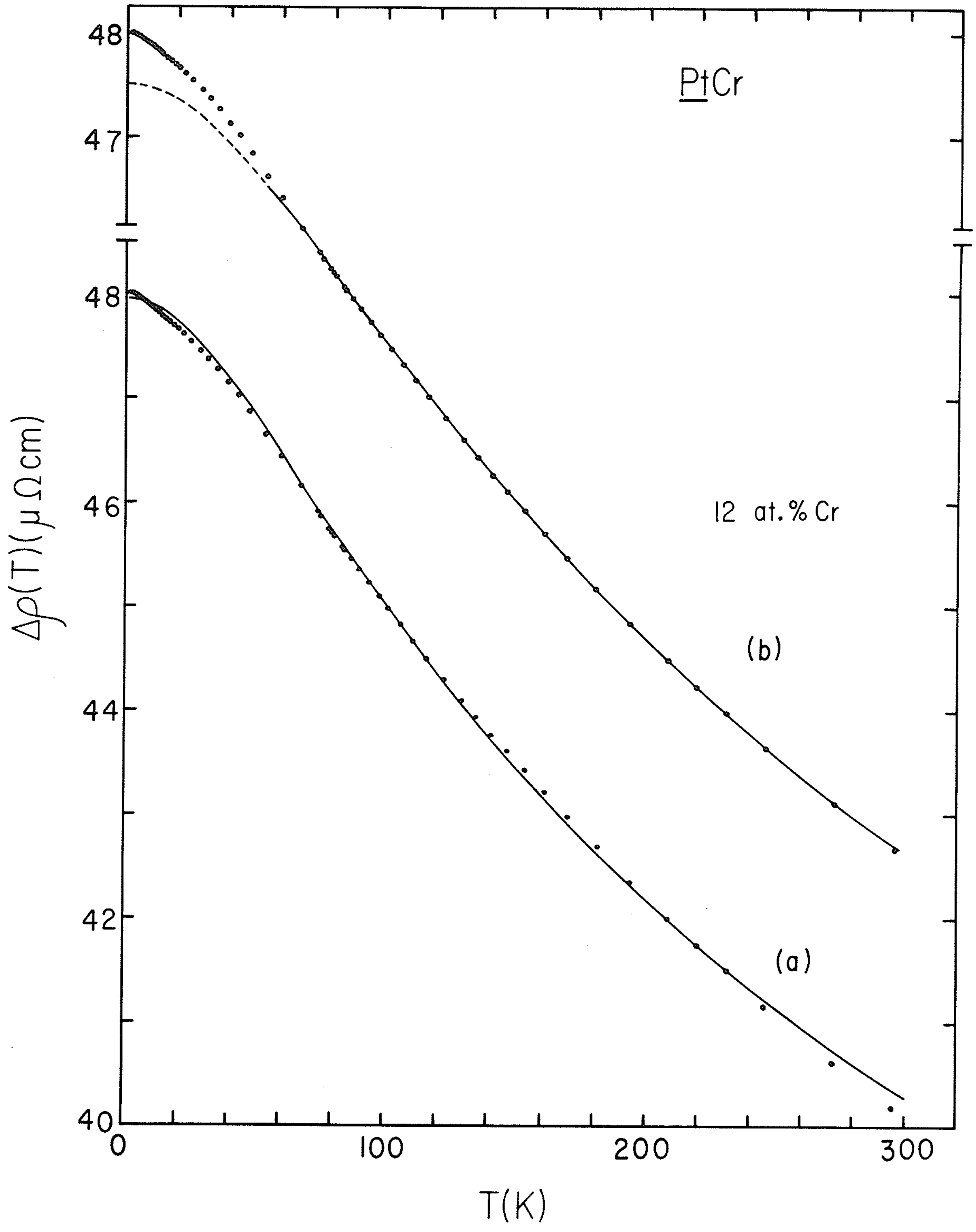

FIG.3.3-5. The incremental resistivity $\Delta\rho(T)$ of the Pt-12 at. % Cr alloy plotted against temperature from 1.4 to 300K : (a) The solid curve is a fit to Eq.(3.3-1) over the entire temperature range; (b) The solid curve is a fit of the data above 54K to Eq.(3.3-1), while the dashed curve is an extension of this fit to lower temperatures.

concentrated PtCr data presented here.

First, an attempt was made to fit the experimental data to Eq.(3.3-1) over the entire temperature range from 1.4 to 300K, using the least-squares fitting procedure previously described in Sec.3.2. The solid curves in FIGS.3.3-3, 3.3-4, and 3.3-5(a) represent the calculated incremental resistivities, $\Delta\rho(T) = Ac + Bc\,\ell n(T^2 + \theta^2)^{\frac{1}{2}}$, obtained from this fitting procedure using the "best-fit" parameters A, B, and θ listed in Table 3.3-2. For the 5 and 6 at.% Cr alloys shown in FIG.3.3-3, Eq.(3.3-1) provides a good fit to the experimental data at temperatures above 30K; below this temperature, however, systematic deviations from the calculated curves begin to appear. These deviations become more pronounced, and begin at higher temperatures, in the 8 and 10 at.% Cr alloys shown in FIG.3.3-4. Moreover, for the alloys containing 10 and 12 at.% Cr (see FIG.3.3-5(a)), there is also disagreement around room temperature. Consequently, it was decided to fit Eq.(3.3-1) to the experimental data over a restricted temperature range, namely $\theta \leq T \leq 300K$. The corresponding calculated $\Delta\rho(T)$ curves are shown in FIGS.3.3-5(b), 3.3-6, and 3.3-7, and the associated "best-fit" parameters are listed in Table 3.3-3. These curves provide a substantially better fit to the experimental data over the appropriate temperature range than do those discussed above. In FIGS.3.3-5(b), 3.3-6, and 3.3-7, the solid curves relate to the temperature range actually covered in the fitting scheme (i.e., 54-300K), while the dashed portions are extensions of these curves to lower temperatures. An inspection of Table 3.3-3 reveals that the parameters A, B, and θ are not concentration

TABLE 3.3-2. Best-fit parameters for Eq.(3.3-1)

PtCr

ALLOY (at. % Cr)	RANGE OF FIT (K)	RMS DEVIATION OVER THIS RANGE (10^{-4} μΩ cm./point-at. % Cr)	θ (K)	A (μΩ cm./at. % Cr)	B (μΩ cm./at. % Cr)
5	1.4 - 300	3.0	50	7.15	- 0.61
6	1.4 - 300	3.8	50	7.04	- 0.59
8	1.4 - 300	6.1	52	6.71	- 0.54
10	1.4 - 300	6.9	56	6.31	- 0.46
12	1.4 - 300	4.8	67	5.76	- 0.42

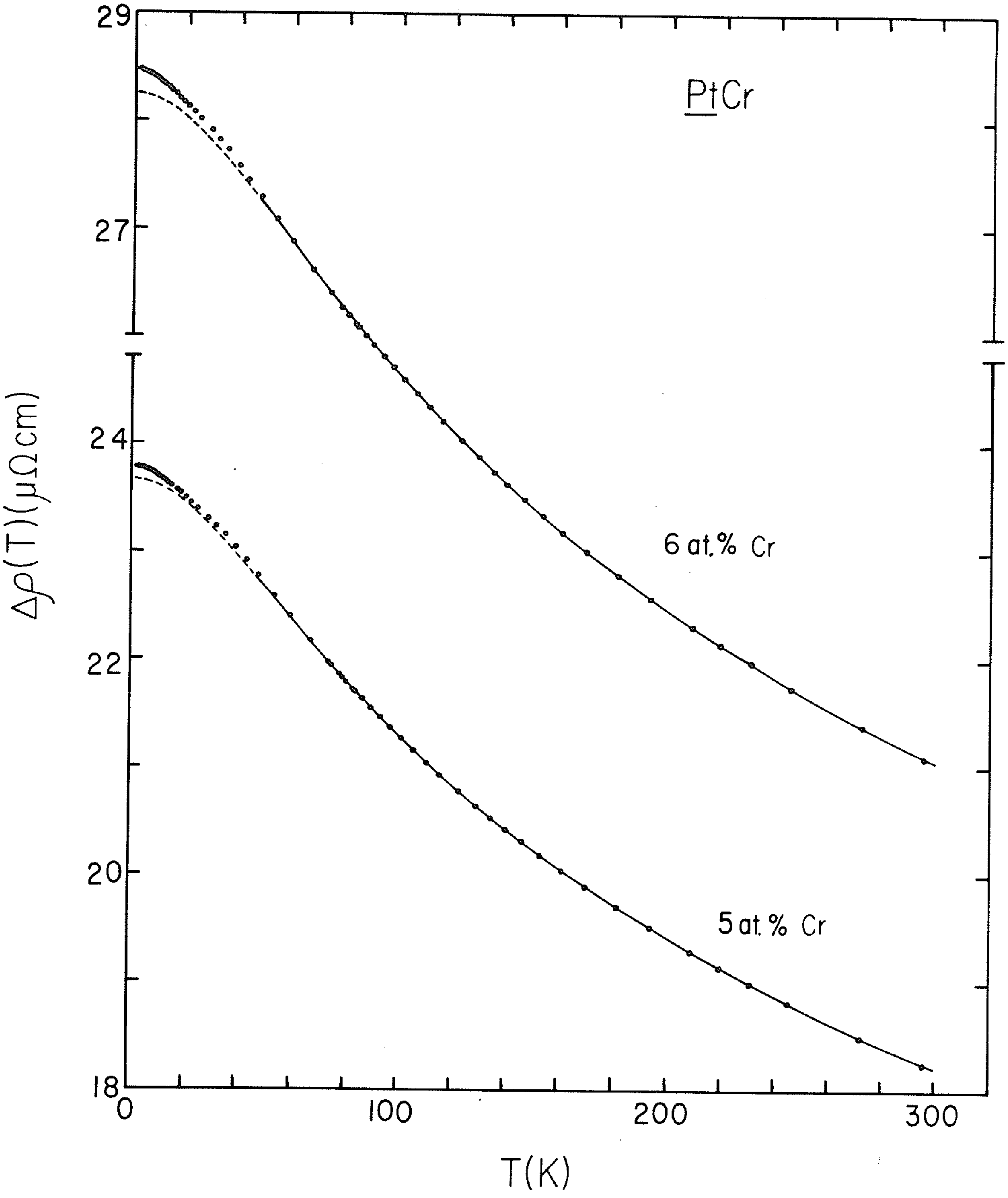

FIG.3.3-6. The incremental resistivities $\Delta\rho(T)$ of the Pt-5 and 6 at.% Cr alloys plotted against temperature from 1.4 to 300K. The solid curves are fits of the data above 54K to Eq.(3.3-1), while the dashed curves are extensions of these fits to lower temperatures.

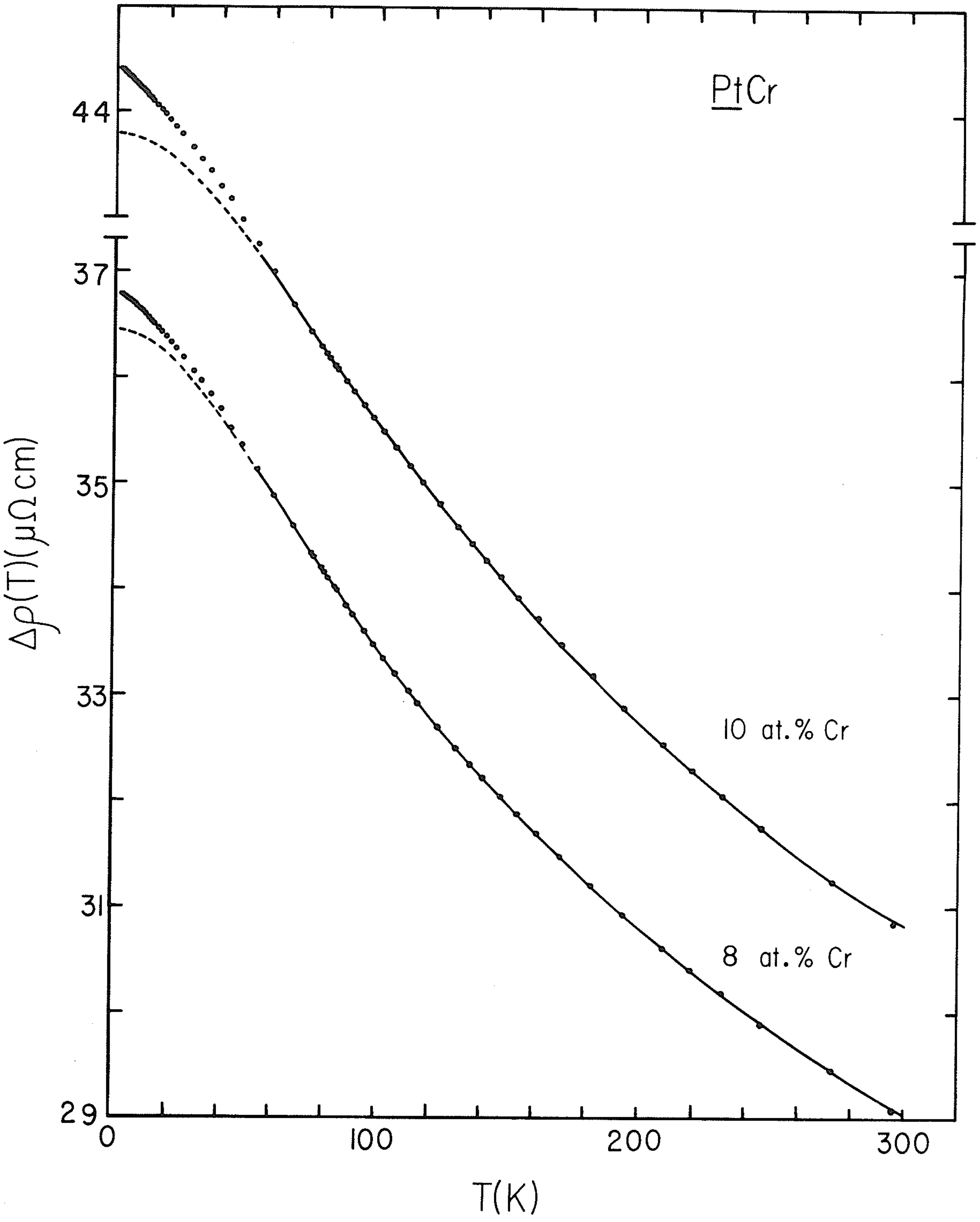

FIG.3.3-7. The incremental resistivities Δρ(T) of the Pt-8 and 10 at.% Cr alloys plotted against temperature from 1.4 to 300K. The solid curves are fits of the data above 54K to Eq.(3.3-1), while the dashed curves are extensions of these fits to lower temperatures.

TABLE 3.3-3. Best-fit parameters for Eq.(3.3-1) : Restricted fitting range

PtCr

ALLOY (at. % Cr)	RANGE OF FIT (K)	RMS DEVIATION OVER THIS RANGE ($10^{-4}\mu\Omega$ cm./point-at. % Cr)	θ (K)	A ($\mu\Omega$ cm./at. % Cr)	B ($\mu\Omega$ cm./at. % Cr)
5	54 - 300	5.1	52.5	7.19	- 0.62
6	54 - 300	4.7	56	7.16	- 0.61
8	54 - 300	6.2	60	6.87	- 0.57
10	54 - 300	6.0	73	6.61	- 0.52
12	54 - 300	4.9	85	6.06	- 0.47

independent; the "best-fit" values for A and $|B|$ *decrease* slightly with increasing Cr concentration, while the "best-fit" values for the characteristic temperature θ *increase* with increasing Cr content.

The incremental resistivities, $\Delta\rho(T) = \rho_{ALLOY}(T) - \rho_{Pd}(T)$, of the five PdCr alloys containing between 4 and 10 at. % Cr are plotted against temperature from 1.4 to 300K in FIGS.3.3-8 and 3.3-9. Following the procedure used in fitting the PtCr data, it was decided to fit the PdCr incremental resistivity data to Eq.(3.3-1) over a restricted temperature range as well. The solid curves in FIG.3.3-8 correspond to a least-squares fit of the incremental resistivities of the 4, 5, and 6 at. % Cr alloys to Eq.(3.3-1) *above* 20K, while the solid curves in FIG.3.3-9 represent a least-squares fit of the experimental data for the 8 and 10 at. % Cr alloys at temperatures *above* 28K and 40K, respectively, where the effects of magnetic ordering should have little influence (i.e., for temperatures $T \geq 2T_{MAX}$). Table 3.3-4 contains a comprehensive list of the "best-fit" parameters A, B, and θ. In PdCr, as in PtCr, the characteristic temperature θ *increases* with increasing Cr concentration, while $|B|$ decreases with increasing Cr content. The coefficient A, on the other hand, initially decreases with increasing Cr concentration, reaching a minimum at around 6 at. % Cr, and then increasing with the further addition of Cr.

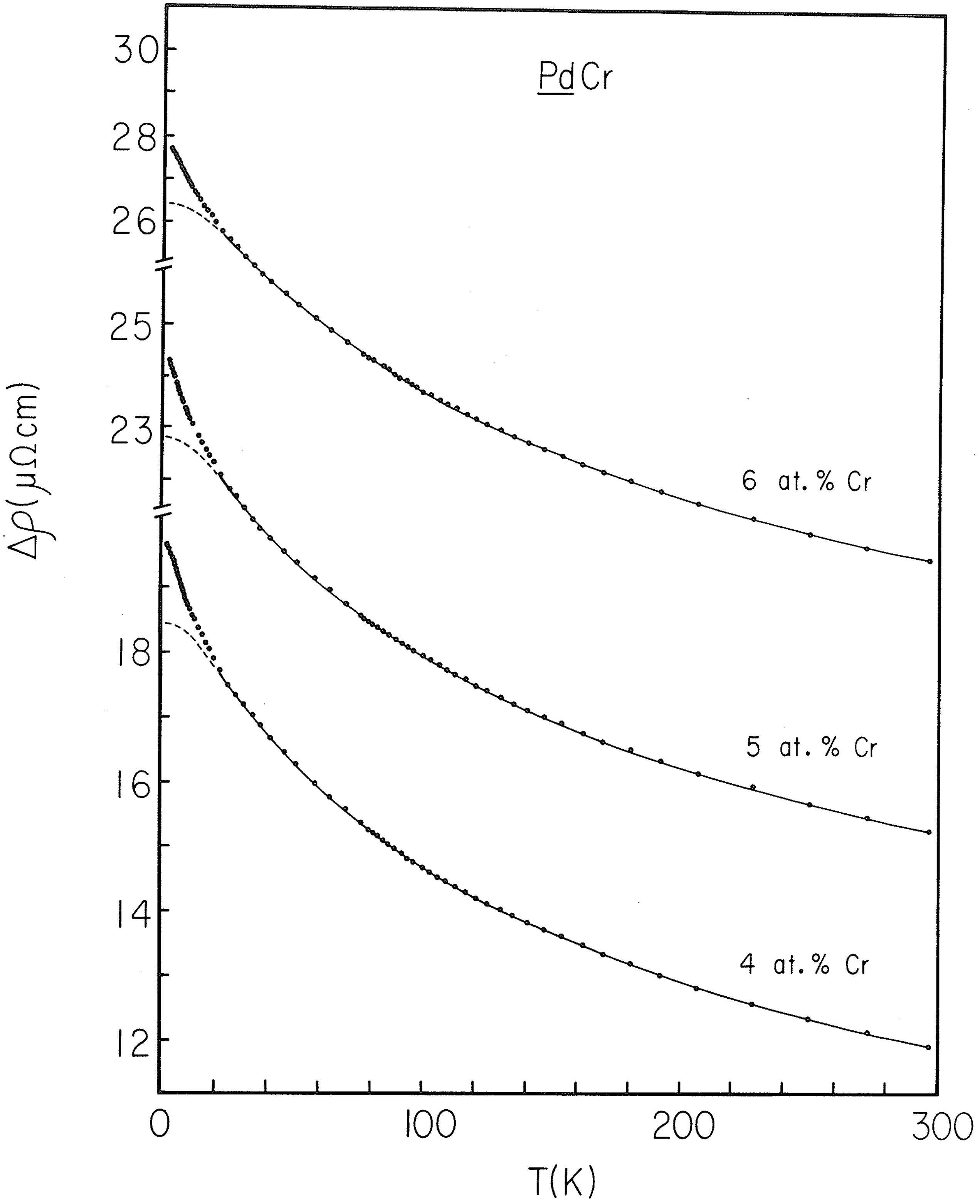

FIG.3.3-8. The incremental resistivities Δρ(T) of the Pd-4, 5, and 6 at.% Cr alloys plotted against temperature from 1.4 to 300K. The solid curves are fits of the data above 20K to Eq.(3.3-1), while the dashed curves are extensions of these fits to lower temperatures.

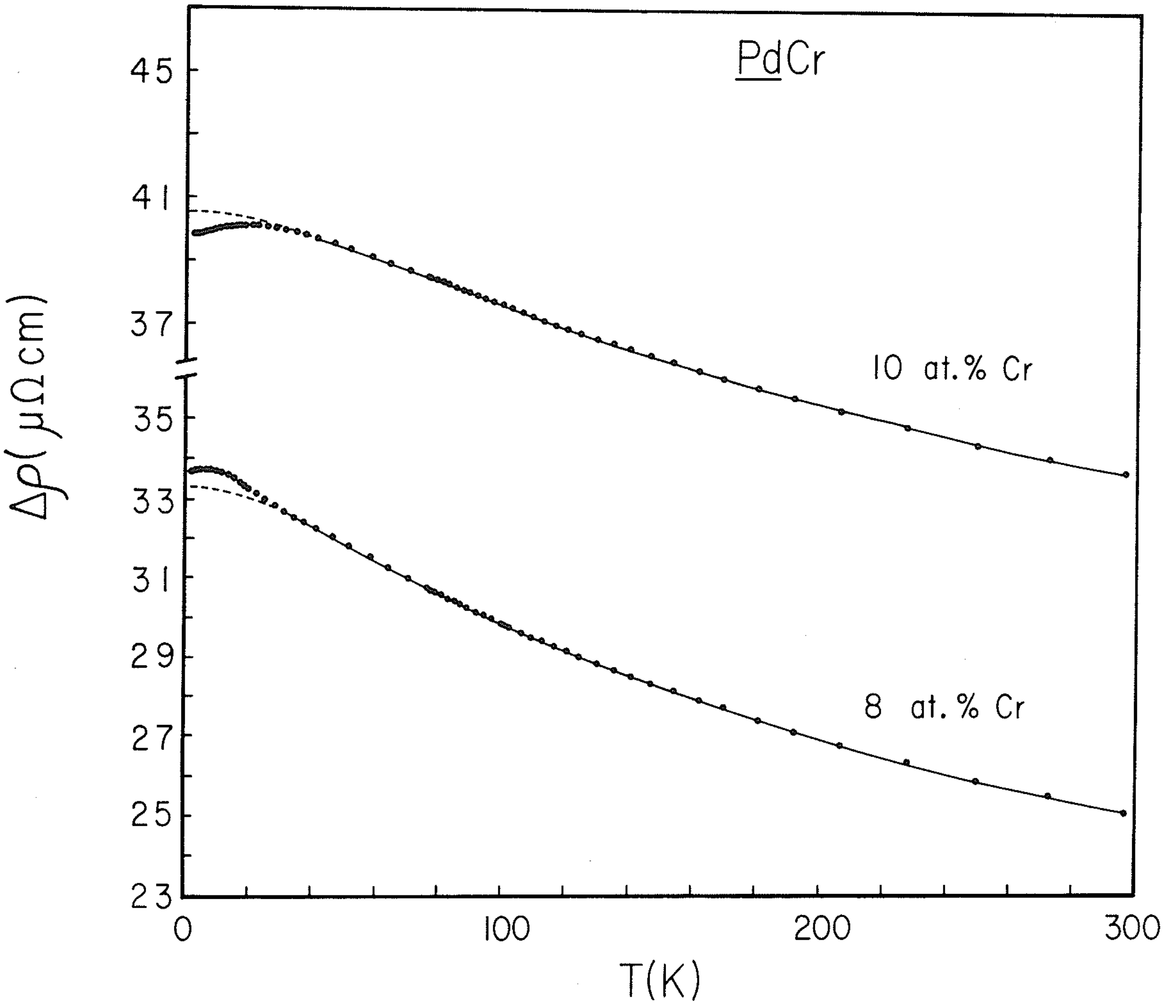

FIG.3.3-9. The incremental resistivities $\Delta\rho(T)$ of the Pd-8 and 10 at.% Cr alloys plotted against temperature from 1.4 to 300K. The solid curves are fits of the data above 28K and 40K, respectively, to Eq.(3.3-1), while the dashed curves are extensions of these fits to lower temperatures.

TABLE 3.3-4. Best-fit parameters for Eq.(3.3-1) : Restricted fitting range

PdCr

ALLOY (at. % Cr)	RANGE OF FIT (K)	RMS DEVIATION OVER THIS RANGE (10^{-3} μΩ cm./point-at. % Cr)	θ (K)	A (μΩ cm./at. % Cr)	B (μΩ cm./at. % Cr)
4	20 - 300	1.24	25.4	6.76	- 0.67
5	20 - 300	1.12	28.2	6.71	- 0.64
6	20 - 300	0.95	33.4	6.58	- 0.62
8	28 - 300	0.60	57.7	6.64	- 0.61
10	40 - 300	0.34	80.4	6.68	- 0.60

3.3.3 Incremental Resistivity --- Low Temperatures

It is apparent from the above discussion that, while Eq.(3.3-1) provides a good description of the incremental resistivity data in both the PdCr and PtCr systems at "high" temperatures, systematic deviations between the measured and predicted $\Delta\rho(T)$ begin to appear at low temperatures (for the Cr concentrations examined here). At low temperatures ($T \ll \theta$), Eq.(3.3-1) predicts a T^2 form for the incremental resistivity $\Delta\rho(T \ll \theta)$:

$$\Delta\rho(T \ll \theta) = Ac + Bc\,\ell n\theta + (Bc/2\theta^2)\,T^2 \quad , \qquad (3.3\text{-}2)$$

and hence a temperature coefficient $d\,[\Delta\rho(T \ll \theta)]/dT$ which varies linearly with temperature for $T \ll \theta$:

$$\frac{d\,[\Delta\rho(T \ll \theta)]}{dT} = (Bc/\theta^2)\,T \quad . \qquad (3.3\text{-}3)$$

Such a T^2 term was indeed observed in the very dilute PdCr and PtCr alloys (containing between .05 and 0.3 at. % Cr) examined in Sec.3.2. However, in the more concentrated alloys examined here, the presence of interactions between impurities modifies the low-temperature single-impurity behaviour in such a way that, for all five PtCr alloys and for the PdCr alloys containing 4, 5, and 6 at. % Cr, the measured values for both $\Delta\rho(T < \theta)$

and $d[\Delta\rho(T \ll \theta)]/dT$ are significantly larger than the corresponding values predicted by Eqs.(3.3-1) and (3.3-3) using the "best-fit" parameters from the high-temperature data. In order to illustrate this point, the measured and calculated low-temperature incremental resistivities for the five PtCr alloys containing between 5 and 12 at. % Cr and the three PdCr alloys containing 4, 5, and 6 at. % Cr are plotted against T^2 in FIGS.3.3-10, 3.3-11, and 3.3-12. Table 3.3-5 lists the values of two parameters, $\left\{[\Delta\rho(1.5K)]_{MEAS} - [\Delta\rho(1.5K)]_{CALC}\right\}$ and $\Delta\rho(1.5K) - \Delta\rho(4.2K)$, extracted from the low-temperature incremental resistivity data. From these figures, the differences between the observed and predicted low-temperature behaviour are clearly visible, with the measured values for the incremental resistivity, $\Delta\rho(T < \theta)$, and the low-temperature slope, $d[\Delta\rho(T \ll \theta)]/dT$, being larger than the predicted values. As discussed in Sec.3.1, this type of behaviour can be attributed to the dominance of the resistivity by single-site scattering events, with interactions between impurities stabilizing the spin fluctuations at individual impurity sites. Moreover, an inspection of the tabulated values for $\Delta\rho(1.5K) - \Delta\rho(4.2K)$ and $\left\{[\Delta\rho(1.5K)]_{MEAS} - [\Delta\rho(1.5K)]_{CALC}\right\}$ shows that the magnitude of the low-temperature slope, as well as the difference between the measured and predicted values for $\Delta\rho(T < \theta)$, initially increases with increasing Cr concentration, passes through a maximum (at around 10 at. % Cr in PtCr and 5 at. % Cr in PdCr), and then decreases with the further addition of Cr. As pointed out in Sec.3.1, such a decrease signals the onset of correlations between fluctuating spins at different impurity sites, indicating a trend

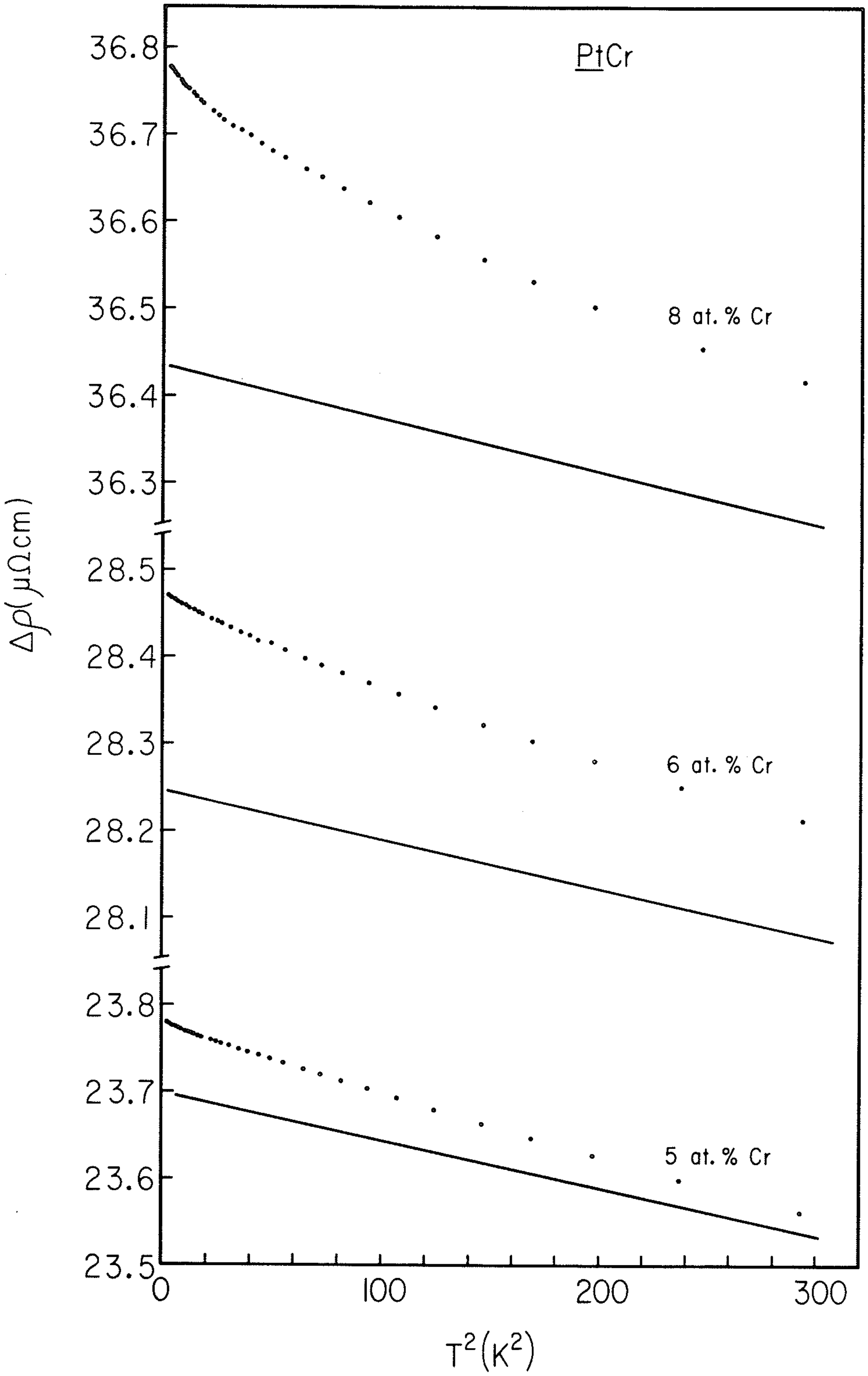

FIG.3.3-10. The low-temperature ($T < 17K$) incremental resistivities $\Delta\rho(T)$ of the Pt-5, 6, and 8 at. % Cr alloys plotted against the square of the temperature. The solid lines are extensions of the high-temperature fits discussed in the text.

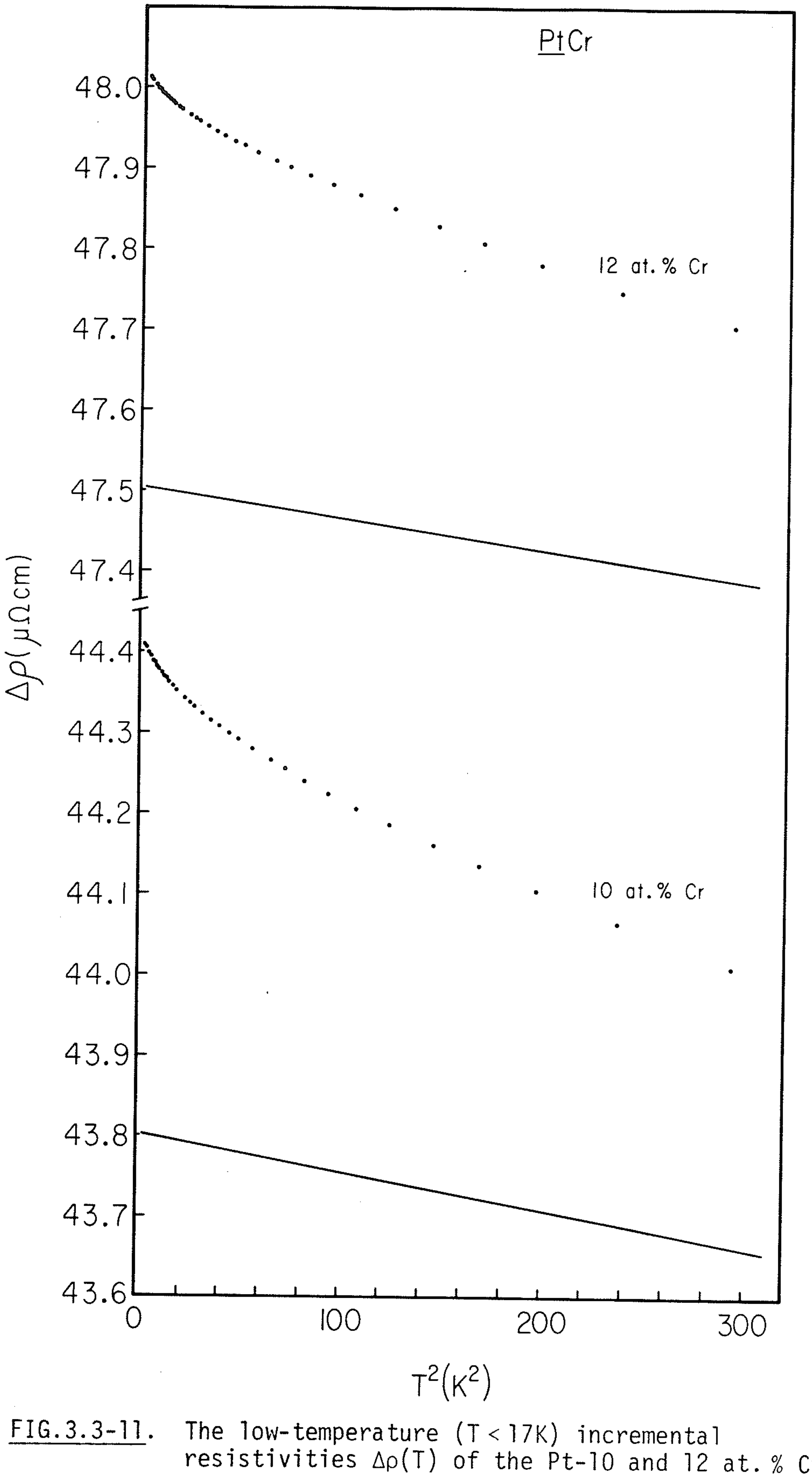

FIG.3.3-11. The low-temperature ($T < 17K$) incremental resistivities $\Delta\rho(T)$ of the Pt-10 and 12 at. % Cr alloys plotted against the square of the temperature. The solid lines are extensions of the high-temperature fits discussed in the text.

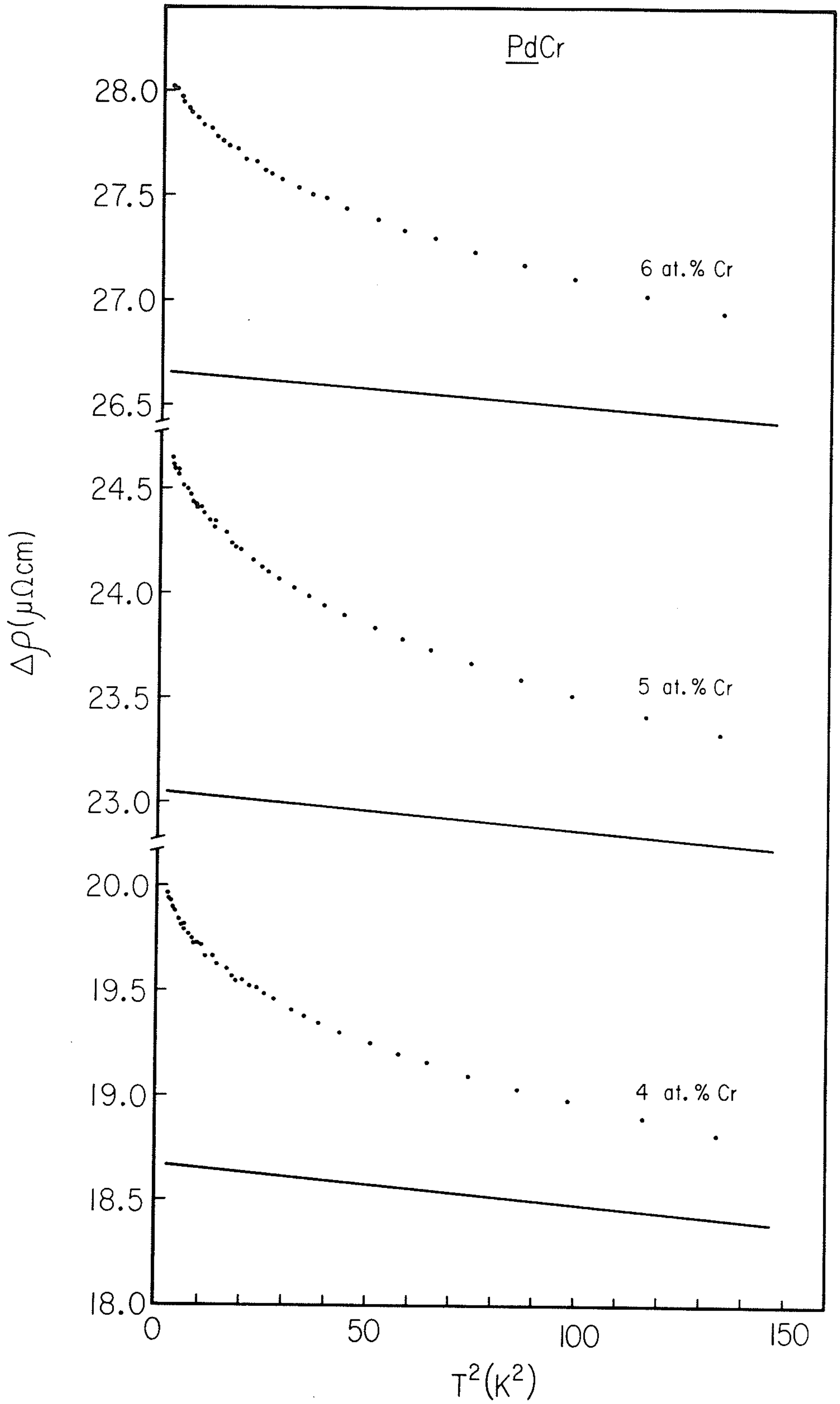

FIG.3.3-12. The low-temperature ($T < 12K$) incremental resistivities $\Delta\rho(T)$ of the Pd-4, 5, and 6 at.% Cr alloys plotted against the square of the temperature. The solid lines are extensions of the high-temperature fits discussed in the text.

TABLE 3.3-5

(a) PtCr

ALLOY (at. % Cr)	$\left\{[\Delta\rho(1.5K)]_{MEAS} - [\Delta\rho(1.5K)]_{CALC}\right\}$ (μΩ cm.)	$\Delta\rho(1.5K) - \Delta\rho(4.2K)$ (μΩ cm.)
5	0.079	.0218
6	0.224	.0290
8	0.342	.0435
10	0.606	.0633
12	0.510	.0550

(b) PdCr

ALLOY (at. % Cr)	$\left\{[\Delta\rho(1.5K)]_{MEAS} - [\Delta\rho(1.5K)]_{CALC}\right\}$ (μΩ cm.)	$\Delta\rho(1.5K) - \Delta\rho(4.2K)$ (μΩ cm.)
4	1.295	+ .390
5	1.588	+ .419
6	1.365	+ .337
8	0.413	- .040
10	- 0.646	- .078

towards a magnetic ordering of the impurity spins. (In fact, for the Pd-8 and 10 at. % Cr alloys, $\Delta\rho(1.5K) - \Delta\rho(4.2K)$ is <u>negative</u>, indicating the presence of a <u>maximum</u> in the corresponding incremental resistivities due to the gradual freezing out of spin-flip scattering events. This point will be discussed in more detail later.)

Such stabilization and correlation effects require the thermal energy k_BT to be of the order of the interaction energy. An estimate of the magnitude of the interaction energy for Cr impurities in Pd and Pt can be obtained from the double-resonance coupling model of Caroli [23] and Blandin [24]. Double-resonance coupling between two impurities separated by a distance R [25] leads to an interaction energy of the form

$$E_{int}(R) = \sum_{\ell} \frac{(2\ell+1)^2}{\pi} E_F \sin\delta_\ell^+ \sin\delta_\ell^- \frac{\cos(2k_FR + \delta_\ell^+ + \delta_\ell^-)}{(k_FR)^3} , \qquad (3.3\text{-}4)$$

where ℓ labels the various partial waves, E_F is the Fermi energy, k_F is the Fermi momentum and δ_ℓ^+ and δ_ℓ^- are the phase shifts for the appropriate [spin up (+) or spin down(-)] ℓth partial wave. The phase shifts appearing in Eq.(3.3-4) can be obtained from the Friedel sum rule [26] :

$$Z = \sum_{\ell} \frac{2\ell+1}{\pi} \left[\delta_\ell^+(E_F) + \delta_\ell^-(E_F) \right] , \qquad (3.3\text{-}5)$$

where Z is the effective valence difference between the impurity and host, while the impurity spin S is given by [27]

$$2S = \sum_{\ell} \frac{2\ell+1}{\pi}\left[\delta_{\ell}^{+}(E_F) - \delta_{\ell}^{-}(E_F)\right] \quad . \qquad (3.3\text{-}6)$$

Assuming d-wave ($\ell = 2$) contributions dominate Eqs.(3.3-4) to (3.3-6), and using $Z = -4$ and $S = 5/2$ for Cr impurities in Pd and Pt, Eqs(3.3-5) and (3.3-6) yield

$$\delta_2^{+} = -\frac{3\pi}{20} \text{ and } \delta_2^{-} = -\frac{13\pi}{20} \quad . \qquad (3.3\text{-}7)$$

In order to estimate $E_{int}(R)$ from Eq.(3.3-4), it is necessary to evaluate k_F and E_F. Recent band-structure calculations for Pt [28] indicate that the Fermi velocity v_F for XW5, the open d-hole surface in the fifth zone, averages approximately to 0.3 a.u.. The bare band mass for this surface [29] is 6.2 and the enhancement factor is 1.67 [28]. The effective mass m_d^* is thus estimated at $10.3\, m_0$, which gives $k_F = 5.9\ \mathring{A}^{-1}$, and the product $k_F R$ for nearest-neighbour Cr impurities is 16.3. The estimated Fermi energy E_F for Pt is 8.9 eV (relative to the zero of potential between muffin-tin spheres [28]). Then, from Eq.(3.3-4), the interaction energy for nearest-neighbour pairs of Cr impurities in Pt is

$$E_{int}(n.n.) = 1.35 \times 10^{-3} eV \simeq 15K, \quad \text{for } \underline{Pt}Cr. \qquad (3.3\text{-}8)$$

This calculation can also be performed for Cr impurities in Pd. For the open d-hole surface XW5 in Pd, the average Fermi velocity v_F is approximately 0.2 a.u. [28]. The enhancement factor for this surface [28] is 1.66 and its bare band mass [24] is 9.1, so that the effective mass m_d^* is 15.1 m_0. This gives $k_F = 5.7\,\text{Å}^{-1}$ and thus the product $k_F R$ for nearest-neighbours is 15.6. Taking E_F as 7.6 eV [28], then the interaction energy for nearest-neighbour pairs of Cr impurities in Pd is

$$E_{int}(\text{n.n.}) = 6.0 \times 10^{-3}\,\text{eV} \simeq 70\text{K}, \qquad \text{for } \underline{\text{Pd}}\text{Cr}. \qquad (3.3\text{-}9)$$

The values for E_{int} in Eqs.(3.3-8) and (3.3-9) are in reasonably good agreement with the observed temperature at which deviations between the measured and calculated incremental resistivities $\Delta\rho(T)$ first begin to appear. While it is true that estimates for E_{int} are very sensitive to the choice of parameters, this calculation is included in order to demonstrate that such a coupling mechanism is capable of yielding interaction energies of the appropriate magnitude, with a reasonable selection for Z and S.

The difference between the measured incremental resistivities and the calculated, isolated-impurity curves at low temperatures in both the $\underline{\text{Pd}}$Cr and $\underline{\text{Pt}}$Cr systems should be dominated initially by "pair" interactions, the energy of which is given by Eqs.(3.3-8) and (3.3-9) (at least for nearest-neighbour pairs). In FIG.3.3-13, an attempt is

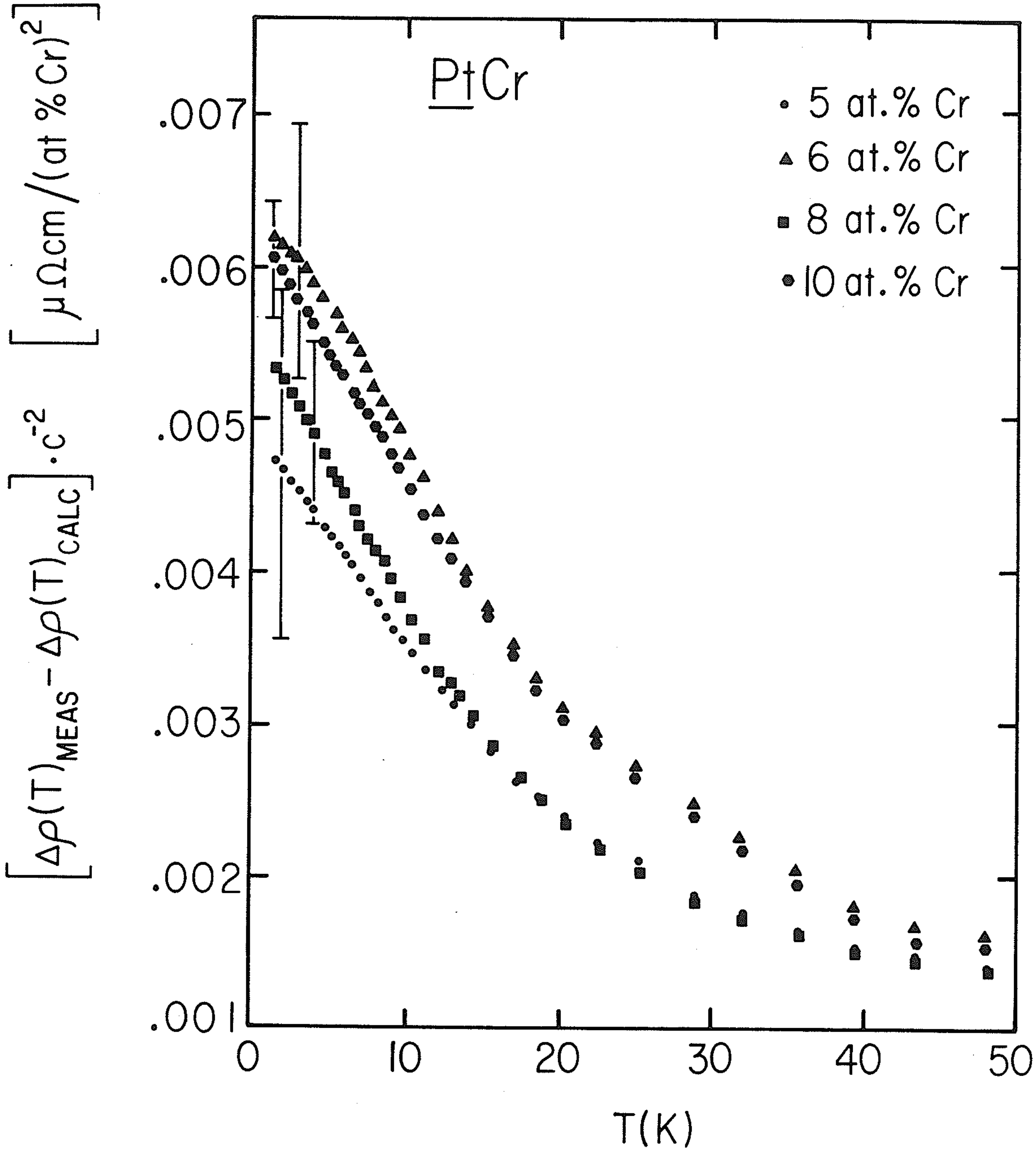

FIG.3.3-13. The difference between the measured and predicted incremental resistivities of the Pt-5, 6, 8, and 10 at. % Cr alloys, divided by the square of the Cr concentration, plotted against temperature below 50K. The vertical error bars correspond to the change in this difference induced by a ± 0.5K change in the characteristic temperature θ used in evaluating the "predicted" incremental resistivity.

made to establish the pair dominance of the excess low-temperature incremental resistivity in PtCr by plotting the difference $\left\{[\Delta\rho(T)]_{MEAS} - [\Delta\rho(T)]_{CALC}\right\}\cdot c^{-2}$ against temperature for the Pt-5, 6, 8, and 10 at. % Cr alloys. The error bars in this figure correspond to a change of ± 0.5K in the characteristic temperature θ (this is the estimated uncertainty in θ). From FIG.3.3-13 it is clear that, within experimental error, the difference $\left\{[\Delta\rho(T)]_{MEAS} - [\Delta\rho(T)]_{CALC}\right\}$ does scale as c^2. The data on the Pt-12 at. % Cr alloy are not included in this figure. While the difference $\left\{[\Delta\rho(T)]_{MEAS} - [\Delta\rho(T)]_{CALC}\right\}\cdot c^{-2}$ for this alloy exhibits a similar dependence on temperature, its magnitude is considerably smaller. For example, $\left\{[\Delta\rho(1.5K)]_{MEAS} - [\Delta\rho(1.5K)]_{CALC}\right\}\cdot c^{-2}$ for the Pt-12 at. % Cr sample is $(3.5 \pm 0.25) \times 10^{-3}\mu\Omega$ cm./(at. % Cr)^2, compared with typically $5 \times 10^{-3}\mu\Omega$ cm./(at. % Cr)^2 for the other alloys. As discussed previously, this decrease is interpreted as arising from the increasing importance of correlation effects between fluctuating spins at different impurity sites, indicating a trend towards magnetic order. The corresponding trend in PdCr appears above about 5 at. % Cr. As a result, the $\left\{[\Delta\rho(T)]_{MEAS} - [\Delta\rho(T)]_{CALC}\right\}\cdot c^{-2}$-vs-T plots for the PdCr alloys examined in this section do not lie on a common curve, as do those for the PtCr alloys in FIG.3.3-13, since, even in the Pd-5 at. % Cr alloy, interaction effects have already progressed well beyond the stage where "pair" interactions dominate.

This leads to the next point -- the absence of magnetic order above 1.5K in PtCr, even for 12 at. % Cr in Pt. A comparison of the magnetic ordering temperature for Cr in Pd, Pt, and typically, Au, indicates that in spite of the effects of exchange enhancement, this temperature decreases across the sequence <u>Au</u>Cr, <u>Pd</u>Cr, <u>Pt</u>Cr, which is also the variation followed by the LSF lifetime τ_{sf} [30]. For dilute alloys in general ($c < 1$ at. %), magnetic order is induced by interimpurity coupling via an oscillatory conduction electron spin polarization. In real systems, there are several factors that contribute to $n^{\pm}(\vec{r})$, the spin density at a distance $\vec{r}$ from a magnetic impurity. The final form for $n^{\pm}(\vec{r})$ can thus be rather complicated [31]. However, in the case of a spherical Fermi surface, and for exchange matrix elements $J(\vec{k},\vec{k}')$ between the initial conduction electron state $\vec{k}$ and the final state $\vec{k}'$, which are functions of $\vec{q} = \vec{k} - \vec{k}'$ alone, then [31]

$$n^{\pm}(\vec{r}) \propto \mp \int \chi_i(q)\, J(q) \cos(\vec{q}\cdot\vec{r})\, dq \quad , \qquad (3.3\text{-}10)$$

where $\chi_i(q)$ is the Fourier component of the <u>static</u> exchange-enhanced (interacting) conduction electron susceptibility. For the systems studied here, particularly at low temperatures, where the conduction electron thermal lifetime $\hbar/k_BT$ becomes very long compared with the spin fluctuation lifetime τ_{sf}, the above form is no longer appropriate. In the same way that an understanding of localized spin fluctuations requires a calculation of the full dynamic (rather than the static) response of an impurity, so the spin polarization $s(\vec{r},t)$ induced by a fluctuating spin should be calculated using the dynamic conduction electron response function $\chi_i(q,\omega_{sf})$, with $\omega_{sf} = k_B\theta/\hbar$, the LSF frequency.

The calculation is based on the following expression [32] for the spin polarization $s(\vec{r},t) = n^+(\vec{r},t) - n^-(\vec{r},t)$ induced at the point $\vec{r}$ at time t by the perturbing field $H(\vec{r}',t')$:

$$s(\vec{r},t) \propto \int d\vec{r}' \int dt' \sum_{\vec{q}} \int d\omega\, \chi_i(\vec{q},\omega)\, e^{i\vec{q}\cdot(\vec{r}-\vec{r}')}\, e^{-i\omega(t-t')}\, H(\vec{r}',t'). \quad (3.3\text{-}11)$$

The simplest representation for the field $H(\vec{r}',t')$ induced by a fluctuating spin at site $\vec{r}'$, interacting with the conduction electrons, is to take $H(\vec{r}',t')$ as sinusoidal in time (with frequency ω_{sf}) and well localized in space :

$$H(\vec{r}',t') = -J S_1\, e^{i\omega_{sf}t'}\, \delta(\vec{r}') \quad . \qquad (3.3\text{-}12)$$

Substituting this expression in Eq.(3.3-11) yields

$$s(\vec{r},t) \propto -J S_1\, e^{i\omega_{sf}t} \sum_{\vec{q}} \chi_i(\vec{q},\omega_{sf})\, e^{i\vec{q}\cdot\vec{r}} \qquad (3.3\text{-}13)$$

For a "static" local moment ($\omega_{sf} = 0$), Eq.(3.3-13) reduces to the conventional RKKY result [33].

If this time-dependent spin polarization $s(\vec{r},t)$ is now coupled to a second fluctuating spin at position $\vec{r}$, then, using the adiabatic approximation, one obtains for this coupling

$$H_{osc}(\vec{r},\omega_{sf}) \propto J^2 \vec{S}_1 \cdot \vec{S}_2 \, e^{i\delta} \sum_{\vec{q}} \chi_i(\vec{q},\omega_{sf}) \, e^{i\vec{q}\cdot\vec{r}} \cdot \lim_{b\to 0} \int_0^\infty e^{i(2\omega_{sf}+ib)t'} dt'$$

$$\propto J^2 \vec{S}_1 \cdot \vec{S}_2 \, \frac{e^{i\delta}}{\omega_{sf}} \sum_{\vec{q}} \chi_i(\vec{q},\omega_{sf}) \, e^{i\vec{q}\cdot\vec{r}} \quad , \qquad (3.3\text{-}14)$$

where δ is simply a phase factor which accounts for the fact that spin fluctuations at different sites are incoherent. If the precise form for $\chi_i(\vec{q},\omega_{sf})$ is neglected, then this rather crude calculation implies that the coupling represented by Eq.(3.3-14) *decreases* as the spin fluctuation frequency ω_{sf} (or LSF temperature θ) *increases*. This is a physically reasonable result in that, as $\omega_{sf} \to \infty$ (no localized magnetic moment), the RKKY-type coupling vanishes. It also allows a qualitative understanding of the decrease in the magnetic ordering temperature across the series *Au*Cr, *Pd*Cr, *Pt*Cr.

3.3.4 Low Temperature Incremental Resistivity of the Pd-8 and 10 at. % Cr Alloys

In Sec.3.3.2 it was shown that the high temperature incremental resistivities of the Pd-8 and 10 at. % Cr alloys were well represented by an expression of the form $\Delta\rho(T) = Ac + Bc\,\ell n(T^2 + \theta^2)^{\frac{1}{2}}$, with θ estimated at about 60K and 80K, respectively. However, at low temperatures, these two alloys undergo magnetic ordering. The low-temperature details of the incremental resistivities for the Pd-8 and 10 at. % Cr alloys are plotted in FIG.3.3-14, which indicates that $\Delta\rho(T)$ for both alloys passes through a rather broad maximum occurring at $T_{MAX} = 4 \pm 0.75K$ and $20 \pm 1K$, respectively. This type of behaviour is familiar in dilute alloys of first row transition metal impurities in noble metal hosts[34], and signals the onset of magnetic order induced by RKKY-type spin density oscillations [3] in the host's conduction band. However, the delay in the appearance of a resistivity maximum in PdCr until the Cr concentration has increased beyond about 7 at. % (and the absence of any such anomaly below 12 at. % Cr in PtCr) suggests that the effectiveness of long-range coupling via conventional RKKY oscillations is considerably reduced in spin-fluctuating systems like PdCr (and PtCr) and hence any magnetic ordering that does occur must, in addition to any RKKY coupling, result primarily from nearest-neighbour d-d overlap between impurities. According to Moriya [35], direct exchange between nearest-neighbour impurities with nearly half-filled d shells (like Cr)

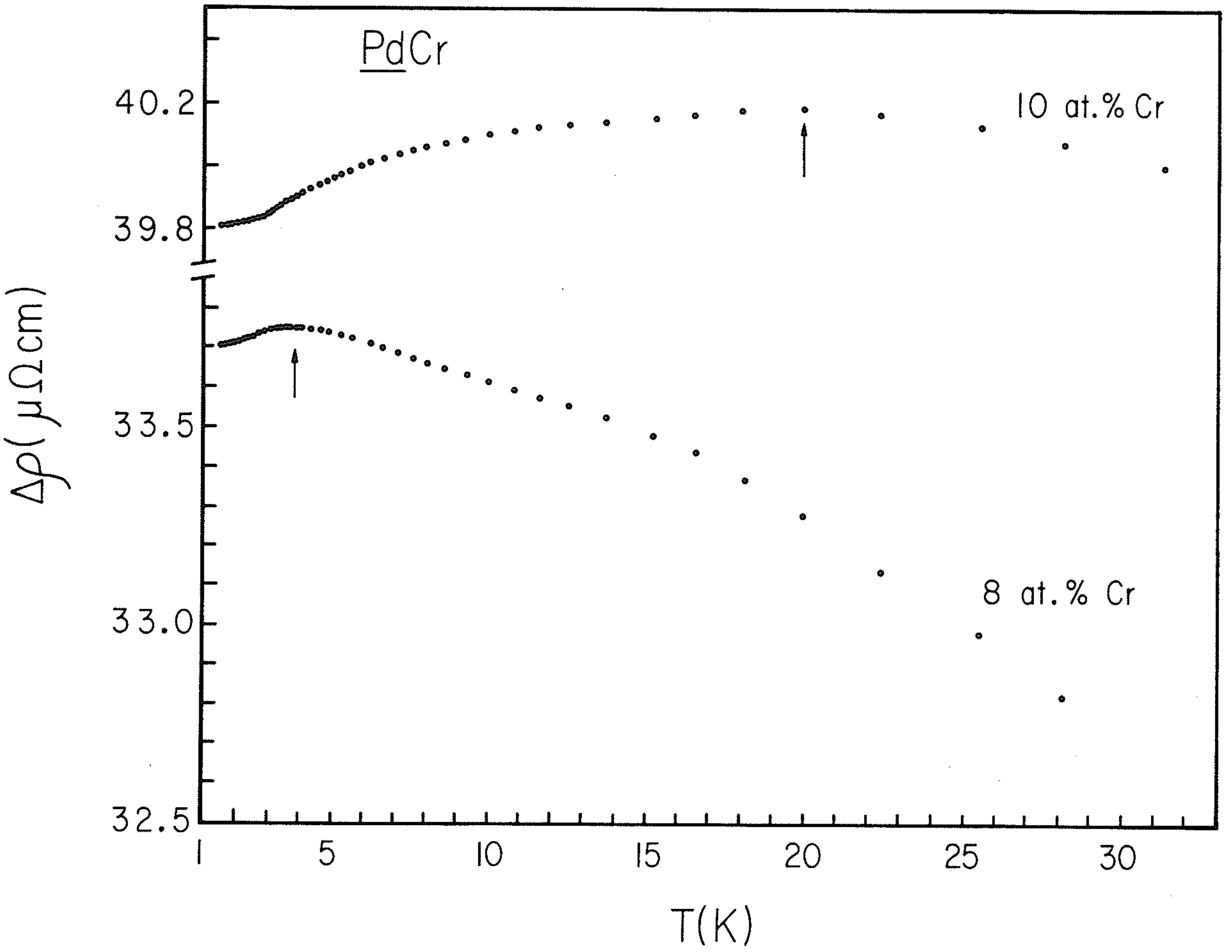

FIG.3.3-14. The incremental resistivities Δρ(T) of the Pd-8 and 10 at.% Cr alloys plotted against temperature between 1.4 and 30 K. The vertical arrows mark the estimated positions of the maxima.

in Pd favours antiparallel spin alignment, so that such a coupling should assist the "conventional" RKKY coupling to produce a "disordered" antiferromagnetic ground state [36]. The temperature T_{MAX} at which the maximum occurs is thus taken as the transition temperature to this spin glass-like ground state.

The first point of interest is that, for a given concentration, T_{MAX} occurs at a much lower temperature than, say, for Cr in Au [34]. In addition, the ratio $[\Delta\rho(T_{MAX}) - \Delta\rho(0)]/\Delta\rho(T_{MAX})$ is also rather small, as can be seen from Table 3.3-6. Using an effective mass treatment of s conduction electron-impurity moment scattering, the following expression can be derived [37] for the difference $\Delta\rho(T_{MAX}) - \Delta\rho(0)$:

$$\frac{\Delta\rho(T_{MAX}) - \Delta\rho(0)}{c} = \frac{3\pi m^*}{2\hbar e^2 E_F}\left(\frac{V}{N}\right) J^2 S \quad , \qquad (3.3\text{-}15)$$

where m^* is the conduction electron effective mass, E_F is the Fermi energy, and N/V is the number of atoms per unit volume. J is the appropriate averaged wavevector $(\vec{q})$-dependent effective exchange coupling [38, 39]; for resistivity it is strongly weighted around $|\vec{q}| = 2k_F$. S is the impurity spin. Using parameters appropriate to the Pd s band [40], the numerical factor on the right-hand side of Eq.(3.3-15) assumes the value 6.56 $\mu\Omega$ cm./$(\text{eV})^2$-at. % impurity [41]. Using a "free-ion" spin of 2 for Cr [42], and the differences $[\Delta\rho(T_{MAX}) - \Delta\rho(0)]\,c^{-1}$ listed in Table 3.3-6, estimates for $|J|$ can be

TABLE 3.3-6. Summary of various parameters for the Pd-8 and 10 at. % Cr alloys

ALLOY (at. % Cr)	T_{MAX} (K)	$\frac{\Delta\rho(T_{MAX})}{c}$ (μΩ cm./at. % Cr)	$\frac{\Delta\rho(0)}{c}$ (μΩ cm./at. % Cr)	$\frac{\Delta\rho(T_{MAX}) - \Delta\rho(0)}{\Delta\rho(T_{MAX})}$	$\lvert J_{LT}\rvert$ (eV)	$\lvert J_{HT}\rvert$ (eV)	$\langle S_{eff}\rangle^{*}_{T_{MAX}}$
8	4 ± 0.75	4.2190	4.2130	0.0014	0.022	0.27	0.013
10	20 ± 1	4.0195	3.9810	0.0096	0.054	0.27	0.08

* Based on a high-temperature spin of 2, and attributing the entire difference to a reduction in $\langle S_{eff}\rangle_{T_{MAX}}$; this is a lower limit.

obtained from Eq.(3.3-15). These are listed in Table 3.3-6 as $|J_{LT}|$.

In the same effective mass treatment, the coefficient B appearing in the expression $\Delta\rho(T) = Ac + Bc\,\ell n(T^2+\theta^2)^{\frac{1}{2}}$ is given by

$$B = \frac{3z}{E_F} J^3 S(S+1)\left[\frac{3\pi m^*}{2\hbar e^2 E_F}\left(\frac{V}{N}\right)\right] \quad , \qquad (3.3\text{-}16)$$

where z is the number of conduction electrons per atom (0.36 for Pd [40]). Using the same value for the numerical factor in square brackets as that used in Eq.(3.3-15) (with $E_F = 1.33$ eV, again from an effective mass treatment of the s band [41]) and with the values for B listed in Table 3.3-4, one obtains the values for J listed in Table 3.3-6 under $|J_{HT}|$(although, since B is negative, J must also be negative). The magnitudes deduced for the exchange coupling J at high (J_{HT}) and low (J_{LT}) temperatures thus appear to differ by at least a factor of 5. For other Pd- and Pt- based transition metal alloys showing similar effects to those observed here -- PdCo [43] and PtFe [44] -- such a procedure does not lead to substantially different values for J_{HT} and J_{LT}, provided that S is identified with the "on-site" impurity spin rather than the "giant moment" spin (on-site spin plus induced d-band polarization). For example, in PdCo, using an "on-site" spin of $S = 1$ [45] gives $J_{HT} = 0.140$ eV and $J_{LT} = 0.134$ eV, while for PtFe, $J_{HT} = 0.082$ eV and $J_{LT} = 0.061$ eV with $S = 1.5$ (as for Fe in Pd [45]). (In both systems, J_{LT} is obtained from the step height measured in a magnetic field, in which case Eq.(3.3-15) is appropriately modified by including an extra factor of $1+4S$ [37].

The apparent discrepancy between these values for J at high and at low temperatures derived from the PdCr resistivity data can possibly be accounted for by a more careful analysis of the relative values for the impurity spin S in Eqs.(3.3-15) and (3.3-16). The estimates for B used in Eq.(3.3-16) are obtained from fitting the experimental data to Eq.(3.3-1) over the temperature range $\theta \leq T \leq 300K$. At 300K the incremental resistivity is approaching its temperature-independent "plateau", and so the use of the "free-ion" spin in Eq.(3.3-16) appears to be justified (several properties of a number of systems exhibit free-spin behaviour at temperatures above θ [43, 44, 46, 47]). However, this is not the case in Eq.(3.3-15). Both resistivity maxima occur at temperatures $T_{MAX} \ll \theta$, and the effective impurity spin is thus expected to be reduced below its high-temperature value [44, 46, 48, 49] (this is in agreement with experimental observation [47, 50], and such effects are clearly demonstrated in the susceptibility of the closely related PtCr system [51]). It follows that values for the effective spin $\langle S_{eff} \rangle_{T_{MAX}}$ at the appropriate temperature T_{MAX} can thus be estimated by substituting into Eq.(3.3-15) the high-temperature values for J obtained from Eq.(3.3-16). These estimates are listed in Table 3.3-6 [52].

Attributing the entire discrepancy between the values for J to a reduction in $\langle S_{eff} \rangle_{T_{MAX}}$, results in an appreciable lowering of the effective-spin value below its high-temperature value. However, the result that $\left\langle S_{eff}(10 \text{ at.\% Cr})\right\rangle_{T_{MAX}} > \left\langle S_{eff}(8 \text{ at.\% Cr})\right\rangle_{T_{MAX}}$ follows the expected pattern. This approach also suggests that as the Cr concentration (and hence T_{MAX}) increases, $\left\langle S_{eff}\right\rangle_{T_{MAX}}$ should increase, tending to the high-temperature spin value when $T_{MAX} \geq \theta$.

3.3.5 Deviations from Matthiessen's Rule

Finally, the possibility of deviations from Matthiessen's rule, which are expected to occur at temperatures such that $\rho_{HOST}(T) \simeq \Delta\rho(T)$ [12], must be considered. An inspection of the incremental resistivity data in FIGS.3.3-3 to 3.3-9 reveals that this condition is approached as the temperature increases. However, even for the least concentrated alloys examined (Pd-4 at.% Cr and Pt-5 at.% Cr), and at the highest temperature attained in this experiment (300K), the condition is never actually satisfied. For example, for the Pd-4 at.% Cr alloy, $\Delta\rho(300K) \simeq 12.15\ \mu\Omega\,cm$. compared with $\rho_{Pd}(300K) = 10.8\ \mu\Omega\,cm$.. Similarly, for the Pt-5 at.% Cr alloy, $\Delta\rho(300K) \simeq 18.2\ \mu\Omega\,cm$. while $\rho_{Pt}(300K) = 9.8\ \mu\Omega\,cm$.. While Matthiessen's rule deviations are thus not expected to occur, the effect of fitting the data for the Pd-4 at.% Cr alloy over the range $20K \leq T \leq T_\alpha$, for T_α varying from 200K to 300K, has been investigated. While this procedure changes θ by up to 1.5K, it does not improve the rms deviation, nor does the calculated curve (using the appropriate best-fit parameters) pass below the high-temperature experimental data, as would be expected if Matthiessen's rule breakdown occurred. It is thus concluded that deviations from Matthiessen's rule are not an important consideration here.

3.3.6 Summary

Measurements of the electrical resistivity of several PdCr alloys containing between 4 and 10 at. % Cr, and several PtCr alloys containing between 5 and 12 at. % Cr, over the temperature range 1.4 to 300K, show that at "high" temperatures, the incremental resistivity, $\Delta\rho(T)$, for all the alloys is well represented by an expression of the form $\Delta\rho(T) = Ac + Bc\,\ell n(T^2 + \theta^2)^{\frac{1}{2}}$, with the characteristic temperature θ increasing with increasing Cr concentration in both systems. However, at low temperatures $(T < \theta)$, differences between the measured and predicted values for $\Delta\rho(T)$ begin to appear. In all the PtCr alloys examined, and in the PdCr alloys containing 4, 5, and 6 at. % Cr, the nature of these deviations is such that the measured values for $c^{-1}\Delta\rho(T < \theta)$ and $c^{-1}\, d[\Delta\rho(T << \theta)]/dT$ are significantly larger than the values predicted by the above expression, using the best-fit parameters from the high-temperature fits. Such behaviour can be attributed to the stabilization of spin fluctuations by interimpurity interactions. Moreover, the temperature at which the deviations occur can be approximately reproduced by calculating the nearest-neighbour-pair interaction energy using the Blandin-Caroli double-resonance coupling mechanism.

For the PdCr alloys containing 8 and 10 at.% Cr, magnetic "freezing" occurs at low temperatures, as evidenced by the presence of resistivity maxima (at 4K and 20K, respectively). However, the delay in the onset of magnetic order in PdCr until the Cr concentration is increased beyond about 7 or 8 at.% , coupled with the absence of magnetic ordering above 1.4K in PtCr, even in the Pt-12 at.% Cr alloy, suggests that the effectiveness of long-range coupling via RKKY oscillations is considerably reduced in systems like PtCr and PdCr, and hence any magnetic ordering which does occur is due primarily to near-neighbour d-d overlap.

3.4 An Investigation of Magnetic "Freezing" in PdCr Via Electrical Resistivity Measurements

The analysis of the PdCr data in Sec.3.3 revealed the presence of a broad maximum in the incremental resistivities, $\Delta\rho(T)$, of both the 8 and 10 at. % Cr alloys. This type of behaviour is familiar in dilute alloys of first row transition metal impurities in noble metal hosts [34], and signals the onset of magnetic order resulting from an indirect coupling between impurities, via RKKY spin-density oscillations in the host's conduction band. However, the delay in the appearance of a resistivity maximum in PdCr until the Cr content has increased beyond 7 at. %, suggests that the conventional long-range RKKY coupling is ineffective in this system. Hence, any magnetic ordering that does occur is probably due primarily to near-neighbour d-d overlap between Cr impurities. However, the structure of the ordered ground state resulting from such interactions is currently not well understood, i.e., is PdCr a spin glass? Although much theoretical and experimental effort has been expended in studying the properties of spin glasses, the most significant portion of this work has concentrated on systems in which the characteristic single-impurity energies (k_BT_{sf} or k_BT_K) are well below typical spin-glass "freezing" temperatures. In the PdCr system this is not the case, and the attendant effect on the ground state is unclear. In this section, the electrical resistivity of several PdCr alloys containing between 11 and 18 at. % Cr is examined, between 1.4 and 300K, in order to provide a comparison between the behaviour of PdCr and that of canonical spin glasses (AuFe, CuMn, and so on).

3.4.1 General Features of the Resistivity

In FIG.3.4-1, the measured resistivities, $\rho(T)$, of the five PdCr alloys are plotted as a function of temperature between 1.4 and 300K. The resistivity of the Pd-11 at. % Cr alloy possesses a weak local minimum around 55K (actually a minimum in the slope, $d\rho/dT$, rather than zero slope), below which a broad maximum appears in the temperature range 30-35K. This structure becomes less pronounced as the Cr concentration increases, with the resistivity of the most concentrated alloy examined (Pd-18 at. % Cr) increasing monotonically with increasing temperature above 4.2K. Below 4.2K, however, the two most concentrated alloys containing 16 and 18 at. % Cr exhibit a very weak minimum, the position and depth of which increase with increasing Cr concentration, as shown in FIG.3.4-2. Table 3.4-1 lists various characteristic features of the resistivity of PdCr alloys containing between 4 and 18 at. % Cr, the range 4 to 10 at. % Cr having been covered in detail in Sec.3.3. The incremental resistivities, $\Delta\rho(T)$, are shown in FIG.3.4-3; below 4.2K, weak minima are observed in the incremental resistivities of the Pd-16 and 18 at. % Cr alloys, as outlined above. Above 4.2K, $\Delta\rho(T)$ initially increases faster than T with increasing temperature,

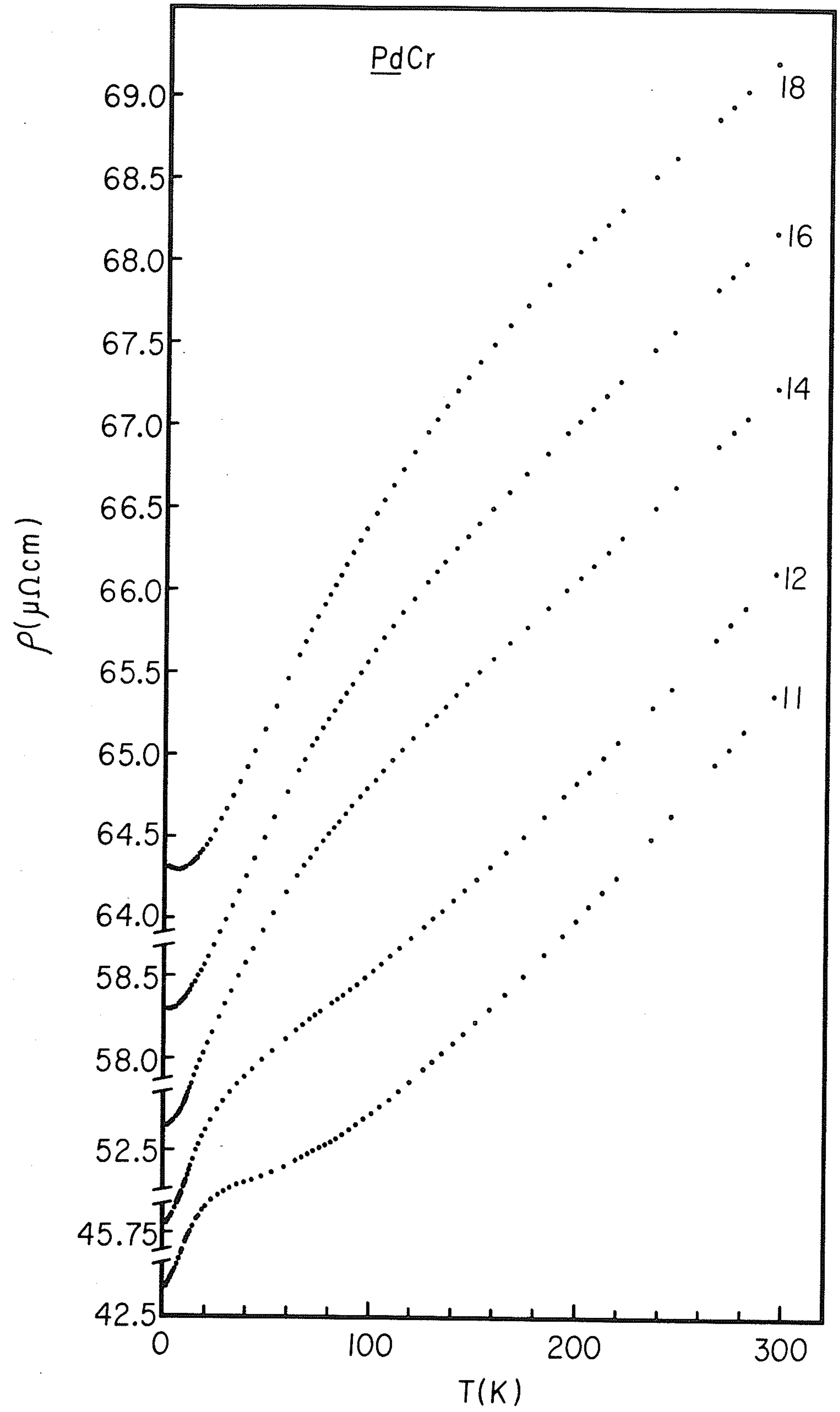

FIG.3.4-1. The measured resistivities ρ(T) of the Pd-11, 12, 14, 16, and 18 at.% Cr alloys plotted against temperature T between 1.4 and 300K.

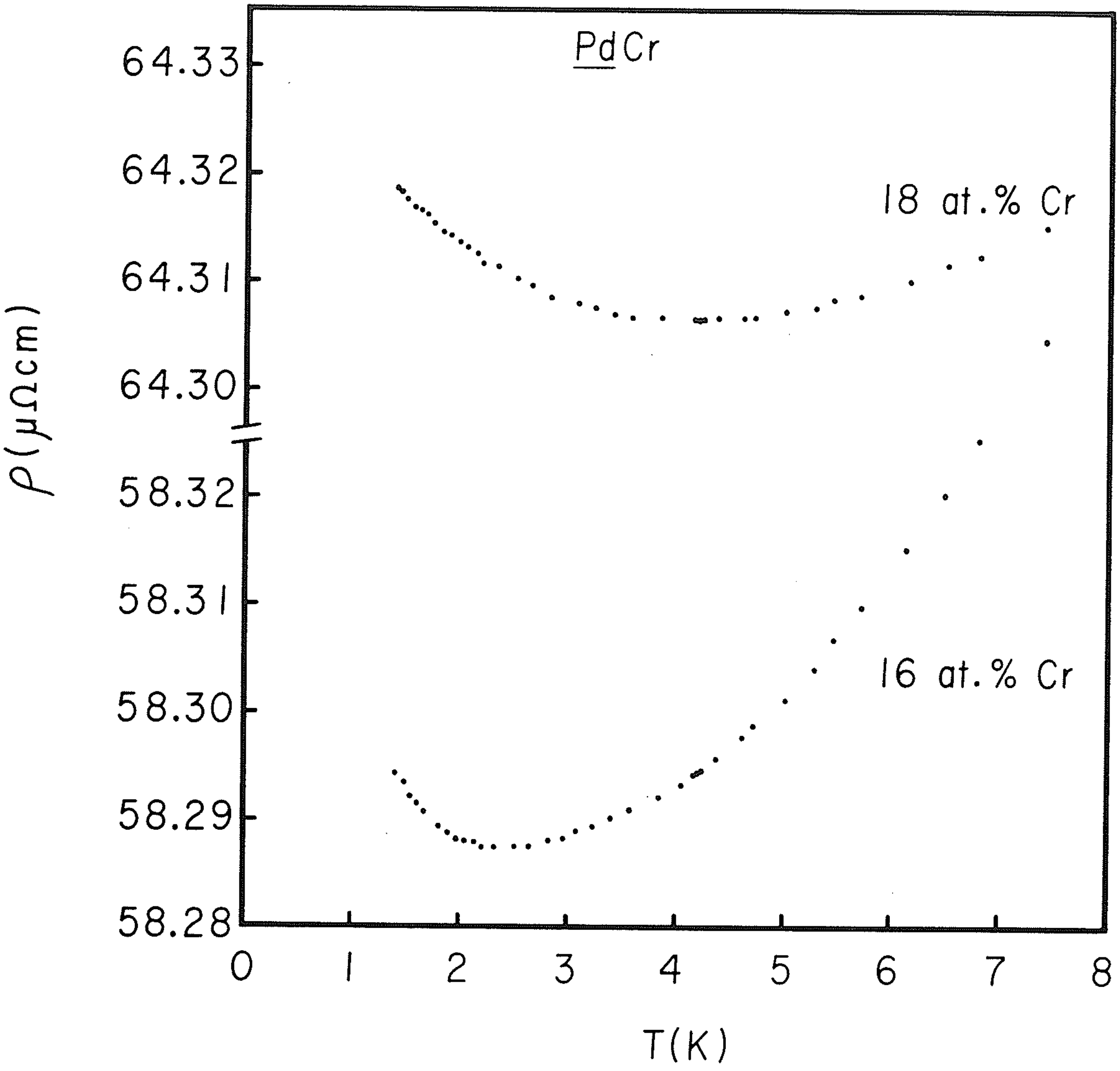

FIG.3.4-2. The resistivities of the two most concentrated alloys examined, showing details of the resistivity minima below 8K.

TABLE 3.4-1. Summary of the resistivity data

Concentration (at. % Cr)	4	5	6	8	10	11	12	14	16	18
Temperature of the minimum in $\rho(T)$ (K)	65	70	75	75 - 80	55*	55*	---	---	---	---
Temperature of the maximum in $\rho(T)$ (K)	---	---	---	4 ± 0.5	21 ± 1	30 - 35*	---	---	---	---
Temperature of the inflection point in $\rho(T)$ (K)	---	---	---	2.5 ± 0.75	4 ± 1.5	6 ± 2.5	9 ± 3	16 ± 3	30 ± 5	50 ± 7

* Local, not absolute

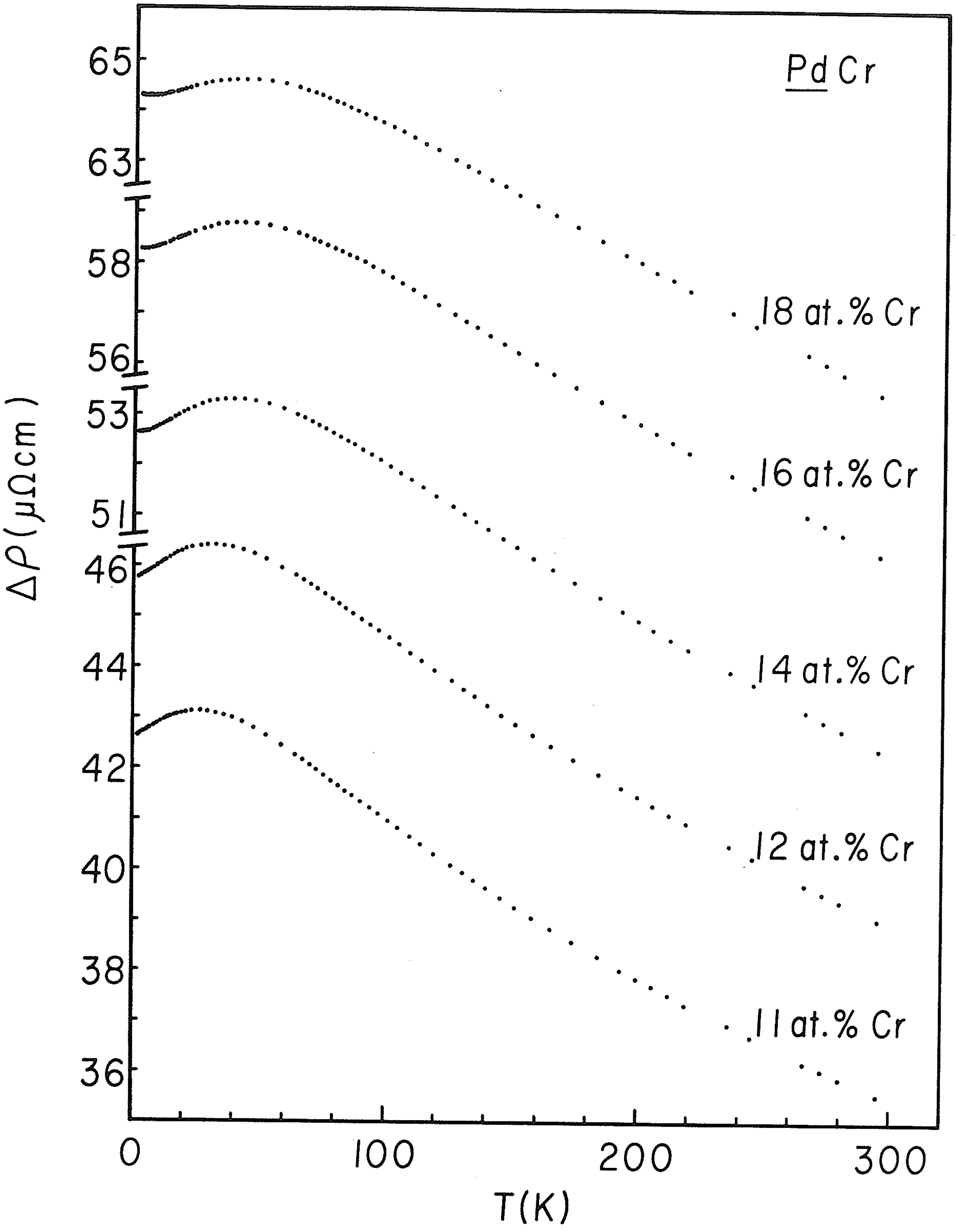

FIG.3.4-3. The incremental resistivities $\Delta\rho(T)$ of the Pd-11, 12, 14, 16, and 18 at. % Cr alloys plotted against temperature from 1.4 to 300K.

TABLE 3.4-2. Incremental resistivity data

Concentration (at. % Cr)	$\Delta\rho(T = 0)$ ($\mu\Omega$ cm.)	T_{MAX} (K)	$\Delta\rho(T_{MAX})$ ($\mu\Omega$ cm.)	Inflection point T_{INFL} (K)
4	20.09 ± 0.03	---		
5	24.80 ± 0.03	---		
6	28.07 ± 0.03	---		
8	34.12 ± 0.03	4 ± 1	34.17	2.5 ± 0.75
10	40.21 ± 0.03	20 ± 1.5	40.60	4 ± 1.5
11	42.63 ± 0.03	25 ± 1.5	43.11	9 ± 2
12	45.77 ± 0.03	31.5 ± 1.5	46.40	12 ± 3
14	52.61 ± 0.03	39 ± 1.5	53.30	17 ± 4
16	58.27 ± 0.03	41.5 ± 1.5	58.77	19 ± 4
18	64.30 ± 0.03	43 ± 1.5	64.61	25 ± 4.5

then passes through an inflection point (at temperature T_{INFL}) and a maximum (at temperature T_{MAX}), above which it decreases with increasing temperature. The estimated values for both T_{INFL} and T_{MAX} are listed in Table 3.4-2 for each alloy.

3.4.2 Behaviour of T_{MAX} and $\Delta\rho(T_{MAX}) - \Delta\rho(0)$

The behaviour described above is typical of the onset of magnetic freezing in many dilute alloy systems [53], although T_{MAX} for PdCr is roughly an order of magnitude smaller than that associated with archetypal spin glass systems (Fe, Cr or Mn in Ag or Au). However T_{MAX} is comparable with the corresponding temperature in PtMn alloys [54] of similar concentration (in this system, however, the behaviour of $\Delta\rho(T)$ is inverted with respect to the usual spin glasses, and thus the appropriate temperature in PtMn is that of the minimum). Various concentration dependences for T_{MAX} have been observed; in the noble-metal-based spin glasses, T_{MAX} is found to be approximately proportional to $c^{\frac{1}{2}}$ [53]; in PtMn, below 12 at. % Mn, "T_{MAX}" (actually T_{MIN}) is proportional to c (above 12 at. % Mn, the resistivity, $\rho(T)$, increases monotonically with increasing temperature [54] and the inflection point in $\rho(T)$ falls on an extrapolation of the "T_{MAX}" - vs - c line for the more dilute alloys). The behaviour of T_{MAX} in PdCr is shown in FIG.3.4-4. From this figure, it can be seen that

$$T_{MAX} \propto c - c_0 \quad , \qquad (3.4\text{-}1)$$

with $c_0 \simeq 7$ at. % Cr. As in PtMn a distinct reduction in the rate at

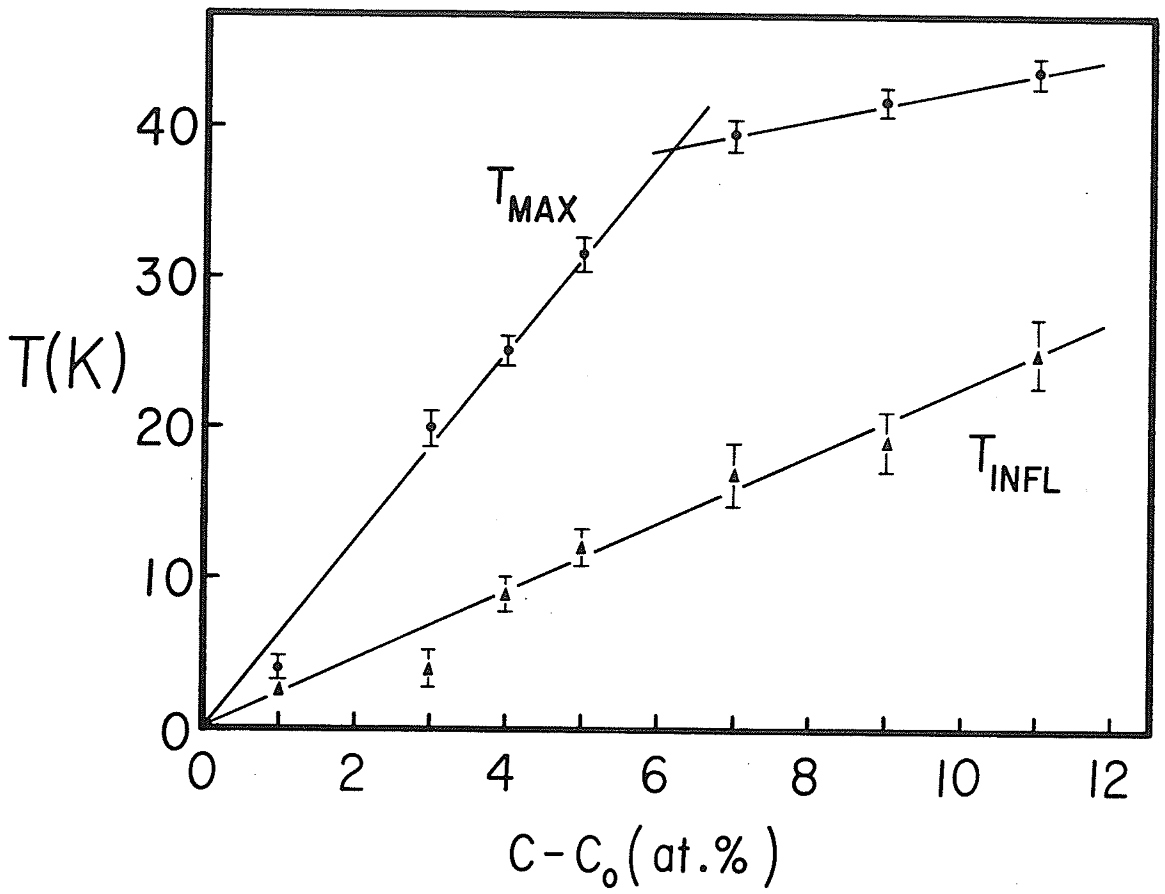

FIG.3.4-4. Plots of the temperature T_{MAX} (in K) at which the incremental resistivity displays a maximum, and the temperature T_{INFL} (in K), the estimated position of the inflection point in $\Delta\rho(T)$, against the reduced concentration $c - c_0$ (in at. %).

which T_{MAX} increases with increasing concentration occurs at around 13 at. % impurity, but unlike the PtMn system, the inflection points in $\rho(T)$ for PdCr (listed in Table 3.4-1) do not lie on an extrapolation of the T_{MAX}-vs-c curve for the less concentrated alloys.

It is also interesting to compare the difference, $\Delta\rho(T_{MAX}) - \Delta\rho(0)$, in PdCr with its value in canonical spin glass systems. As the data in Table 3.4-2 shows, not only is this difference a strongly nonlinear function of Cr concentration, but it is also up to an order of magnitude smaller in PdCr (0.4 μΩ cm for 10 at. % Cr in Pd) than in archetypal spin glasses (4 μΩ cm for 10 at. % Fe in Au).

3.4.3 Behaviour of $\Delta\rho(T)$ below T_{MAX}

Recent investigations [53] of noble-metal-based spin glasses have identified the spin "freezing" temperature, T_0, as the temperature at which the derivative $d[\Delta\rho(T)]/dT$ exhibits a maximum. (This estimate for the freezing temperature is in rough agreement with the temperature of the cusp in the low-field susceptibility.) FIG.3.4-5 shows the details of the incremental resistivities, $\Delta\rho(T)$, below T_{MAX}, in order to allow further comparison with the behaviour of archetypal spin glasses. The vertical arrows in this figure mark the estimated inflection points (T_{INFL}) in $\Delta\rho(T)$ for the various alloys. The rapid increase in $\Delta\rho(T)$ with increasing temperature above 4.2K is clearly visible in this figure. However, unlike canonical spin glasses, $\Delta\rho(T)$ is linear only

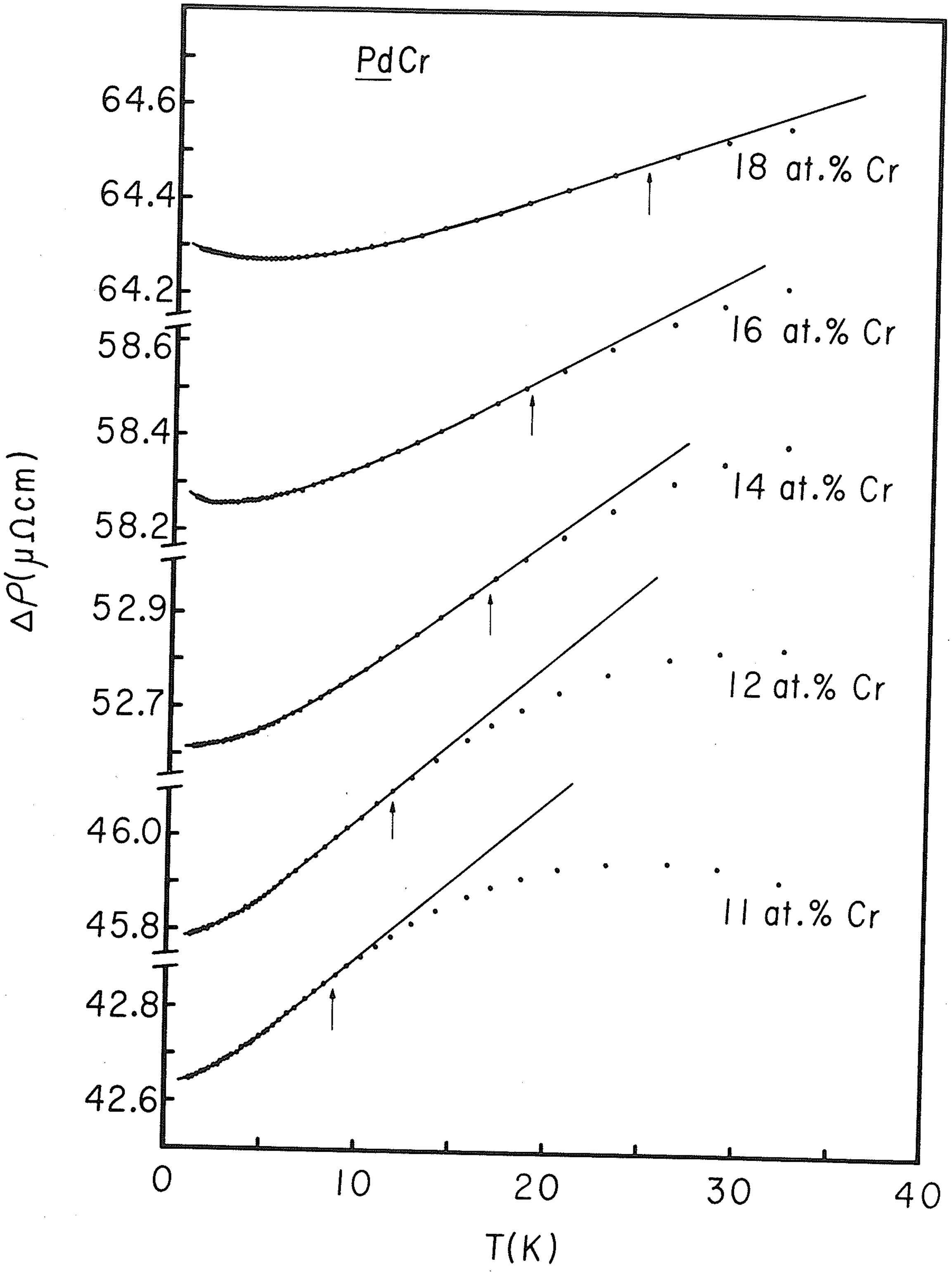

FIG.3.4-5. Details of the incremental resistivity $\Delta\rho(T)$ at temperatures below T_{MAX}. The vertical arrows mark the estimated inflection points (T_{INFL}) in $\Delta\rho(T)$.

over a small temperature range around T_{INFL}. Such a difference may simply arise from the compressed temperature scale over which spin glass-like behaviour is observed in PdCr, as compared with canonical spin glass systems. The estimates for T_{INFL} are plotted as a function of Cr concentration in FIG.3.4-4, from which it follows that

$$T_{INFL} \propto c - c_0 \tag{3.4-2}$$

over the concentration range 8 to 18 at. % Cr, with $c_0 \simeq 7$ at. % Cr.

One of the characteristic features of spin glass ordering is the presence of a $T^{3/2}$ term in the incremental resistivity, $\Delta\rho(T)$, at temperatures below T_{INFL}, with the coefficient, A, of this term varying only weakly with impurity concentration ($A \propto -\log_{10} c$ or $c^{-1/5}$). The origin of this term in such systems is currently attributed [55] to the inelastic scattering of conduction electrons from the low-temperature elementary excitations of the spin glass (known as spin-diffusion modes). FIG.3.4-6 summarizes the results of a $\Delta\rho(T)$ vs $T^{3/2}$ plot for the PdCr alloys examined here. From this figure, it can be seen that, for the Pd-11 and 12 at. % Cr samples, $\Delta\rho(T)$ does indeed vary as $T^{3/2}$, down to the lowest temperatures attained in this investigation. In the Pd-14 at. % Cr alloy, deviations away from $T^{3/2}$ (towards T^2) are observed, thus resembling the behaviour reported for comparable amounts of Cr in Au [53, 56], and smaller amounts of Mn in Cu [57]. For the Pd-16 and 18 at. % Cr alloys, the presence of the weak minimum in the

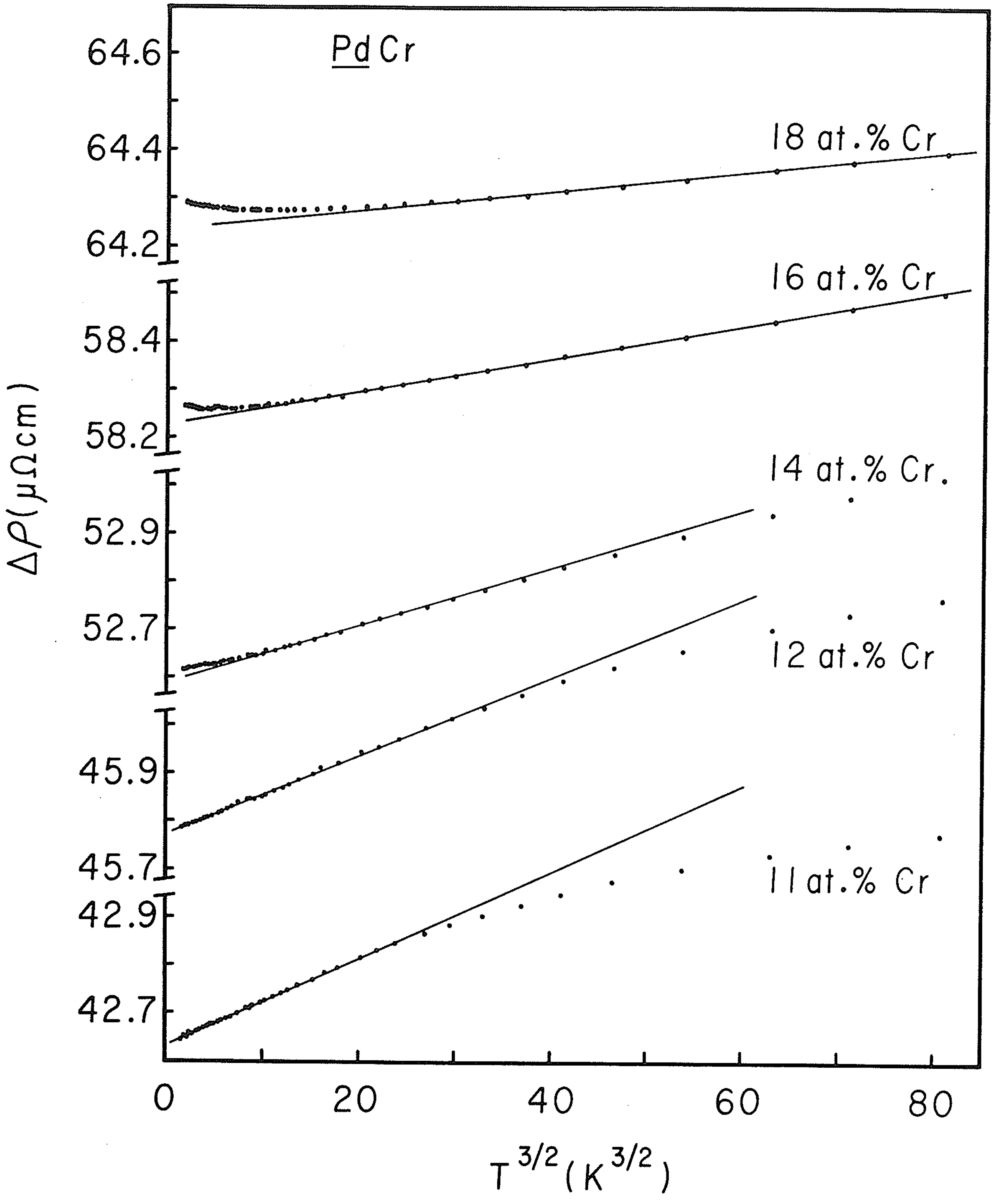

FIG.3.4-6. Plots of the incremental resistivity $\Delta\rho(T)$ against $T^{3/2}$.

TABLE 3.4-3. Incremental resistivity data below T_{MAX}

Concentration (at. % Cr)	8	10	11	12	14	16	18
A (nΩ cm./$K^{3/2}$)	---	---	9.07 ± 0.15	8.38 ± 0.15	5.94 ± 0.15	3.50 ± 0.15	2.05 ± 0.15
T_1 (K)	---	---	8 ± 1	8 ± 1	8.5 ± 1	13.3 ± 1	17.5 ± 1
$\Delta\rho(T_{INFL})$ (μΩ cm.)	34.16	40.30	42.86	46.08	52.97	58.51	64.48

incremental resistivity below 4K rules out the possibility of a limiting ($T \rightarrow 0$) $T^{3/2}$ temperature dependence. However, at temperatures above the minima, $\Delta\rho(T)$ does follow a $T^{3/2}$ dependence over a substantial temperature range. Table 3.4-3 contains a list of the coefficients A, estimated from the data in FIG.3.4-6, along with the temperature T_1 above which the incremental resistivity, $\Delta\rho(T)$, departs from the initial $T^{3/2}$ law. FIG.3.4-7 shows that the coefficient A exhibits a $-\log_{10}c$ concentration dependence as in canonical spin glasses. (The concentration range covered by the present investigation is very much smaller than that covered in canonical spin glasses, especially when expressed on a logarithmic scale; however, this is due to the fact that PdCr does not order below 7 at.% Cr, and consequently exhibits a measureable $T^{3/2}$ term only above about 10 at.% Cr.) In PdCr, the $T^{3/2}$ coefficient, A, exhibits a concentration dependence (36 nΩ cm/$K^{3/2}$ per decade of concentration) which is an order of magnitude larger than in AuFe (3 nΩ cms/$K^{3/2}$ per decade). However, this type of behaviour is not unreasonable, since there appears to be an inverse correlation [53] between A and T_1 (T_1, T_{INFL}, and T_{MAX} are all much smaller in PdCr than in canonical spin glasses).

One possible mechanism which can account for the $T^{3/2}$ to T^2 transition observed in the low temperature incremental resistivity of the Pd-14 at.% Cr alloy is the removal of the slowest spin-diffusion modes from the elementary excitation spectrum of the spin glass (possibly due to conduction electron mean-free-path limitations as the impurity

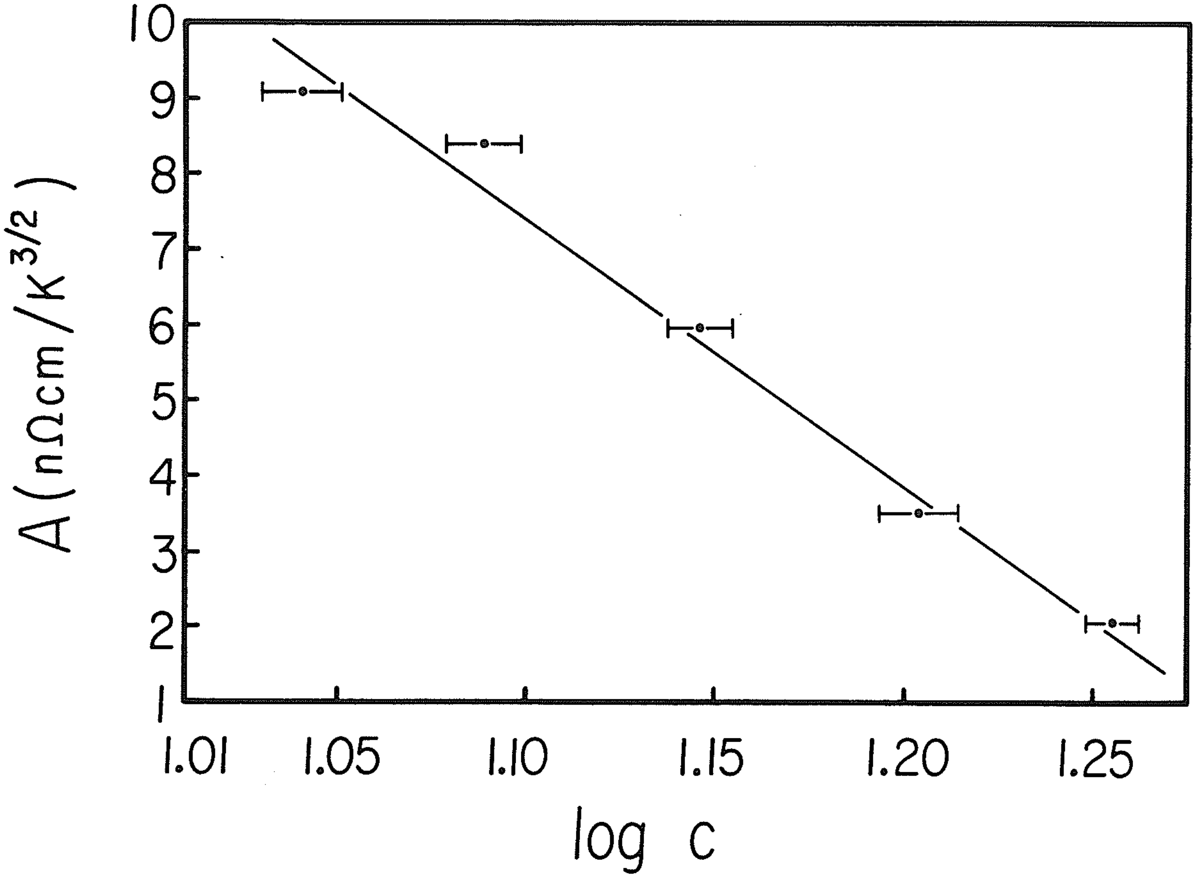

FIG.3.4-7. The coefficient A of the $T^{3/2}$ term (in $n\Omega$ cm./$K^{3/2}$) plotted against $\log_{10} c$.

content increases), as suggested [55] for CuMn and AuCr. Such an approach, however, does not seem capable of explaining the presence of resistivity minima at slightly higher Cr concentrations in both the present system and in AuCr [58]. The presence of weak minima at low temperatures (often below the magnetic ordering temperature) in reasonably concentrated alloys is not confined to the two systems mentioned above (AuCr and PdCr). Such minima have also been observed in PdNi [59], PdAg [60], and PtCo [61]. Moreover, the concentration and temperature range over which these minima occur, coupled with the magnetic field independence [11] of the minima in PdCr, seems to suggest that they do not arise from inelastic spin-flip scattering mechanisms. However, a crystalline analog of the recently proposed [62] structural source for minima of nonmagnetic origin in amorphous conductors provides a possible alternative explanation.

3.4.4 Numerical Tests for Spin Glass Behaviour

Theoretical investigations of the electrical properties of spin glasses have been confined to "good moment" systems, where T_K or $T_{sf} \ll T_{INFL}$. For these systems, two spin glass consistency tests have been suggested [55], and these tests were applied to the PdCr resistivity data presented here, in spite of the fact that PdCr (with $T_{sf} \sim T_{INFL}$) is not a good moment system. The first test is :

$$T_{INFL} = 2.23\ T_1 \quad . \qquad (3.4\text{-}3)$$

An inspection of the data in Tables 3.4-2 and 3.4-3 shows that, while the ratio T_{INFL}/T_1 is roughly constant in <u>Pd</u>Cr, its magnitude (~1.5) is less than that predicted by Eq.(3.4-3). However, this discrepancy between the observed and predicted values for T_{INFL}/T_1 is no greater in <u>Pd</u>Cr than in canonical spin glasses [53]. The second test is :

$$[\Delta\rho(T_{INFL}) - \Delta\rho(0)] = \frac{1}{6}[\Delta\rho(\infty) - \Delta\rho(0)] \quad . \qquad (3.4\text{-}4)$$

This test is more difficult to implement than the first. While $\Delta\rho(T_{INFL}) - \Delta\rho(0)$ is easily extracted from the experimental data, $\Delta\rho(\infty) - \Delta\rho(0)$ is not. Even in good moment systems (T_K, $T_{sf} << T_{INFL}$), the logarithmic nature of single-impurity scattering of conduction electrons (i.e., the Kondo effect) produces a resistivity maximum at high temperatures (T_{MAX}) by depressing the resistivity below its temperature-independent spin disorder plateau [37]. (This effect is observed even when the temperature at which the spin disorder plateau is attained is several orders of magnitude larger than the single-impurity characteristic temperature, T_K or T_{sf}.) This leads to considerable uncertainty in estimating $\Delta\rho(\infty) - \Delta\rho(0)$ [55], but such uncertainties are substantially greater in systems where $T_{sf} \sim T_{INFL}$, when the high-temperature slopes are up to an order of magnitude larger than in canonical spin glasses (see Table 3.4-2 and the data in Ref.53). As a result, Eq.(3.4-4) has been used to "predict" $\Delta\rho(\infty) - \Delta\rho(0)$ in the present system, using the measured values for $\Delta\rho(T_{INFL})$ and $\Delta\rho(0)$ listed

TABLE 3.4-4. Estimates for $\Delta\rho(\infty) - \Delta\rho(0)$ for PdCr

ALLOY (at. % Cr)	$\Delta\rho(\infty) - \Delta\rho(0) = 6[\Delta\rho(T_{INFL}) - \Delta\rho(0)]$ ($\mu\Omega$ cm.)
8	0.24
10	0.54
11	1.38
12	1.86
14	2.16
16	1.44
18	1.08

in Tables 3.4-2 and 3.4-3. In canonical spin glasses, the difference $\Delta\rho(\infty) - \Delta\rho(0)$ is observed to vary monotonically with increasing concentration (although the precise concentration dependence can be complicated [55]). However, an inspection of Table 3.4-4 shows that this is not the case for PdCr, with $\Delta\rho(\infty) - \Delta\rho(0)$ initially increasing with increasing Cr concentration up to 14 at. % Cr, and then decreasing with the further addition of Cr. Even if an attempt is made to correct for the presence of the weak minima in the more concentrated alloys by taking $\Delta\rho(0)$ as the incremental resistivity found by extrapolating the $T^{3/2}$ dependence to $T = 0$, the "predicted" values for $\Delta\rho(\infty) - \Delta\rho(0)$ behave in exactly the same way. No comparable effect has been observed in canonical spin glasses. As mentioned above, the most likely explanation for such differences is the significantly larger value of T_{sf} in PdCr.

3.4.5 Summary and Conclusions

The electrical resistivity of PdCr alloys containing between 10 and 18 at. % Cr exhibits several features which resemble those of archetypal noble-metal-based spin glasses : (i) the incremental resistivity, $\Delta\rho(T)$, exhibits a $T^{3/2}$ temperature dependence at low temperatures, the coefficient, A, of which varies as $-\log_{10}c$ over the concentration range examined. (ii) The range of validity ($T < T_1$) of this $T^{3/2}$ dependence correlates inversely with A, being small in PdCr where A is comparatively large. (iii) At higher temperatures, $\Delta\rho(T)$ passes through an inflection point (at T_{INFL}), and then a maximum (at T_{MAX}), above which it falls off with increasing temperature. (iv) The ratio T_{INFL}/T_1 is roughly constant over the concentration range examined, as predicted by recent spin glass theories, although, as in canonical spin glasses, its magnitude is smaller than the theoretical estimate. (v) In the more concentrated PdCr alloys, deviations from the $T^{3/2}$ law begin to appear at the lowest temperatures. In fact, weak minima (which are suspected to be of nonmagnetic origin) occur in the resistivities of the most concentrated alloys examined (Pd-16 and 18 at.% Cr). Such minima have been observed in a variety of reasonably concentrated alloys, including spin glasses.

The most striking differences between PdCr and canonical spin glasses arise from quantitative comparisons : (vi) Both the temperature, T_{MAX}, at which the maximum in $\Delta\rho(T)$ occurs, and the difference $\Delta\rho(T_{MAX}) - \Delta\rho(0)$, are nearly an order of magnitude smaller in PdCr than in archetypal spin glasses of comparable concentration. (vii) However, the slope of the incremental resistivity above T_{MAX} is nearly an order of magnitude larger in PdCr than in canonical spin glasses. These quantitative differences probably arise from the fact that canonical spin glasses have T_K or $T_{sf} << T_{INFL}$, whereas in PdCr, $T_{sf} \sim T_{INFL}$. Point (vii) above provides strong support for such an argument, since, even in "good moment" systems, the logarithmic nature of conduction-electron-single-impurity scattering (the Kondo effect) depresses the high-temperature resistivity below its spin disorder plateau, in spite of the fact that this plateau is reached at temperatures several orders of magnitude above T_K. With T_K(or T_{sf}) $\sim T_{INFL}$, such effects are expected to be more pronounced, and this is indeed observed.

3.5 Electrical Resistivity and Magnetic Susceptibility of PtCr Near the Percolation Limit

The analysis of the PtCr resistivity data in Sec.3.3 showed that, in spite of the absence of a resistivity maximum in all of the alloys examined (5 to 12 at. % Cr), a trend towards magnetic order (in the form of a decrease in the value of $\Delta\rho(1.5K) - \Delta\rho(4.2K)$) is beginning to appear in the PtCr system above about 10 at. % Cr. As pointed out, the delay in the appearance of this trend until the Cr content has increased beyond 10 at. %, and the absence of a resistivity maximum below 12 at. % Cr, suggests that the conventional RKKY coupling is ineffective in this system, and hence any magnetic ordering that does occur is produced primarily by nearest-neighbour d-d overlap between Cr impurities. In this section, the electrical resistivity and A.C. susceptibility of several PtCr alloys containing between 13 and 21 at. % Cr are examined over the temperature range 1.4 to 300K in order to determine whether the ordered ground state resulting from such direct overlap is similar to that occurring in spin glasses. In the PtCr system, the situation is further complicated by the presence of an atomic order-disorder transformation [63] which occurs above about 18.5 at. % Cr. Such structural changes can affect the magnetic behaviour of the Cr impurities by modifying the local environment around each Cr impurity.

3.5.1 Features of the Resistivity

FIG.3.5-1 shows the measured resistivities, $\rho(T)$, of six PtCr alloys containing between 13 and 18 at.% Cr, plotted as a function of temperature from 1.5 to 300K. Table 3.5-1 contains a list of various characteristic parameters extracted from these resistivity plots. All of the alloys shown in FIG.3.5-1 were given identical heat treatments : a 24-hour anneal at 610°C in a vacuum of 10^{-6} Torr. Furthermore, X-ray diffraction measurements revealed an FCC structure for all the alloys, with no evidence of superlattice lines.

Starting from the low-temperature regime, for all the alloys shown in FIG.3.5-1, $\rho(T)$ initially decreases with increasing temperature, passes through a resistivity minimum, and then increases with increasing temperature. In the concentration range from 13 to 18 at.% Cr, the temperature T_{MIN} at which this minimum occurs decreases with increasing Cr content from 38K for 13 at.% Cr to 10K for 18 at.% Cr (see Table 3.5-1). The concentration dependence of T_{MIN} in PtCr thus mirrors that observed in PdCr, initially increasing with increasing Cr content, reaching a maximum (at around 10 at.% Cr in Pt), and then decreasing with the further addition of Cr [11, 64]. However, in the PdCr system, when the Cr concentration is increased beyond that value for which T_{MIN} is a maximum, a further anomaly is observed at temperatures well below T_{MIN} in the form of a rapid drop in $\rho(T)$ with decreasing temperature, which translates into a maximum in the incremental resistivity $\Delta\rho(T)$.

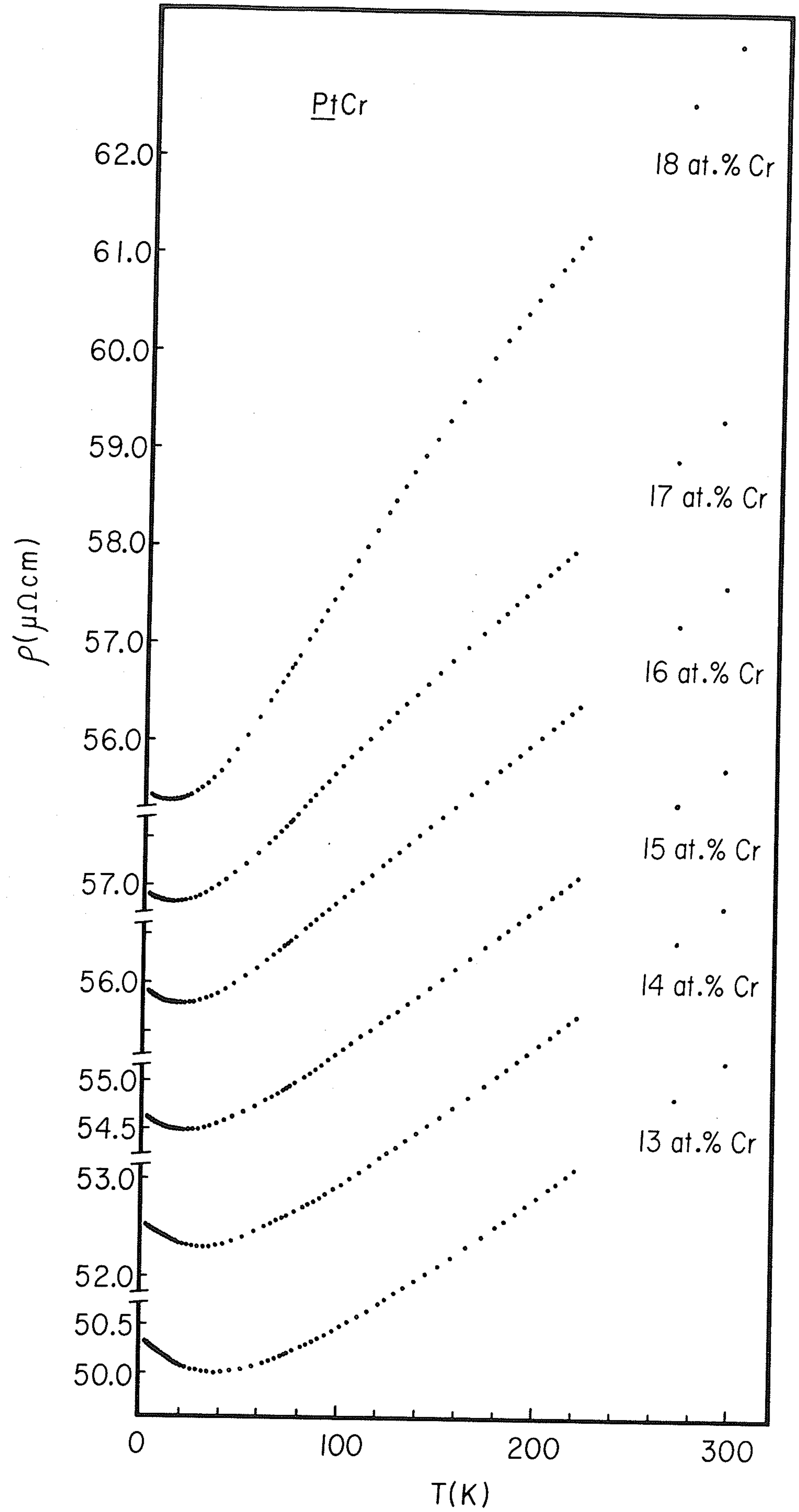

FIG.3.5-1. The measured resistivities ρ(T) of the Pt-13, 14, 15, 16, 17, and 18 at.% Cr alloys plotted against temperature between 1.5 and 300K.

TABLE 3.5-1. Characteristic features of the alloy resistivities.

Cr concentration (at. %)	13	14	15	16	17	18
$\rho(T = 300K)$ ($\mu\Omega$ cm.)	53.28	55.90	58.32	60.16	61.68	63.19
$\rho(T = 4.2K)$ ($\mu\Omega$ cm.)	50.29	52.49	54.59	55.88	56.87	55.39
$\rho(T = 1.5K)$ ($\mu\Omega$ cm.)	50.34	52.53	54.63	55.92	56.90	55.41
T_{MIN} (K)	38 ± 3	31 ± 3	20 ± 2	18 ± 2	14 ± 2	10 ± 2
$\rho(T_{MIN})$ ($\mu\Omega$ cm.)	50.03	52.32	54.51	55.81	56.79	55.37
T_{INFL} (K)	---	---	---	---	50 ± 20	70 ± 20
High-temperature slope($T > 200K$) ($\mu\Omega$ cm. K^{-1}) x 10^2	1.45 ± 0.01	1.49 ± 0.01	1.50 ± 0.01	1.64 ± 0.01	1.70 ± 0.01	2.56 ± 0.01
$\rho(1.5K) - \rho(4.2K)$ ($\mu\Omega$ cm.)	0.05	0.04	0.04	0.04	0.03	0.02
$\rho(1.5K) - \rho(T_{MIN})$ ($\mu\Omega$ cm.)	0.31	0.21	0.12	0.11	0.11	0.04
$\rho(300K) - \rho(T_{MIN})$ ($\mu\Omega$ cm.)	3.25	3.58	3.81	4.35	4.89	7.82
T_0 (K) (A.C. susceptibility)	---	---	---	---	26 ± 2	37 ± 2

As the data in FIG.3.5-1 shows, no such drop in $\rho(T)$ at temperatures below T_{MIN} is observed in any of the six Pt<u>Cr</u> alloys containing between 13 and 18 at. % Cr, in spite of the fact that T_{MIN} clearly decreases with increasing Cr concentration in this range. Furthermore, an inspection of FIGS.3.5-2 and 3.5-3, in which the incremental resistivities $\Delta\rho(T) = \rho_{ALLOY}(T) - \rho_{Pt}(T)$ are plotted as a function of temperature, shows the absence of a maximum in $\Delta\rho(T)$, even for 18 at. % Cr in Pt (a detailed plot of $\Delta\rho(T)$ at low temperatures is included at the top of FIG.3.5-3 in order to emphasize this point). In spite of this last result, it is apparent from FIG.3.5-1 that the behaviour of the four more dilute samples (13 to 16 at. % Cr) differs in many respects from that of the two more concentrated alloys (17 and 18 at. % Cr), both above and below T_{MIN}.

For example, at temperatures well below T_{MIN}, the low temperature slope $\left.\frac{d\rho}{dT}\right|_{T\to 0}$ (represented by the difference $\rho(1.5K) - \rho(4.2K)$ in Table 3.5-1) is about twice as large for the 13 to 16 at. % Cr alloys as it is for the 17 and 18 at. % Cr samples. However, it is at temperatures <u>above</u> T_{MIN} that the differences become most pronounced. As FIG.3.5-1 shows, the $\rho(T)$ curves above T_{MIN} for the four alloys containing between 13 and 16 at. % Cr are concave up with respect to the temperature axis, so that $d\rho/dT$ <u>increases</u> with increasing temperature, before finally saturating at high temperatures ($T > 200K$). This high-temperature slope increases slightly with increasing Cr content from $1.45 \times 10^{-2} \mu\Omega\, cm/K$ for 13 at. % Cr to $1.64 \times 10^{-2} \mu\Omega\, cm/K$

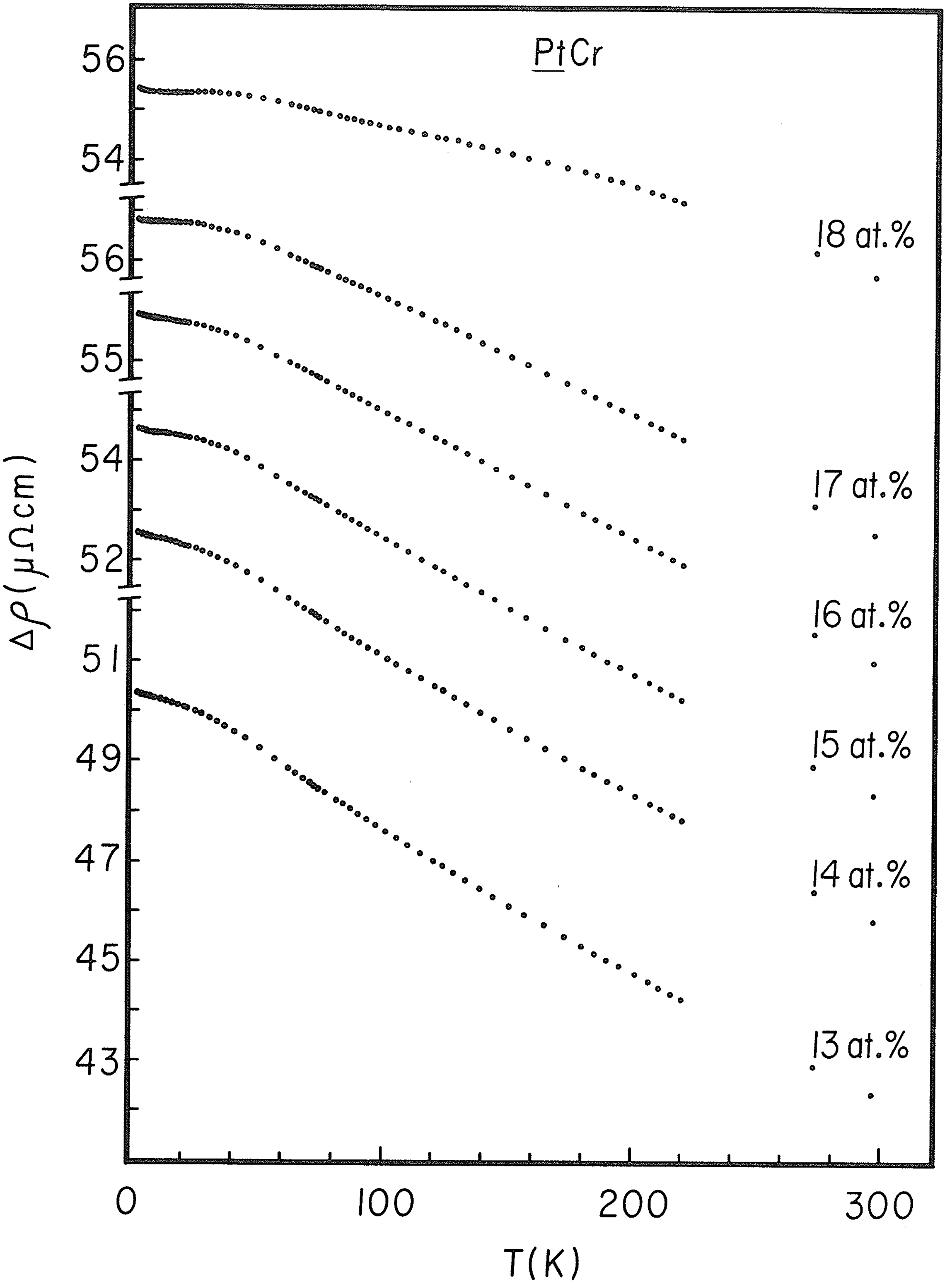

FIG.3.5-2. The incremental resistivities Δρ(T) of the Pt-13, 14, 15, 16, 17, and 18 at. % Cr alloys plotted against temperature from 1.5 to 300K.

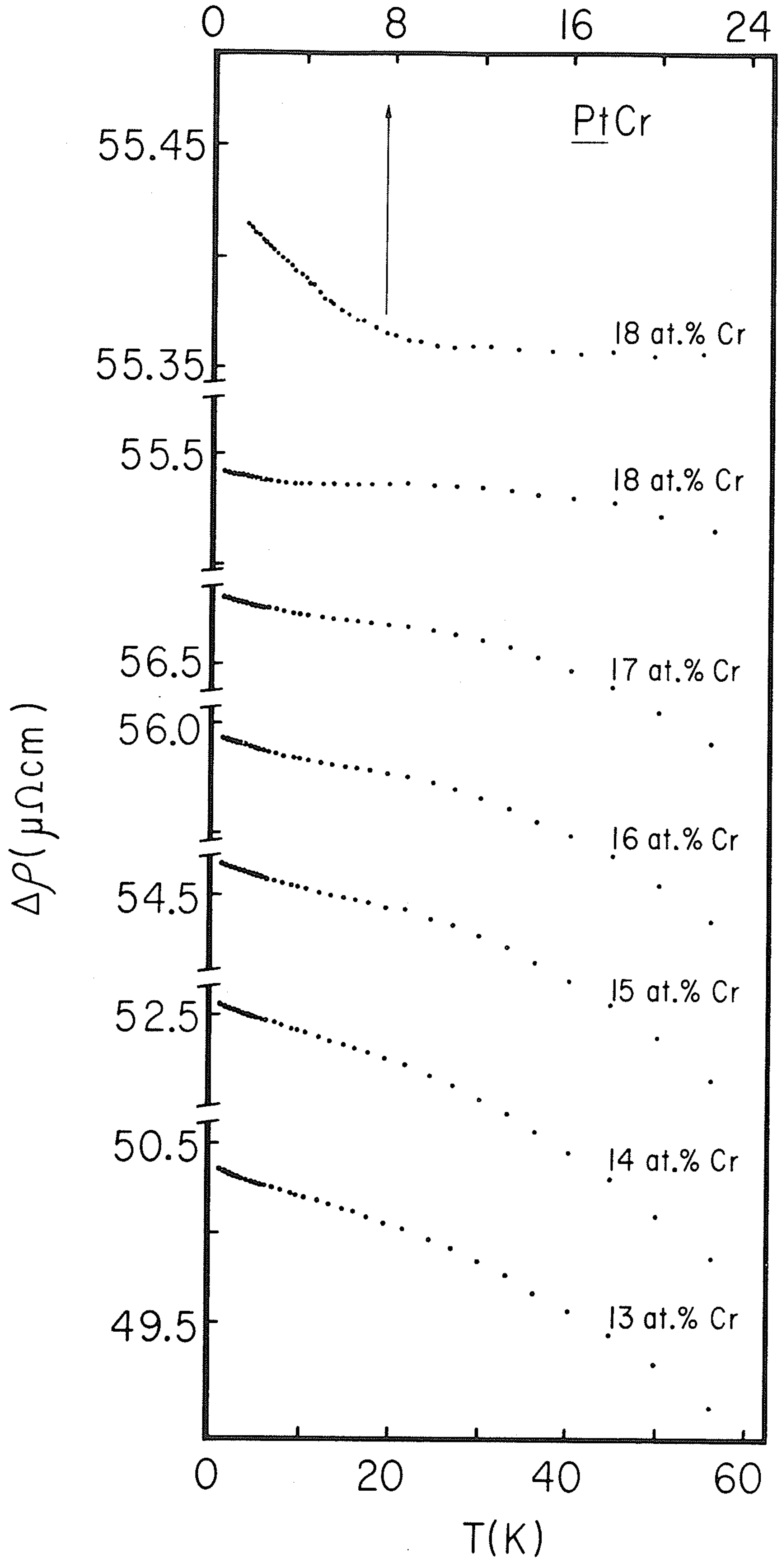

FIG.3.5-3. Details of the incremental resistivities Δρ(T) of the Pt-13, 14, 15, 16, 17, and 18 at. % Cr alloys at low temperatures (T < 60K). The data for the Pt-18 at. % Cr alloy is replotted at the top of the figure on an expanded resistivity and temperature scale.

for 16 at. % Cr (see Table 3.5-1). The resistivities of the 17 and 18 at. % Cr alloys are quite different. For these alloys, $\rho(T)$ possesses an inflection point above T_{MIN} followed by a "knee" at higher temperatures, so that $d\rho/dT$ initially increases with increasing temperature and then decreases as $\rho(T)$ passes through the inflection point, eventually levelling off at a constant value above the "knee". Moreover, the value of this high-temperature slope, $\left.\frac{d\rho}{dT}\right|_{T>T_{KNEE}}$, increases rapidly from $1.70 \times 10^{-2}\,\mu\Omega\,\mathrm{cm/K}$ for 17 at. % Cr to $2.56 \times 10^{-2}\,\mu\Omega\,\mathrm{cm/K}$ for 18 at. % Cr. The behaviour of the 18 at. % Cr alloy is clearly anomalous.

The resistivity of these systems at high temperatures is dominated by three types of scattering events : (i) electron-phonon scattering, (ii) interband or s-d scattering, and (iii) electron-impurity scattering. The addition of up to 18 at. % Cr to Pt is certainly expected to cause substantial changes in both the phonon spectrum and the bandstructure, and hence to contributions (i) and (ii) above. However, it seems unlikely that an increase of 1 at. % Cr, from 17 to 18 at. %, would be able to produce a 50% increase in the high-temperature value for $d\rho/dT$, particularly when similar additions at lower concentrations (over the entire range from 5 to 17 at. %, in fact) show no evidence for such discontinuities. The temperature dependence of the incremental resistivity $\Delta\rho(T)$, shown in FIG.3.5-2, emphasizes this point. Increasing the Cr concentration in steps of 1 at. % from 13 to 17 at. % produces rather small changes in the high-temperature slope of $\Delta\rho(T)$, yet on passing from 17 to 18 at. % this slope is noticeably reduced. To reiterate the point made above, it is not strictly permissible to evaluate $\Delta\rho(T)$ by subtracting the pure Pt resistivity from the measured alloy resistivity due to changes induced in the host resistivity on alloying. However, the experimental data indicates (via, for example, the smoothly decreasing high-temperature slope of $\Delta\rho(T)$ as the Cr concentration increases) that these modifications proceed without noticeable discontinuity over the entire concentration range from 5 to 17 at. %, and so it appears that a further 1 at. % increase from 17 to 18 at. % is not likely to cause changes in the host resistivity which are sufficient to produce the observed high-temperature differences.

Structural changes, such as an atomic order-disorder transformation, can also modify the phonon spectrum and the band structure of the alloy, as well as the spatial distribution of the Cr impurities, and hence can affect all three scattering processes referred to above. Moreover, as the phase diagram [63] in FIG.3.5-4 shows, PtCr undergoes such a spatial order-disorder transformation at around 18.5 at. % Cr. In order to determine whether the anomalous behaviour observed in the Pt-17 and 18 at. % Cr alloys is due to the presence of atomic order, a set of PtCr alloys containing 18, 19, 20, and 21 at. % Cr were prepared. For each concentration, two samples were prepared and these were subjected to different heat treatments : one of the samples was annealed at 650°C for 24 hours in a vacuum of 10^{-6} Torr, while the other sample was

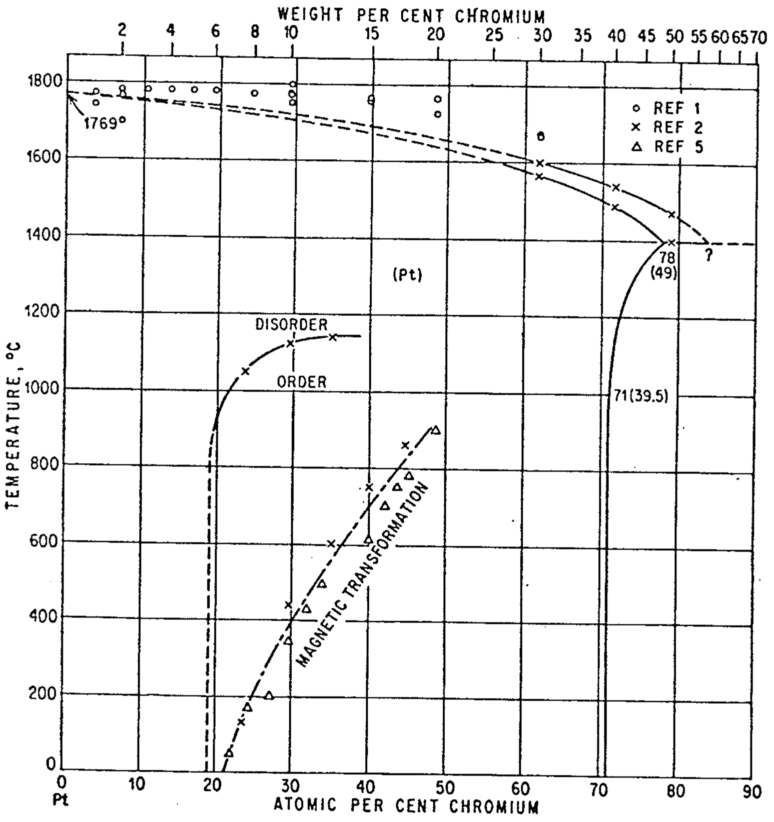

FIG.3.5-4. Phase diagram for the PtCr system showing the presence of an atomic order-disorder transformation at around 18.5 at. % Cr [63].

sealed in a glass tube under an argon atmosphere, heated up to 1170°C, and then quenched in water. From the phase diagram in FIG.3.5-4, it follows that the annealed sample is atomically ordered, while the quenched sample is atomically disordered. This was confirmed by X-ray diffraction measurements which revealed the presence of superlattice lines in the annealed 19, 20, and 21 at.% Cr samples. The absence of superlattice lines in the annealed 18 at.% Cr alloy suggests that this alloy is close to the order-disorder boundary in the phase diagram, so that the atomic order is probably of a short range nature. The measured resistivities of the eight PtCr alloys are plotted in FIGS.3.5-5 to 3.5-8 as a function of temperature from 1.5 to 300K. In each of these figures, the curves labelled "ordered" and "disordered" correspond to the resistivities of the annealed and quenched samples, respectively. Tables 3.5-2 and 3.5-3 contain a list of various parameters extracted from the data in these figures.

An inspection of FIGS.3.5-5 to 3.5-8, along with Tables 3.5-2 and 3.5-3, reveals the following differences between the resistivities of the corresponding ordered and disordered alloys :

1. The residual resistivity, represented by $\rho(1.5K)$ in Tables 3.5-2 and 3.5-3, is larger in the disordered alloys than in the corresponding ordered alloys. Moreover, the systematic decrease in $\rho(1.5K)$ with increasing Cr concentration in the ordered alloys reflects the gradual trend towards periodicity in the lattice potential (perfect periodicity is attained in the ordered stoichiometric compound Pt_3Cr).

FIG.3.5-5. The measured resistivities ρ(T) of the ORDERED and DISORDERED Pt-18 at. % Cr alloys plotted against temperature between 1.5 and 300K. The inserts in the upper left and lower right hand corners of the diagram show the details of the low-temperature behaviour of the resistivity.

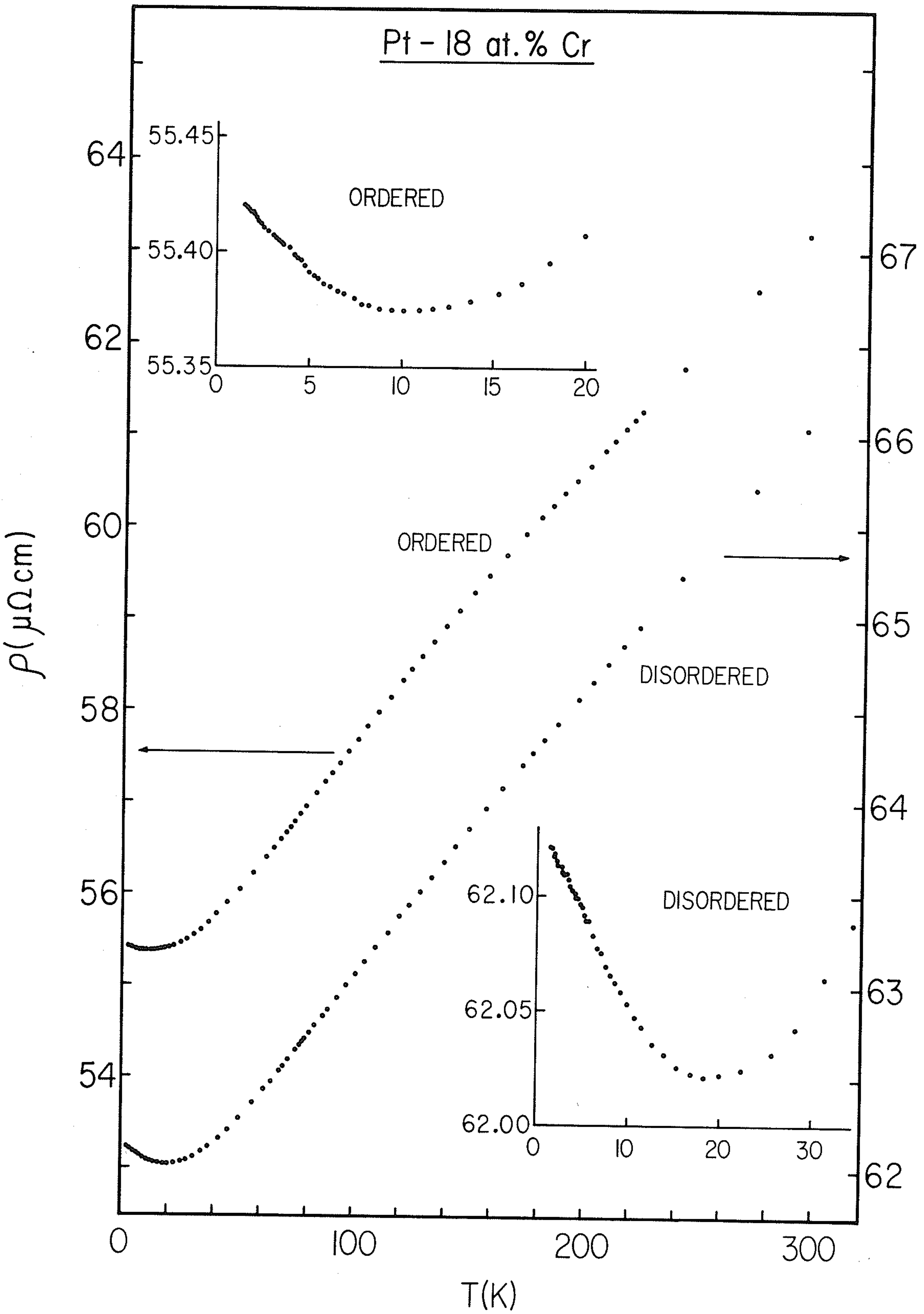
Pt - 18 at.% Cr
ORDERED
55.45
55.40
55.35
0
5
10
15
20
ORDERED
DISORDERED
DISORDERED
62.10
62.05
62.00
0
10
20
30
64
62
60
58
56
54
67
66
65
64
63
62
ρ(μΩcm)
0
100
200
300
T(K)

FIG.3.5-6. The measured resistivities ρ(T) of the ORDERED and DISORDERED Pt-19 at.% Cr alloys plotted against temperature between 1.5 and 300K. The inserts in the upper left and lower right hand corners of the diagram show the details of the low-temperature behaviour of the resistivity.

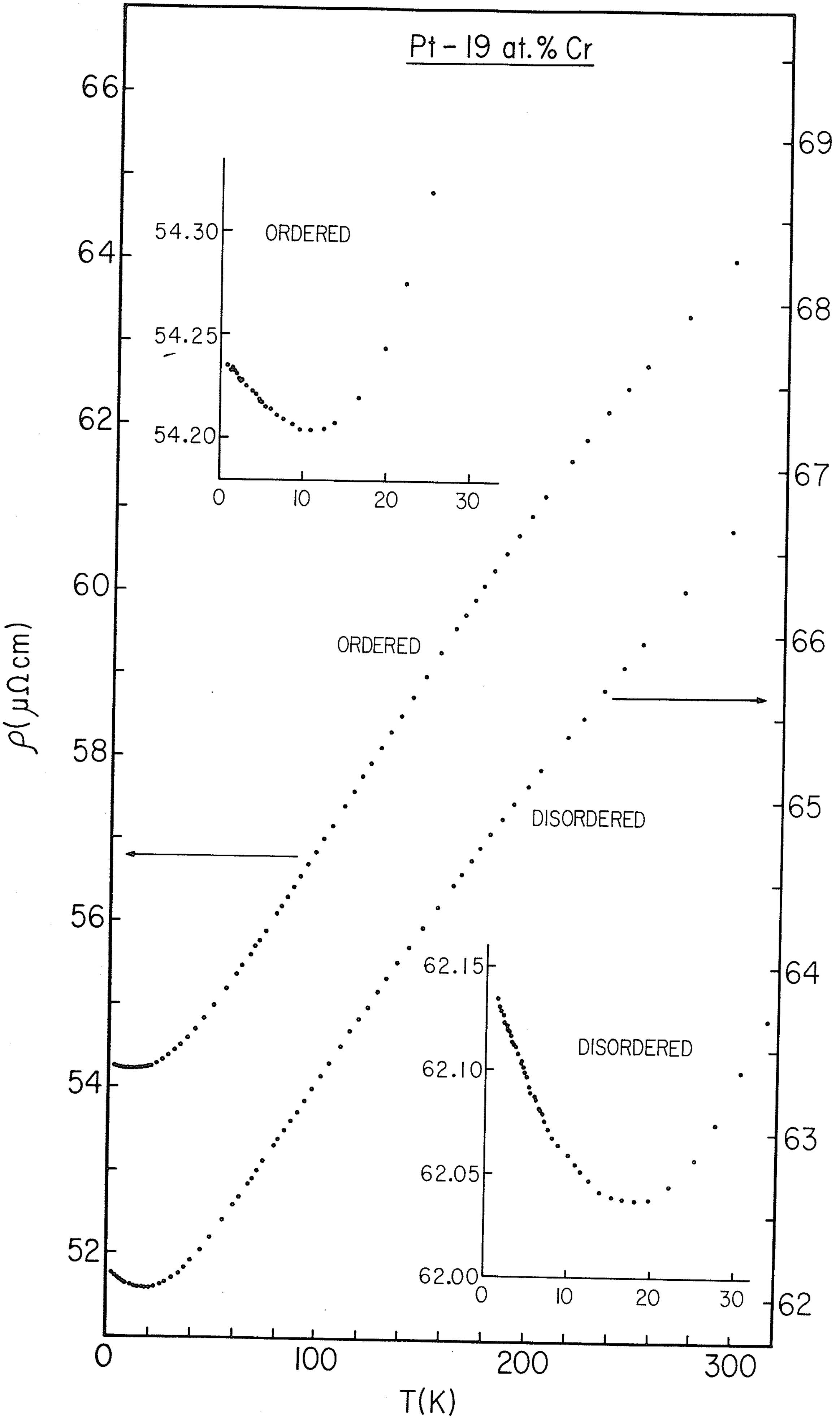
Pt-19 at.% Cr
ρ(μΩcm)
T(K)
66
64
62
60
58
56
54
52
0
100
200
300
69
68
67
66
65
64
63
62
ORDERED
DISORDERED
54.30
54.25
54.20
0
10
20
30
ORDERED
62.15
62.10
62.05
62.00
0
10
20
30
DISORDERED

FIG.3.5-7. The measured resistivities ρ(T) of the ORDERED and DISORDERED Pt-20 at. % Cr alloys plotted against temperature between 1.5 and 300K. The inserts in the upper left and lower right hand corners of the diagram show the details of the low-temperature behaviour of the resistivity.

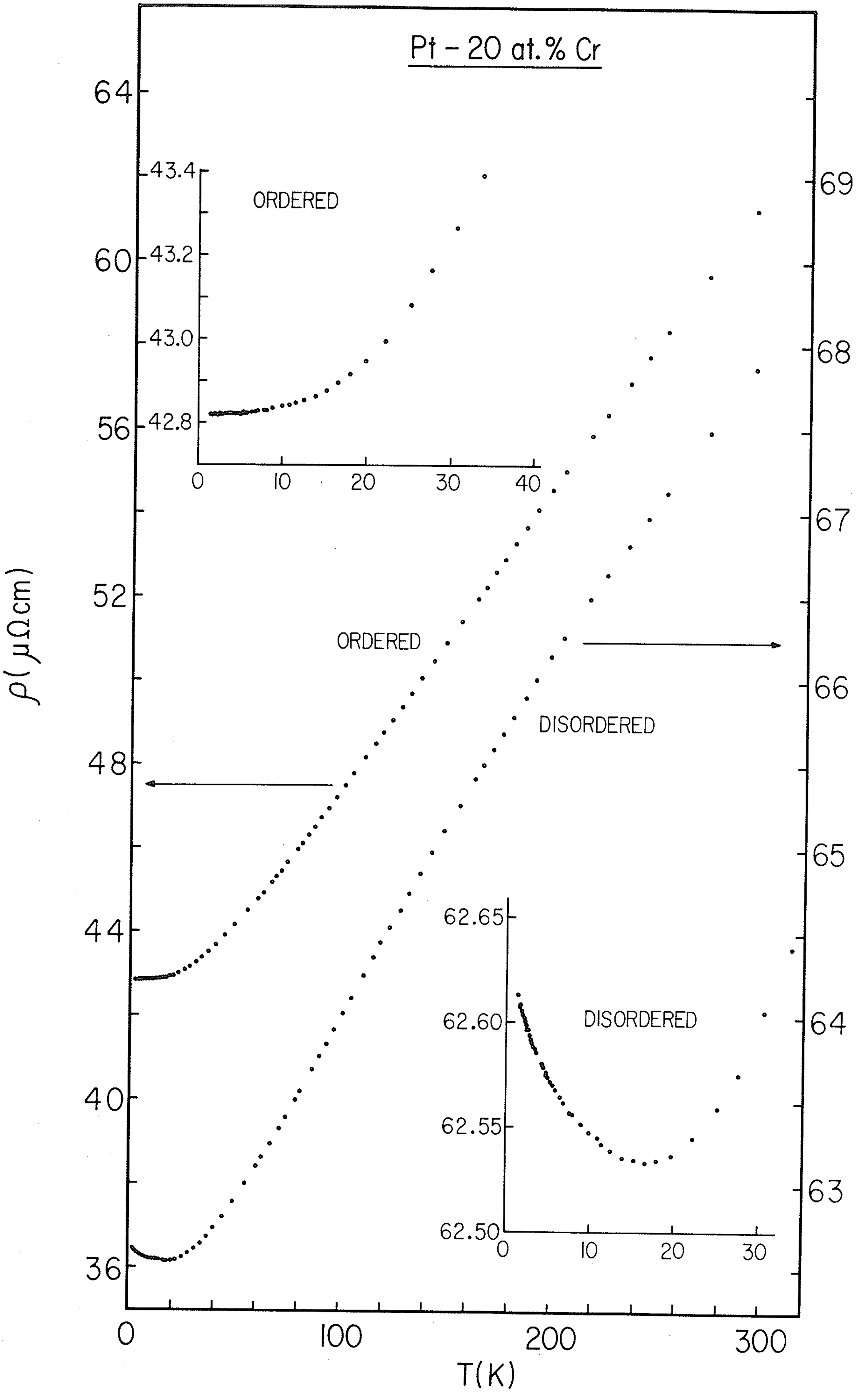
Pt – 20 at.% Cr
ORDERED
43.4
43.2
43.0
42.8
0
10
20
30
40
64
60
56
52
48
44
40
36
69
68
67
66
65
64
63
ρ(μΩcm)
ORDERED
DISORDERED
DISORDERED
62.65
62.60
62.55
62.50
0
10
20
30
0
100
200
300
T(K)

FIG.3.5-8. The measured resistivities $\rho(T)$ of the ORDERED and DISORDERED Pt-21 at. % Cr alloys plotted against temperature between 1.5 and 300K. The inserts in the upper left and lower right hand corners of the diagram show the details of the low-temperature behaviour of the resistivity.

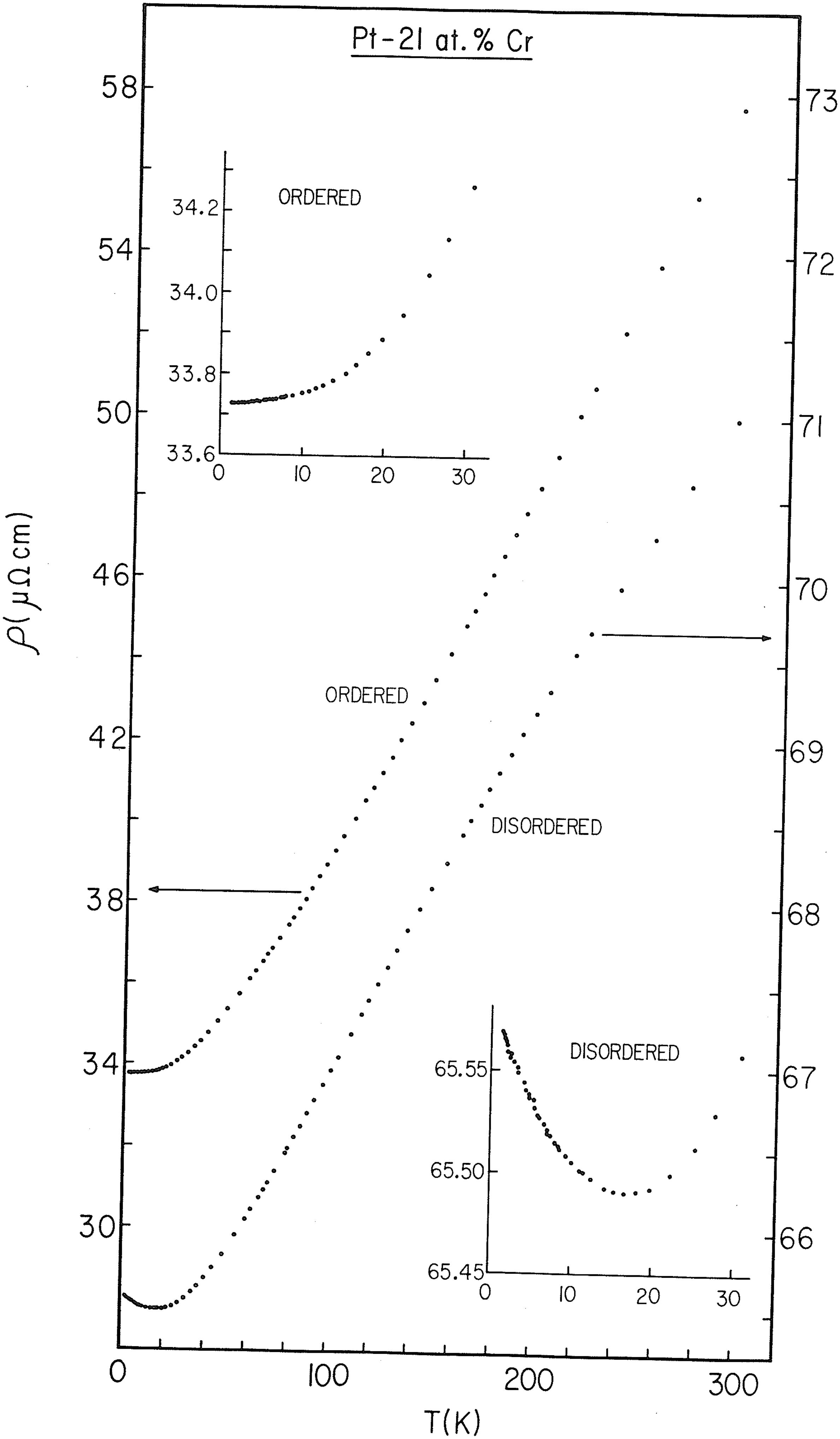
Pt-21 at.% Cr
ρ(μΩ cm)
T(K)
58
54
50
46
42
38
34
30
73
72
71
70
69
68
67
66
0
100
200
300
ORDERED
DISORDERED
ORDERED
34.2
34.0
33.8
33.6
0
10
20
30
DISORDERED
65.55
65.50
65.45
0
10
20
30

TABLE 3.5-2. ORDERED PtCr ALLOYS

ALLOY (at. % Cr)	HIGH-TEMPERATURE SLOPE ($T > T_{KNEE}$) (μΩ cm./K)	$\rho(1.5K)$ (μΩ cm.)	T_{MIN} (K)	$\rho(T_{MIN})$ (μΩ cm.)	$\rho(300K)$ (μΩ cm.)	$\rho(1.5K) - \rho(T_{MIN})$ (μΩ cm.)	$\rho(300K) - \rho(1.5K)$ (μΩ cm.)
18	2.66×10^{-2}	55.420	10 ± 1.5	55.374	63.310	0.046	7.890
19	3.04×10^{-2}	54.245	11 ± 1	54.213	64.170	0.032	9.925
20	6.93×10^{-2}	42.825	---	---	61.600	----	18.775
21	ABOVE 300K	33.750	---	---	58.170	----	24.380

TABLE 3.5-3. DISORDERED PtCr ALLOYS

ALLOY (at. % Cr)	HIGH-TEMPERATURE SLOPE ($T > T_{KNEE}$) (μΩ cm./K)	$\rho(1.5K)$ (μΩ cm.)	T_{MIN} (K)	$\rho(T_{MIN})$ (μΩ cm.)	$\rho(300K)$ (μΩ cm.)	$\rho(1.5K) - \rho(T_{MIN})$ (μΩ cm.)	$\rho(300K) - \rho(1.5K)$ (μΩ cm.)
18	1.50×10^{-2}	62.121	18.5 ± 1	62.021	66.115	0.100	3.994
19	1.61×10^{-2}	62.134	18 ± 1	62.037	66.710	0.097	4.576
20	1.75×10^{-2}	62.610	16.5 ± 1	62.533	67.950	0.077	5.340
21	1.85×10^{-2}	65.569	16.5 ± 1.5	65.490	71.100	0.079	5.531

2. The total change in the resistivity between 1.5 and 300K, represented by the difference $\rho(300K) - \rho(1.5K)$ in Tables 3.5-2 and 3.5-3, is substantially larger in the ordered phase than it is in the disordered phase.

3. The depth of the minimum in the resistivity at low temperatures is also affected by the presence of atomic order, with $\rho(1.5K) - \rho(T_{MIN})$ being smaller in the ordered phase than in the disordered phase. In fact, the minimum disappears entirely in the ordered 20 and 21 at. % Cr alloys.

4. The high-temperature slope, $\left.\frac{d\rho}{dT}\right|_{T>T_{KNEE}}$, is significantly larger, and increases much more rapidly with increasing Cr concentration, in the ordered alloys than in the corresponding disordered alloys.

These differences between the resistivities of the ordered and disordered alloys suggests that the anomalous behaviour observed in the Pt-18 at. % Cr alloy (and to a lesser extent in the Pt-17 at. % Cr alloy) in FIG.3.5-1 is probably due to the presence of atomic order, although the precise scattering mechanism which is responsible for the changes (electron-phonon, electron-impurity or interband scattering) is uncertain. However, the changing character of the low-temperature (below 60K) incremental resistivity data depicted in FIG.3.5-3 is reminiscent of the type of structure developed in the $\underline{V}$Fe system [65] at concentrations around 27.5 at. % Fe near the onset of weak ferromagnetic ordering. In fact, several investigations on other transition metal alloys [54, 66] have correlated the appearance of an inflection point in $\rho(T)$ with the occurrence of spin freezing or spin glass behaviour, the appearance of which also produces sharp peaks in the low-field A.C. susceptibility.

3.5.2 Features of the A.C. Susceptibility

Following the remarks made in the preceding paragraph, it seemed reasonable to examine the A.C. susceptibility of these alloys as a function of temperature.

FIGS.3.5-9 and 3.5-10 summarize the results of such measurements performed at 2400 hz in an A.C. driving field of 1.6 Oe RMS and in zero applied static field. FIG.3.5-9 shows the A.C. susceptibilities of the disordered (or quenched) PtCr samples containing between 17 and 21 at. % Cr plotted as a function of temperature, while FIG.3.5-10 shows the susceptibilities of the corresponding ordered (or annealed) samples. Within experimental resolution [67], no peak could be resolved in the A.C. susceptibility of those alloys containing between 13 and 16 at. % Cr. As mentioned previously, the samples used in these measurements were obtained by folding the resistivity strips into a multiple-hairpin shape with contacting surfaces electrically insulated from each other. No attempt was made to correct for demagnetization effects; however, since the magnetizations of the samples were small ($\sim 10^{-3}$ to 10^{-4} emu), such corrections are negligible. While the susceptibility is thus presented in arbitrary units, the relative amplitudes of the curves shown in FIGS.3.5-9 and 3.5-10 are reliable to within 10 %.

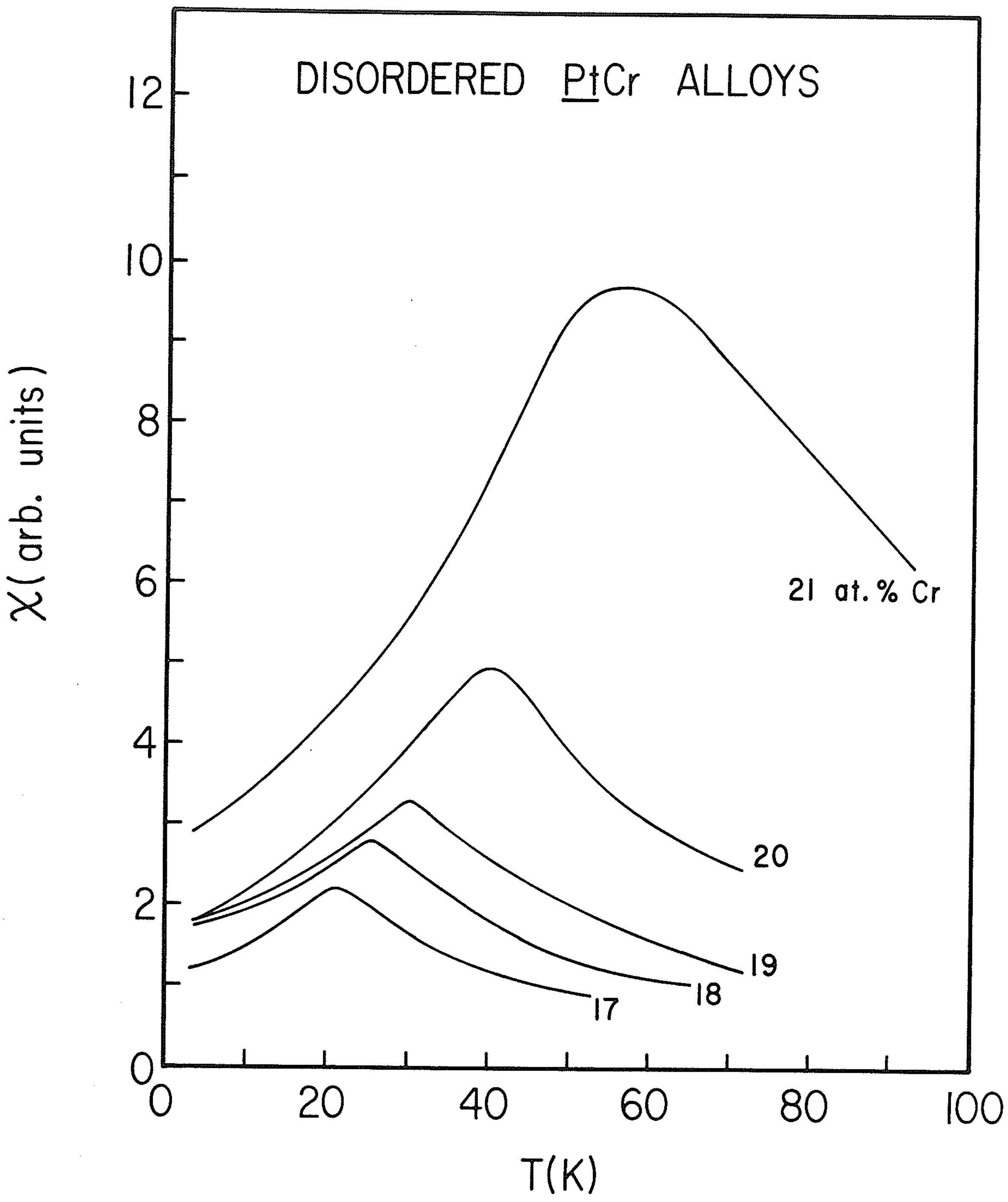

FIG.3.5-9. The A.C. susceptibility χ(T) (in arbitrary units), in zero D.C. biasing field, plotted as a function of temperature for the DISORDERED PtCr alloys containing between 17 and 21 at. % Cr.

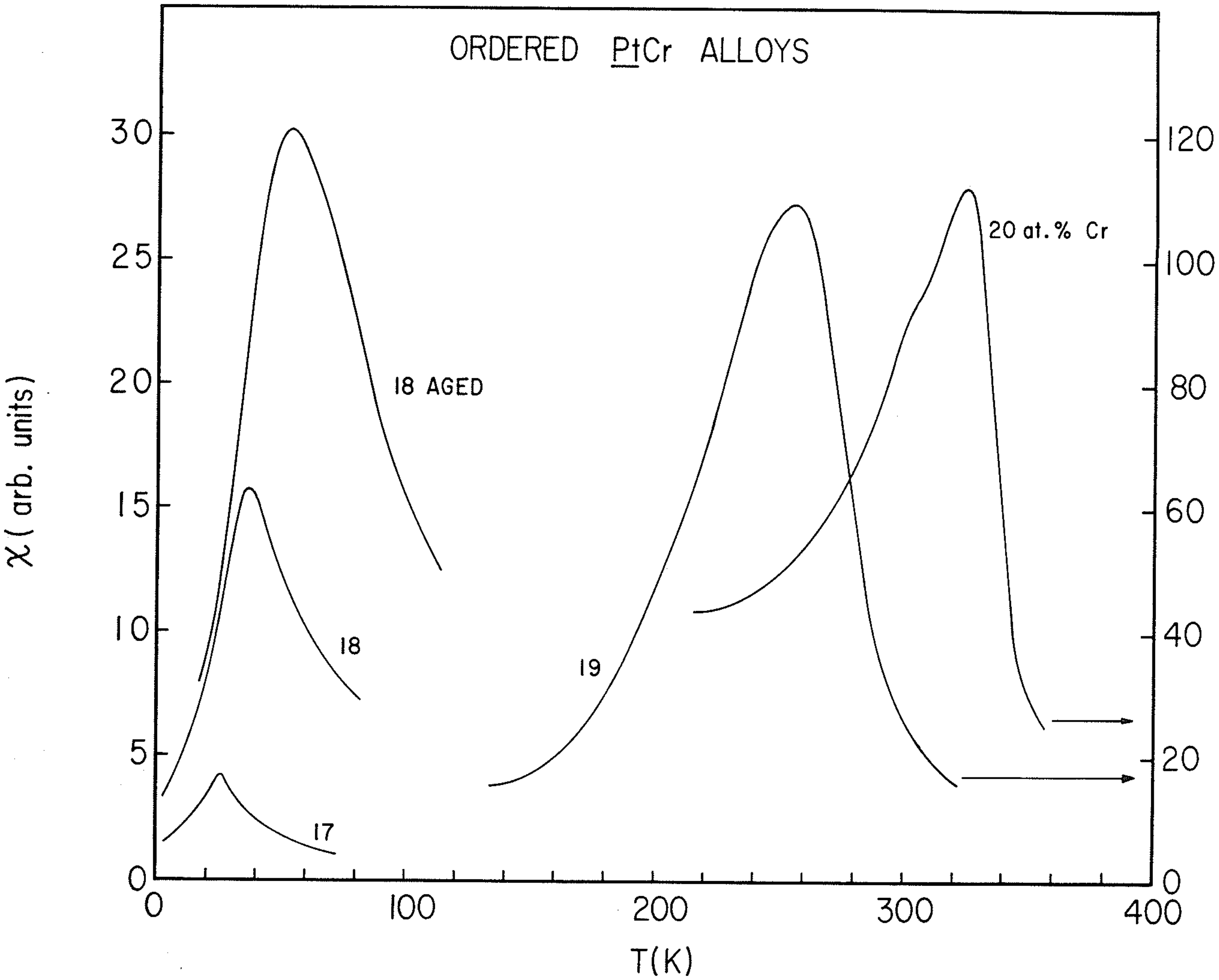

FIG.3.5-10. The A.C. susceptibility $\chi(T)$ (in arbitrary units), in zero D.C. biasing field, plotted as a function of temperature for the ORDERED PtCr alloys containing between 17 and 20 at. % Cr.

TABLE 3.5-4. Summary of A.C. susceptibility data for ordered and disordered PtCr alloys

(a) DISORDERED (QUENCHED) SAMPLES

ALLOY (at. % Cr)	T_0 (K)	$\chi(T_0)$ (arbitrary units)
17	21 ± 0.5	2.2 ± 10%
18	25.5 ± 0.5	2.8
19	30 ± 0.5	3.3
20	40 ± 1	4.9
21	57 ± 1	9.7

(b) ORDERED (ANNEALED) SAMPLES

ALLOY (at. % Cr)	T_0 (K)	$\chi(T_0)$ (arbitrary units)
17	26 ± 2	4.2 ± 10%
18	37 ± 2	15.8
18 AGED	53 ± 2	30.3
19	256 ± 3	109
20	325 ± 3	112
21	--- ABOVE ROOM TEMPERATURE ---	

For all the alloys shown in FIGS.3.5-9 and 3.5-10, the A.C. susceptibility in zero applied field possesses a maximum. These maxima are not sharp as in canonical spin glass systems (AuFe, for example [68]) but are considerably more rounded, thus resembling those observed in hydrogenated giant moment systems [69, 70]. For both the ordered and disordered samples, the temperature T_0 at which the maximum in the susceptibility occurs increases with increasing Cr concentration, as does the height of the maximum $\chi(T_0)$. Estimates for both T_0 and $\chi(T_0)$ are listed in Table 3.5-4. Moreover, a comparison of FIGS.3.5-9 and 3.5-10 shows that, for the Cr concentrations examined here, both T_0 and $\chi(T_0)$ are larger for the ordered alloy than for the corresponding disordered alloy. (This effect is particularly noticeable for the 19 and 20 at.% Cr alloys, where T_0 increases by approximately a factor of 6 on going from the disordered to the ordered state.) Also included in FIG.3.5-10 is the A.C. susceptibility of the ordered 18 at.% Cr sample after aging at room temperature for approximately a month. Clearly, the effect of aging is to increase the peak height and to shift the peak to higher temperatures.

The effect of static applied fields on the A.C. susceptibility have also been investigated, and these results are shown in FIGS.3.5-11, 3.5-12, and 3.5-13 for the ordered 18, 19, and 20 at.% Cr samples, respectively. The ordered 18 and 19 at.% Cr samples (FIGS.3.5-11 and 3.5-12) behave like canonical spin glasses, with the applied static field simply reducing the peak amplitude, but not changing its position.

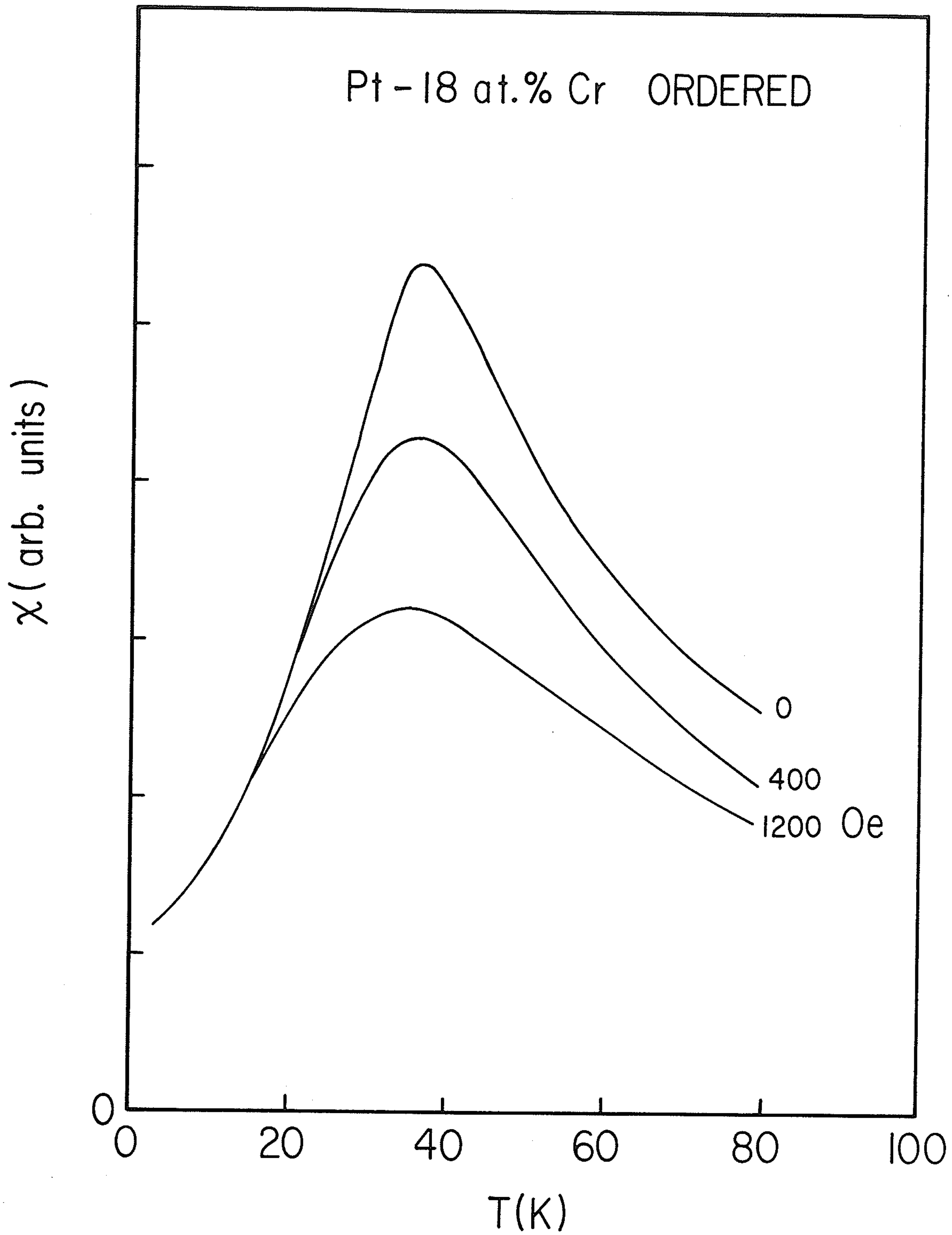

FIG.3.5-11. The A.C. susceptibility $\chi(T)$ (in arbitrary units) of the ORDERED Pt-18 at.% Cr alloy as a function of temperature in D.C. biasing fields of 0, 400, and 1200 Oe.

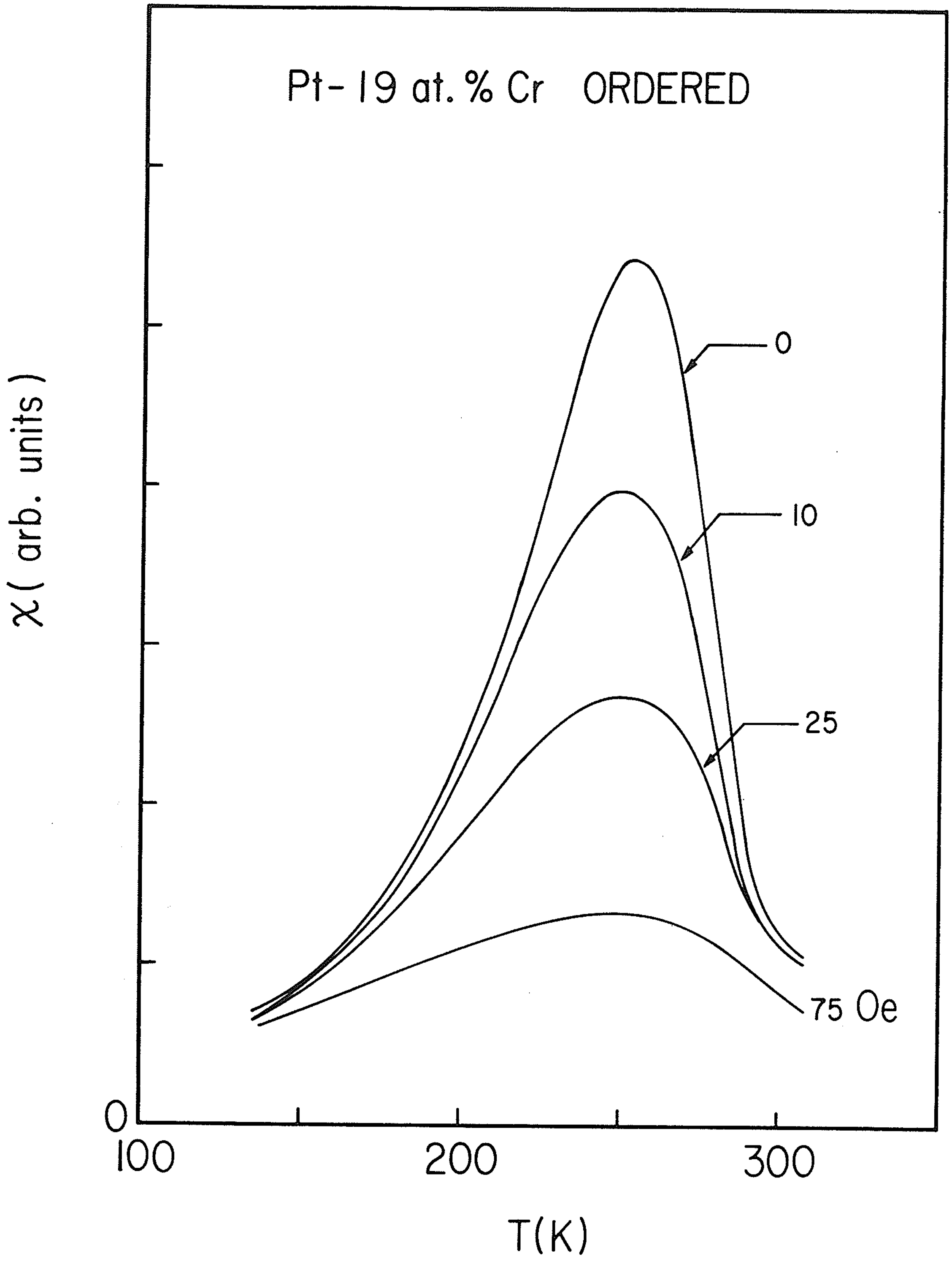

FIG.3.5-12. The A.C. susceptibility $\chi(T)$ (in arbitrary units) of the ORDERED Pt-19 at. % Cr alloy as a function of temperature in D.C. biasing fields of 0, 10, 25, and 75 Oe.

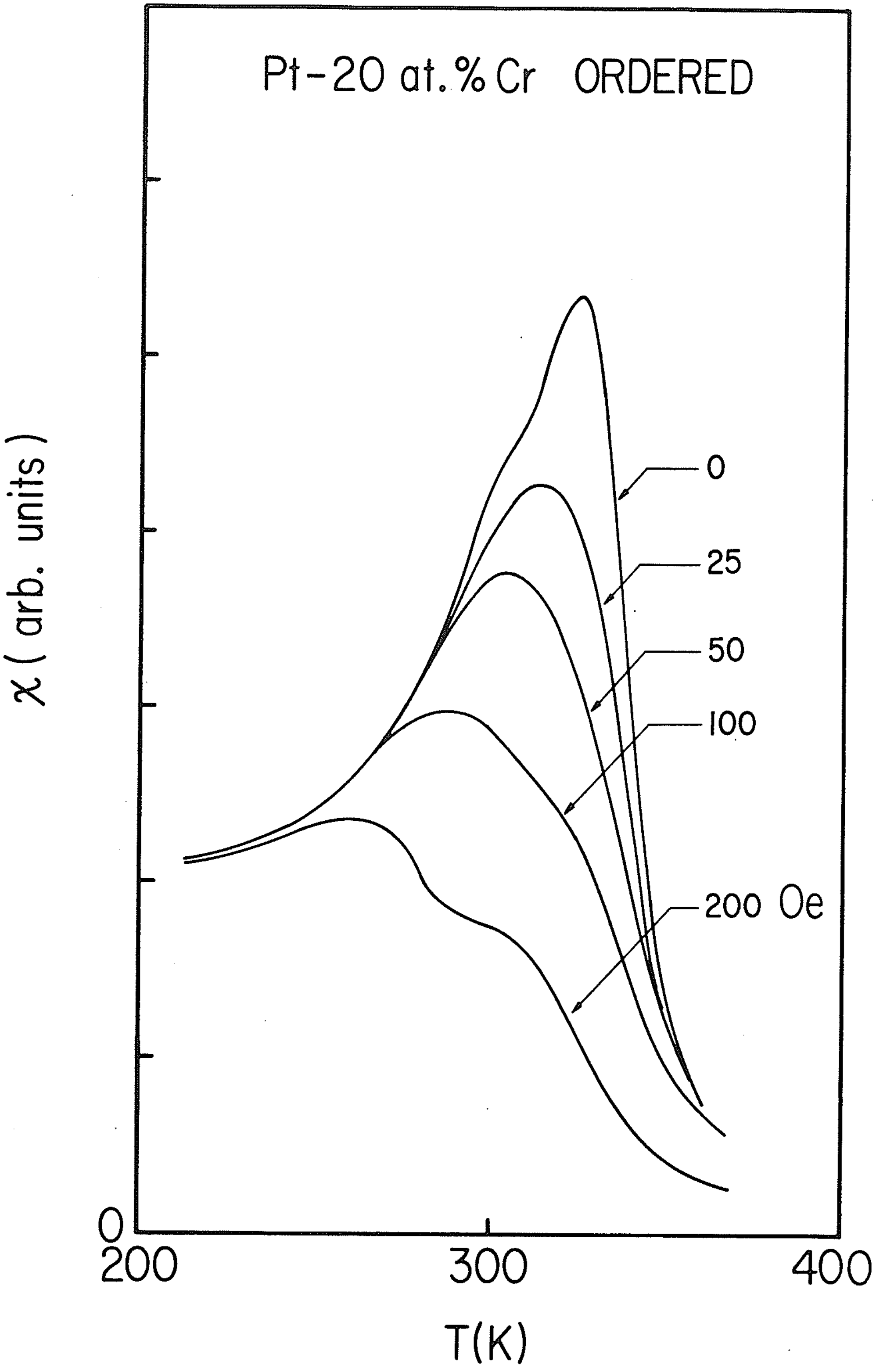

FIG.3.5-13. The A.C. susceptibility $\chi(T)$ (in arbitrary units) of the ORDERED Pt-20 at. % Cr alloy as a function of temperature in D.C. biasing fields of 0, 25, 50, 100, and 200 Oe.

The behaviour of the ordered 20 at. % Cr sample is not so straightforward, with the application of an applied magnetic field revealing the presence of structure (multiple peaks) in the A.C. susceptibility (see FIG.3.5-13). However, departures from simple spin glass-like behaviour are to be expected at these high concentrations and probably reflect the presence of a more complicated magnetic ground state.

The ordered Pt-20 at. % Cr sample also exhibits magnetic hysteresis, a feature which is characteristic of both spin glasses and ferromagnets below their respective freezing temperatures (T_0 and T_C). This is illustrated in FIG.3.5-14, which shows the susceptibility of this sample plotted as a function of the applied magnetic field, H, at several fixed temperatures T. For temperatures above the freezing temperature T_0 (=325K, from Table 3.5-4), $\chi(H)$ is a single-peaked curve with $\chi(0)$ increasing with decreasing temperature. However, below T_0, $\chi(H)$ changes into a double-peaked curve, with the peaks symmetrically arranged about $H = 0$ and with the distance between the peaks increasing with decreasing temperature.

The A.C. susceptibility data thus reinforces the conclusions drawn from the resistivity data, namely, the onset of anomalous behaviour in the <u>Pt</u>Cr system for Cr concentrations around 17 to 18 at. %.

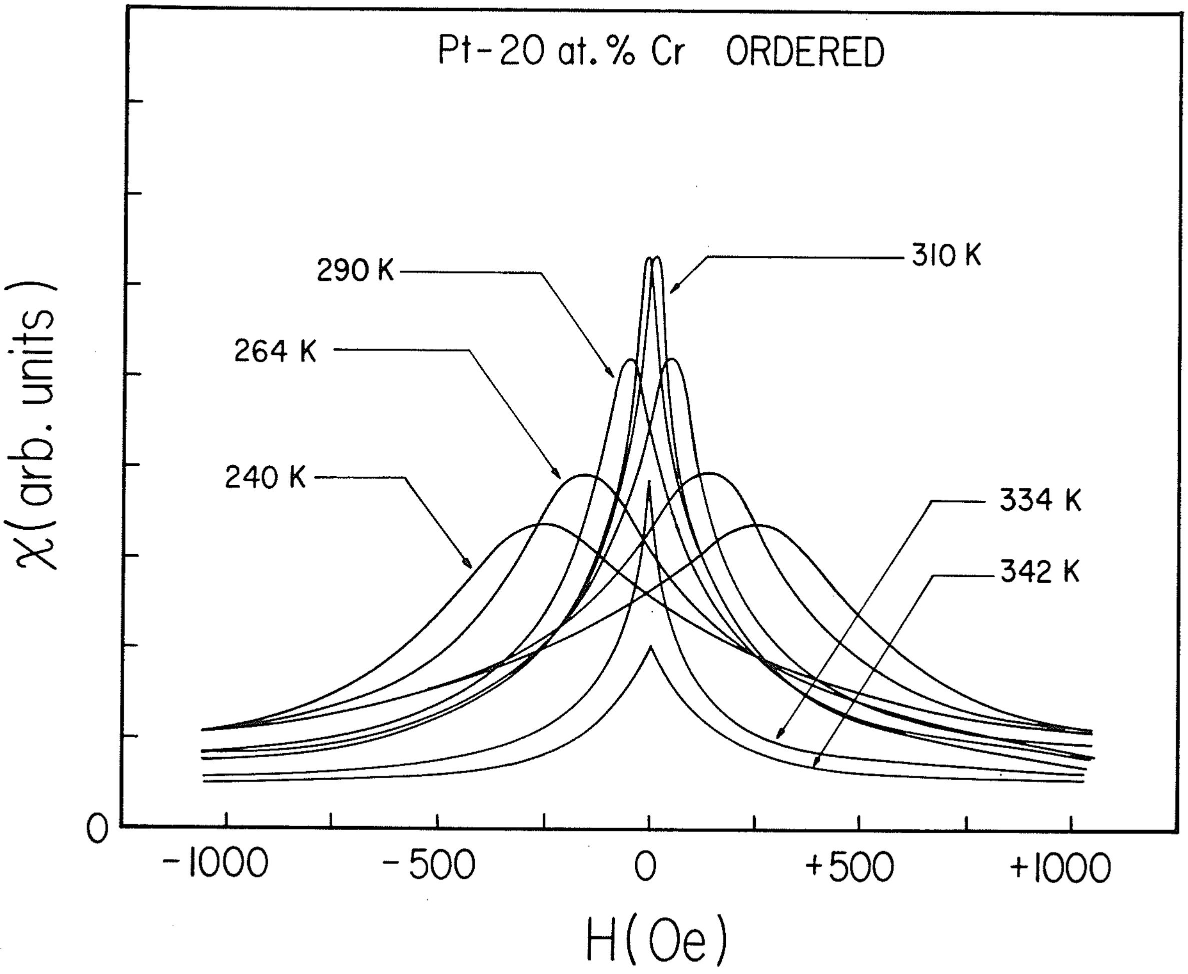

FIG.3.5-14. The A.C. susceptibility of the ORDERED Pt-20 at. % Cr alloy plotted as a function of the D.C. biasing field H (in Oe.) for several fixed temperatures T.

3.5.3 Summary and Discussion

The results of the present investigation imply that in order to observe any of the characteristics traditionally associated with the extended freezing of the impurity magnetization, the impurity concentration must be raised to a level close to the percolation limit (19.5 at. % for an FCC lattice [71]). A comparison then with canonical spin glasses or other systems would imply that interimpurity coupling of the RKKY type is very ineffective, and any freezing that does occur must result from impurity near-neighbour d-d overlap. As previously suggested in Sec.3.3.3 (see Eq.(3.3-14)), a reduced RKKY coupling energy could result from a comparatively high single-impurity frequency $\omega_s = k_B\theta_s/\hbar$.

As far as the appearance of extended magnetic freezing is concerned, the present analysis is in agreement with static magnetization studies [72], which have been interpreted as indicating the presence of a spontaneous magnetization (nonlinear M-vs-H plots at 20K, with the high-field data extrapolating to a substantial zero-field magnetization) which becomes progressively stronger as the Cr content is increased beyond 18 at. %. For Cr concentrations in excess of 19 at. %, the added difficulty of a spatial order-disorder transformation has to be considered. In the ordered phase, the spontaneous magnetization climbs to a maximum value at the stoichiometric composition Pt_3Cr (or Pt-25 at. % Cr) and then decreases with the further addition of Cr, whereas the estimated ordering temperature increases monotonically to above 1000K for $c > 40$ at. % Cr, at which point the spontaneous magnetization has declined to nearly zero, signalling the onset of antiferromagnetism in ordered PtCr (attributed to two opposing Cr sublattices and virtually zero induced Pt moment). Neutron scattering data [73] suggests a ferromagnetic type structure for ordered Pt_3Cr : the Cr atoms occupy the corners of a face-centered cubic structure and carry a moment of 2.33 μ_B/atom which is directed antiparallel to the (induced) Pt moments of 0.27 μ_B/atom residing at the face centers. The reported behaviour for the spatially disordered alloys is quite different. Here the measured magnetization in all fields is typically two orders of magnitude smaller than in the corresponding ordered alloy, leading to a comparably smaller spontaneous magnetization (which itself may be due to the presence of small residual regions with spatial order) and a reduced high-field slope (by a factor of 5 to 10) which displays a weak temperature dependence.

From the resistivity and A.C. susceptibility data presented here, along with the observation of a large additional contribution to the linear term in the specific heat of a Pt-17.3 at. % Cr alloy [74] of comparable magnitude to that observed in canonical spin glasses [75], it is inferred that the nature of the magnetic freezing observed in the disordered alloys containing between 17 and 21 at. % Cr is probably of the spin glass type, principally brought about, however, by near-neighbour d-d overlap (which also serves to stabilize the magnetic moment at the

Cr site) as opposed to long-range RKKY type coupling. Clearly, the type of magnetic order occurring in ordered Pt_3Cr and PtCr, discussed above, yields an antiferromagnetic Cr-Cr nearest-neighbour interaction and a ferromagnetic Cr-Cr next-nearest-neighbour interaction, which is precisely the spatial variation required to provide short-range spin glass type "clusters" in the random disordered alloys studied here. That environmental effects (i.e., the extent of nearest- and next-nearest-neighbour Cr-Cr interactions) are important in stabilizing such moments and determining the nature of the frozen ground state is evidenced by the large increase in magnetization (and susceptibility) accompanying the disorder to order transformation in alloys of composition in the vicinity of Pt_3Cr. This enhancement of the magnetic behaviour of the Cr impurities in the ordered state can modify the contribution to the electrical resistivity due to electron-impurity scattering and hence provides a possible explanation for the abrupt increase in the high-temperature slope of the resistivity, $\left.\frac{d\rho}{dT}\right|_{T>T_{KNEE}}$, on passing from the disordered to the ordered state. However, as pointed out previously, the presence of atomic order can also cause substantial changes in both the phonon spectrum and the bandstructure of the alloy, and these changes can also account for the observed increase in the high-temperature value for $d\rho/dT$.

3.6 Summary

The preceding sections represent an attempt to study, in a systematic way, the effects of impurity-impurity interactions and the onset of magnetic freezing in the PdCr and PtCr systems via measurements of the electrical resistivity and A.C. susceptibility. The results of this investigation can be summarized by plotting both the characteristic temperature θ and the difference $\Delta\rho(1.5K) - \Delta\rho(4.2K)$ for the two systems as a function of the nominal Cr concentration (c). Table 3.6-1 lists the values of the two parameters θ and $\Delta\rho(1.5K) - \Delta\rho(4.2K)$ for the PdCr and PtCr alloys containing between .05 and 18 at. % Cr. FIGS.3.6-1 and 3.6-2 show the variation of the characteristic temperature θ with Cr concentration for the PdCr and PtCr systems, respectively. As discussed in Sections 3.2 and 3.3, these estimates for θ were obtained by fitting the "high" temperature incremental resistivity data to an expression of the form $\Delta\rho(T) = Ac + Bc\,\ell n(T^2 + \theta^2)^{\frac{1}{2}}$. (At "low" temperatures, the measured incremental resistivities deviate from the "predicted" single-impurity curve ; in the very dilute alloys this effect was attributed to deviations from Matthiessen's rule, while in the more concentrated alloys it was assumed to arise from interactions between impurities.) For the most dilute PdCr and PtCr alloys examined ($.05 \leq c \leq 0.3$ at. % Cr), θ is independent of Cr concentration, suggesting a single-impurity characteristic temperature θ_s of ~44K for Cr impurities in Pd and ~73K for Cr impurities in Pt. As pointed out in Sec.3.2, these values for θ_s

TABLE 3.6-1

PdCr			PtCr		
ALLOY (at. % Cr)	θ (K)	$\Delta\rho(1.5K) - \Delta\rho(4.2K)$ ($\mu\Omega$ cm.)	ALLOY (at. % Cr)	θ (K)	$\Delta\rho(1.5K) - \Delta\rho(4.2K)$ ($\mu\Omega$ cm.)
.05	43.5	+ 0.0001	.05	73	+ .0001
0.1	45	+ 0.0001	0.1	71.5	+ .0001
0.2	43	+ 0.001	0.2	74	+ .001
0.3	44	+ 0.002	0.3	72.5	+ .001
4	25.4	+ 0.390	5	52.5	+ .0218
5	28.2	+ 0.419	6	56	+ .0290
6	33.4	+ 0.337	8	60	+ .0435
8	57.7	- 0.040	10	73	+ .0633
10	80.4	- 0.078	12	85	+ .0550
11	----	- 0.065	13	----	+ .0465
12	----	- 0.059	14	----	+ .0413
14	----	- 0.032	15	----	+ .0394
16	----	+ 0.0001	16	----	+ .0355
18	----	+ 0.012	17	----	+ .0296
			18	----	+ .0212

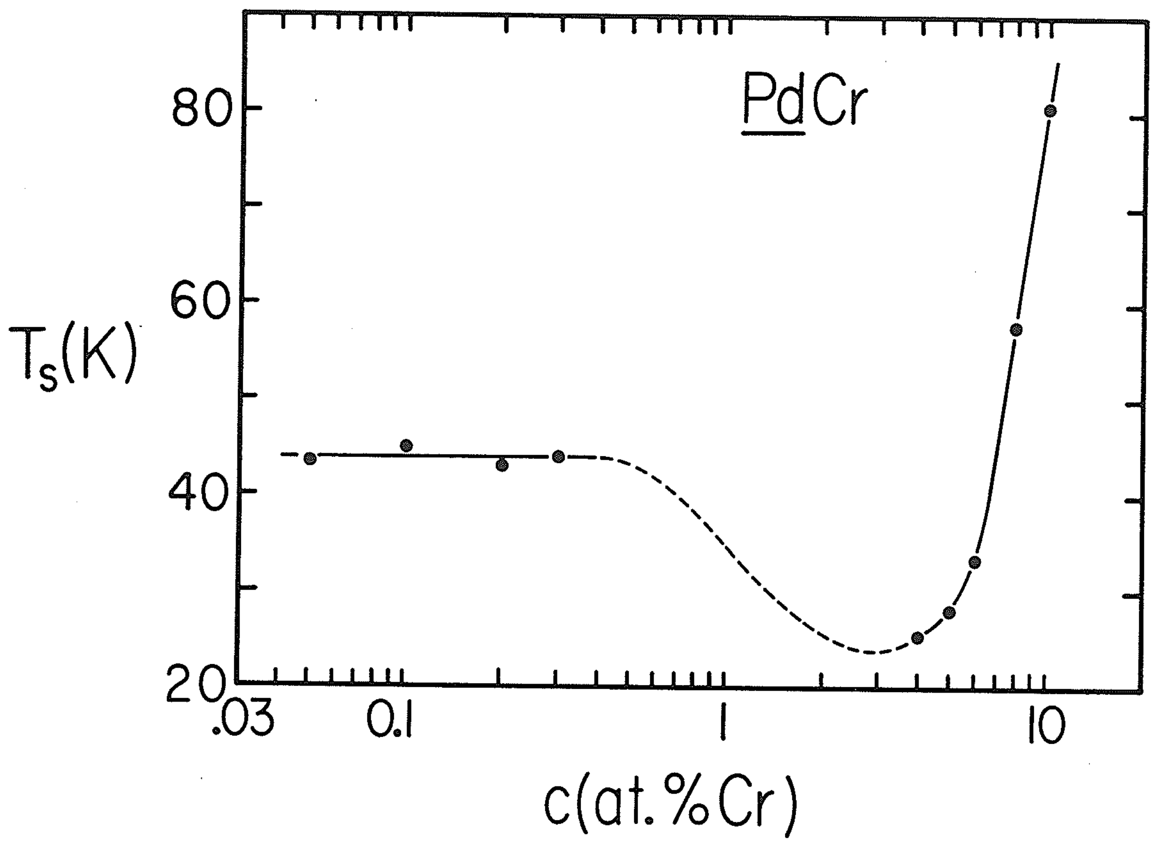

FIG.3.6-1. A plot of the characteristic temperature θ as a function of the nominal Cr concentration for PdCr alloys containing between .05 and 10 at. % Cr.

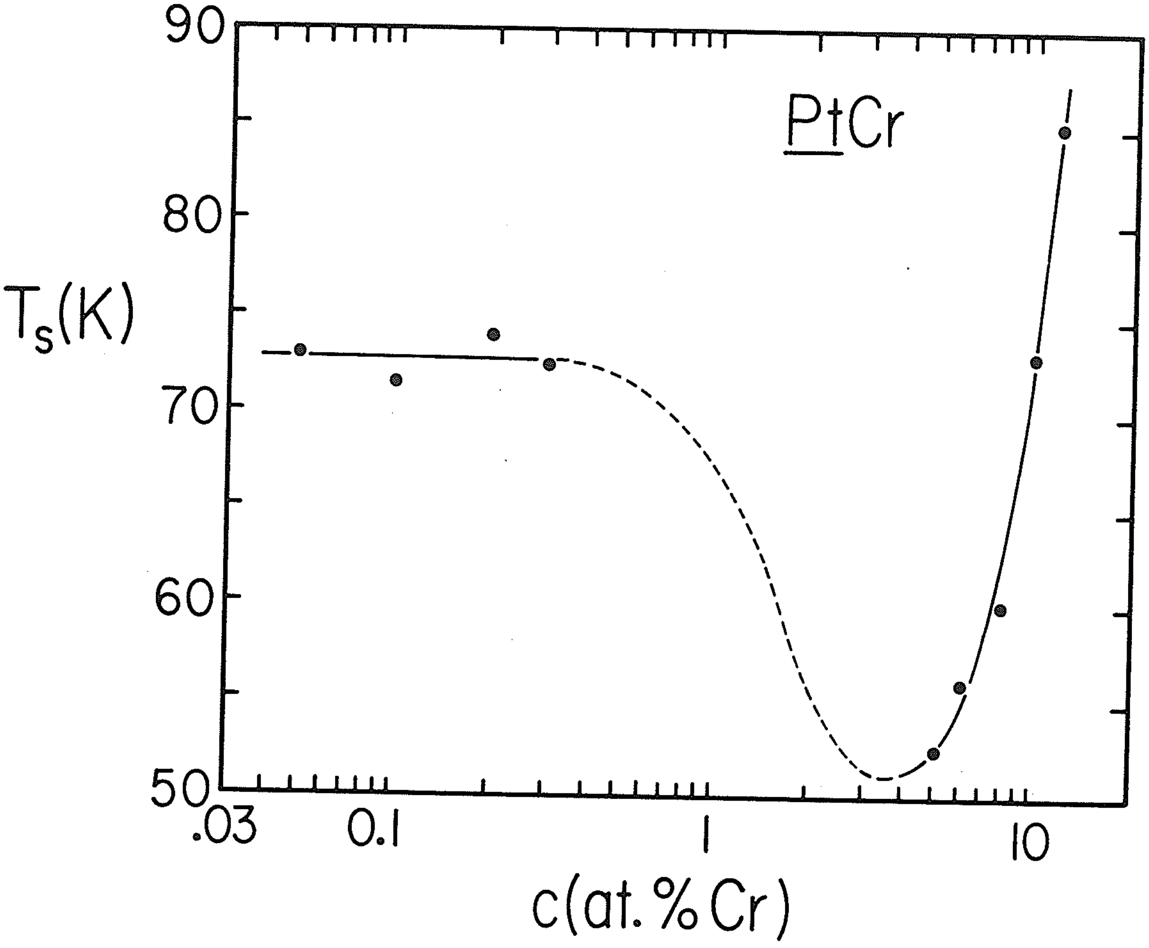

FIG.3.6-2. A plot of the characteristic temperature θ as a function of the nominal Cr concentration for PtCr alloys containing between .05 and 12 at.% Cr.

are intermediate between typical Kondo and LSF temperatures and as a result there is some uncertainty as to whether Cr impurities dissolved in Pd and Pt should be regarded as having a well-defined spin with a relatively high Kondo temperature T_K, or a fluctuating spin with a comparatively low LSF temperature T_{sf}. For higher Cr concentrations, θ initially decreases with increasing Cr concentration, passes through a minimum, and then increases with a further increase in Cr content. The behaviour of θ as a function of c thus resembles that outlined in the "phase" diagram in FIG.3.1-3.

In FIGS.3.6-3 and 3.6-4 the difference $\Delta\rho(1.5K) - \Delta\rho(4.2K)$ is plotted as a function of the nominal Cr concentration for the PdCr and PtCr systems, respectively. From these figures it can be seen that $\Delta\rho(1.5K) - \Delta\rho(4.2K)$ exhibits a peak as a function of impurity concentration, with the peak occurring at approximately 5 at.% in PdCr and 11 at.% in PtCr. This type of behaviour has also been observed in PdNi [9], RuFe [10], and RhFe [76], and can be interpreted by referring to FIG.3.6-5 which shows the effect of interactions between impurities on the incremental resistivity, $\Delta\rho(T)$, in various concentration regimes. FIG.3.6-5(a) shows the resistivity due to the scattering of conduction electrons from a single (or isolated) impurity and has the form $\Delta\rho(T) = Ac + Bc\,\ell n(T^2 + \theta_s^2)^{\frac{1}{2}}$, where θ_s is the single-impurity characteristic temperature. Above θ_s the impurity behaves as if it possesses a well-defined static local moment, while below θ_s the impurity becomes progressively less magnetic. In this latter regime $(T < \theta_s)$, the impurity

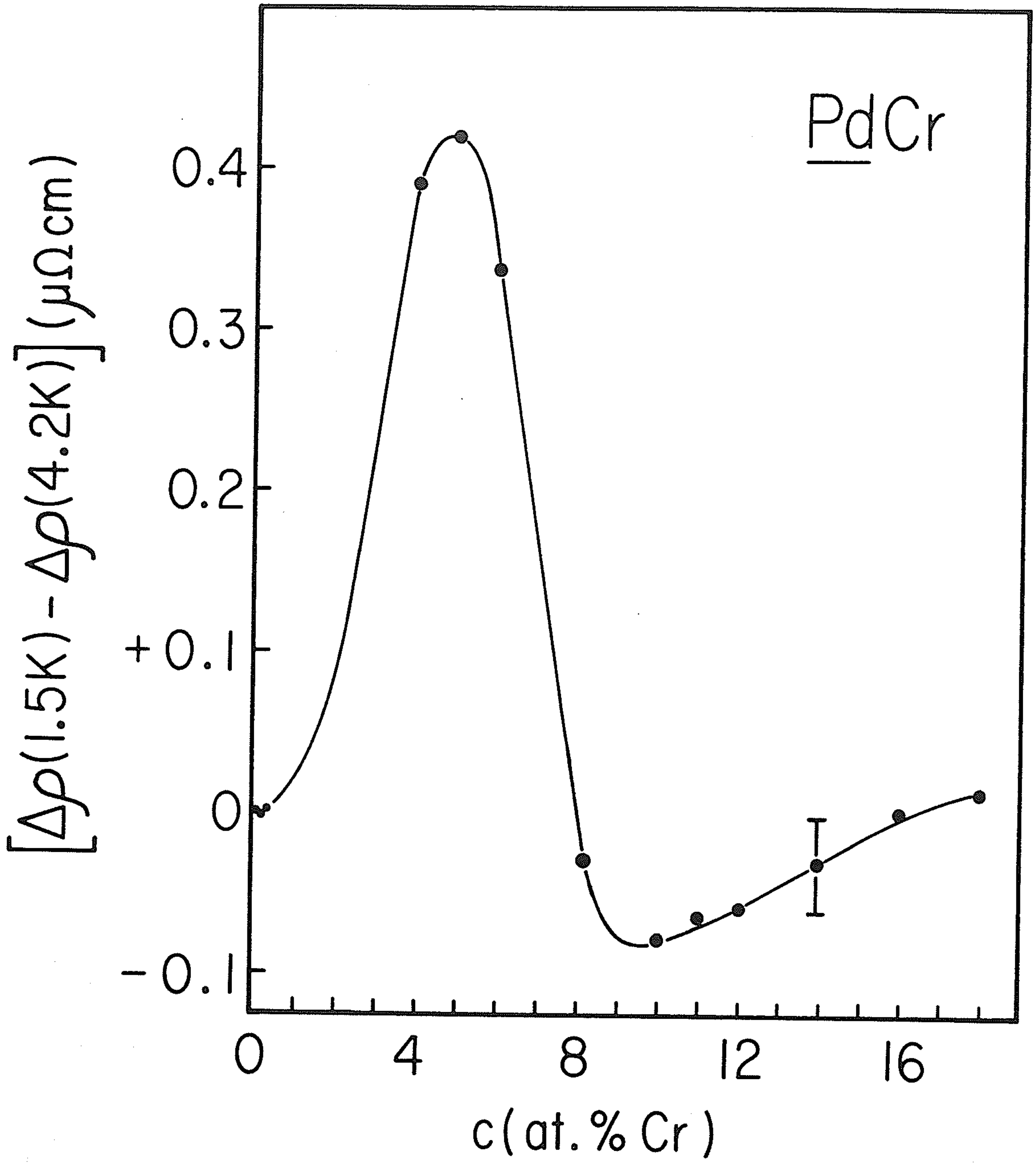

FIG.3.6-3. A plot of $\Delta\rho(1.5K) - \Delta\rho(4.2K)$ as a function of the nominal Cr concentration for PdCr alloys containing between .05 and 18 at. % Cr.

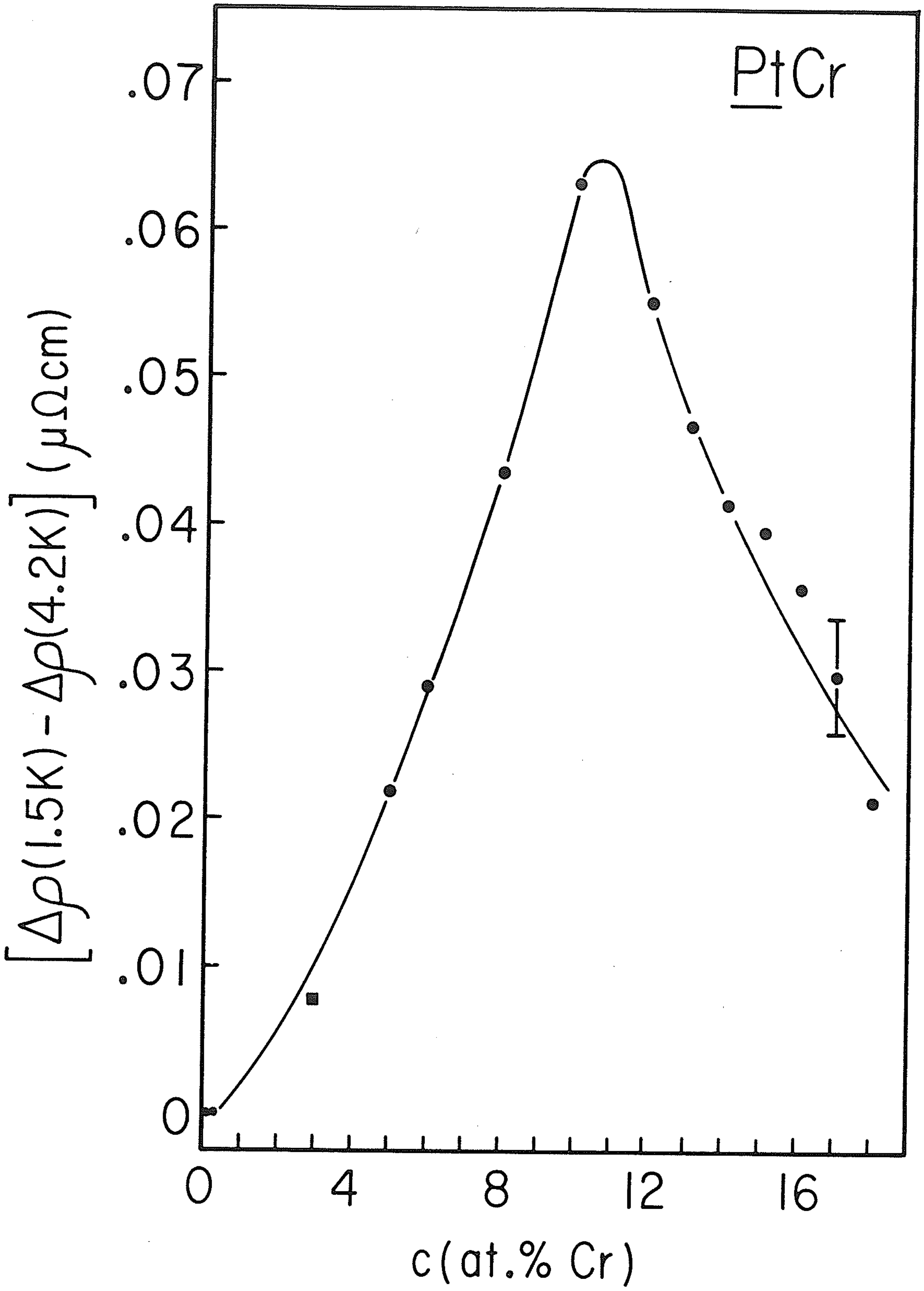

FIG.3.6-4. A plot of $\Delta\rho(1.5K) - \Delta\rho(4.2K)$ as a function of the nominal Cr concentration for PtCr alloys containing between .05 and 18 at. % Cr.

spin may be regarded as fluctuating with time (whether the system is described by the s-d model or the LSF model), so that the time-averaged value of the local moment vanishes. As the impurity concentration is increased above the dilute ($c \rightarrow 0$) limit, the impurities begin to interact and the measured incremental resistivity deviates from the isolated-impurity curve at low temperatures, i.e., at temperatures where the thermal energy, $k_B T$, is less than the interaction energy. The effect of interactions at low temperatures will be twofold. Initially, the interactions will tend to slow down or stabilize the spin fluctuations at individual impurity sites, thus increasing the time-averaged value for the z-component of the impurity spin $\langle S_z \rangle$. Such moment stabilization is equivalent to lowering the single-impurity characteristic temperature θ_s, and this leads to an increase in both the low-temperature incremental resistivity, $\Delta\rho(T \ll \theta) \propto (Bc/2\theta_s^2)T^2$, and the low-temperature slope, $d[\Delta\rho(T \ll \theta)]/dT = (Bc/\theta_s^2)T$, over their isolated-impurity values. This effect is illustrated in FIG.3.6-5(b). As the concentration is increased, the interactions also induce correlations between fluctuating spins on different impurity sites, and this leads to a decrease in the resistivity below the isolated-impurity curve due to the "freezing out" of second-order spin-flip scattering processes [1] (which are responsible for the logarithmic increase in $\Delta\rho(T)$ with decreasing temperature), as shown in FIG.3.6-5(c). Simple mean-free-path considerations suggest that, as the solute concentration is increased from the isolated-impurity regime, moment stabilization will dominate initially, with further

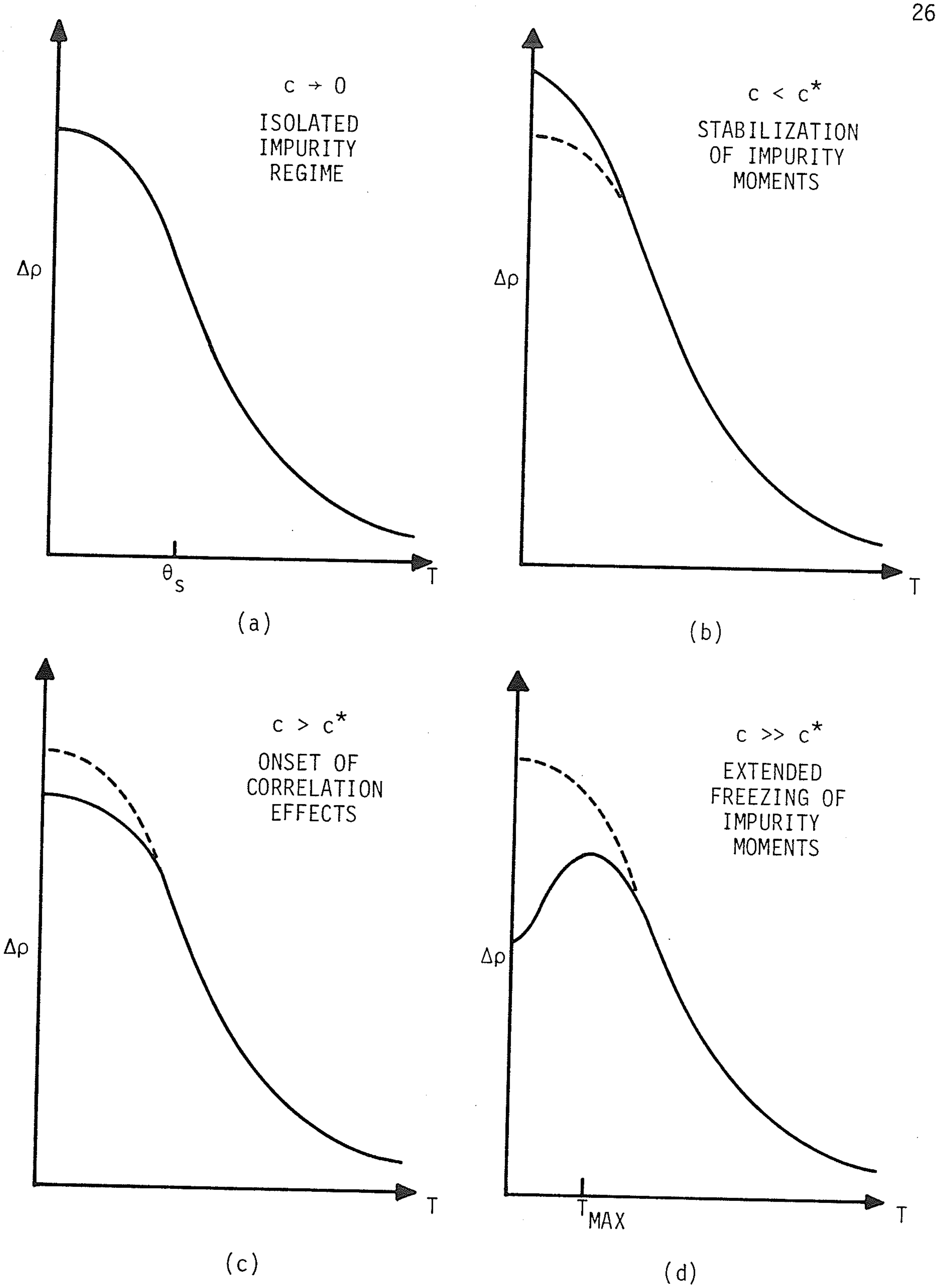

FIG.3.6-5. The effects of interactions between impurities on the incremental resistivity in various concentration regimes. The dotted curves represent the behaviour of an isolated impurity.

increases in the concentration enhancing the role played by impurity-impurity correlations. In figures (b) and (c), c^* denotes the critical concentration at which correlation effects begin to dominate moment stabilization effects. Finally, increasing the solute concentration eventually results in an extended (or long range) freezing of the impurity moments into a ferromagnetic or spin glass structure at low temperatures, and this is characterized by a maximum in the incremental resistivity due to the removal of first order spin-flip scattering processes [37], as shown in FIG.3.6-5(d). Clearly the type of behaviour outlined in FIG.3.6-5 for the incremental resistivity implies that the difference $\Delta\rho(1.5K) - \Delta\rho(4.2K)$ should initially increase with increasing impurity concentration as interactions stabilize the spin fluctuations at individual impurity sites, pass through a maximum around c^*, and then decrease as interactions induce correlations between fluctuating spins at different impurity sites, with negative values for $\Delta\rho(1.5K) - \Delta\rho(4.2K)$ signalling the onset of an extended freezing of the impurity spin system. FIGS.3.6-3 and 3.6-4 show that both PdCr and PtCr exhibit this type of behaviour, with $c^* \simeq 5$ at. % for PdCr and 11 at. % for PtCr. Moreover, from these figures it can be seen that, for Cr concentrations $c \leq 18$ at. %, only the PdCr system exhibits features characteristic of an extended freezing of the impurity moments, i.e., negative values for $\Delta\rho(1.5K) - \Delta\rho(4.2K)$ and a maximum in the incremental resistivity. However, the delay in the appearance of a resistivity maximum in PdCr until the Cr concentration has reached 8 at. %, and the absence of any such anomaly in PtCr below 18 at. %, suggests that the conventional, long range RKKY coupling is relatively ineffective in these systems, with any magnetic freezing arising primarily from direct d-d overlap between nearest-neighbour Cr impurities. The resistivity measurements on PdCr in Sec.3.4 suggest that the ground state resulting from such direct overlap is similar to that occurring in spin glasses. In PtCr, the appearance of extended magnetic freezing (manifested by the presence of a peak in the low-field A.C. susceptibility) coincides with the onset of an atomic order-disorder transformation, from which it is inferred that local environmental effects (i.e., nearest- and next-nearest-neighbour Cr-Cr interactions) play an important role in stabilizing the impurity moments and in determining the nature of the frozen ground state.

References

1. J. Kondo, Progr. Theoret. Phys. (Kyoto) 32, 37 (1964).
2. M. D. Daybell and W. A. Steyert, Rev. Mod. Phys. 40, 380 (1968).
3. M. A. Ruderman and C. Kittel, Phys. Rev. 96, 99 (1954) ; T. Kasuya, Progr. Theoret. Phys. (Kyoto) 16, 45 (1956) ; K. Yosida, Phys. Rev. 106, 893 (1957).
4. B. R. Coles, in *Amorphous Magnetism*, edited by H. O. Hooper and A. M. de Graaf (Plenum, New York, 1973), pp. 169-184.
5. J. W. Loram, R. J. White and A. D. C. Grassie, Phys. Rev. B5, 3659 (1972).
6. A. B. Kaiser and S. Doniach, Intern. J. Magnetism 1, 11 (1970).
7. N. Rivier and V. Zlatic, J. Phys. F : Metal Phys. 2, L87 (1972) ; J. Phys. F : Metal Phys. 2, L99 (1972).
8. H. Suhl, Phys. Rev. Lett. 20, 656 (1968) ; J. W. Garland, K. H. Bennemann, A. Ron, and A. S. Edelstein, J. Appl. Phys. 41, 1148 (1970) ; B. Giovannini, Phys. Lett. 31A, 62 (1970) ; D. Gainon and A. J. Heeger, Phys. Rev. Lett. 22, 1420 (1969).
9. A. Tari and B. R. Coles, J. Phys. F : Metal Phys. 1, L69 (1971).
10. B. V. B. Sarkissian and B. R. Coles, J. Less Common Metals 43, 83 (1975).
11. W. M. Star, E. de Vroede and C. van Baarle, Physica 59, 128 (1972).
12. J. S. Dugdale and Z. Basinski, Phys. Rev. 157, 552 (1967).
13. F. C. C. Kao, M. E. Colp and G. Williams, Phys. Rev. B8, 1228 (1973).
14. E. K. Azarbar and G. Williams, Phys. Rev. B14, 3301 (1976).
15. A. I. Schindler and M. J. Rice, Phys. Rev. 164, 759 (1967).

16. P. Lederer and D. L. Mills, Phys. Rev. 165, 837 (1968).
17. G. Williams, Solid State Comm. 19, 821 (1976).
18. L. L. Hirst, Phys. Kond. Mat. 11, 255 (1970).
19. L. L. Hirst, in Magnetism and Magnetic Materials - 1974, edited by C. D. Graham, Jr., G. H. Lander, and J. J. Rhyne, AIP Conference Proceedings No. 24 (American Institute of Physics, New York, 1975), p. 11.
20. W. M. Star, B. M. Boerstel, J. E. van Dam and C. van Baarle, in Proceedings of the 11th International Conference on Low Temperature Physics, edited by J. F. Allen, D. M. Finlayson and D. M. McCall (University of St. Andrews Press, St. Andrews, Scotland, 1969), p. 1280.
21. W. M. Star and B. M. Boerstel, Phys. Lett. 29A, 26 (1969).
22. R. Schwaller and J. Wucher, Compt. Rend. 264B, 116 (1967).
23. B. Caroli, J. Phys. Chem. Solids 28, 1427 (1968).
24. A. Blandin, in Proceedings of the International School of Physics "Enrico Fermi", Course XXXVII, 1966 (Academic Press, New York, 1967).
25. Although Eq.(3.3-4) is valid only for large values of R, it is used here to estimate the nearest-neighbour interaction energy since, at these concentrations, there must be a substantial fraction of near-neighbour impurities.
26. J. Friedel, Nuovo Cimento Suppl. 7, 287 (1958).
27. A. Blandin, in Magnetism, Vol. 5, edited by H. Suhl (Academic Press, New York, 1973), p. 73.
28. O. Krogh Andersen, Phys. Rev. B2, 883 (1970).
29. O. Krogh Andersen and A. R. Mackintosh, Solid State Comm. 6, 285 (1968).

30. The observation of a well-defined $\ell n\, T$ term in $\Delta\rho(T)$ for AuCr in the liquid-helium range implies an LSF temperature θ well below 1K.

31. R. E. Watson, S. Koide, M. Peter and A. J. Freeman, Phys. Rev. 139A, 167 (1965) ; R. E. Watson and A. J. Freeman, Phys. Rev. 152, 566 (1966) ; Phys. Rev. 178, 725 (1969) ; R. E. Watson, A. J. Freeman and S. Koide, Phys. Rev. 186, 625 (1969).

32. See, for example, R. M. White, "Quantum Theory of Magnetism" (McGraw-Hill, New York, 1970), p. 13.

33. See, for example, Ref. 32, p. 198.

34. D. K. C. Macdonald, W. B. Pearson, and I. M. Templeton, Proc. Roy. Soc. (London) A266, 161 (1962).

35. T. Moriya, in Proceedings of the International School of Physics "Enrico Fermi", Course XXXVII, 1966 (Academic Press, New York, 1967).

36. In the absence of detailed information, the effects of exchange enhancement on the "conventional" RKKY oscillations are neglected (although, according to I. A. Campbell, J. Phys. C 1, 687 (1968), the d-band polarization is antiparallel to the Cr moment ; however, the spatial extent of this polarization is not currently known).

37. K. Yosida, Phys. Rev. 107, 396 (1957). The expression given in Eq.(3.3-15) is valid when potential scattering is much stronger than exchange scattering.

38. A. J. Freeman and R. E. Watson, Phys. Rev. 152, 566 (1966).

39. M. Peter, J. Dupraz and H. Cottet, Helv. Phys. Acta 40, 301 (1967).

40. J. J. Vuillemin, Phys. Rev. 144, 396 (1966).

41. G. Williams, G. A. Swallow and J. W. Loram, Phys. Rev. B3, 3863 (1971).

42. J. P. Burger, Ann. Phys. (Paris) 9, 345 (1964).

43. J. W. Loram, G. Williams and G. A. Swallow, Phys. Rev. B3, 3060 (1971).

44. J. W. Loram, R. J. White and A. D. C. Grassie, Phys. Rev. B5, 3659 (1972).

45. G. G. Low and T. M. Holden, Proc. Phys. Soc. (London) 89, 119 (1966).

46. A. B. Kaiser and S. Doniach, Int. J. Mag. 1, 11 (1970).

47. M. P. Maley, R. D. Taylor and J. L. Thompson, J. Appl. Phys. 38, 1249 (1967).

48. H. Nagasawa, Solid State Comm. 10, 33 (1972).

49. J. Souletie, J. Low Temp. Phys. 7, 141 (1972).

50. T. A. Kitchens, W. A. Steyert and R. D. Taylor, Phys. Rev. 138A, 467 (1965).

51. H. Nagasawa, J. Phys. Soc. (Japan) 27, 787 (1969).

52. It is assumed that internal fields (interactions) stabilize $\left\langle S_{eff} \right\rangle T_{MAX}$ at its T_{MAX} value for temperatures below T_{MAX}.

53. P. J. Ford and J. A. Mydosh, J. Phys. (Paris) 35, 241 (1974) ; J. A. Mydosh, P. J. Ford, M. P. Kawatra and T. E. Whall, Phys. Rev. B10, 2845 (1974).

54. B. V. B. Sarkissian and R. H. Taylor, J. Phys. F : Metal Phys. 4, L243 (1974).

55. N. Rivier and K. Adkins, J. Phys. F : Metal Phys. 5, 1745 (1975).

56. P. J. Ford, E. Babic, and J. A. Mydosh, J. Phys. F : Metal Phys. 3, L75 (1973).

57. O. Laborde and P. Radhakrishna, J. Phys. F : Metal Phys. 3, 1731 (1973).

58. Y. Shiozaki, Y. Nakai, and N. Kunitomi, Solid State Comm. 12, 429 (1973).

59. A. I. Schindler and D. J. Gillespie, in Proceedings of the 12th International Conference on Low Temperature Physics, Kyoto, edited by E. Kanda (Keigaku, Tokyo, 1971), page 777.

60. C. W. Chen, L. R. Edwards and S. Legvold, Phys. Status Solidi 26, 611 (1968) ; L. R. Edwards, C. W. Chen, and S. Legvold, Solid State Comm. 8, 1403 (1970).

61. O. Laborde, B. Loegel, and P. Radhakrishna, J. Phys. (Paris) C4 35, 247 (1974).

62. R. W. Cochrane, R. Harris, J. O. Strom-Olsen, and M. J. Zuckermann, Phys. Rev. Lett. 35, 676 (1975).

63. M. Hansen, "Constitution of Binary Alloys" (McGraw-Hill, New York, 1959), p. 553.

64. F. C. C. Kao and G. Williams, Phys. Rev. B7, 267 (1973).

65. H. Claus and J. A. Mydosh, Solid State Comm. 14, 209 (1974).

66. P. J. Ford and J. A. Mydosh, Phys. Rev. B14, 2057 (1976).

67. This, for our hairpin-shaped samples with the dimensions given previously, is estimated to be $\chi \simeq 10^{-5}$ emu/gm-Oe, corresponding to an induced magnetization of about 1.6×10^{-5} emu/gm. for the A.C. driving fields used.

68. V. Cannella and J. A. Mydosh, Phys. Rev. B6, 4220 (1972).

69. J. P. Burger and D. S. MacLachlan, Solid State Comm. 13, 1563 (1973).

70. J. P. Burger, D. S. MacLachlan, R. Mailfert and B. Souffache, in Proceedings of the 14th International Conference on Low Temperature Physics, edited by M. Krusius and M. Vuorio (American Elsevier Publ. Co., New York, 1975), 3, 278

71. M. F. Sykes and J. W. Essam, Phys. Rev. 133A, 310 (1964).

72. M. J. Bensus and A. J. P. Meyer, Phys. Stat. Solidi (b) 55, 521 (1973); Phys. Stat. Solidi (b) 58, 533 (1973).

73. S. P. Pickart and R. Nathans, J. Appl. Phys. 34, 1203 (1963).

74. R. Kuentzler and D. E. Moody, in Proceedings of the International Conference on Magnetism (Publ. House Nauka, Moscow, 1973) 6, 312.

75. L. E. Wenger and P. H. Keesom, Phys. Rev. B11, 3497 (1975).

76. R. L. Rusby, J. Phys. F : Metal Phys. 4, 1265 (1974).